Fabrication and characterization of transition metal dichalcogenide alloys and their heterostructures

The University Of Sheffield.

Alessandro Catanzaro

Department of Physics and Astronomy
The University of Sheffield

A thesis submitted in partial fulfilment of the requirements for the degree of
Doctor of Philosophy

June 2019

To Elsa.

Declaration

I hereby declare that the contents of this dissertation are original and have not been submitted in whole or in part for consideration for any other degree or qualification in this, or any other university. This dissertation is my own work, the contribution to the data shown and results presented in each of the chapters are listed below:

- **Chapter four**
  This chapter is extracted from a paper submitted in Nano Letters by E. M. Alexeev (I am the second-name author) to which I considerably contributed for the sample fabrication, optical measurements (either at high and low temperature), data analysis and scientific discussion about the results. O. V. Skrypka also contributed for the optical measurement and data analysis. I developed the thermal annealing process, designing and performing all the related experiments. I performed the AFM scanning also performed the data processing. All the work presented in this chapter that is not included in the original paper was done by me. CVD samples were grown by Pramoda K. Nayak, Seongjoon Ahn, and Hyeon Suk Shin from Ulsan National Institute of Science and Technology (UNIST) and Sangyeon Pak, Juwon Lee, and Jung Inn Sohn, from University of Oxford.

- **Chapter five**
  This chapter is originated by my principal PhD research project. A paper is in preparation with the content included in this chapter. This work was done by myself in large; I also contributed to supervision. A relevant help was provided by A. Genco for the optical and time-resolved measurements, data analysis and scientific discussion. A. Kozikov and J. Howarth (National Graphene Institute, Manchester) contributed to sample fabrication. L. Sortino contributed to lifetime measurements. D. Gillard, E. M. Alexeev and C. Louca contributed to sample fabrication and optical measurements. R. Pisoni and his supervisor, K. Ensslin trained me in the use of the glove box at ETH that I used to fabricate a portion of the fully encapsulated samples.

- **Chapter six**
  The data shown in this chapter are originated by a collaboration between me and O. V. Skrypka. A paper is in preparation with the content included in this chapter. I've fabricated all the samples and developed the procedure to identify multilayer materials. I've performed optical measurements and data processing with the contribution of O. V. Skrypka.

This dissertation contains fewer than 80,000 words excluding footnotes, bibliography and appendices.

Alessandro Catanzaro
June 2019

Acknowledgements

The first acknowledgement that I want to deliver is to the European Union. Since the M.Sc. my education was forged and supported by European projects, funded by the EU. And I think in this uncertain times, characterized more by the division that unity, it is important to give the deserved credit to what allow me to be here, writing this words.

After this necessary preamble, I would like to thank my supervisor: Prof. Tartakovskii for the sometimes complicated, but intriguing and never obvious research project that I undertake in the last three years of my life. This is a special thanks because I had the possibility to grow a lot, both scientifically and as a person, due to the vast freedom he always gave to me.

It should be not a surprise that the next places will be taken by Italians. Armando for the continuous support, as a scientist and as a person. I'll miss the pilgrimage to your office sometimes for questions and other times (a LOT of other times) just for boredom. Probably you'll miss a lot less, but I do understand you! I really think you pal save my entire PhD. I was, and still I am, proud of sharing my highest result so far with you.

I'll miss a lot of things about Ruggero: the discussions, the complaints about work and science, the Friday evenings spent watching Propaganda Live... But I don't want to tell about them. All I will instead say is just: thanks friend, thanks comrade. It has been a true surprise, but also a honour, to serve with you.

Thanks to Davide, although we share little times together in Sheffield, we have a lot of laughs together, I wish all the best buddy, you'll be great!

Thanks to Giuseppe for the crazy discussion we had, but despite the unmentionable topics, it always carry a meaning inside them. Whether serious or not.

I want to thank Tom for all the support he gave to me, especially to improve a bit my horrible writing skills, revising with infinite patience all the stuff that I ask him to have a look on, even though he has been fairly repaid by a lot of DOC Italian food. I'll miss all the dinners we had together, and for sure I can tell that there will be no other like you to share with a fun story about Italy in front of a piece of cheese (which came from Italy as well).

Thanks to Pambos, for relieving me from the laboratory duties when I was too busy writing the thesis and questioning myself what I was doing with my entire life. You have

been a fantastic learner and I am sure that you will reach results that I could not even imagine now. But for now, keep exfoliating and searching!

Thanks to Poncho for the prompt response to my very unusual questions which with I bother him, from time to time. Dan for the discussion and the laughter we had, especially about the infinite black hole of stupidity which is Brexit. Eugene for the training and the useful suggestions.

Thanks to Luca for the sometimes harsh but never meaningless discussion, we had such a great time in our never ending pilgrimage across Europe for the Spin NANO events. Also thanks to the other crew: Matt, Najwa, Alejandro, Marco, Riccardo, Sigurd, Yanick, Fabio, Samarth, Stephan, Andrii, Matteo, Valeria, Aroosa. Thank you guys, you all give me a lot!

And also I would like to thank the hidden mans behind the scene or, more precisely, the hidden women: Sandrine for the infinite passion she put in teaching us what does it mean become excellent professionals and not only good scientist. Angie for the caring attention she put in her HR position and the continuous, infinite support. Sally for the excellent network organization, and the little attention that make not only my day, but the entire PhD.

A very special thanks to Rony, for mentoring me when I was younger, and giving me the real and truly life changing experience in his research group, in Mons. Also I would like to thanks all the professor of my undergraduate courses, with the special mention of Prof. D'Urso for her excellent and always caring supervision in the most troubled time of my M. Sc.

Thanks to my family that I had to left behind for long month, but despite an entire continent of distance, always find a way to make me feel better in troubled periods. Thanks also for the time we spent together during the holidays I get during these three years.

I also want to thank from the deepest of my heart the friends that I could not see as much as I would, but nevertheless will forever be in my mind... in my heart... in my soul: Salvo, Michela, Salvo and Daniela, Viviana,Antonio and Rosa and their nephew Raffaele, Jessica, Andrea, Silvia, Adriana, Anita. If it was not for you guys, I wouldn't be here, writing this words. Thank you, thanks to all of you.

Last but not least, I want to thank Stefania. For giving me something that in spite of all my titles and knowledge, I would've never really understood... if not thanks to her. And, for this reason, I will never forget her. And I say to her: thank you. Thank you, my friend.

Per aspera ad astra.

Abstract

Two-dimensional materials captured the attention of a huge number of researchers across the world. Their attractive properties caused an exponential increase of the investigation efforts, rapidly promoting them to one of the most researched platform for fundamental research and practical application. Also, the possibility to isolate and stack different 2D materials on top of each other open new prospectives and opportunities to fabricate atomically-thick devices, which are named van der Waals heterostructures. In 2D materials research, these represent the ultimate frontier for design and assembly of highly tailored nanometer-size devices. In this thesis, I report about the results of the optical investigations of such van der Waals heterostructures, focusing mostly on transition metal dichalcogenide heterobilayers. They form an atomically thin type-II heterojunction due to the materials band offset, which causes the rise of interlayer excitons, formed by electrostatically-bound carriers confined in different layers.

In particular, I present the photoluminescence imaging technique by the mean of a modified optical microscope. With this imaging technique it is possible to unambiguously identify semiconductor monolayers on different substrates. Also, it is possible to monitor the electronic coupling of two vertically stacked transition metal dichalcogenide and the formation of interlayer excitons.

In the second part, I present the results of band structure engineering of a series of $WSe_2/Mo_xW_{(1-x)}Se_2$ heterobilayers. The effect of the band offset (controlled via chemical composition) on the PL emission of the interlayer excitons is observed. The gradual change from a hetero to homobilayer is studied and a general model is proposed.

In the third part, I report on a study of $Mo_xW_{(1-x)}S_2$ alloys in their mono- bi- and trilayer from. The optical properties of these samples are probed to study the band structure dependence on the sample thickness and the material composition.

Table of contents

List of figures **xv**

List of tables **xxvii**

1 Two-dimensional materials: fundamental properties and devices **1**

1.1 Structure and properties of two dimensional materials 1

1.1.1 Graphene 2

1.1.2 Hexagonal boron nitride 4

1.2 Transition metal dichalcogenides 5

1.3 Band structure of TMDs and the role of quantum confinement 7

1.4 Intralayer excitons and their properties 10

1.5 Valley properties of TMDs 12

1.5.1 Temperature dependence of PL emission in TMDs 14

1.5.2 Defect-bound states 16

1.5.3 Results of reflectance contrast (RC) measurements in TMDs 18

1.6 Transition metal dichalcogenide alloys 20

1.6.1 Photoluminescence of TMD alloys 21

1.6.2 Orbital contribution in TMD alloy band structure 23

1.6.3 Spin orbit splitting in TMD alloys and temperature dependence of their optical properties 24

2 Van der Waals heterostructures, heterobilayers and their properties **27**

2.1 Van der Waals heterostructures 27

2.2 TMD Heterobilayers 31

2.3 Theory of heterobilayer and orbital hybridization 33

2.4 Formation of interlayer excitons and optical investigation of TMDs heterobilayers 35

2.4.1 Interlayer excitons in van der Waals heterobilayer 35

2.4.2 Effect of twist angle on the IX optical properties 39
2.4.3 Electrical dipole and long lifetimes of IX 40
2.5 Structure of the IX PL emission 43

3 Materials and Methods 49
3.1 Micromechanical exfoliation 49
3.2 Flake identification and crystal axes recognition 54
3.3 Transfer setup and procedures 59
3.3.1 PDMS-based fabrication 61
3.3.2 PMMA-based fabrication 63
3.3.3 PC-based fabrication 64
3.3.4 Comparison 66
3.4 Micro-PL/micro RC optical setup 67

4 Imaging of Interlayer Coupling in van der Waals Heterostructures Using a Bright Field Optical Microscope 71
4.1 Abstract 71
4.2 Introduction 72
4.3 Experimental procedure and PL imaging of monolayer TMDs 75
4.4 Selective imaging and monitoring of interlayer coupling in heterobilayers . 80
4.5 Investigation of thermal annealing and self-cleaning mechanism process . . 84
4.6 Observation of the formation of interlayer excitons in TMD heterobilayers using PL imaging 94
4.7 Twist angle dependence of the interlayer charge transfer 97
4.8 Conclusions 99

5 Band-structure engineering in alloy-based transition metal dichalcogenide van der Waals heterobilayers 101
5.1 Abstract 101
5.2 Conceiving the experiment 103
5.3 State of the art 105
5.4 Optical characterization of TMDs alloys 109
5.5 Emergence of IX photoluminescence in alloy-based heterostructures 112
5.6 PL characterization of alloy-based heterobilayers with varied composition of $Mo_xW_{(1-x)}Se_2$ 117
5.7 Reflectance-contrast characterization of alloy-based heterobilayers with varied composition of $Mo_xW_{(1-x)}Se_2$ 122

5.8 Probing the IX behavior . . . 124
5.9 Discussion . . . 128
5.10 Conclusions . . . 131

6 Optical investigation of $Mo_xW_{(1-x)}S_2$ transition metal dichalcogenide alloys 133
6.1 Abstract . . . 133
6.2 Introduction . . . 134
6.3 Identification of $Mo_xW_{(1-x)}S_2$ flake thicknesses trough optical contrast . . . 137
6.4 Optical analysis of monolayer $Mo_xW_{(1-x)}S_2$ samples. . . . 142
6.5 Optical analysis of bilayer $Mo_xW_{(1-x)}S_2$ samples. . . . 144
6.6 Optical analysis of trilayer $Mo_xW_{(1-x)}S_2$ samples. . . . 148
6.7 Discussion . . . 151
6.8 Conclusions . . . 155

7 Conclusions 157
7.1 Suggestions for future work . . . 159

References 161

List of figures

1.1 Schematic structure of the different dimensionality of carbon-based allotropes. It is highlighted how graphene is the source material for all the different structures, via folding (fullerenes - 0D), wrapping (carbon nanotubes - 1D) or stacking (graphite - 3D). Image adapted from ref.[5]. 3

1.2 Representation of the different 2D materials and their respective energy gap range as a function of their chemical structure. The visible range is highlighted by the rainbow on the top. Image adapted from ref.[10]. 4

1.3 **a)** Top, lateral and in-space view of the TMD single layer lattice structure. Purple circles are the transition metals atoms while yellow circles represent the chalcogen. **b-e)** Evolution of the band structure in MoS_2. The layer thickness is indicated in the inset of the image, the energy gap shift from momentum indirect to momentum direct moving from bilayer to monolayer. Image adapted from ref. 6

1.4 Representation of the orbital contribution across the BZ for MoS_2. The relative contribution is highlighted with dots of different sizes. Aquamarine color **(Panel a)** represent Mo- d_{z^2} orbitals (d^0 in the image) oriented perpendicularly to the TMD plane. Dark blue colo **(Panel b)** represent Mo- d_{xy} and Mo- $d_{x^2-y^2}$ orbitals (d^2 in the image) oriented parallel to the TMD plane. Red color **(Panel c)** represent S- p_{xy} orbitals oriented parallel to the TMD plane. Green color **(Panel d)** represent S- p_z orbitals oriented perpendicularly to the TMD plane. The second row **(Panel e-h)** displays the same calculations in the form of bands. Image adapted from ref.[17]. 9

1.5 **a)** Electron-hole interaction in 3D and 2D limits. Panel **b)** show the differences in the optical absorption. Image adapted from ref.[23]. 11

1.6 **a)** Lateral view of the spin split valleys in a TMD. The effect is shown only for the VB, where is particularly prominent, and ignored in the CB. Image adapted from ref.[32]. **b)** Optical selection rules for the K and K' valleys, they couple with circular polarized light with opposite helicity. Image adapted from ref.[33]. **c)** Summary of the valley structure in Mo- and W- based TMDs. The red curve indicate the spin up states, blue curves indicate spin down states. The yellow and gray arrow indicate spin allowed (optically bright) and spin forbidden (optically dark) transitions in the adjacent valleys. 13

1.7 **a)** Temperature dependence of the PL in WSe_2 and **b)** $MoSe_2$ monolayers. Green spectra are taken at low temperature, red spectra at high temperature. **c)** Integrated intensity of the PL emission for the two materials. Image adapted from ref.[36]. 15

1.8 **a)** Spin allowed transitions in a WX_2 material. The two edge states are antiparallel. Blue arrow indicates the A excitons while orange arrow indicate B excitons. **b)** Reflectance-contrast spectra of four TMDs. The A excitons peak is fitted with a coloured line. Image adapted from ref.[45]. 19

1.9 **a)** Schematic in plain structure of the $Mo_xW_{(1-x)}S_2$ alloy. Light blue dots are W atoms, dark gray dots are Mo atoms, yellow dots are sulphur atoms. **b)** PL emission energies as a function of the alloy composition for A and B excitons (red and black squares respectively); blue line and dots represent the theoretical calculations. Image adapted from [56, 61]. 22

1.10 **a)** Band structure at K point of $Mo_xW_{(1-x)}Se_2$ alloys. The solid black and dashed blue line indicate the two spin split states respectively. The central panel show the absence of degeneracy in the CB at a specific sample stochiometry. **b)** Experimental spectra at low temperature of three $Mo_xW_{(1-x)}Se_2$ alloys, the A exciton transition is indicated in each spectra. The W- composition is indicated in the inset. Image adapted from ref.[25]. . 25

2.1 LEGO model of a van der Waals heterostructure. Different materials are represented by different colors. Image adapted from ref.[9]. 28

2.2 **a)** PL spectra of a free standing flake of $MoSe_2$ on SiO_2. The FWHM of the X^0 is indicated. **b)** PL spectra of a hBN encapsulated $MoSe_2$ flake. The linewidth is much narrower. Image adapted from ref.[43]. 30

2.3 **a)** Schematic band structure of the two isolated TMD flakes. Each one exhibit their own intralayer excitons.**b)** Formation of the heterobilayer, the type-II band alignment causes the migration of the charge carriers (blue and red arrow respectively). The intralayer exciton emission is suppressed as a consequence of the charge separation. **c-e)** Bright field, dark field and PL imaging of the sample. The PL is suppressed in the area of the heterostructure. 32

2.4 Band structure of the $MoSe_2$/WSe_2 heterostructure. The red and blue spots at the K point of the BZ represent the Mo- and W- states respectively. The inset shows the wavefunction distribution of such states which is confined in the two layers, respectively. In the Λ (Q) point of the CB and the Γ point of the VB the green spots indicate a hybrid nature of the valley. The wavefunction is distributed in both layers. Image adapted from ref.[86]. 34

2.5 **a)** Photoluminescence of isolated WSe_2 monolayer (top panel), $MoSe_2$/WSe_2 heterobilayer (middle panel) and isolated $MoSe_2$ monolayer (bottom panel) at low temperature. Image adapted from ref.[83]. **b)** Band structure at the K point of a $MoSe_2$/WSe_2 heterobilayer. The solid green and red lines indicates the band edge states of the two materials, the dashed arrows represent the excitons binding energies for Mo (green) and W (red) DX. The binding energy of the IX is represented by the blue dashed arrow. Solid arrows indicate the energy of the photons originated from each optical transition. It can be observed that the interlayer exciton emission (blue solid arrow) is at lower energies than the two intralayer excitons emissions (red and green solid arrows). Image adapted from ref.[97]. 36

2.6 **a)** Lateral view of the device. The hBN act as a spacer between the two TMD flakes. **b)** PL spectra of the sample. When the numbers of hBN layers overcome three, the two TMD layers show unperturbed PL emission and the interlayer coupling is suppressed. Image adapted from ref.[69]. 38

2.7 **a)** Momentum mismatch of the K valleys of the two materials in a heterobilayer generated by the twist angle. The radiative recombination can occurr if their momentum gap ΔK is compensated by a lattice phonon. Image adapted from ref.[113]. **b)** Effect of twist angle on the IX PL emission. For large twist angles the IX emission is strongly quenched, as a consequence of the momentum mismatch of the K valleys. Image adapted from ref.[101]. . . . 38

2.8 **a)** Energy of the $MoSe_2$/WSe_2 interlayer exciton peak versus the twist angle. A redshift of 45 meV can be observed. Image adapted from ref.[101]. **c)** IX PL emission energies for MoS_2/WSe_2 heterobilayers (red dots) with different twist angles. The calculated interlayer distance (black dots) is overlapped and follow the same trend. Image adapted from ref.[114]. 39
2.9 **a)** Lateral view of the device used by Rivera et al. [83]. The IX dipoles are shown overlapped with the sample structure. **b)** Effect of the band structure for an unbiased and biased sample respectively. The band edge states of both materials are modified and the band offset is increased. **c)** Map of IX PL as a function of applied gate voltage. The IX peak blueshift of 45 meV as the gate voltage is reduced. Image adapted from ref.[83]. 41
2.10 PL lifetimes of the interlayer excitons in co- and cross-polarization of the excitation and detection (top and bottom panel, respectively). The data are taken at 10K under moderate pumping power (10 μW) and reveal a lifetimes of tens of ns. Image adapted from ref.[100]. 42
2.11 PL spectra of a $MoSe_2$/WSe_2 heterobilayer (red curve). The spectra is fitted with two Gaussians (blue and green for IX and IX', respectively). The black dashed line represents the fit sum. 44
2.12 **a)** IX PL emission spectra from ref.[83] (black curve). The two Lorentian curves represent the two transitions (red and green curves, respectively). Blue curve indicates the fit sum. **b)** Schematic model of the origin if the double component of the IX. The two IX peaks observed are related to the two spin split states of $MoSe_2$ CB at the *K*point of the BZ. Image adapted from ref.[83]. 45
2.13 **a)** IX PL emission of the sample presented in ref.[128]. Two regions of the sample are displayed (green and red curve, respectively) The inset shows the splitting, the temperature and the probe wavelength. **b)** Calculated band structure of the $MoSe_2$/WSe_2 heterostructure. The black and gray dashed lines indicate the origin of the IX double peak structure. **c)** Schematic representation of the heterostructure band structure. Image adapted from ref.[128]. 46
2.14 **a)** PL spectra of the heterostructure presented in ref.[100]. The signal of $MoSe_2$and WSe_2 DX is increased for better visibility. The red and blue Gaussian peaks indicate the two components of the IX peak. **b)** Schematic model of the origin of the two IX components. Image adapted from Ref. [100]. 47

3.1 Steps of the micromechanical exfoliation: **a)** The bulk crystal is positioned on the sticky tape. **b)** The crystal is gently pressed to ensure the contact. **c)** The crystal is peeled off. Some material is left on the tape surface. **d)** The process is repeated until the tape is reasonably covered. **e)** Another piece of tape is put in contact on top of the thin crystals. **e)** Peeling the top tape away causes the micromechanical exfoliation. 51

3.2 Substrate dependent procedures. for PDMS (a-c) PMMA (d-f) and silicon (g-i). **a)** The tape is aligned with the PDMS layer. **b)** The adhesion is promoted by a gentle press with a cotton bud. **c)** The tape is peeled off. Some material will stay on the polymer. **d)** The tape is aligned on the PMMA-coated substrate when is still on the hotplate. **e)** A firm press ensure the contact between tape and polymer. **f)** When the substrate is cold the tape is peeled away. **g)** The silicon is heated up to 110°. **h)** The tape is put in contact with a gentle finger press. **i)** The tape is slowly peeled off. 52

3.3 **a)** Bright field image at 20X magnification of a WSe_2 monolayer on PDMS. The monolayer edges are highlighted in cyan. **b)** Same flake at 50X magnification. The contrast is enhanced. **c)** Bright field image at 20X magnification of a WSe_2 monolayer on PMMA/PMGI. The flake monolayer edges are highlighted in blue. **d)** Same image under green filter. The contrast of the monolayer is dramatically enhanced. **e)** Bright field image at 50X magnification of a WSe_2 monolayer on 90 nm SiO_2/Si. The monolayer edges are highlighted in green. **f)** Same flake at 100X magnification. The visibility is increased. In all the images the scalebar is indicated in red. 56

3.4 **a)** Schematic structure of a TMD monolayer. Yellow circle indicate the chalcogen atoms, red circles indicate transition metal atoms. The black dashed line indicate an increase of 30°each. The correspondent crystal axes are highlighted in green and blue for zigzag and armchair respectively. **b)** WSe_2 flake exfoliated on PMMA-PMGI. The edges are highlighted in white, the bold edges indicate the identified crystal axes. All of them are rotated by a multiple of 30°. **b)** WSe_2 flake exfoliated on PMMA-PMGI. No crystal axes could be identified. The scalebar is 10 μm. 58

3.5 **a)** Large view of the transfer setup. The critical component are indicated by red arrows. **b)** Detail of the mechanical arm and the hotplate. The critical component are highlighted as well. 61

3.6 Transfer process for flakes exfoliated on PDMS. 62

3.7 Transfer process for flakes exfoliated on PMMA/PMGI. The first five steps (I-V) are necessary to lift the membrane with the target flake, the last three step is the transfer process. 64
3.8 Transfer process for flakes exfoliated on 90 nm SiO_2/Si. The first five steps (I-V) represent the pickup process. These steps might be repeated multiple time to assemble the desired device (step VI). The last two steps show how to release the heterostructure. 66

4.1 **a)** Schematic representation of the PL imaging setup based on the optical microscope. **b-c)** bright field images of mechanically exfoliated few-atomic-layer crystals on PDMS substrates: WSe_2 in panel b and $Mo_{0.2}W_{0.8}Se_2$ in panel c. **d)** PL spectra recorded in monolayer (blue), bilayer (green), and trilayer (red) regions of the WSe_2 sample shown in panel b. **e)** PL image of the WSe_2 sample acquired with a 1 s acquisition time and 9.6x analog gain on the camera, showing PL from the monolayer region only. **f)** PL image of the $Mo_{0.2}W_{0.8}Se_2$ sample shown in panel c with clearly identifiable regions of a monolayer (yellow) and a bilayer (purple). Image recorded with 1 s acquisition time and 3.4x analog gain. 77
4.2 **a)** Bright field image of a WSe_2 flake on PMMA/PMGI substrate. The green color is due to a band edge filter used to enhance the contrast of the monolayer. The scalebar is 100 μm **b)** Dark field image of the same flake. The scalebar is 100 μm. **c)** PL image of the same flake. The image is acquired at 4 sec and 3.4x analog gain. The scalebar is 100 μm. **d)** Bright field image of a WSe_2 flake on PDMS substrate. The scalebar is 10 μm. **e)** Dark field image of the same flake. The transparency and uneven surface of the PDMS causes the prominent background. The scalebar is 10 μm. **f)** PL image of the same flake. The image is acquired at 4 sec and 3.4x analog gain. The scalebar is 10 μm. **g)** Bright field image of a WSe_2 flake on 90 nm SiO_2/Si substrate. The scalebar is 10 μm. **h)** Dark field image of the same flake. The scalebar is 10 μm. **i)** PL image of the same flake. The image is acquired at 4 sec and 3.4x analog gain. 79

4.3 **a)** Bright field image of a WSe_2 flake exfoliated onto PMMA-PMGI substrate under green illumination. **b)** PL image of the sample. The image is acquired at 4 sec and 3.4x analog gain. **c)** PL spectrum recorded in the monolayer region of the sample using a micro-PL setup. **d)** Bright field image of a $MoSe_2$ flake exfoliated onto PDMS. **e)** PL image of the sample. The image is acquired at 4 sec and 3.4x analog gain. **f)** PL spectrum recorded in the monolayer region of the sample using a micro-PL setup. The scalebar in the optical images is 10 μm. 81

4.4 **a)** Bright field image of a $MoSe_2/WSe_2$ heterostructure assembled on a Si/SiO_2 substrate by viscoelastic stamping. **b)** PL image of the sample acquired using a 2.06 (600 nm) longpass filter in front of the microscope camera, showing emission from the monolayer regions of both materials. **c)** Selective PL image of WSe_2 acquired using 1.65 eV (750 nm) bandpass filter for detection **d)** and 1.57 eV (790 nm) bandpass filters for detection. **e)** PL spectra acquired in the heterostructure (top), isolated $MoSe_2$ (middle) and WSe_2 (bottom) regions. 82

4.5 **a-c)** Bright field, dark-field, and PL images of a $MoSe_2$/ WSe_2 heterostructure before the annealing. **d-f)** bright field, dark-field, and PL images of the same structure after annealing in high vacuum at 120°C for 2 hours. All scale bars in the figure correspond to 10 μm. PL images are recorded with a 1 second acquisition time and 9.6x analog gain. 85

4.6 Bright field (first column), PL imaging (second column), and dark field images (third column), of a series of as-fabricated $MoSe_2$ flakes. The last columns show the AFM scan of the flakes. 87

4.7 Bright field (first column), PL imaging (second column), and dark field images (third column), of a series of $MoSe_2$ flakes after vacuum annealing. The conditions are displayed in the first column. The last columns show the AFM scan of the flakes after the annealing. 89

4.8 Evolution of the PL optical properties of $MoSe_2$ as a function of the annealing conditions. The details are shown in the inset of the graph on the left. PL intensity and linewidth are shown in the two panel on the right (top and bottom respectively). The spectral analysis was performed at T<10K. . . . 90

4.9 **a-b-c)** Bright field, dark-field, and PL images of a $MoSe_2$/ WSe_2 heterostructure before the annealing. **d, e, f)** Bright field, dark-field, and PL images of the same structure after annealing in high vacuum at 50°C for 2 hours. All scale bars in the figure correspond to 10 μm. PL images are recorded with a 1 second acquisition time and 9.6x analog gain. 91

4.10 **a-b)** RT PL of the $MoSe_2$/WSe_2 heterostructure before (a) and after (b) the annealing step, the probed location is identical. **c-d-e)** LT PL in three different region of the device after the annealing: isolated WSe_2 (c), isolated $MoSe_2$ (d) and heterobilayer region (e). The peak arising around 1.35 eV is related to the interlayer exciton emission. 93

4.11 **a-b)** Bright field and PL image of $MoSe_2$/WS_2 heterostructure. The thick lines indicate the crystal axes used for alignment. **c-d)** Bright field and PL image of the device after the thermal annealing. **e)** Band alignment of the presented device. Intralayer exciton (DX) emission is indicated by red and green arrow (for $MoSe_2$ and WS_2, respectively) while interlayer exciton (IX) emission is indicated by black arrows. 95

4.12 **a)** RT spectra of the $MoSe_2$/WS_2 heterostructure before the annealing. The $MoSe_2$ signal are manually enhanced for visibility, the scaling factor is indicated in the inset. **b)** LT spectra of the device before annealing. **c)** RT spectra of the $MoSe_2$/WS_2 heterostructure after the thermal annealing **d)** LT spectra of the heterostructure after the thermal annealing step. The black part of the spectra indicate the IX contribution. 96

4.13 **a)** Bright field image of a $MoSe_2$/WS_2 heterostructure assembled on a SiO_2/Si substrate from individually CVD-grown layers. Dashed white triangles indicate the orientation of the large triangular WS_2 flake, the one visible edge of which is marked by a solid white line. To make the relative rotation angles more obvious, the edges of the selected $MoSe_2$ monolayers were highlighted by solid colored lines. **b)** PL image of the sample showing varying degrees of the intralayer PL quenching in the overlap regions (see dark triangles), recorded with 10 s acquisition time and 9.6x analog gain. **c)** PL spectra measured in the heterobilayer regions with varying twist angles (shown on the right above each spectrum). The spectra are multiplied by the factors shown on the graph (on the right above each spectrum). The brightness indicated above each curve on the left is extracted from the PL image. 98

5.1 **a)** Lateral view of a random $Mo_xW_{(1-x)}Se_2$ heterostructure. The top layer of hBN may be present or not, depending on the fabrication procedure. The presence of intralayer excitons in $Mo_xW_{(1-x)}Se_2$ (red dashed line) and WSe_2 (blue dashed line) is shown next to the interlayer excitons (purple dashed line). The out of plane orientation of IX is evident. **b)** Corresponding band structure of the device, the gradient arrow indicate the effect of the stochiometry on the alloy band structure. Dashed blue line are the projection of WSe_2 CB and VB excitonic states. **c)** Schematic band structure of the experiment: six different alloys are shown)each one in a differnt color). Each is combined with WSe_2 (dashed blue line). The IX energy increase as the band offset is reduced. 104

5.2 **a)** Normalized PL spectra of isolated $Mo_xW_{(1-x)}Se_2$ alloys. The composition is indicated by the color gradient. **b)** Peak position of neutral (diamond) and charged (stars) excitons from PL (full) and RC (empty) data. **c)** RC spectra acquired on the same spot of the PL data. The parabola fitting is included (solid and dashed line for PL and RC data, respectively). **d)** *A*-*B* exciton energy difference as a function of alloy composition. The solid line is the corresponding linear fit. 110

5.3 **a)** BF image of the heterobilayer, grayscale color show the enhanced contrast where the two flakes overlaps. The red line is the silhouette of the $Mo_{0.85}W_{0.15}Se_2$ flake while green solid line indicates the WSe_2 flake. **b)** PL imaging of the heterostructure. The quenching of the PL signal in the heterobilayer region indicates the electronic coupling and the charge separation. **c)** LT PL map of the heterostructure in the IX region (1.3-1.45 eV energy range). Bright PL is detected in correspondence of the heterobilayer and absent in the other regions. **d)** LT PL map of the heterostructure in the DX region (1.5-1.7 eV energy range). The image look complementary to the one shown in panel c. **e)** PL spectra acquired in different point of the heterostructure, WSe_2 (green spectra), $Mo_{0.85}W_{0.15}Se_2$ flake (red spectra) and heterobilayer (blue spectra). 113

5.4 **a)** Power dependence spectra of DX in the heterostructure region. Color gradient indicates the power adopted (violet-low and brown-high) **b)** Powerdependence spectra of IX in the heterostructure region. **c)** Intensity of the DX (gray dots) IX (red dots) and IX' (blue dots) emissions as a function of pumping power. The DX show a linear trend while IX signal show nonlinear trend. **d)** Blueshift of the DX (gray dots) IX (red dots) and IX' (blue dots) under increasing pumping power. The data indicate the shift compared to the original position of the peak. 114

5.5 Lifetime of the IX in $Mo_{0.85}W_{0.15}Se_2/WSe_2$ heterostructure. The orange dot indicate the experimental data, blue line is the fitting curve, black line is the IRF. 116

5.6 **a)** Normalized PL spectra of the alloy-based heterobilayers. The color gradient indicate the composition of the alloy flakes. **b)** Peak position of the IX (squares) and IX' (circles) as a function of alloy composition, the error bars are contained in the point. Violet solid line and diamonds are the DX of isolated $Mo_xW_{(1-x)}Se_2$ alloys. Dashed black line indicate the expected trend where the IX can be tuned close in energy to DX. 118

5.7 **a)** Bright field microscope image of the $Mo_{0.21}W_{0.79}Se_2/WSe_2$ device. The red silhouette highlight the alloy monolayer, the blue silhouette highlight the monolayer WSe_2 and the light green sihlouette highlight the naturally exfoliated WSe_2. **b)** PL image of the device. It is possible to distinguishing a weak emission arising from both the heterobilayer and the bilayer WSe_2. **c)** Low temperature PL map of the device. The integration range is between 1.512 and 1.503 eV, focusing on the IX emission. The inset spectra show in red the targeted spectral region. **d)** Same LT PL map show in the previous panel but with a different integration range between 1.589 and 1.510 eV, focusing on the momentum-indirect transitions. The spectra in the inset show in red the spectral region. 120

5.8 Energy difference between IX and IX' as a function of alloy composition. . 121

5.9 **a)** Normalized RC spectra of the alloy-based heterobilayers. The colors gradient indicate the composition of the alloy flakes. **b)** Peak position of the alloy (triangle) and WSe_2 (circles) absorption peak as a function of the alloy composition in the device. When not displayed the error bars are contained in the point. Square dot indicate the *K*-*K* transition in momentum-indirect WSe_2 bilayer sample. Stars indicate the absorption energy of the hybridized transitions. 123

5.10 **a)** Intensity of the IX emission as a function of pumping power. The colored label indicate the amount of Mo in the alloy lattice structure. **b)** Blueshift of the IX peak in all the heterobilayers as a function of pumping power. **c)** Normalized PL of IX in different devices as a function of the time. The alloy composition is indicated in the legend. 125
5.11 IX lifetime as a function of the sample composition, the *y* axes is in log scale for better visibility. The dashed line indicate the experimental setup temporal resolution limit. 128
5.12 Proposed model of the evolution of the excitonic states in a heterobilayer. The composition is displayed in the top panel. The mid line represent the chemical structure of the heterobilayer. The last line show the evolution of the K and Q valleys. The solid arrow indicate the most energy favorable transition, while dashed lines indicate the competitive transition. 129

6.1 Microscope images of a WS_2 flake on 90 nm SiO_2/Si. Blue, red and green silhouettes highlights monolayer, bilayer and trilayer regions respectively. **a).** Optical bright field image of the sample. **b).** Dark field image. **c).** PL imaging, monolayers shine bright due to their direct gap. **d).** PL spectra of monolayer (blue) bilayer (red) and trilayer (green) compared to each other. . 138
6.2 **a)** Bright field image of a WS_2 flake on PDMS. The monolayer, bilayer and trilayer regions are highlighted in blue, red and green respectively. The optical contrast of each thickness is indicated in the inset. **b)** Correspondent PL image of the WS_2 flake. Emission can be detected in monolayer and bilayer areas. **c-d)** Bright field image of $Mo_{0.4}W_{0.6}S_2$ and $Mo_{0.8}W_{0.2}S_2$ flakes both on PDMS. The optical contrast is indicated in the inset for monolayer, bilayer and trilayer areas as well. The scale bar is 10 μm. . . . 139
6.3 Bright field (first column), dark field (second column) and PL images (third column) of a series of TMD alloy with a composition ranging from WS_2 (**a**) to MoS_2 (**i**). The colors vary from yellow to dark red. In the last column are indicated the values of the red, green and blue channel of the CCD. The scalebar of the sample pictures is 10 μm. 141

6.4 Optical characterization of monolayer $Mo_xW_{(1-x)}S_2$ samples. **a).** Photoluminescence spectra. *A* exciton (A) and charged excitons (A*) emission is detectable in all samples. *B* exciton signal (B) can be detected only for high molybdenum concentrations. **b).** Reflectance contrast spectra. *A* and *B* excitonic transitions are clearly detectable. **c).** Peak position versus x concentration in the sample stochiometry extracted from PL (solid squares and continuous lines) and RC (empty squares and dashed lines) fitting. Blue colour is related to *A* excitons, red colour for *B* excitons. **d).** *A*-*B* exciton splitting in monolayer versus x concentration in $Mo_xW_{(1-x)}S_2$ alloys. 143

6.5 Optical characterization of bilayer $Mo_xW_{(1-x)}S_2$ samples. **a)** Photoluminescence emission spectra. A-exciton (A) and indirect gap emission (I) are detectable for all compositions. B exciton (B) are visible only for high Molybdenum concentrations. **b)** Reflectance contrast spectra. A and B excitonic transition are labeled. **c)** Peak position extracted from PL (solid dots and continuous lines) and RC (empty dots and dashed lines) fitting. Blue colour is related to A excitons, red colour for B excitons, green for indirect emission (I). **d)** A-B excitons splitting (violet, calculated from RC data) and I-A energy difference (orange, calculated from PL data) in bilayer $Mo_xW_{(1-x)}S_2$ alloys. 146

6.6 Optical characterization of trilayer $Mo_xW_{(1-x)}S_2$ samples. **a)** Photoluminescence emission spectra. *A* excitons (A) and indirect gap emission (I) are detectable for all compositions. *B* excitons (B) are visible only for high molybdenum concentrations. **b)** Reflectance contrast spectra of the trilayer samples. *A* and *B* excitonic transitions are labeled. **c)** Peak position extracted from PL (solid dots and continuous lines) and RC (empty dots and dashed lines) fitting. Blue colour is related to *A* excitons, red colour for *B* excitons, green for indirect emission (I). **d).** *A*-*B* energy splitting (violet, calculated from RC data) and *I*-*A* energy difference (orange, calculated from PL data) in trilayer $Mo_xW_{(1-x)}S_2$ alloys. 149

List of tables

4.1 Summary of the values extracted from the AFM profiles before the annealing. 88
4.2 Summary of the values extracted from the AFM profiles after the annealing. 88

5.1 IX lifetimes 126

6.1 Summary of the values extracted from the *A* exciton fitting across the different thicknesses and probing methods (first and second column, respectively). $\boldsymbol{E^{PL}}_{\boldsymbol{MoS_2}}$ indicate the extracted PL energies for the MoS_2 *A* excitons. $\boldsymbol{E^{PL}}_{\boldsymbol{WS_2}}$ indicate the extracted PL energies for the WS_2 *A* excitons. *b* represents the bowing parameter extracted from *A* exciton fitting. $\mathbf{A_{Ex}}$ $\Delta\mathbf{E}$ are the highest and lowest experimental values of the *A* exciton energies. ΔA represents the energy range of the *A* excitons peak as a function of the composition. 152
6.2 Summary of the values extracted from the *B* exciton fitting across the different thicknesses and probing methods (first and second column, respectively). $\boldsymbol{E^{PL}}_{\boldsymbol{MoS_2}}$ indicate the extracted PL energies for the MoS_2 *B* excitons. $\boldsymbol{E^{PL}}_{\boldsymbol{WS_2}}$ indicate the extracted PL energies for the WS_2 *B* excitons. *b* represents the bowing parameter extracted from *B* exciton fitting. $\mathbf{B_{Ex}}$ $\Delta\mathbf{E}$ are the highest and lowest experimental values of the *B* exciton energies. $A-B$ represents the energy difference between *A* and *B* excitons. The larger and smaller energy difference values are provided. The $*$ indicate a partial set of data. . 153
6.3 Summary of the values extracted from the *I* transition fitting across the different thicknesses and probing methods (first and second column, respectively). $\boldsymbol{E^{PL}}_{\boldsymbol{MoS_2}}$ indicate the extracted PL energies for the MoS_2 *I* transition. $\boldsymbol{E^{PL}}_{\boldsymbol{WS_2}}$ indicate the extracted PL energies for the WS_2 *I* transition. *b* represents the bowing parameter extracted from *I* transition fitting. $\mathbf{I_{Tr}}$ $\Delta\mathbf{E}$ are the highest and lowest experimental values of the *I* PL peak. $A-I$ represents the energy difference between *A* exciton peak and *I* peak. The larger and smaller energy difference values are provided. 153

Chapter 1

Two-dimensional materials: fundamental properties and devices

1.1 Structure and properties of two dimensional materials

Dimensionality is a key parameter to consider in order to describe the properties and understand the physical phenomena exhibited by a material. Although at the very beginning, solid-state material science was limited to bulk materials due to the lack of microfabrication techniques that would give access to samples with dimensionality lower than three, the situation has dramatically changed in the last century. Following the creation of transistors and the consequent refinement of the micro- and nanofabrication processes, the scientific community is now able to create and study technological devices at the atomic scale, granting access to a new family of structures that do not differ from each other by the chemical composition, but simply by their physical confinement in space. As an example let's consider carbon, which was probably the most studied element in history due to the fundamental role it plays in biology. Two of its allotropes exist only in a reduced dimensionality: the fullerenes [1] and carbon nanotubes [2], that are respectively quasi zero-dimensional and one-dimensional. The discovery of these low-dimensional allotropes was a big surprise in the scientific community. In this form all atoms that compose the structure are confined on

a surface. This fact make the material more reactive than its bulk counterpart, because all the atoms are energetically activated and thermodynamically unstable, usually exhibiting phenomena such as decomposition or segregation, that has been observed when the materials were confined in thin structures (many tens of layers) [3]. In this scenario the isolation of stable low-dimensional materials was totally unexpected and, on top of this, since the bulk phase is absent, they show new and intriguing physical and chemical properties, impossible to obtain with the conventional thin film technology approach.

1.1.1 Graphene

The two dimensional (2D) allotrope of carbon was discovered years later, in 2004, by mechanical exfoliation of highly oriented pyrolytic graphite [4]. Since the graphite structure is remarkably anisotropic, composed by strong covalent bonds within the same plane and weak van der Waals bonds between adjacent layers, it allows the isolation of few- and single-sheets of carbon atoms, conveniently called few-layer and monolayer graphene [5]. This discovery was awarded with the Nobel Prize for physics in 2010 and paved the way for an unprecedented rush to discover all the fascinating properties that this new material could offer.

As a consequence of its 2D nature, electrons in graphene are almost massless and capable of moving at 10^6 m/s. The mobility of electrons in graphene has been discovered to be up to 10^6 cm^2/ V*s in suspended samples, with ballistic transport properties at room temperature [6]. Graphene also exhibits the integer and fractional quantum Hall effect [7] and ultra-high conductivity even when the carrier concentration tends to zero [5]. Each layer of graphene absorbs 2.3% of the incident light in the visible spectrum [8], is chemically inert, and possesses high mechanical strength [5, 9]. Despite its importance, the discovery of graphene was only the tip of the iceberg. A whole new family of elemental non-carbon based 2D materials now undergoes an extensive investigation. Despite the substantial differences in

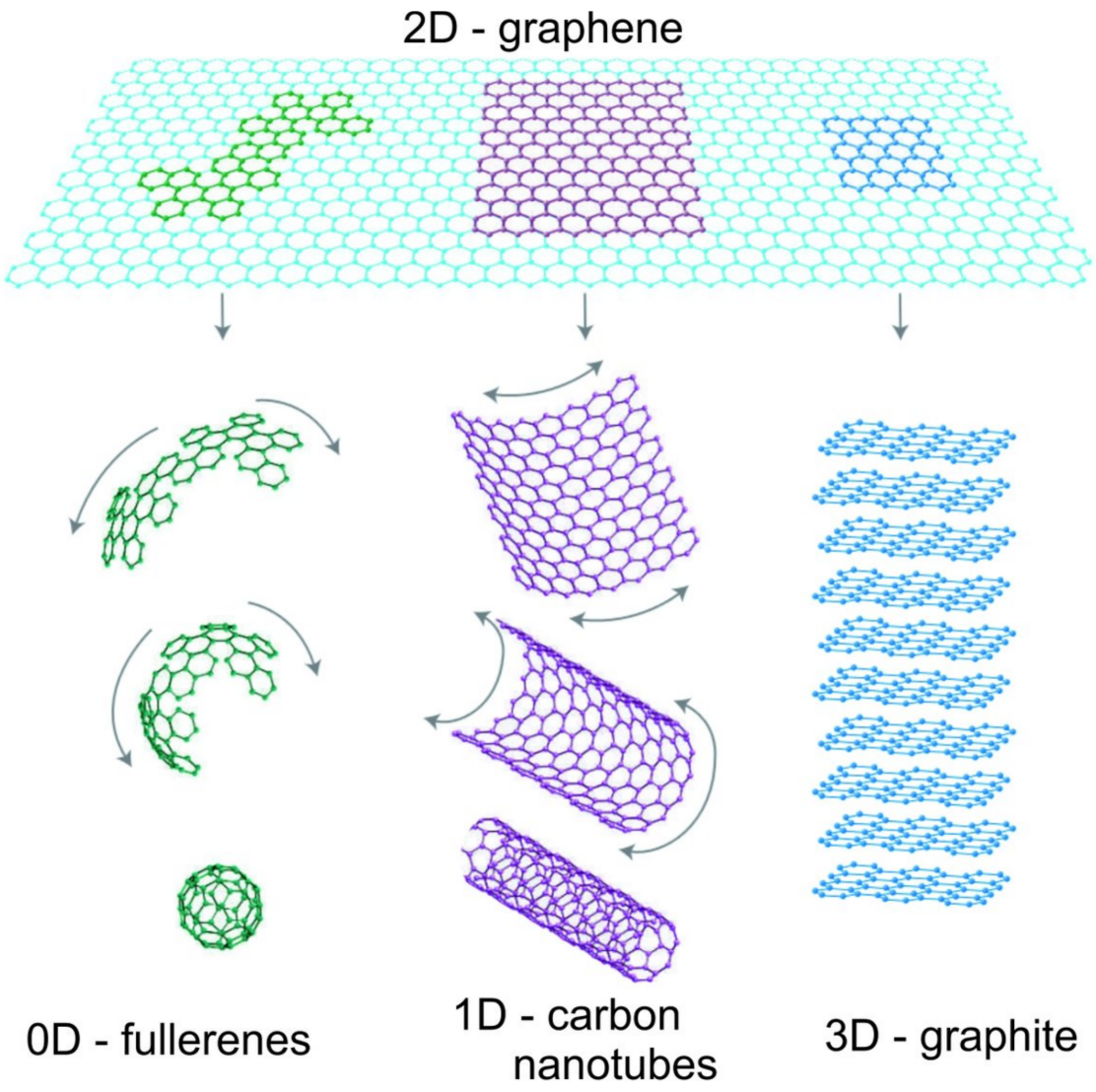

Fig. 1.1 Schematic structure of the different dimensionality of carbon-based allotropes. It is highlighted how graphene is the source material for all the different structures, via folding (fullerenes - 0D), wrapping (carbon nanotubes - 1D) or stacking (graphite - 3D). Image adapted from ref.[5].

their chemical structure, all these materials have the peculiar feature that they can be obtained in a two-dimensional form due to their layered nature, although their specific properties vary in a huge range according to their chemical composition.

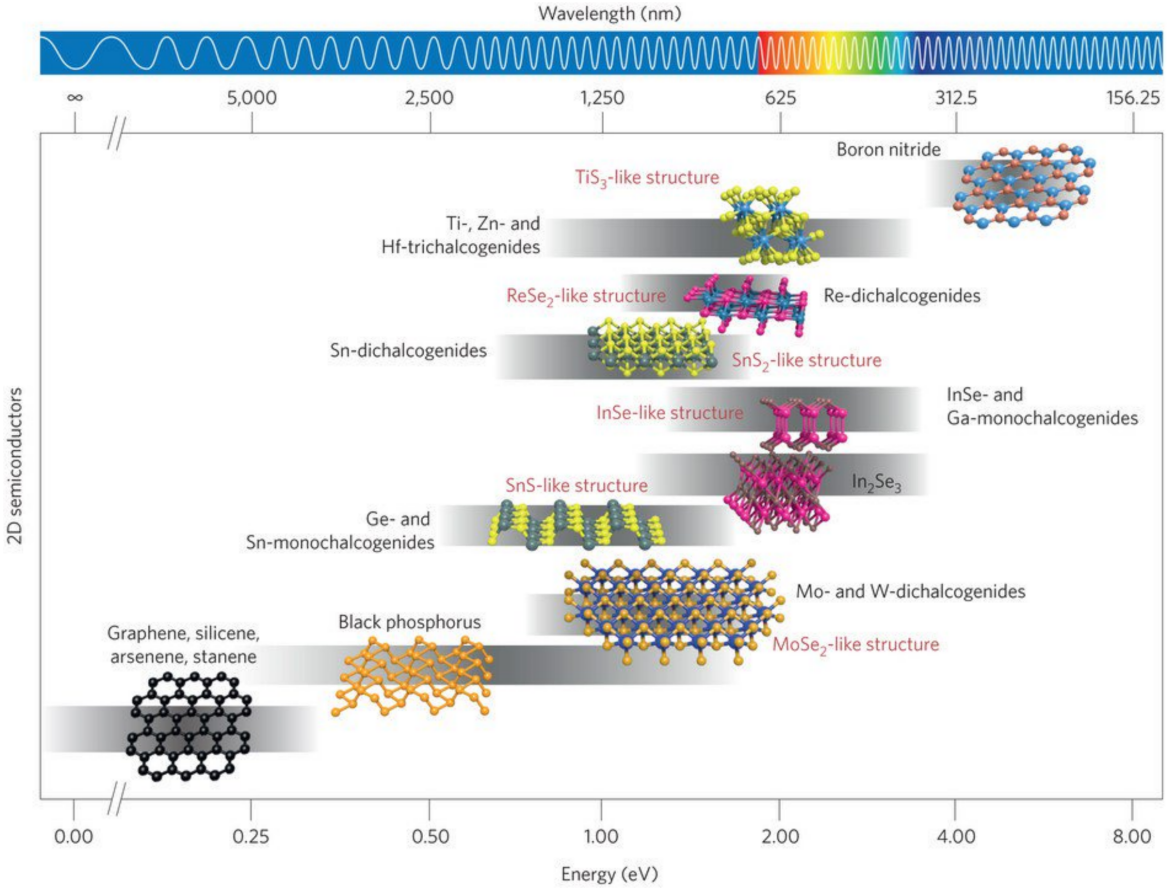

Fig. 1.2 Representation of the different 2D materials and their respective energy gap range as a function of their chemical structure. The visible range is highlighted by the rainbow on the top. Image adapted from ref.[10].

1.1.2 Hexagonal boron nitride

It is worth to discuss now a particular material that belongs to the 2D crystals and occupies a relevant role in this field. Hexagonal boron nitride (hBN) is made by hexagonal rings of alternating boron (B) and nitrogen (N) atoms, held together in plane by strong covalent chemical bonds. On the other hand the layers in the bulk material are held together by weak van der Waals forces. hBN is chemically stable and inert, mechanically resilient, even at high temperatures, and, most importantly, it possesses a large energy gap ($\sim$6 eV) which classifies it as an insulator even when confined in a few-layer thick arrangement [11]. Although it is a material that by itself attracted a non-negligible interest for its optical properties in the

ultraviolet (UV) region [11], it provides also an almost perfect dielectric in the 2D limit [12]. Moreover, the chemical inertness, the mechanical resistance, and the insensitivity to corrosion, along with an almost atomically flat surface, promotes hBN as the most attractive material for encapsulation of other less stable 2D materials.

Graphene and hBN compose the most striking example that reveals how the properties of a 2D material family of materials are affected by the chemical composition. Considering the fact that the family of layered materials that could be isolated in a 2D layer has been predicted to include thousands materials, the immense potential of this field of research is evident.

Since graphene is a perfect 2D metal, hBN on the other hand is a 2D insulator, it is possible then to rethink the silicon-based transistors (based on the bulk properties of the material), which are the beating heart of the technological devices in use nowadays, with a conceptually similar new family of devices, based on 2D materials.

1.2 Transition metal dichalcogenides

In the field of layered materials, transition metal dichalcogenides (TMDs) have attracted considerable attention from the scientific community in the last years [13, 14]. Their success is related to several attractive properties and a promise for device applications [15]. TMDs have a lamellar structure, in which one layer of transition metal atoms, generally labelled as M (like Mo, W, Nb, etc...), is sandwiched between two layers of chalcogen atoms, labelled as X (S, Se, Te). Depending on the combination of metal and chalcogen atoms the properties of the material can range from metallic, to semiconductors, to semimetal, to insulators and superconductors. Particular focus of this thesis is on the class of materials formed by molybdenum and tungsten as transition metal atoms and sulphur and selenium as chalcogen. They are semiconductors and have great potential in the development of nanotechnological optoelectronic devices.

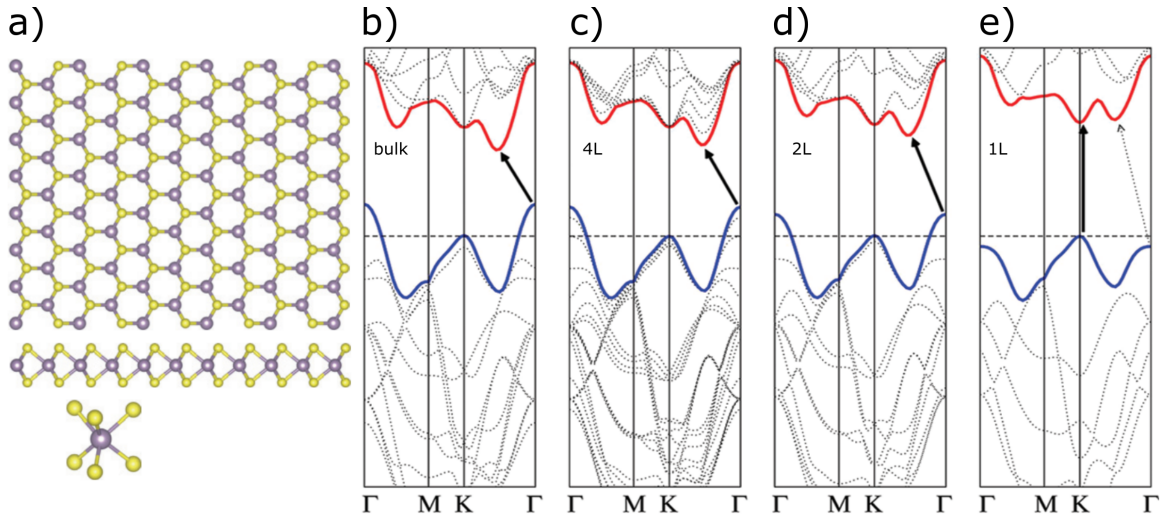

Fig. 1.3 **a)** Top, lateral and in-space view of the TMD single layer lattice structure. Purple circles are the transition metals atoms while yellow circles represent the chalcogen. **b-e)** Evolution of the band structure in MoS_2. The layer thickness is indicated in the inset of the image, the energy gap shift from momentum indirect to momentum direct moving from bilayer to monolayer. Image adapted from ref. .

In this class of materials, each transition metal atom is coordinated with six chalcogen atoms in a trigonal prismatic arrangement [16] as shown in the bottom panel of Fig.1.3 (a). The middle panel of the same image show the side view of a TMD single layer. It is worth pointing out that the chalcogen atoms are chemically bonded only with the transition metals atoms in direct contact with them and they have no dangling bonds outside the plane. Therefore multiple layers are held together only by weak forces, classifying these materials as layered, despite their thickness being larger than a single atom, as in the case of graphene and hBN. Thanks to the weak van der Waals forces, which are holding together the layers, these materials can be thinned down to the single layer limit. The top view of an isolated layer is shown in the top panel of Fig.1.3 (a) in which the hexagonal arrangement of the lattice along each plane is evident. The bulk material is composed by alternating layers, each of them twisted by 180°with respect to the layer directly underneath it. This structure was known long ago, and these materials were exploited as dry lubricants in industrial processes, especially MoS_2. Electronically, they are indirect bandgap semiconductors in their bulk form

with an energy gap of $\sim$1eV. The major feature that led to a renaissance of these materials is the strong dependence of their electronic band structure on the material thickness.

1.3 Band structure of TMDs and the role of quantum confinement

When cleaved down to a monolayer limit, TMDs become direct bandgap semiconductors, due to the evolution of the band structure in the Γ and Q point of the Brillouin zone (BZ) as shown in Fig.1.3 (b-e) [13, 15]. Since the hexagonal lattice structure in the plane is similar to graphene, it can be taken as a template to describe the properties of TMD monolayers. When the electrons move in a periodic lattice structure, such as in a solid state crystalline layer, they also move in a periodical potential landscape. This motion is described by the Bloch equation, with the corresponding eigenvalues forming a continuous band in momentum space. This forms the electronic structure of the Brillouin zone and, due to the lattice periodicity, it can be considered the unitary cell in energy/momentum space.

In the case of graphene, since all the atoms that form the lattice are identical, the theoretical model produces two bands, an upper one that has a minimum (conduction band minimum - CBM) and a lower one that has a maximum (valence band maximum - VBM) that touch each other at the K points of the Brillouin zone, making graphene a zero-bandgap semiconductor [4].

In TMDs, the adjacent atoms are not equivalent anymore in the lattice hexagonal structure, also they are different from each other compared to graphene, made by pure carbon. This leads to a mixed contribution of the transition metal d-orbitals and the chalcogen atom p-orbitals to the band structure. In the single layer limit, the band edge states are still located at the K point of the BZ, as in graphene, but the dispersion looses its linearity in favor of a parabolic one, leading to an effective mass for the electrons and, most importantly, to

an opening of the energy gap. Remarkably, the energy gap is in the visible range of the light spectrum (from 1.6 to 2.0 eV) and this feature is particularly promising for many technological applications.

As mentioned before, the most significant difference between graphene and TMDs is the different contribution of atomic orbitals in the band structure, and this is the key property to consider in order to understand the thickness-dependence of the electronic structure in TMDs. As an example, let us consider MoS_2 as a representative compound of the whole family of semiconducting TMDs and probably the most studied. The orbital contribution along the BZ has been considered in several theoretical works based on tight-binding models. This revealed that the *K* point in the CBM is mostly formed by Mo- d_{z^2} orbitals, meanwhile the VBM is composed by mixed Mo- d_{xy} and Mo- $d_{x^2\text{-}y^2}$ orbitals. Sulphur's *p*- orbitals have a negligible contribution in the *K* points of both CBM and VBM, as can be seen in Fig.1.4 [17–19].

Since the wavefunction of the molybdenum *d* orbitals is strongly localized on the transition metal atoms, they are insensitive to the electronic perturbation generated when another layer of the material is added or removed from the structure. This explains the insensitivity of the band structure in the *K* point as a function of the material thickness. On the other hand, in the *Q* point of the BZ, the orbital contribution in CBM is by Mo- d_{xy} and Mo- $d_{x^2\text{-}y^2}$ with a non negligible contribution of S- p_x and p_y orbitals as shown in panel 3 and 4 of Fig.1.4. This causes the delocalization of the wavefunction towards the outer edges of the monolayer, therefore the evolution of the *Q* point as a function of the crystal thickness is much more pronounced compared to the *K* point, but not still very strong, due to the in-plane orientation of the chalcogen p_x and p_y orbitals. In the Γ point of the VB once again there is a mixed contribution of Mo- d_{z^2} orbital and S- p_z orbitals. This mixed contribution causes a drastic modification of the band structure in this point as a function of layer number. This

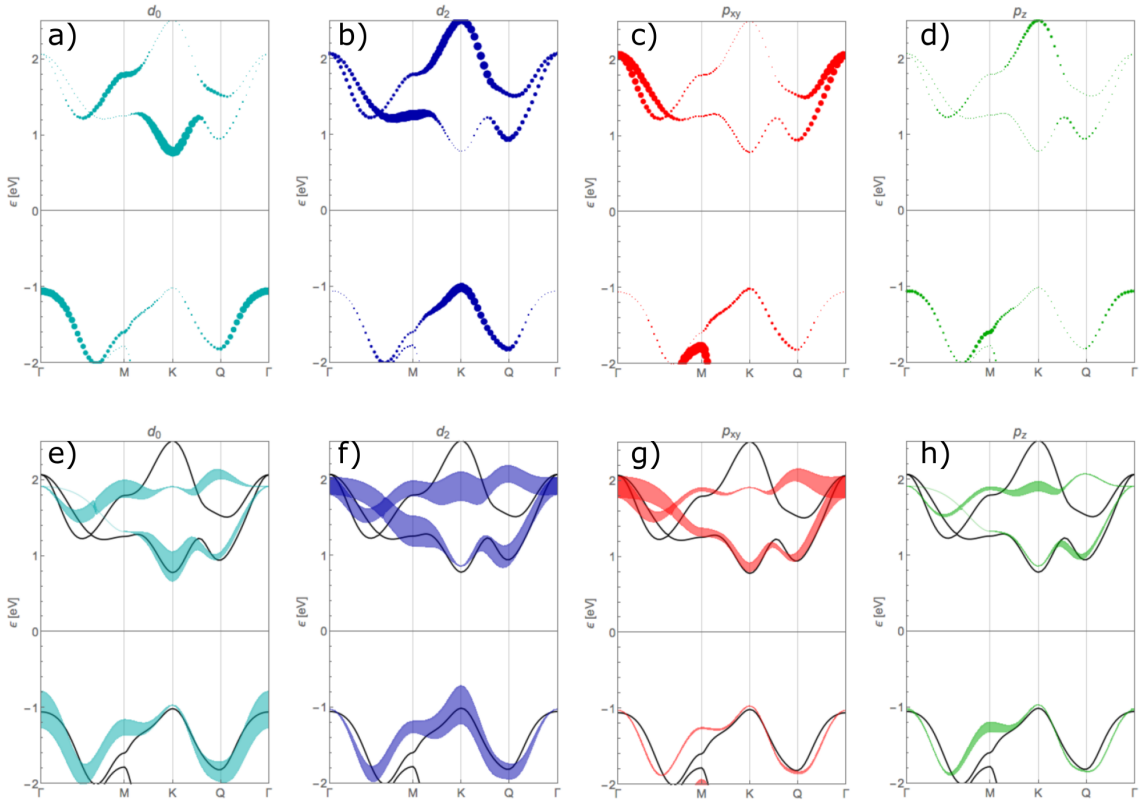

Fig. 1.4 Representation of the orbital contribution across the BZ for MoS_2. The relative contribution is highlighted with dots of different sizes. Aquamarine color **(Panel a)** represent Mo- d_{z^2} orbitals (d^0 in the image) oriented perpendicularly to the TMD plane. Dark blue colo **(Panel b)** represent Mo- d_{xy} and Mo- $d_{x^2-y^2}$ orbitals (d^2 in the image) oriented parallel to the TMD plane. Red color **(Panel c)** represent S- p_{xy} orbitals oriented parallel to the TMD plane. Green color **(Panel d)** represent S- p_z orbitals oriented perpendicularly to the TMD plane. The second row **(Panel e-h)** displays the same calculations in the form of bands. Image adapted from ref.[17].

dependence is stronger than the Q valley in the CB due to the out of plane orientation of the S- p_z orbitals involved.

This band structure modification causes the lowering of the Q point of the CB and the increasing in energy of the Γ point of the VB as the thickness of the material increases. This evolution of the band structure has been studied for several TMD materials [17, 18, 20] and in all cases it result in an indirect bandgap for bilayer TMDs. Although for some materials the simulations indicate clearly the valleys which are the band edge states, for the case of

MoS_2 the debate is still open. Several work predict the K valley of the CB as the lowest state, while other indicate the Q valley as the band edge state [20, 21]. Nevetheless the bandgap evolution in MoS_2 results clearly in a VBM located in the Γ point of the VB, making it an indirect bandgap semiconductor, as any other bilayer TMD.

1.4 Intralayer excitons and their properties

For semiconducting TMDs in their monolayer form, it is possible to excite charge carriers simply by photon excitation. Electrostatic doping and electrical injection are also valid methods to pursue. These properties combined are critical for their practical applications in working devices. The introduction of electrons (e^-) and holes (h^+) gives rise to a Coulomb interaction between them, forming an exciton. Those particles are formed when the strength of the Coulomb interaction is larger than the thermal energy. They are a hydrogen-like system, in which the electron and hole are in a stable orbit around each other. This is a common feature of many semiconductor materials [22].

What makes this feature so special in TMDs is consequential to their quantum confinement in a 2D system. This effect contributes to a reduced dielectric screening inside the single layer when it is isolated, and consequently, surrounded by materials with lower dielectric constants, as shown in Fig.1.5 (a).

In the monolayer limit, the strength of the Coulomb interaction that holds together the excitons is very high, of the order of several hundreds of meV [24, 25]. This fact leads to a very small Bohr radius of the exciton in TMDs and a very large oscillator strength [22]. Thus in TMDs the optical response is dominated by the below bandgap excitonic transitions represented in Fig.1.5 (b) rather than conventional band edge transitions. These excitons, due to their large binding energy, are stable even at room temperature, in contrast to most III-V and II-VI semiconductors which need to be cooled down to liquid He temperature to observe these phenomena. Also, more complex quasiparticles can be observed in TMDs such

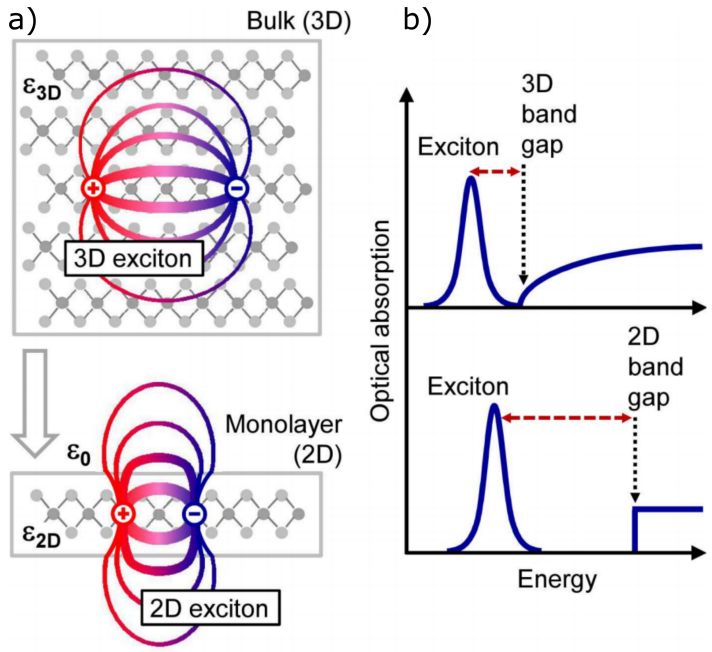

Fig. 1.5 **a)** Electron-hole interaction in 3D and 2D limits. Panel **b)** show the differences in the optical absorption. Image adapted from ref.[23].

as: charged excitons or trions formed when a free carrier (an electron or a hole) is coupled to an exciton, forming a three particle complex [26]; biexcitons, a quasiparticle formed by two electrons and two holes [27] and charge biexcitons, also called quintons [28, 29]. In monolayer TMDs, due to their direct bandgap, intense photoluminescence (PL) emission arises from the radiative recombination of excitons. This ranges from 650 to 800 nm (1.90 to 1.55 eV) , according to the TMD specific composition and is two-three orders of magnitude enhanced compared to the bulk material [30]. The high oscillator strength of the excitons makes these materials ideal candidates for observation of strong light matter interaction, since a single monolayer of a TMD can absorb up to 15% of incident sunlight per nm thickness [31].

1.5 Valley properties of TMDs

As described before, the band edge structure of TMDs, especially in the K valley, is dominated by transition metal d-orbitals. Therefore the electrons that reside in these states are prone to a strong coupling between the atomic orbital angular momentum and the spin angular momentum. This phenomenon is called spin orbit (SO) coupling, and in transition metal atoms it is particularly strong. Density functional theory (DFT) calculations showed that the presence of a mirror symmetry in the middle of the monolayer TMD plane implies that the spins that point in the out-of plane-direction should exhibit SO splitting. Moreover the lack of inversion symmetry in monolayer TMDs, due to their intrinsic 2D nature, determines the rise of a spin-sensitive spin orbit field that lifts the spin degeneracy at the band edges. Because the SO-coupling depends mainly on the transition metal d-orbitals, and there is a different higher order correction in the CBM (d_{z^2}) and the VBM (d_{xy} and $d_{x^2\text{-}y^2}$), the effect is more pronounced in the valence band, in which the splitting can reach hundreds of meV, while in the conduction band it does not exceed a few tens of meV [25]. Since opposite valleys and opposite spins are correlated by the time reversal symmetry, the spin splitting is opposite for the valleys in the $+K$ (K) and $-K$ (K') points of the Brillouin zone. Therefore the electrons which reside at the band edge have a valley orbital magnetic momentum, which acts similarly as a pseudospin ($\pm 1/2$), but is related to valley states. So they are commonly labelled as $+K$ (K) when the pseudospin assumes +1/2 value and $-K$ (K') when the pseudospin assumes -1/2 value, as indicated in Fig.1.6 (a).

The joint effect of the SO coupling and the time reversal symmetry causes an opposite trend of the valleys in the K and K' edges of the Brillouin zone. In the K point the upper level of the valence band is a spin up state (Fig.1.6 (a) red state) and the lower level as spin down (Fig.1.6 (a) blue state). In K' valley the effect is reversed, the upper level of valence band will be a spin down (Fig.1.6 (a) blue state) and the lower level is a spin up state (Fig.1.6 (a) red state).

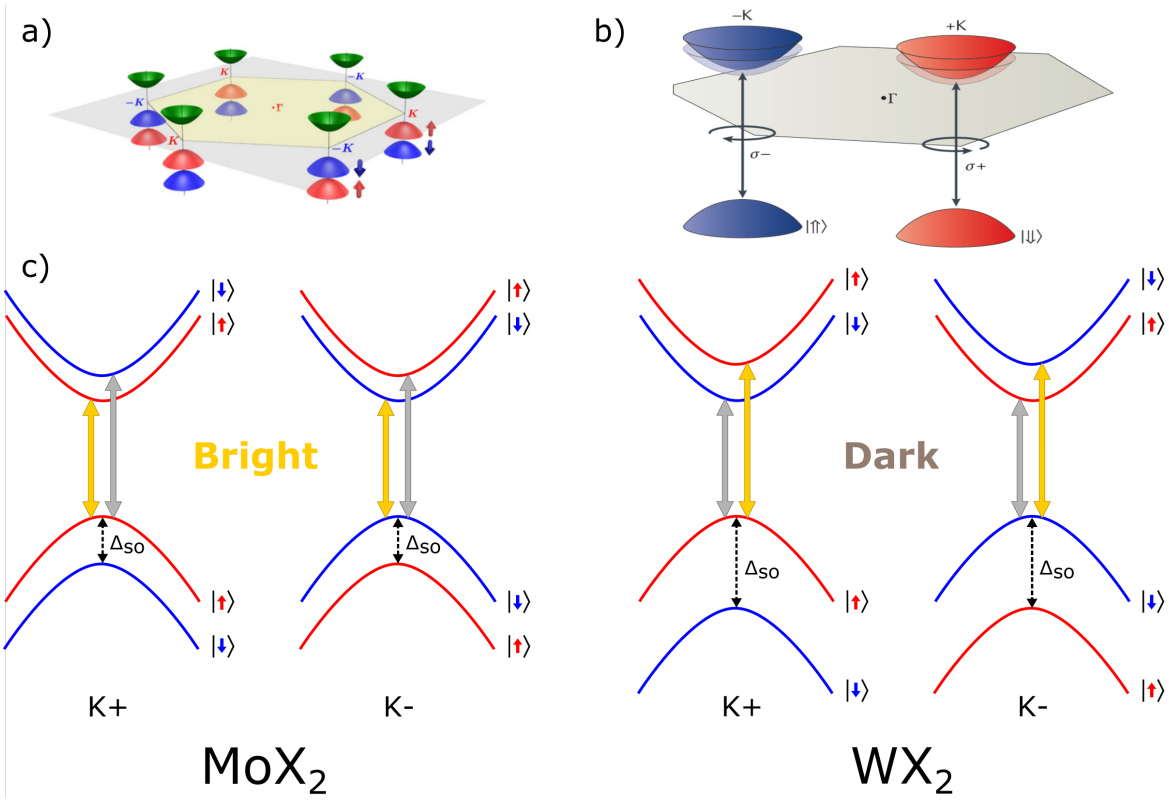

Fig. 1.6 **a)** Lateral view of the spin split valleys in a TMD. The effect is shown only for the VB, where is particularly prominent, and ignored in the CB. Image adapted from ref.[32]. **b)** Optical selection rules for the K and K' valleys, they couple with circular polarized light with opposite helicity. Image adapted from ref.[33]. **c)** Summary of the valley structure in Mo- and W- based TMDs. The red curve indicate the spin up states, blue curves indicate spin down states. The yellow and gray arrow indicate spin allowed (optically bright) and spin forbidden (optically dark) transitions in the adjacent valleys.

Since the electron scattering from the K to K' valleys requires not only a large change of the momentum, but also a spin flip, the possibility to have intervalley scattering is strongly suppressed [33]. This effect is called spin-valley locking effect, as it strongly binds the electron spin degree of freedom with their valley index. This effect influences the interaction between light and interband electronic transitions in the TMDs K (K') point of BZ. In an atomic picture, the optical transitions are ruled by the angular momentum conservation principle on the basis of the quantum numbers of the initial and final states. In a TMD the situation is similar, but the valley orbital magnetic moment of the two valleys introduces a new selection rule that dictates that the transition in each of the two valleys couples with

circularly polarized light of different helicity, as summarized in Fig.1.6 (b). This fact takes place when both carriers which form an exciton reside in the same valley. The final effect is that in these materials it is possible to selectively introduce carriers in a specific valley using light with opposite helicity, which creates valley polarization [33]. Notably, due to the long depolarization time due the suppressed valley scattering described before, this property can be exploited to store and manipulate information based on the valley degree of freedom, in a picture similar to spintronics, but based on the rich valley physics of these materials, and therefore called valleytronics [18].

1.5.1 Temperature dependence of PL emission in TMDs

The most evident effect of the spin orbit splitting is the temperature dependence of PL intensity in TMDs. Depending on the spin states the fundamental transition can be spin-forbidden (optically dark) (gray arrows in Fig.1.6 (c)), because the spin flip is a process much slower than the radiative recombination and the non-radiative relaxation; or spin-allowed (optically bright) when no spin flip is required (yellow arrows in Fig.1.6 (c)) [25]. The lifetimes of the two transitions are different: due to the large oscillator strength the bright transition possesses an extremely fast lifetime (few picoseconds), while lifetime of dark excitons can be one order of magnitude longer [34].

Carriers confined at the band edges follow the Boltzmann energy distribution. When the sample is cooled down the carriers will relax to the lower spin state of the conduction band (for electrons) and upper spin state of the valence band (for holes). Depending on the spin orbit splitting, the lowest energy optical transition can therefore be enhanced or suppressed, depending on the parallel or antiparallel spin configuration between CB and VB states. Consequently the PL emission intensity may be enhanced or suppressed. Since the spin orbit splitting in the conduction band is opposite in the Mo-based and W-based TMDs [18] as shown in Fig.1.6 (c), two different temperature dependent trends of PL behavior

are observed for these two materials. Considering as an example monolayer $MoSe_2$, the ground state excitonic transition will be between states with the same spin, so it will be optically bright. When the sample is cooled down to 4.5 K this transition will be greatly enhanced thanks to the increased number of excitons in low energy states. Experimentally, $MoSe_2$ monolayer PL emission is remarkably enhanced at low temperatures compared to room temperature emission as shown in Fig.1.7 (b). For WSe_2 the opposite is true, due to the valley configuration, the ground state excitonic transition is between valleys with the opposite spin, so it is optically dark. Accordingly, for WSe_2, the PL at low temperature is strongly suppressed, relative to room temperature as shown in Fig.1.7 (a) as a consequence of the reduced carrier population in the optically bright state (which is at a higher energy) [35].

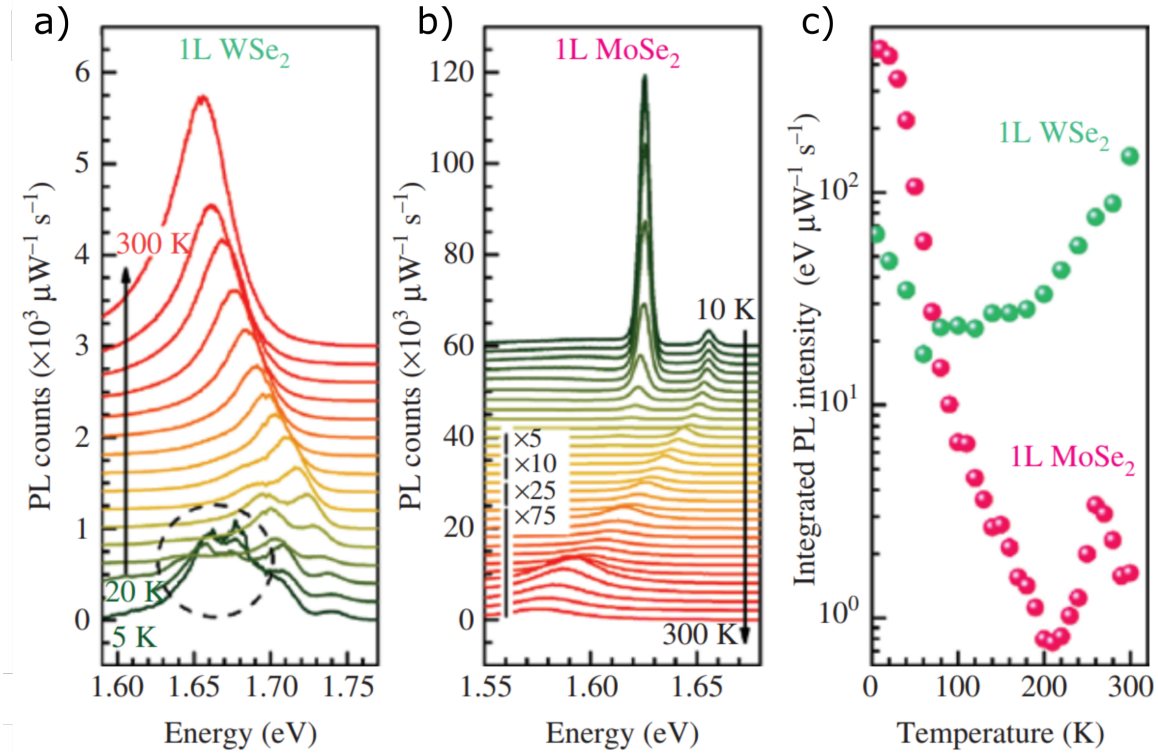

Fig. 1.7 **a)** Temperature dependence of the PL in WSe_2 and **b)** $MoSe_2$ monolayers. Green spectra are taken at low temperature, red spectra at high temperature. **c)** Integrated intensity of the PL emission for the two materials. Image adapted from ref.[36].

Temperature-dependent behavior of monolayer TMDs is important for understanding of the processes governing their optical properties. Cooling the sample down to liquid He temperature is the only possible way to observe excitons in conventional III-V semiconductor quantum wells, because their binding energy is so low that they thermalize at high temperatures. On the other hand, excitons in TMDs, due to their large binding energy, can be observed at room temperature. Nevertheless, low temperature PL measurements provide an invaluable tool for exploration of the exciton physics of these materials.

As discussed previously, the PL intensity is strongly dependent on the optically bright or optically dark nature of the material itself. Two other features can be noticed in Fig.1.7: a blueshift of the PL emission and a narrowing of the PL optical features as the temperature is lowered. The temperature dependence of PL emission is described by fitting of the standard equation elaborated for semiconductors [37]. As an example, the band gap in $MoSe_2$ at 4K is 80 meV smaller, compared to room temperature. The second effect is a narrowing of the PL emission. This is particularly relevant in $MoSe_2$, due to its optically bright nature. This narrowing is related to the suppression of acoustic phonons in the sample which cause a significant broadening of the PL emission at RT [38], and also causes an increase of the PL emission lifetime [34]. Therefore, as a function of temperature, the linewidth of the PL emission of TMD decrease from 50-60 meV, commonly observed at room temperature, down to 8-10 meV at 4K. Also the lifetime of the PL emission has a strong dependence as a function of temperature: at room temperature the TMD PL lifetime is 1-5 nanoseconds, while at low temperature it decreases down to 4-5 picoseconds [34].

1.5.2 Defect-bound states

Especially in optically dark samples (WSe_2, WS_2) and materials that have a close proximity of the spin split CB states (MoS_2), the PL narrowing might be shadowed by the rise of a broad band at low energy (evidenced in Fig.1.7 (a) by a dashed circle). This emission arises

from excitons localized to any perturbation of the TMD band structure. The same effect might be observed in highly defective $MoSe_2$ [39, 40]. In TMDs these defects induce an exciton relaxation and trapping effect in the energy band of the material, which shrinks the optical gap in correspondence of the defect position [41]. This causes a drift of excitons to those defective states, and a consequent carrier accumulation, due to the energy relaxation. The presence of the defect and the high carrier concentration causes the activation of radiative and nonradiative relaxation paths which appear in PL spectra as a broad emission formed by the sum of all these defective states [42]. The ambiguity in defining these defect states is reflected in their origin, since the it could be very different:

- **Charge disorder:** Recently the effect of the substrate on the optical properties of TMD monolayers has been investigated , commonly thermally grown SiO_2/Si; it has been proved that the presence of the silicon dioxide directly beneath the monolayer induces a strong charge disorder in it due to the presence of unbalanced charges trapped in the silicon dioxide layer [43].

- **Doping:** The presence of even a minimal amount of contaminant in TMD structures, either interstitial or substitutional, are responsible for emission broadening, because they practically act as a dopant, creating new excitonic states and causing a broadening of the PL emission.

- **Flake strain** The strain of the flake is another key point to consider to understand the PL emission; in fact the presence of strain modifies the interband energy states allowing tuning of optical properties, but it also induces completely new energetic levels [44], determining the presence of a prominent broad emission at lower energy related to the presence of strain-induced defect states.

- **Physical defects:** The presence of defects in the TMD atomic structure can also alter the optical properties. Defects on an atomic scale, such as dislocations or, on a

macroscopic scale, folding or cracks of the layer, can alter the excitonic states creating non negligible disorder in proximity of monolayer edges. Also the substrate roughness is transferred to the monolayer causing a non homogeneity of the band structure.

- **Surface contamination:** The presence of molecules on the TMD monolayer surface and trapped between the substrate and the ML induces a band rearrangement that causes a broadening of the PL emission and a reduced optical response of the material.

- **Lifting of the optical selection rules:** For W-based materials the presence of a broad band of defect-bound states is guaranteed in almost every sample. This is due to the lifting of optical selection rules in proximity of a defect that therefore act as a beacon providing a preferential radiative decay path to the photogenerated carriers.

1.5.3 Results of reflectance contrast (RC) measurements in TMDs

Another important feature in TMDs materials can be identified in light absorption experiments. Since the CB and VB are split into two pseudospin states, two absorption resonances that do not require a spin flip can occur: the first is the lowest energy one, which in the case of Mo-based TMDs occurs between the CB and VB extreme edges (red curves in Fig.1.6 (c)), meanwhile in W-based materials it involves the top VB spin state and the higher energy spin split band in the CB (red curves in Fig.1.6 (c)). It is worth to mention that due to the difference in energy splitting in CB (tens of meV) and VB (hundreds of meV), this lowest-energy absorption is determined mainly by the VB top spin state. Comparing Fig.1.6 (c) and Fig.1.8 (a), the second spin-allowed transition occurs between the other two spin states, and is named *B* exciton. It is always at higher energy than the *A* exciton absorption, due to the asymmetry of the spin splitting in the CB and VB, as can be observed in Fig.1.8 (b).

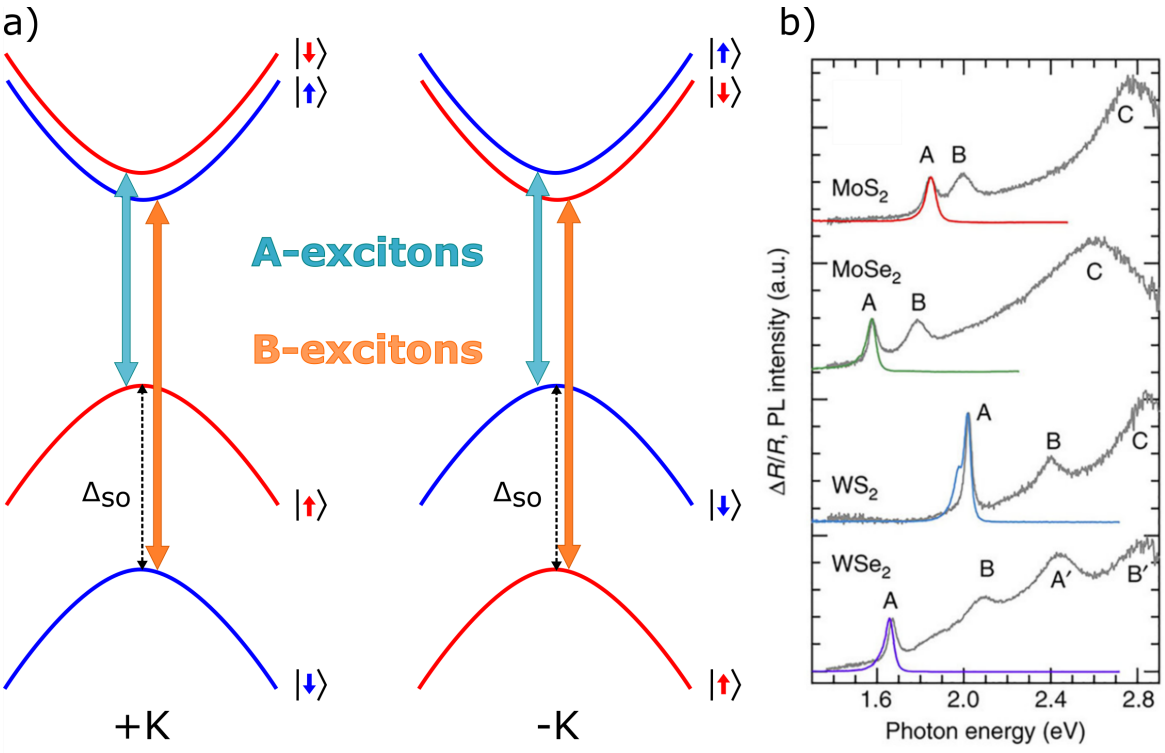

Fig. 1.8 **a)** Spin allowed transitions in a WX_2 material. The two edge states are antiparallel. Blue arrow indicates the *A* excitons while orange arrow indicate *B* excitons. **b)** Reflectance-contrast spectra of four TMDs. The *A* excitons peak is fitted with a coloured line. Image adapted from ref.[45].

Other higher order transitions can be identified at higher energies (named *C* excitons, etc.) but they are originated from absorption between non-ground states in the band structure arising from different orbital contributions. The *A* and *B* excitons absorption are useful tools to gain an insight on the SO splitting between these band edge states and better understand the spin-valley physics. Also, compared to PL spectroscopy, reflectance contrast (RC) is largely insensitive to defective states, since it probes transitions which takes place between band edges with a large densities of states [46]. Experimentally RC spectra are given by the difference between reflectance of the substrate, with and without the material, normalized by the reflectance of the bare substrate [47].

1.6 Transition metal dichalcogenide alloys

Tuning of the chemical composition of the material via alloying is a powerful tool for controlling the optoelectronic properties. The use of alloys is lost in the mists of time, since the creation of bronze in the ancient era. Nowadays the same approach can be pursued in the new 2D frontier to address the same goal. Alloying of different bulk semiconductor materials offers a wide range of possibilities for tuning the electronic structure and the lattice parameters [48].

From a structural point of view it is rather challenging to create a crystalline alloy between atoms which belong to different chemical groups, due to the different coordination configuration, significant lattice mismatch and multiple crystalline phases. On the other hand, alloying materials that belong to the same chemical group is relatively easy. As an example for TMDs, the lattice mismatch between MoX_2 and WX_2 (X: S, Se, Te) does not exceed 1% [30]. This fact makes possible the formation of a pure crystalline phase with the same symmetry and structure of a standard TMD with the only exception that, to any degree, a transition metal in the lattice is replaced with a different one. The same discussion is valid for chalcogen-alloyed TMDs and have been experimentally demonstrated as well [49, 50].

Although theoretical calculations show that the ordered phase in a TMD monolayer alloy is more stable than random phases [51], the growth techniques currently employed require heating the substrate to high temperatures. Therefore temperature can induce the formation of a disordered phase. This situation takes place especially during the growth of atomically thin TMDs with techniques such as physical vapor deposition [52], chemical vapor deposition [53, 54], metal-organic chemical vapor deposition [55] or chalcogen exchange process [56]. These approaches allow to control the chemical composition of the flakes during the growth, creating a radial composition gradient in the flake grown, modifying the precursor supply during the synthesis process [57]. On the other hand materials synthesized in such ways will be highly defective, making the interpretation of the optical features rather challenging.

Another approach is to synthesize the TMD alloys in their bulk form. As mentioned above, when the alloying does not require a significant coordination or lattice parameter modification between chemical species, the layered structure of TMDs is largely preserved. Therefore the micromechanical exfoliation can be performed on alloys like in any other chemically pure TMD material [58]. The bulk alloys obtained in these ways, especially the ones based on Mo/W and S/Se, are perfectly mixed on atomic scale, as represented in Fig.1.9 (a), without any significant phase separation, as predicted by the calculation of internal energy and free energy of mixing in a primitive cell, and demonstrated by atomic-scale composition sensitive techniques such as high annular dark-field (HAADF) scanning transmission electron microscopy (STEM) [59] and scanning tunneling spectroscopy (STS) [47].

Alloying is particularly relevant because it opens a new degree of freedom in TMDs which allows a fine and continuous tuning of their optical and electric properties.

1.6.1 Photoluminescence of TMD alloys

Similarly to many III-V semiconductors, single layer TMD alloys follow Vegard's law [58]. It is an empirical law which describes an intrinsic feature of the alloy material (such as bandgap size) as a linear combination of the same property of the two pure materials, with the correction of a quadratic term, called the bowing parameter (b) originating from lattice mismatch and orbital hybridization in the alloy [60]:

$$PL_{Mo_xW_{1-x}S_2} = xPL_{MoS_2} + (1-x)PL_{WS_2} - bx(1-x), \tag{1.1}$$

where $PL_{Mo_xW_{1-x}S_2}$ express the energy of the alloy PL peak, PL_{MoS_2} and PL_{WS_2} represent the energy of the PL emission of the two chemically pure materials, respectively, x indicates the concentration of molybdenum atom in the lattice structure, and b is the bowing parameter. According to the chemical composition, the PL energy of MX_2 (M: Mo, W; X: S, Se) can be

tuned from 2 to 1.55 eV (620 to 800 nm) at room temperature, as shown in Fig.1.9 (b) [61], without losing any of the properties which characterize the monolayer TMDs.

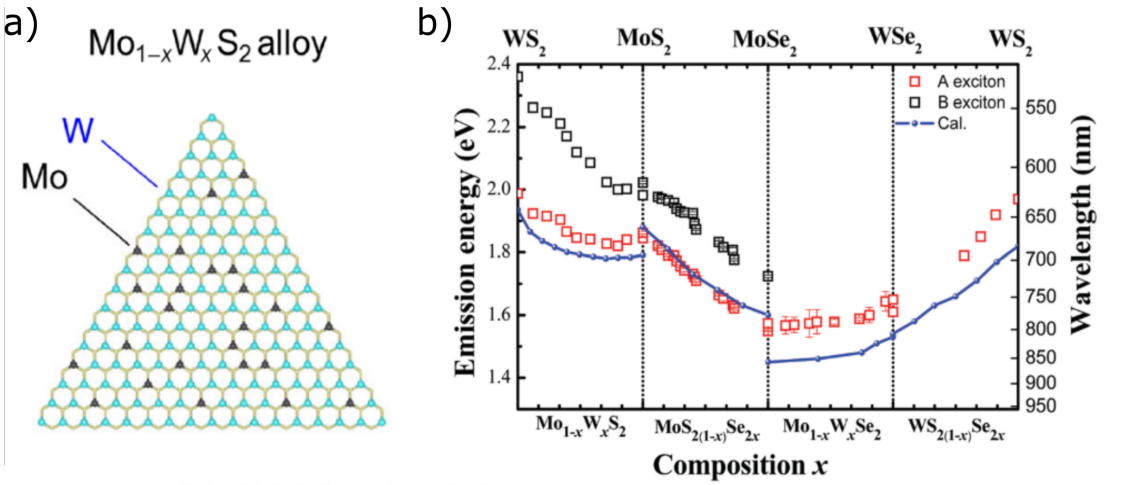

Fig. 1.9 **a)** Schematic in plain structure of the $Mo_xW_{(1-x)}S_2$ alloy. Light blue dots are W atoms, dark gray dots are Mo atoms, yellow dots are sulphur atoms. **b)** PL emission energies as a function of the alloy composition for *A* and *B* excitons (red and black squares respectively); blue line and dots represent the theoretical calculations. Image adapted from [56, 61].

For example, for the $Mo_xW_{(1-x)}S_2$ alloy, it has been shown how the PL emission non linearly shifts from 1.82 to 1.99 eV as predicted [58]. It exhibits a redshift for $x < 0.4$ and then monotonically blueshifts for $x > 0.4$ [58]. Also the total redshift does not exceed 10 meV, while the blueshift is an order of magnitude larger. Intriguingly, this asymmetric behavior is reduced when sulphur atoms are replaced with selenium atoms. In fact, in the $WS_xSe_{(2-x)}$ alloy, the PL emission almost linearly blueshifts from 1.65 up to 1.99 eV [57] as shown in Fig. 1.9 (b) . In this case the bowing parameter assumes values closer to zero and can be ignored, simplifying Vegard's law to an almost linear correlation, with minor deviation for the quadratic term. This indicates that the asymmetric behavior of the PL emission as a function of alloy composition seen in $Mo_xW_{(1-x)}S_2$ alloy is related to the transition metal atom properties and almost independent of the chalcogen atom.

1.6.2 Orbital contribution in TMD alloy band structure

To shed some light on this behavior, let us consider the atomic orbitals which compose the band edge points in the *K* point of the BZ in monolayer TMDs, with a particular attention of the transition metal orbital involved. As discussed before, the tight binding model and density functional theory calculation address the transition metal *d*-orbitals as the main constituent of the *K* point of the BZ. In the case of VBM, the projected density of states (PDOS) in the band edge reveals that the orbitals involved are $d_{x^2\text{-}y^2}$ and d_{xy} for both Mo and W atoms [62]. Since the set of orbitals involved are the same for both atoms, the evolution of the VB edge state as function of transition metal composition results to be linear and does not show bowing effects. PDOS of W-like states increases linearly as a function of W composition [58], therefore the VBM linearly increase in energy with the W composition. For CBM the situation is more complicated. For MoS_2, the PDOS identifies the orbital d_{z^2} of Mo as the only relevant contribution, but in WS_2 the PDOS reveals a combination of all three d_{z^2}, $d_{x^2\text{-}y^2}$ and d_{xy} orbitals of W [62]. Moreover, the PDOS in the CB reveals that the W orbitals contribute less to the VB edge states compared to Mo orbitals, since they are energetically higher [58]. This implies that moving from a MoS_2 chemical composition to a WS_2 composition the CB shows a nonlinear evolution, which is mostly sensitive to low-Mo concentration in the TMD chemical structure.

Experimentally this phenomenon has been observed in PL experiments [58, 63] and it can be noticed from the PL behavior how the $Mo_xW_{(1\text{-}x)}X_2$ nonlinearity is particularly pronounced when a small amount of Mo (<40%) is added to a mostly W-like structure. The origin of this phenomenon resides in the difference of transition metal *d* orbital contribution in the CB.

This nonlinear effect of CB compared to VB is reflected also in electron transport properties of alloy TMDs. First principle calculations show that the hole effective mass in TMD alloys decreases linearly with W composition [62]. This can be related to the fact that

orbital contributions in the VB is preserved across the alloy composition, maintaining a linear trend also in transport properties. On the other hand, this fact do not take place in the CB, therefore electrons in alloys exhibit greater effective mass than electrons in atomically pure Mo and W TMDs [64], as a consequence of symmetry point orbital mixing.

1.6.3 Spin orbit splitting in TMD alloys and temperature dependence of their optical properties

Another feature that deserves to be considered in the CB description is the SO coupling. In the CB, SO coupling generates two spin split states only few meV apart from each other. Since the two ground spin states are opposite in Mo and W based TMDs, alloying offers the possibility to engineer the spin properties of the material itself, moving from an optically bright state (in Mo-based compounds) to a optically dark state (in W-based compounds). This is an important degree of freedom to be considered in order to create engineered valleytronic devices. A detailed analysis of TMD conduction bands has been performed by Kosminder et al. [65]. Although they do not focus specifically on alloys, they use the same DFT and tight-binding model for all the four MX_2 (M: Mo, W; X: S, Se) monolayer materials, taking into account also the SO coupling, which has a major role, due to the smaller splitting compared to the VB. Therefore their results can be used as extreme cases to get an insight in the CB of TMD alloys. Their model identifies two contributions that cumulate to determine the evolution of the CB states. Their work revealed that WS_2 and WSe_2 exhibits a net positive splitting in the CB. Meanwhile $MoSe_2$ exhibit a large net negative splitting. MoS_2 is a material particularly difficult to simulate since the two contributions nearly cancels each other. This becomes evident in their different behavior moving from room temperature to cryogenic temperatures.

Up to now there is a lack of low temperature ($T < 5K$) PL data on TMDs alloys, although the pure materials have been extensively studied at both RT and LT conditions. Only one

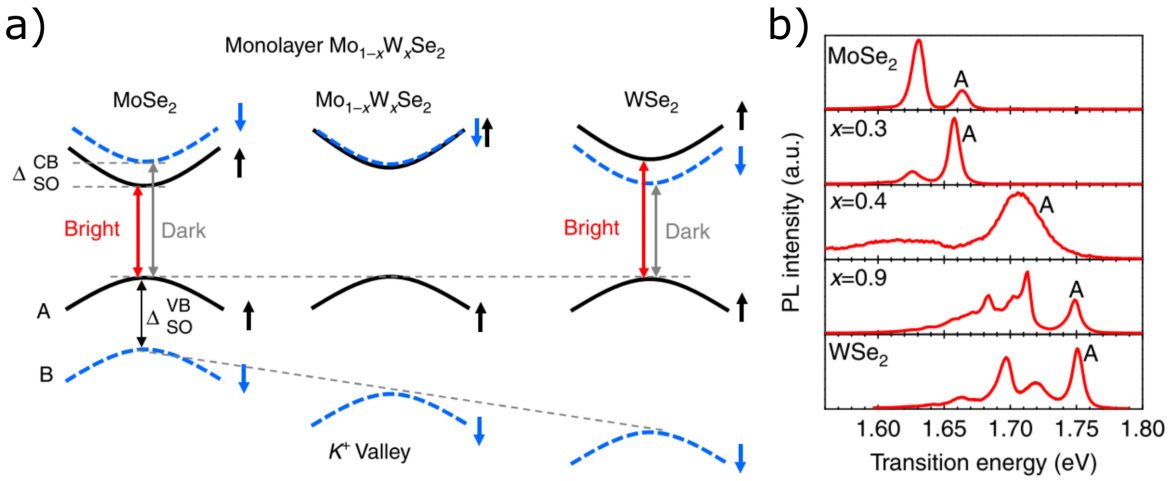

Fig. 1.10 **a)** Band structure at *K* point of $Mo_xW_{(1-x)}Se_2$ alloys. The solid black and dashed blue line indicate the two spin split states respectively. The central panel show the absence of degeneracy in the CB at a specific sample stochiometry. **b)** Experimental spectra at low temperature of three $Mo_xW_{(1-x)}Se_2$ alloys, the *A* exciton transition is indicated in each spectra. The W- composition is indicated in the inset. Image adapted from ref.[25].

paper reports on monolayer TMD alloys behavior at LT [25], highlighting the fact that the spin orbit splitting is a property of such materials, which can be tuned through alloying as represented in Fig.1.10 (a). It suggests also that, at a precise stochiometric ratio between Mo and W in the lattice structure, the two contributions identified by Konsminder et al. [65] should exactly cancel each other, to create a material with degenerate spin states in the CB. To prove this idea, LT measurements are fundamental. Their measurement was performed on $Mo_xW_{(1-x)}Se_2$ alloys, showing the transition from a $MoSe_2$-like PL to a more complex WSe_2 like PL emission. Interestingly, this change does not appear to be smooth. While moving from $Mo_{0.7}W_{0.3}Se_2$ to $Mo_{0.6}W_{0.4}Se_2$ alloy the PL emission broadens consistently, and it assumes the shape of a WSe_2-like emission for $Mo_{0.1}W_{(0.9)}Se_2$ alloy [25]. Also, the transition from a $MoSe_2$-like behaviour to a WSe_2-like behaviour appears to be abrupt, raising questions about the sample quality, which is reflected by the PL emission. Unfortunately the poor quality of the spectra reported makes the interpretation of the LT PL behavior rather challenging.

Another spectroscopic analysis performed on TMD alloys is reflectance-contrast (RC), which allows to overcome the problem of defect related states that interfere with the PL emission at LT. It has been shown that in $Mo_xW_{(1-x)}S_2$ alloys the *A* exciton absorption gradually redshifts from 2.02 eV in WS_2 to 1.95 eV in MoS_2 [58]. The trend is similar to the one observed in RT PL, as expected. Interestingly, the *B* exciton transition shows less pronounced quadratic behavior and the tuning range is much broader than that reported for *A* excitons. This is a consequence of the large SO coupling in the WS_2 VB compared to MoS_2. In fact, the two spin split states are pushed apart from 150 meV in Mo-based material up to 400 meV in W-based. This continuous tuning of spin orbit splitting is extremely intriguing to develop spin-engineered devices using TMD alloys.

Chapter 2

Van der Waals heterostructures, heterobilayers and their properties

2.1 Van der Waals heterostructures

The concept of a heterostructure is simple as it is powerful. Once two different materials are joined together, they form a superstructure whose properties are not just a combination of the properties of the two materials, but also are influenced the way in which they interact with each other. In the last years, heterostructures created by interfacing different materials have allowed the development of engineered materials with new properties [66–68]. 2D materials are excellent candidates to build vertical and lateral devices, which nowadays represent the ultimate frontier in the field of atomically thin devices. Heterostructures made by 2D material are also known as van der Waals heterostructures (vdW heterostructures) as the layers are held together by these weak forces. In fact, while III-V heterostructures rely on covalent bonding at the heterojunction, in vdW devices only weak forces keep the layers together. Although the strength of the interaction of a single bond is much lower, the hierarchical effect and the large in-plane surface make them perfectly stable. Moreover, vdW heterostructures

offer unprecedented possibilities to design and tailor the optoelectronic properties of these devices.

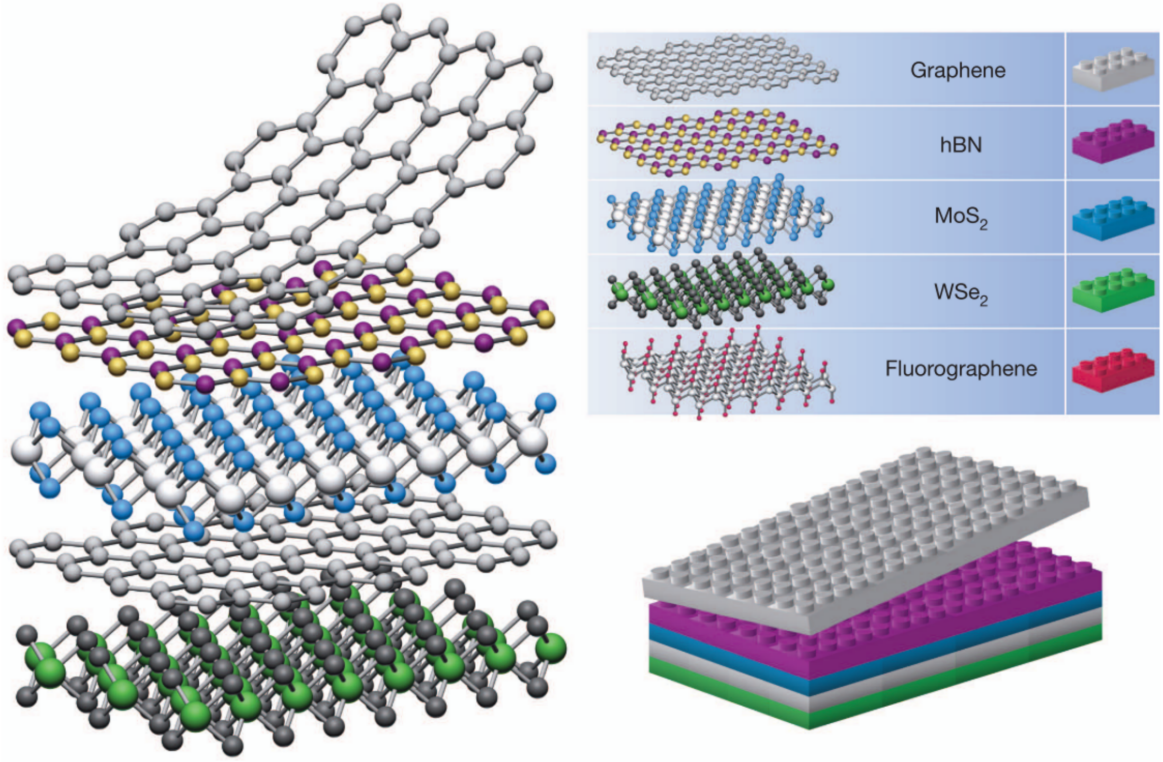

Fig. 2.1 LEGO model of a van der Waals heterostructure. Different materials are represented by different colors. Image adapted from ref.[9].

- **Relaxed lattice parameters** III-V semiconductors require that the two materials possesses an almost-matching lattice periodicity to create a clear, non-defective, heterojunction. This constraint reduces the batch of materials that can be combined to form a heterostructure. In vdW heterostructures, since the covalent bonding is not required anymore, the devices have greatly relaxed lattice parameters, making possible the vertical stacking of layers with drastically different lattice periodicity and structure.

- **Interdiffusion between layers** Another advantage related to the absence of strong chemical bonds between layers is to prevent the atom interdiffusion between layers. This feature is often absent in III-V semiconductors due to the chemical bonds at the

interface. Consequently the interface, instead of appearing as a sharp composition step from one material to another, assume a gradual composition profile with a region of blended atoms.

- **Atomically sharp interfaces** Also the 2D structure of both exfoliated and grown materials makes possible the creation of atomically sharp interfaces, while in III-V semicondutors the junction often is terraced or more inhomogeneous. Some growth techniques allow the formation of atomically sharp layers even on high aspect ratio substrates (such as ALD or MBE) but the disadvantages is their long processing time, that prevent the growth of thicker or highly structured devices

- **Twist angle flexibility** Due to the lack of covalent bonds, vdW heterostucture allow to align the 2D layers with any given twist angle. This degree of freedom is impossible to realize in III-V semiconductors since the bonding of the two materials at the interface requires a specific lattice direction, to keep the interface clean. It is impossible to modify the lattice direction of one of the two layers since it would causes a mismatch of lattice periodicity. Moreover the twist angle between layers is impossible to continuously change, since it will prevent the formation of chemical bonds at the interface.

The weak forces that subsist at the interface allow the mechanical and also the electronic coupling between adjacent layers, as a consequence of the partial wavefunction superposition. This is a key feature, since it ensures the formation of a full, III-V like, heterostructure. Last but not least the heterostructure devices based on 2D materials are flexible, compatible with the actual nanopatterning techniques and thin film technology and only few nanometer thick. These are the fundamental features which makes these structures intriguing for fundamental physical studies and new applications [69–71]. The structures that can be assembled by alternating layers of semiconductors (like TMD monolayers), insulators (like hBN mono and

multilayer) and conductors (like graphene) are practically unlimited in terms of numbers and applications [9, 72]. One simple heterostructure is formed by a top layer of hBN, middle layer of graphene and bottom layer of hBN. This is called encapsulated device. Encapsulation in hBN preserves the properties of graphene from the external environment, creating high quality devices, thanks to the atomic flatness of hBN [73] and its charge homogeneity [74]. Moreover hBN protects the sandwiched graphene from electronic scattering effects, related to the presence of the substrate, surface states or charge disorder [75]. Thus encapsulation in hBN has become a standard procedure for most of the vdW heterostructures fabricated nowadays.

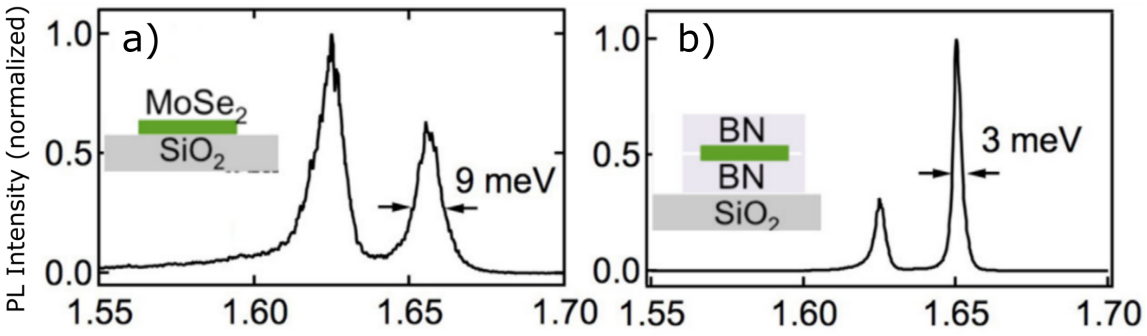

Fig. 2.2 **a)** PL spectra of a free standing flake of $MoSe_2$ on SiO_2. The FWHM of the X^0 is indicated. **b)** PL spectra of a hBN encapsulated $MoSe_2$ flake. The linewidth is much narrower. Image adapted from ref.[43].

For hBN-encapsulated TMD heterostructures it has been proved that the encapsulation results in a much narrower PL emission at low temperatures compared to flakes deposited on SiO_2, as shown in Fig.2.2. hBN encapsulation narrows down the linewidth of the TMD PL emission for a series of reasons: it acts as a dielectric barrier between the TMD flake and the substrate, so the optically induced charges in the substrate cannot migrate on the TMD, preventing the PL broadening caused by charge doping. Also, hBN reduces the effect of the local electric field fluctuations present in the substrate, preserving the charge homogeneity in the TMD. Due to its atomically flat surface, it does not induce wrinkles on the TMD layer, reducing the effect of non-uniform strain. hBN encapsulation protects the TMD layer from

phisisorption and chemisorption that causes the rise of defect-bound states. Last but not least, it helps to preserve the sample quality across several thermal cycles due to the similar thermal expansion coefficient between hBN and TMD. All these effects improve significantly the TMD PL emission. As shown in Fig.2.2 (a-b) for a bare $MoSe_2$ monolayer sample, standing on a conventional SiO_2/Si substrate, the exciton PL emission show a FWHM of 9 meV, but this can be narrowed down to 3 meV in a fully hBN encapsulated sample [43]. Similar results were obtained for all the other TMD monolayers [76]. Interestingly, the hBN encapsulated samples exhibit a redshift of the PL emission compared to free standing flakes. This is related to the modified dielectric environment in close proximity to the TMD flake [76]. Also, hBN can be used as a dielectric material and not only as a protective layer of the heterostructure to create a quantum well-like structure using 2D materials as fundamental components instead of conventional semiconductor thin films [77].

2.2 TMD Heterobilayers

Of particular relevance to this thesis are van der Waals heterobilayers [78–80]. They are formed by two semiconducting TMD monolayers in direct contact with each other. The whole structure can also be encapsulated in hBN. Since each TMD has a different work function and band gap, when two TMD monolayers are electronically coupled, according to their band structure, they generally form a type-II heterojunction, where the CBM and VBM are located in the two different monolayers [51, 81].

In the type-II heterojunction the charge carriers can migrate between layers, as shown in Fig.2.3 (a-b). Electrons will flow in the monolayer which has the lowest conduction band (in the presented heterostructure, $MoSe_2$), while holes will be confined in the other layer, which has the highest valence band (WSe_2 in Fig.2.3). This carrier separation is confirmed by the dramatic quench of the PL in the heterostructure, which is generated from intralayer exciton radiative recombination, as clearly visible in Fig.2.3 (e) [81–83]. More precisely, in

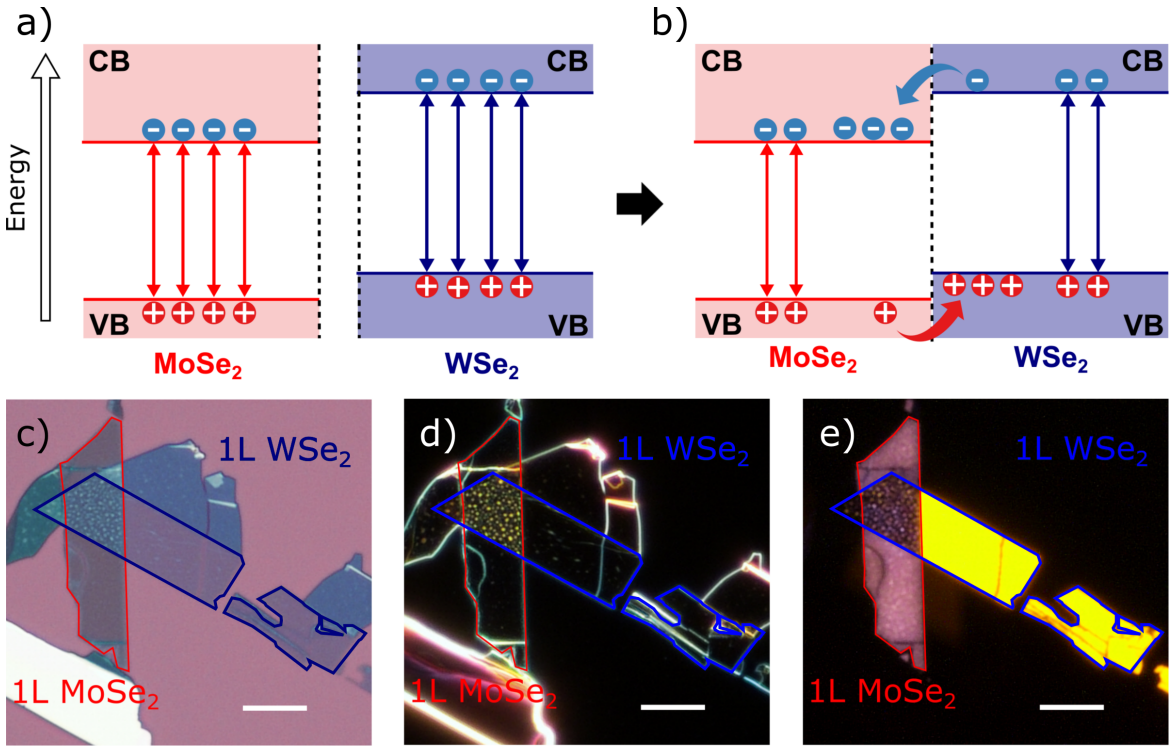

Fig. 2.3 **a)** Schematic band structure of the two isolated TMD flakes. Each one exhibit their own intralayer excitons.**b)** Formation of the heterobilayer, the type-II band alignment causes the migration of the charge carriers (blue and red arrow respectively). The intralayer exciton emission is suppressed as a consequence of the charge separation. **c-e)** Bright field, dark field and PL imaging of the sample. The PL is suppressed in the area of the heterostructure.

the overlap area of the two flakes, the PL emission (pink for $MoSe_2$ and yellow for WSe_2) is suppressed by the carrier separation. Despite the strong binding energy of the intralayer excitons, the charge separation was reported to occur on a subpicosecond timescale [84]. For the holes it was found that they become spatially confined in the highest VB layer in less than 50 fs [81]. This extremely short carrier separation timescale has been proposed to be related to the close proximity of the TMD layers, so that the carriers must only move less than 1 nm to enable the charge segregation. Moreover, compared to other charge separation processes observed in organic photovoltaic devices or Gretzel's cells, in 2D materials every point of the interface is a type-II heterojunction, massively promoting the charge separation

process with no need of intralayer charge migration steps. This is an extremely intriguing feature for light detecting and energy harvesting devices.

2.3 Theory of heterobilayer and orbital hybridization

Orbital hybridization in a heterobilayer is far from being deeply understood. Because many different devices were studied and the theoretical results differ from one to another, the discussion will be focused on one particular combination of materials, that is also one of the most well studied heterostructure, formed by $MoSe_2$/WSe_2 monolayers with AA stacking (same crystal axes alignment between the two layers and in the approximation of equal lattice parameters for both monolayers [85]). As discussed in the section 1.3, the main orbital contributions at the *K* point of the BZ come from the transition metal d_{z^2} orbitals in the CBM and $d_{x^2\text{-}y^2}$ and d_{xy} orbitals in the VBM [86].

Fig.2.4 shows the heterobilayer band structure across the whole BZ. As can be seen, the *K* point of the BZ is composed by four energy states, two marked in red, generated by Mo-*d* orbitals, while the blue are generated by W- *d* orbitals, both in the CB and the VB. As can be observed from the spatial distribution of the wavefunction (white area in the inset images), these states are strongly localized on the respective transition metal atoms. So the *K* point of the BZ can be considered as a simple superposition of unperturbed states arising from Mo- and W-orbitals. This fact implies that in a heterobilayer the energy configuration of the states at the *K* (*K*') point of the BZ does not show a shift compared to the isolated monolayers [31, 87–92]. Moving away from the *K* point, into the Λ (*Q*) point of the BZ, the situation is different. This valley is formed by both transition metal $d_{x^2\text{-}y^2}$ and d_{xy} orbitals, with a non negligible contribution of chalcogen p_x and p_y orbitals. Similarly, in the Γ point the orbital contribution is a mix between the transition metal d_{z^2} and chalcogen p_z orbitals. As can be seen in Fig2.4, the wavefunction distribution at the Λ and the Γ point of the BZ is delocalized between both transition metal atoms. Consequently the heterobilayer band

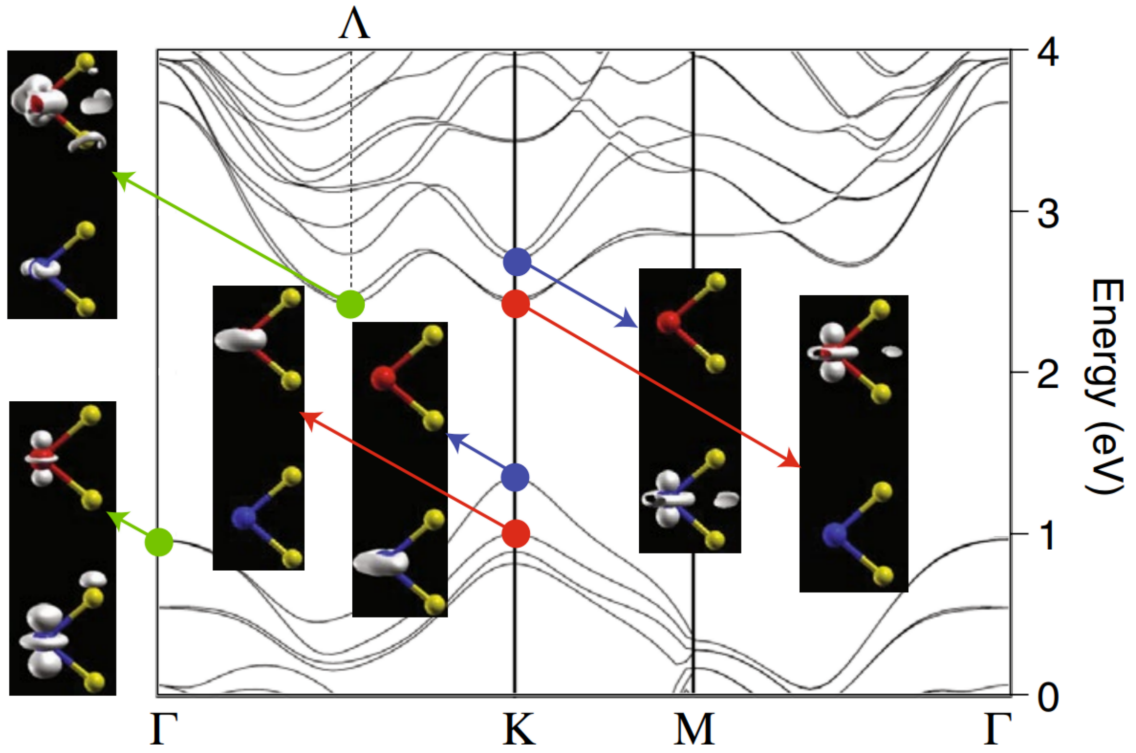

Fig. 2.4 Band structure of the $MoSe_2/WSe_2$ heterostructure. The red and blue spots at the K point of the BZ represent the Mo- and W- states respectively. The inset shows the wavefunction distribution of such states which is confined in the two layers, respectively. In the Λ (Q) point of the CB and the Γ point of the VB the green spots indicate a hybrid nature of the valley. The wavefunction is distributed in both layers. Image adapted from ref.[86].

structure, away from the K point of the BZ, is different from the isolated monolayers. Several theoretical works analyze the reciprocal position of the band edge states in the K, Λ and Γ points, largely agreeing that in the $MoSe_2/WSe_2$ heterobilayer CBM and VBM are still located in the K (K') point of the BZ, so that in the heterobilayer the direct bandgap is still preserved. These calculations also show the strong sensitivity on the assumed interlayer distance, which appears to be a critical parameter in the simulations [93–95]. So far, many different combinations of materials have been experimentally investigated , based on both CVD or mechanically exfoliated flakes.

To keep the discussion consistent, only the case of $MoSe_2/WSe_2$ heterobilayer will be discussed here. Experimental work on these structures revealed, by the mean of micro

angular resolved photoemission spectroscopy (μ-ARPES), that the VB is still located at the K point of the BZ, without orbital hybridization. But the stronger hybridization at the Γ point determine the rise of another band, similar to the one that can be observed in bilayer materials. Although μ-ARPES does not provide data on the CB, the simulations presented in the cited work, refined with the support of the VB experimental data, indicates that the band edge minimum of the CB is located at the K point of BZ as well. These experimental results are consistent with theory predictions [96, 97]. In conclusion, theory and experiment agree in describing the vdW heterobilayer as engineered materials with the band edge states still located at K (K') point of the BZ.

2.4 Formation of interlayer excitons and optical investigation of TMDs heterobilayers

2.4.1 Interlayer excitons in van der Waals heterobilayer

In TMD heterobilayers electrons and holes, spatially confined in the two different layers of the heterojunction by the band alignment, continue to interact through the Coulomb force. This results in the formation of a so-called interlayer exciton in which the two carriers reside in two different materials. These particles are also known as spatially indirect excitons [83, 84, 98]. For the rest of the report, in order to distinguish between the two excitonic species, excitons that reside in a single layer will be called intralayer or direct excitons (DX), while excitons that are formed by carriers in two different layers will be called interlayer excitons (IX). Although interlayer excitons (IX) are similar to an intralayer exciton (DX), the spatial confinement of the IX introduces new features and possibilities, making them another invaluable tool to probe the properties of 2D heterostructures.

The IX also possesses an interesting set of optical properties that are very important for the work presented here. Despite their spatial confinement, IXs can radiatively recombine.

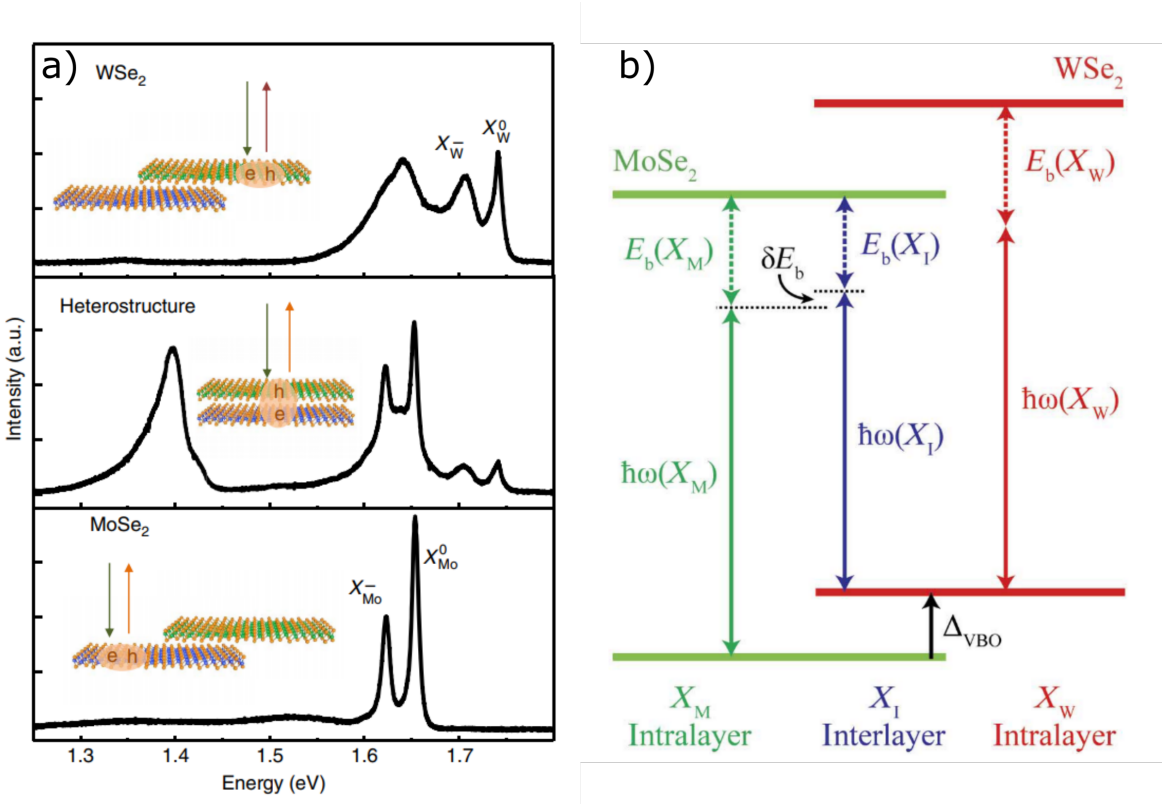

Fig. 2.5 **a)** Photoluminescence of isolated WSe_2 monolayer (top panel), $MoSe_2/WSe_2$ heterobilayer (middle panel) and isolated $MoSe_2$ monolayer (bottom panel) at low temperature. Image adapted from ref.[83]. **b)** Band structure at the K point of a $MoSe_2/WSe_2$ heterobilayer. The solid green and red lines indicates the band edge states of the two materials, the dashed arrows represent the excitons binding energies for Mo (green) and W (red) DX. The binding energy of the IX is represented by the blue dashed arrow. Solid arrows indicate the energy of the photons originated from each optical transition. It can be observed that the interlayer exciton emission (blue solid arrow) is at lower energies than the two intralayer excitons emissions (red and green solid arrows). Image adapted from ref.[97].

This determines the rise in the heterobilayers of a low energy PL emission peak, clearly detectable with optical experiments, as can be observed in the middle panel of Fig. 2.5 (a). Moreover this PL emission peak is localized only in the heterobilayer area, and is absent in the single flake regions, as shown in Fig.2.5 (a). Many different heterostructures show such a feature, such as: MoS_2/WS_2 [89, 93, 98], $MoSe_2/WSe_2$ [83, 97, 99–102], $MoSe_2/WS_2$ [103, 104], MoS_2/WSe_2 [69, 105], $MoSe_2/MoS_2$ [106, 107], and WS_2/WSe_2 [108]. The IX position in the energy spectrum depends on two parameters: the band offset between the

two materials that form the heterojunction (Δ_{VBO} in Fig.2.5 (b)) and the interlayer exciton binding energy ($E_b(X_I)$ in Fig.2.5 (b)). Depending on the combination of materials adopted in the heterojunction the band offset can assume a broad range of values [51, 109].

The reported binding energies of IX are dependent on the material involved, and also on the technique adopted to probe them [23, 110, 111]. The spatial separation of the carriers in the two layers implies that the IX binding energy should be reduced, compared to their intralayer counterpart. Experimental evidence is being provided using a $MoSe_2/WSe_2$ heterobilayer probed with both μ-ARPES and optical spectroscopy [96]. The results revealed that the band offset, with this particular material combination, is around 300 meV and the IX binding energy is around 200 meV, consistent with other results [97]. This makes the interlayer exciton less tightly bonded than DX, as expected, but nevertheless the carrier interaction is very strong. The IX radiative recombination is very dependent on the interlayer electronic coupling. When the orbital wavefunctions of the two TMD layers are kept apart by a spacer or a contamination trapped between two layers, the electronic superposition of the wavefunctions is partially or totally suppressed, depending on the spacer thickness, causing a quench of the IX PL peak and a partial or total restoration of the intralayer exciton emission. It has been shown that using a terraced hBN flake as a spacer between a $MoSe_2$ and a WSe_2 monolayers, the IX emission is still present when the hBN thickness is one layer, but increasing the hBN thickness trilayer the IX PL emission is suppressed [69], as shown in Fig.2.6, and as also predicted by theoretical calculations [112].

The twist angle between the two TMD layers also have an effect on the IX emission. The real-space lattice alignment of the two monolayers is related to the momentum-space BZ alignment, henceforth it follows that if a twist angle between the two TMD layers is introduced (intentionally or unintentionally), the K valleys in the two layers are shifted apart in the momentum space, as shown in Fig.2.7 (a).

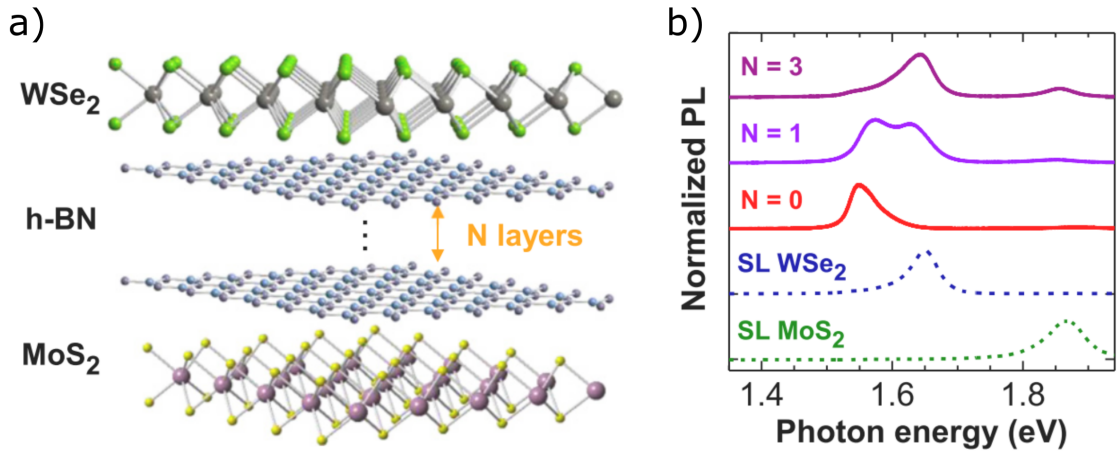

Fig. 2.6 **a)** Lateral view of the device. The hBN act as a spacer between the two TMD flakes. **b)** PL spectra of the sample. When the numbers of hBN layers overcome three, the two TMD layers show unperturbed PL emission and the interlayer coupling is suppressed. Image adapted from ref.[69].

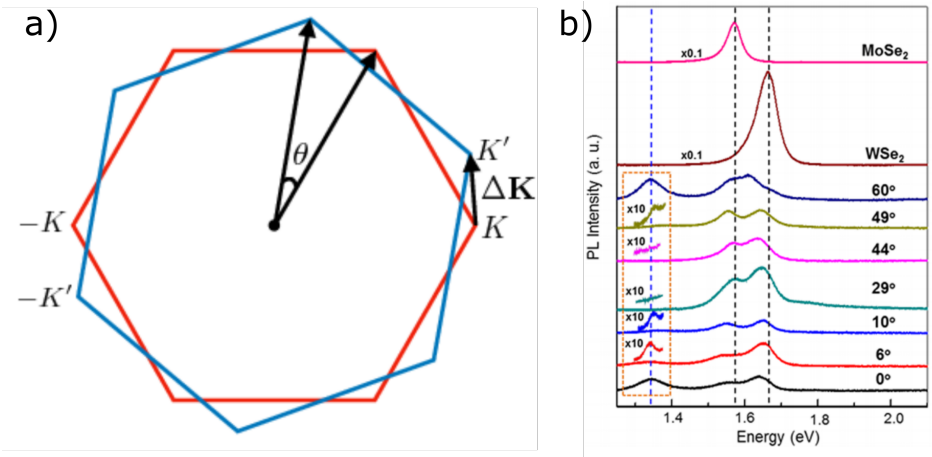

Fig. 2.7 **a)** Momentum mismatch of the K valleys of the two materials in a heterobilayer generated by the twist angle. The radiative recombination can occurr if their momentum gap ΔK is compensated by a lattice phonon. Image adapted from ref.[113]. **b)** Effect of twist angle on the IX PL emission. For large twist angles the IX emission is strongly quenched, as a consequence of the momentum mismatch of the K valleys. Image adapted from ref.[101].

The red and blue hexagons indicate the Brillouin zones of the two TMD layers, respectively. The twist angle (θ) between the layers causes a shift of the K points of the BZ in the two materials. The shift will be larger as the twist angle increases, following a 60°periodicity, according to the hexagonal symmetry of the BZ. For large twists ($\theta > 10°$) the spatially

confined electron-hole radiative recombination process require a large shift in momentum (ΔK in Fig.2.7 (a)). This leads to suppression of the radiative recombination of IX, quenching dramatically their emission, as experimentally observed and shown in Fig.2.7 (b) [101, 113].

2.4.2 Effect of twist angle on the IX optical properties

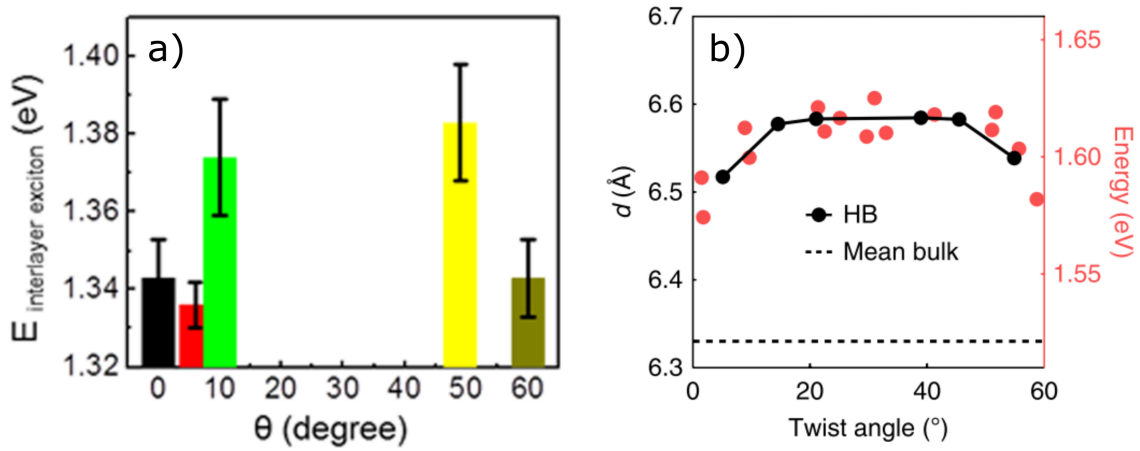

Fig. 2.8 **a)** Energy of the $MoSe_2/WSe_2$ interlayer exciton peak versus the twist angle. A redshift of 45 meV can be observed. Image adapted from ref.[101]. **c)** IX PL emission energies for MoS_2/WSe_2 heterobilayers (red dots) with different twist angles. The calculated interlayer distance (black dots) is overlapped and follow the same trend. Image adapted from ref.[114].

The twist angle between the two monolayers also induces other phenomena in the IX emission. It was described before how the IX PL intensity is dependent on the twist angle, but also the peak position of IX exhibits a dependence. A work on a set of $MoSe_2/WSe_2$ heterobilayers with different twist angles, ranging from aligned (θ= 0°) to antialigned (θ= 60°) configuration, show that IX energies redshift up to 50 meV for large twist angles (10°< θ < 60°), as shown in Fig.2.8 (a) [101]. Similar results were found for a MoS_2/WSe_2 heterobilayer set, as represented in Fig.2.8 (b).

The effect of twist angle is strongly dependent on the layer separation. Experimentally, it has been demonstrated that when a single hBN monolayer is inserted between a $MoSe_2/WSe_2$

heterostructure, the IX emission is suppressed as a consequence of the reduced electronic coupling between TMD layers. Also, the effect of the twist angle becomes negligible [101].

2.4.3 Electrical dipole and long lifetimes of IX

IX have also an out-of-plane component of the electric dipole moment. This feature arises from the charge separation between layers [115, 116]. It allows the IX energy to be tuned through a vertical gate voltage [117], as shown in Fig.2.9 (a-c).

Since the IX dipoles are aligned with each other, due to the staggered band alignment, a strong repulsive interaction takes place between IX, related to the electrostatic repulsion between dipoles. This causes a blueshift of the exciton PL peak under increasing excitation power [80]. This effect has been studied also in III-V quantum wells, using the mean field approximation [118, 119] which leads to the plate capacitor formula:

$$\delta E = \frac{4\pi N e^2 d}{\varepsilon}, \tag{2.1}$$

where δE is the blueshift of the IX PL peak, N is the density of charge carriers, d is the interwell distance and ε is the dielectric constant. A linear dependence between δE and N is expected, but in TMD heterobilayer a pronounced sublinear trend of the IX emission energy has been observed experimentally [80]. This deviation from the expected linear dependence is a consequence of the exciton-exciton annihilation process. The formula, which describes it, has been applied for intralayer excitons in several TMD materials [120–124]:

$$\frac{dN}{dt} = -kN^2, \tag{2.2}$$

where N is the exciton density at a given time t and k is the annihilation rate. The solution to this differential equation is:

$$N(t) = \frac{N_0}{1 + kN_0 t} \tag{2.3}$$

where N_0 is the initial exciton density. This equation shows that the exciton-exciton annihilation process is strongly dependent on the exciton density, and it is used to model the radiative decay time of the exciton PL signal. This annihilation process has been also identified to be the cause of the deviation from the expected linear shift of the interlayer exciton PL emission [80].

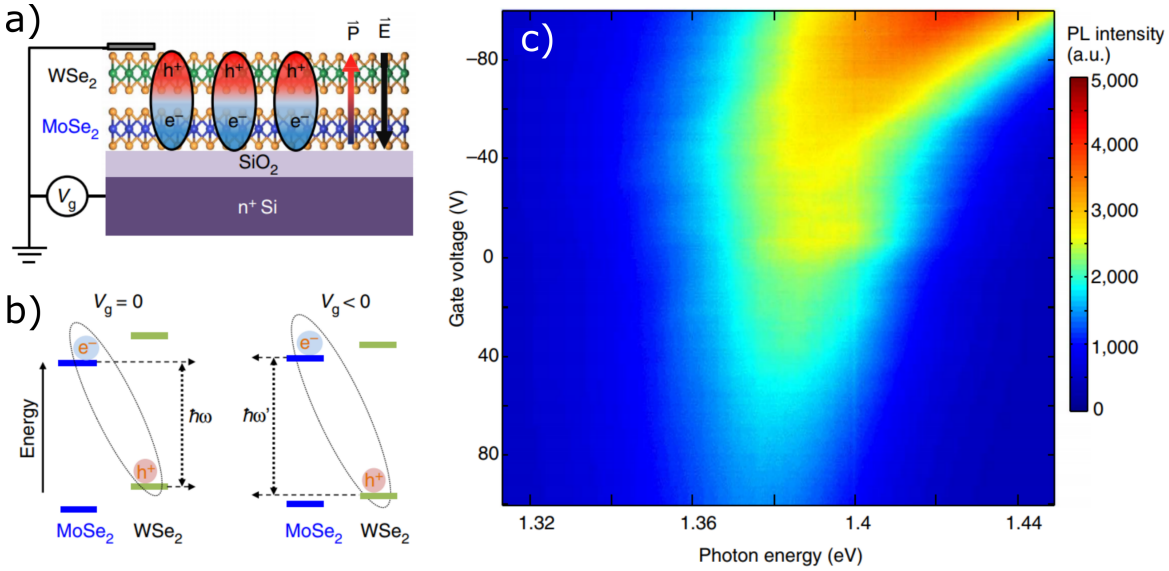

Fig. 2.9 **a)** Lateral view of the device used by Rivera et al. [83]. The IX dipoles are shown overlapped with the sample structure. **b)** Effect of the band structure for an unbiased and biased sample respectively. The band edge states of both materials are modified and the band offset is increased. **c)** Map of IX PL as a function of applied gate voltage. The IX peak blueshift of 45 meV as the gate voltage is reduced. Image adapted from ref.[83].

Another intriguing fact is that IX energy configuration is the lowest as possible and their spatially indirect nature leads to a low oscillator strength, about 50 times smaller than for the intralayer excitons [86, 125]. This results in a long radiative lifetime of IXs, from few, to hundreds of nanoseconds [83, 86, 100].

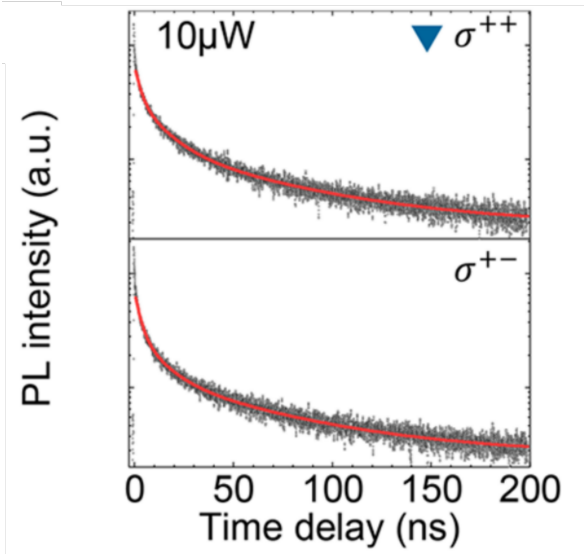

Fig. 2.10 PL lifetimes of the interlayer excitons in co- and cross-polarization of the excitation and detection (top and bottom panel, respectively). The data are taken at 10K under moderate pumping power (10 μW) and reveal a lifetimes of tens of ns. Image adapted from ref.[100].

The combination of the long lifetime and the IX-IX annihilation process lead to a saturation of PL intensity as a function of increasing pumping power. Furthermore it is possible to define a rate equation, to determine the exciton density in the material:

$$\frac{dN}{dt} = \frac{I}{A\hbar\omega} - \frac{N}{\tau} - kN^2. \tag{2.4}$$

The exciton generation rate over time (dN/dt) is ruled by three factors: The first term represents the optical pumping with a continuous laser; I express the pump power; A indicates the beam size and $\hbar\omega$ is the photon energy. The second term describe the exciton radiative recombination: N is the exciton density and τ is the recombination lifetime. The last term expresses the exciton - exciton annihilation through an annihilation coefficient k. With this formula it is possible to calculate the exciton dynamic in a heterobilayer under a steady state [117, 121, 126].

The combination of the IX long lifetime with enhanced IX-IX interaction arising from a permanent out-of-plane oriented dipole would make possible the observation of intriguing

many body effects such as Bose-Einstein condensation, or exciton superfluidity making 2D heterobilayer an excellent platform for observing complex and extreme physical phenomena [127].

2.5 Structure of the IX PL emission

Many works pointed out that the IX PL emission in $MoSe_2/WSe_2$ heterostructures consist of two different components, clearly visible in Fig.2.11. In recent years, due to the refinement of the fabrication techniques, the origin of these two features are emerging more clearly than in the previous reports. This is the only heterostructure case that will be discussed in this section for two reasons: first, it is the most studied heterobilayer; secondly, it is the most relevant heterostructure for the work presented in this thesis, particularly for the work presented in Chapter 5. Although the observation of the IX in $MoSe_2/WSe_2$ heterobilayer is definitely experimentally confirmed, the interpretation of the double peak structure is far from a trivial problem.

Several different explanations were presented and each will be discussed in a separate section of this paragraph. It is very important to point out that it is still an open field of research, with different evidences from each theory and often in contradiction between them. Unfortunately, most of the works present a very poor statistical analysis on different samples, or even no statistics at all.

- **Spin split states in the K valley of $MoSe_2$**

  The first theory indicates that the double peak structure originates from the spin split state of the $MoSe_2$ K point in the conduction band, so that the two transitions are optically bright and optically dark, respectively. This theory was proposed by Rivera et al. in 2015 [83]. Despite the broad linewidth of the IX PL emission (Fig.2.12 (a)), the authors identified two components. Under increasing excitation power they

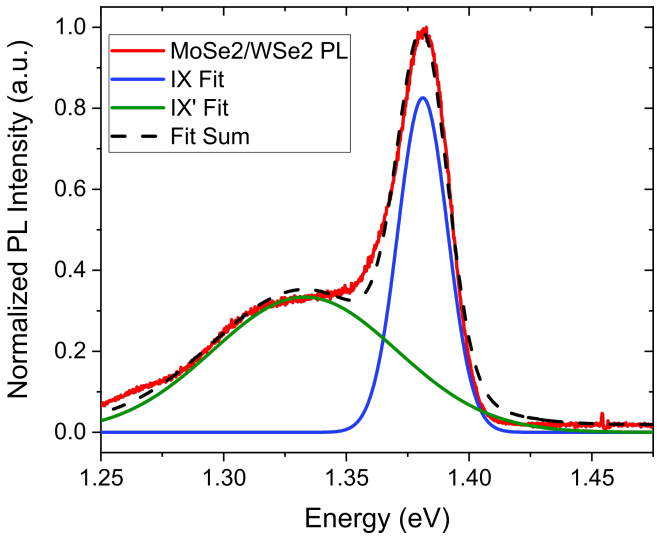

Fig. 2.11 PL spectra of a $MoSe_2/WSe_2$ heterobilayer (red curve). The spectra is fitted with two Gaussians (blue and green for IX and IX', respectively). The black dashed line represents the fit sum.

report a similar blue shift of the two PL peaks and a clear saturation of the intensity of the emission. These effects, joined with the nanosecond lifetime of this emission, indicate that is originated from interlayer excitons. Their conclusion that the double peak originates from the $MoSe_2$ spin split state is supported by the energy splitting of the two IX peaks, which is 25 meV, in agreement with first principle calculations of the SO splitting of the $MoSe_2$ CB and the different evolution of the relative intensities (Fig.2.12 (b)).

- **Spin split states in the Q valley of $MoSe_2$**

  Another similar interpretation is presented by Hanbicki et al. [128]. The sample presented in this work show two fully resolved peaks that also show an opposite trend in PL intensity under different circularly polarized light excitations (Fig.2.13 (a)). This opposite behavior corroborates the idea that the double peak structure is related to the spin split states of the $MoSe_2$ CB. They observe a splitting of 24 meV between the two peaks, compatible with the previous report. The temperature dependence

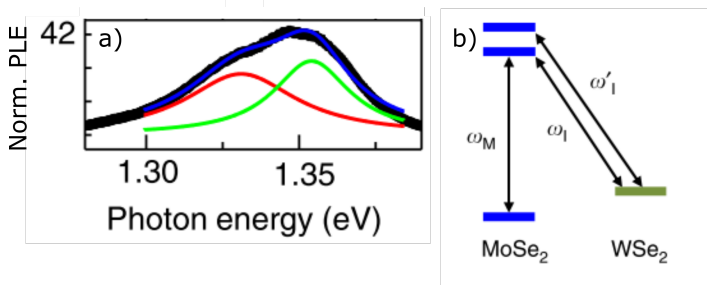

Fig. 2.12 **a)** IX PL emission spectra from ref.[83] (black curve). The two Lorentian curves represent the two transitions (red and green curves, respectively). Blue curve indicates the fit sum. **b)** Schematic model of the origin if the double component of the IX. The two IX peaks observed are related to the two spin split states of $MoSe_2$ CB at the *K*point of the BZ. Image adapted from ref.[83].

behavior of the IX emission is consistent with the spin split states showing a reverse emission moving from 5K to 50K. Their model is different from the previous work, which identifies the IX transition emission as both momentum indirect, taking place from the hybrid Q point of the conduction band to the K point of the WSe_2 valence band. They justify this idea considering the comparable intensities of the two IX peaks and excluding the K-K transition, as they show that the Q point should be involved. The authors support their interpretation considering the hybrid nature of the Q point in a heterobilayer that, according to their picture, promotes the radiative recombination between spatially confined carriers (Fig.2.13 (b-c)). The K point, due to its nonhybridized nature that prevents the carrier recombination and the reduced e-h wavefunction superposition, is considered irrelevant for the IX emission. Similar conclusions are given in another recent work which shows the highest optical quality of the vdW heterostructure. In this work Ciarrocchi et al. show IX PL emerges in two fully resolved peaks which shows opposite trend under different circularly polarized light [129]. When the TMD flakes are grounded and a voltage is applied on the top gate, it is possible to induce and electrostatic doping on the heterobilayer. The results are consistent with the SO spin split state dynamics of the $MoSe_2$ CB. They identify the optical transition according to the model presented by Hanbicki et al., which considers

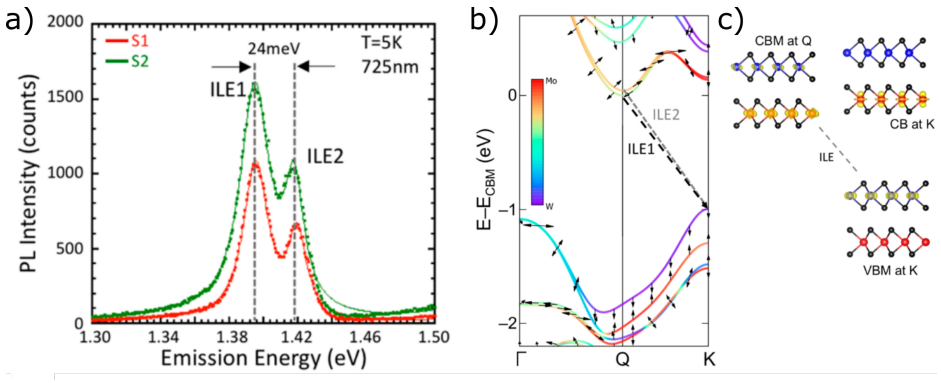

Fig. 2.13 **a)** IX PL emission of the sample presented in ref.[128]. Two regions of the sample are displayed (green and red curve, respectively) The inset shows the splitting, the temperature and the probe wavelength. **b)** Calculated band structure of the $MoSe_2/WSe_2$ heterostructure. The black and gray dashed lines indicate the origin of the IX double peak structure. **c)** Schematic representation of the heterostructure band structure. Image adapted from ref.[128].

a momentum indirect, spin split transition between the Q and K points of the CB and VB, respectively.

- **Momentum direct and momentum indirect transitions**

  Another interpretation of the double IX PL features came from Miller et al. [100]. Their conclusion is that the two peaks are related to two different transitions in two different valleys. The first, less energetic transition is momentum indirect, taking place between the K-Q (the authors call this point as Σ) valleys of the CB and VB, respectively. The high energy transition is almost momentum direct, taking place between the K-K valleys of CB and VB. The authors also pointed out that the two ground states of both valleys have the same spin states of the top states of the WSe_2 VB, making both transitions optically bright. Differently from the other previous sample, the two IX emissions are shifted apart by 50 meV, and also the IX PL signal is overwhelming, compared to the weaker direct excitons signal (Fig.2.14 (a)). Although the absolute intensity is dependent on the instrumental efficiency and the experimental conditions, the intensity within the same spectra can give a rule of thumb indication

about the heterostructure response. This is in contrast with the previous works which show an IX signal comparable or even dimmer than the residual DX emission.

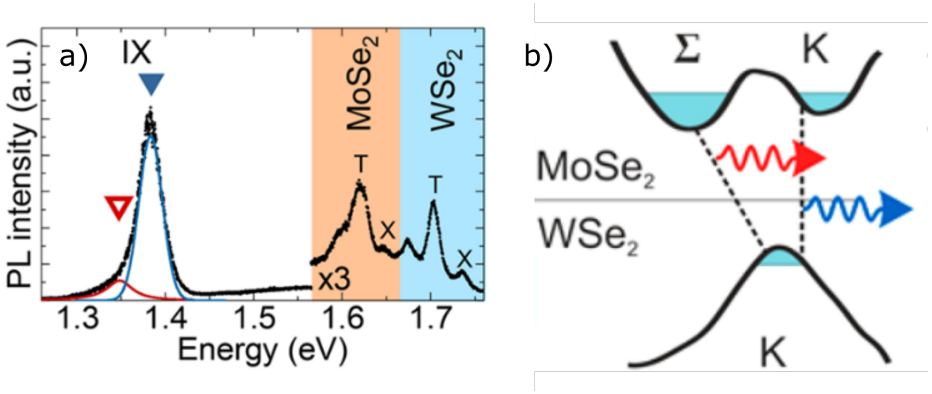

Fig. 2.14 **a)** PL spectra of the heterostructure presented in ref.[100]. The signal of $MoSe_2$and WSe_2 DX is increased for better visibility. The red and blue Gaussian peaks indicate the two components of the IX peak. **b)** Schematic model of the origin of the two IX components. Image adapted from Ref. [100].

The authors also present a full characterization of temperature, power dependences and lifetimes of the two peaks that show opposite trends in all such analysis. At lower pumping power the low energy peak dominates the PL spectrum, while at higher powers the high energy transition becomes more prominent. A similar effect is observed under increasing temperature. Both results are compatible with the proposed model (Fig.2.14 (b)). Lifetime measurements revealed that the high energy peak has a much faster decay that the low energy peak, confirming the momentum indirect nature of this last transition. In the final part of the discussion the authors consider two other alternative explanations for the double IX peak: the presence of charged interlayer excitons and two transition from SO split states. They exclude the presence of charged excitonic species because the high energy peak relative contribution to the PL spectra decreases under increasing pumping power, which is the opposite trend than that expected. The SO split is excluded because the temperature dependence does not reveal a brightening of the supposed optically dark transition to the highest spin

split state of $MoSe_2$. Moreover the two peaks shift differently at different temperatures, and this is in contrast with the valley physics.

Chapter 3

Materials and Methods

In this section we describe the procedures and the equipment used to assemble and characterize van der Waals heterostructures. The first section describes the processes for isolation and identification of single layer TMDs. We also discuss how to recognize their crystal axis. The second part describes in detail the three flake transfer methods used. We provide a comparison between the three main methods. At the end of the chapter there is a detailed description of the optical setup used to carry out the characterization of the devices.

3.1 Micromechanical exfoliation

As discussed in the introduction, mechanically exfoliated flakes provide the highest optical quality of single layer material. As discovered by Geim and Novoselov [4], the scotch tape technique is a valid method to promote the delamination of layered materials and access a few and single layers. Exfoliated materials from bulk crystals are used in all the experiments and structures presented in this thesis. The bulk crystals were prepared by conventional growth techniques to ensure the best chemical purity of the materials. Depending on the bulk crystal quality, it is possible to obtain large flakes to create larger heterostructures, which is beneficial for optical investigations, but is also important for the fabrication steps, as will be

discussed later. From this point of view TMD alloy performance are definitely lower than chemically pure TMDs, due to their internal structure disorder that greatly reduces the size of the single crystal domains. Therefore, getting large area single layer TMD alloys present an additional challenge. The micromechanical exfoliation process has been performed either in a clean room environment (Class 1000) or a regular optical laboratory without any difference in the optical quality of the devices. To promote the exfoliation, large area surfaces of bulk crystals must be exploited. Any cracks, steps or wrinkles, should be avoided in order to promote the cleaving process and increase the yield of few layer materials.

The first step is to stick the bulk material on a piece of a sticky tape (Nitto® BT-150E-CM water soluble tape), as displayed in Fig.3.1 (a). The poly-ethylene terephthalate (PET) side of the tape is used to gently press the crystal down to the tape (Fig.3.1 (b)). This ensures a good adhesion between the two. Once the cover is removed, the tape can be gently bent to promote the detachment of the bulk material. This step usually is not enough to completely lift the crystal, therefore, by the mean of a sharp pair of tweezers the crystal can be totally detached from the sticky surface (Fig.3.1 (c)).

As can be seen from the image, some portions of the crystal remain on the sticky surface. This cleaved material is the seed that will produce the monolayers. The process is repeated until the tape is densely covered with mechanically thinned crystals (Fig.3.1 (d)).

The next step is to thin down this crystal even more, but the reduced thickness prevents any other direct macroscopic manipulation with hand-controlled tools. Therefore a new piece of blue tape with no crystal on it is gently put in contact with the previous one, with the two sticky sides facing each other. The crystals are now sandwiched between the two adhesive layers (Fig.3.1 (e)).

When the tape on top is peeled off, the sticky part holds the bulk crystal on it, creating a replica of the bottom pattern, so the crystals are thinned down even more (Fig.3.1 (f)).

Repeating this procedure few times ensures a good compromise between the tape surface coverage, thicknesses and lateral sizes of the exfoliated layers.

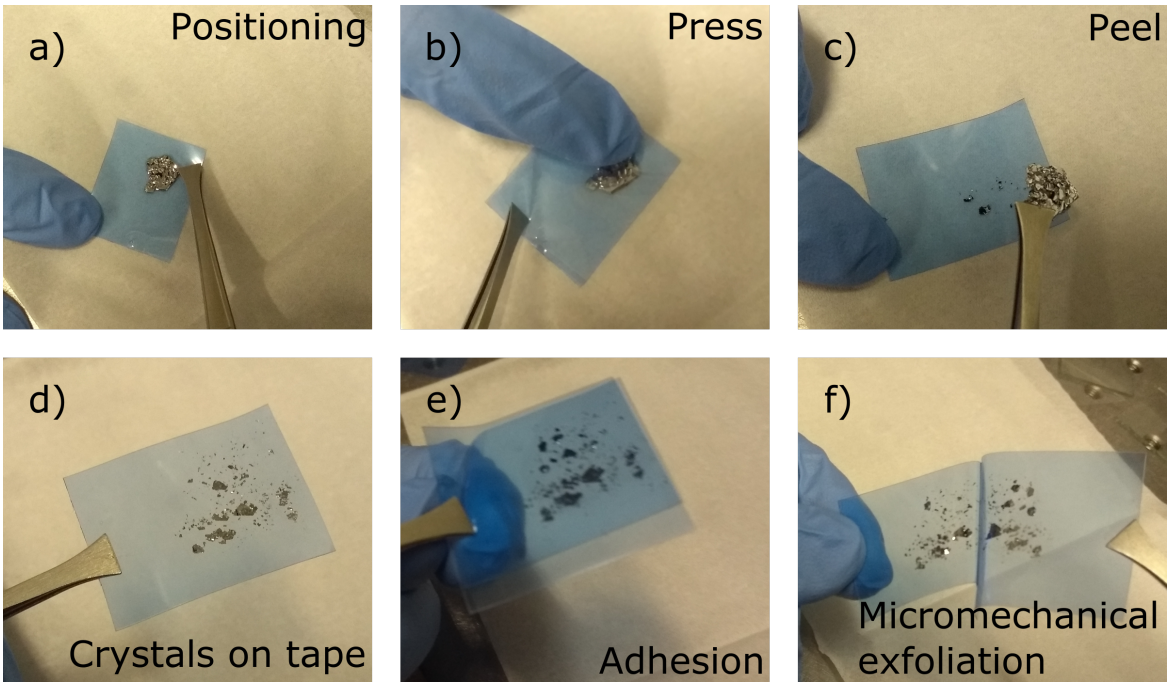

Fig. 3.1 Steps of the micromechanical exfoliation: **a)** The bulk crystal is positioned on the sticky tape. **b)** The crystal is gently pressed to ensure the contact. **c)** The crystal is peeled off. Some material is left on the tape surface. **d)** The process is repeated until the tape is reasonably covered. **e)** Another piece of tape is put in contact on top of the thin crystals. **e)** Peeling the top tape away causes the micromechanical exfoliation.

The final step of the micromechanical cleaving is to choose the appropriate substrate to perform the final step of the exfoliation. How to make an appropriate choice will be discussed later. Now the fabrication methods to follow in each of the three cases are introduced.

- **PDMS** Exfoliating on poly-dimethylsiloxane (PDMS) requires the preparation of a microscope glass slide, that acts as a template, with a square of commercially available PDMS that should not exceed 1.5 cm in lateral size. The tape can be slightly bent to promote the contact (Fig.3.2 (a)). With the aid of a cotton bud the tape is gently pressed down on the polymeric substrate (Fig.3.2 (b)). Heating is not required for this process. Looking at the tape color allows to identify if the contact was effective or if

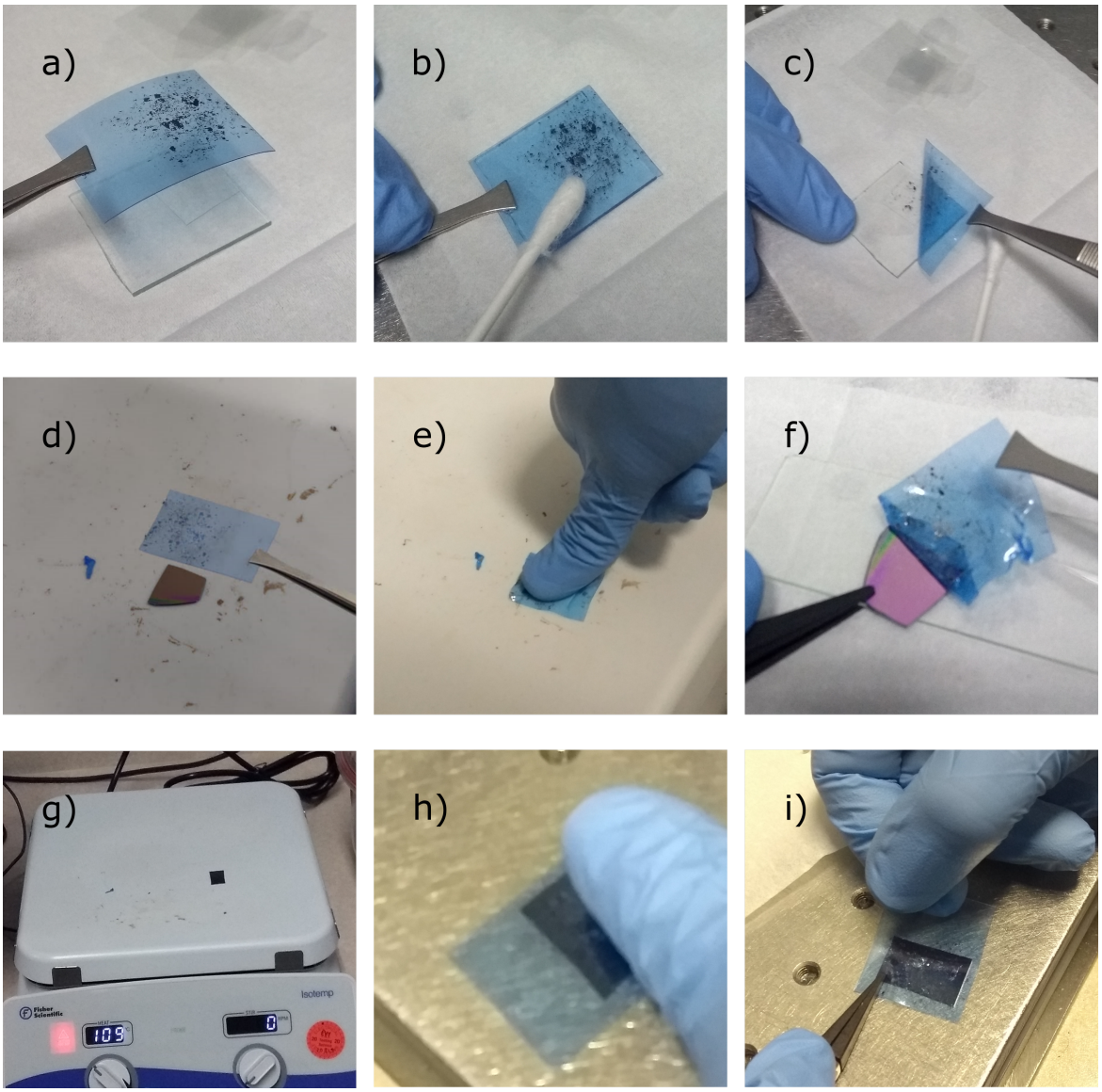

Fig. 3.2 Substrate dependent procedures. for PDMS (a-c) PMMA (d-f) and silicon (g-i). **a)** The tape is aligned with the PDMS layer. **b)** The adhesion is promoted by a gentle press with a cotton bud. **c)** The tape is peeled off. Some material will stay on the polymer. **d)** The tape is aligned on the PMMA-coated substrate when is still on the hotplate. **e)** A firm press ensure the contact between tape and polymer. **f)** When the substrate is cold the tape is peeled away. **g)** The silicon is heated up to 110°. **h)** The tape is put in contact with a gentle finger press. **i)** The tape is slowly peeled off.

there is an air bubble trapped underneath the tape that prevents contact. Once that the tape and the polymer are stuck together, the blue tape can be peeled off (Fig.3.2 (c)).

Since PDMS is a viscoelastic substrate, its stickiness depends on the forces applied: if the tape is peeled very slowly the PDMS tend to release the crystals stuck on top, leading to a poor yield of exfoliation. If the tape is peeled quickly the PDMS tends to retain the crystal layer promoting the exfoliation [130]. During this step it is important to avoid the detachment between PDMS and the glass slide, because the bending of the polymer can affect the exfoliation yield. PDMS softness promotes the exfoliation step, hence using this polymer it is possible to find larger flakes, usually 25μm, but also monolayers of hundreds of microns in lateral size can be found. Also, they often have a regular shape that exhibits one or more corners, the angle of multiples of 30°that makes possible a much more reliable recognition and alignment between the crystal axes.

- **PMMA/PMGI/Si** Exfoliation on poly methylmetacrylate (PMMA) require the preparation of a polymeric double layer structure on a silicon wafer. First a thin layer (200-300 nm) of poly-dimethylglutarimide (PMGI) is spin coated on top of a silicon wafer. The layer must look even and uniformly colored. Baking the wafer promotes the evaporation of the solvent. Then a thicker PMMA layer is spin coated on top of the PMGI layer (1μm) [131, 132]. The wafer is baked again and at the end, if it looks uniformly colored, it can be cleaved in squares of 1-2 cm size each, that will be the final target of the exfoliation. The blue tape with the crystals is deposited on the substrate avoiding the presence of air bubbles (Fig.3.2 (d)). After this step the substrate is put on a hotplate heated at 120°C and left there for 30 seconds. The blue tape during the heating become softer promoting the exfoliation step. Also, the difference in thermal expansion between tape and crystals promotes the process. While the tape is still on the hotplate, a firm thumb press on top of the tape ensures the strong contact between crystals and polymers (Fig.3.2 (e)). During this step is important to avoid lateral shacking to the substrate and be sure that the pressure is evenly applied across

the substrate. Then, once the substrate has been cooled down, the blue tape can be slowly peeled off, paying attention to not damage the polymeric layer underneath it (Fig.3.2 (f)).

- **Silicon** Exfoliation on SiO_2/Si substrate is the most straightforward. The silicon substrate is cleaved in squares 1-2 cm size each and heated at 110°C. After a few minutes the silicon substrate is removed from the hotplate. The tape with cleaved crystal is quickly put in contact on it before it can completely cool down, avoiding the formation of bubbles (Fig3.2 (h)). Once that the substrate is at room temperature the blue tape is peeled off extremely slowly (Fig.3.2 (i)). Since the interaction between SiO_2 and TMD is very weak, a slow and steady peel is required to get an exfoliation instead of a cracking of the crystals.

At this step every substrate is ready for the flake hunt process.

3.2 Flake identification and crystal axes recognition

Flake identification is a critical step of the fabrication process and the most time consuming. Depending on the substrate adopted, the few-layer materials looks completely different from each other, but nevertheless it is possible to identify the single layer simply by their optical contrast compared to the isolated substrate by the mean of a normal optical microscope [133]. Although the process might seem ambiguous, a well trained eye, together with extensive experience, can identify the monolayers with superb levels of precision and reliability. The advantage is the quickness of this approach compared to other techniques, such AFM or Raman spectroscopy [4, 134], that still are used to provide the final proof of flake thickness. Also the thickness of the PMMA and the SiO_2/Si layers are optimized to greatly enhance the contrast of the thin material deposited on top, promoting the identification [135]. For PDMS substrates, the absence of thin film on the surface prevent this process, but the contrast of the

flakes is still high enough to make them visible without the need of additional processing. An important thing that is worth mentioning is that, despite their chemical differences, all the TMDs and their alloys (Mo, W/S, Se) look identical in bright field images if exfoliated on the same substrate.

- **PDMS** TMD flakes on PDMS looks like in Fig.3.3 (a-b), no light filtering is required to identify them. The contrast of the flakes using a 20x magnification objective (Fig.3.3 (a)) is rather low ($\sim$6%) and with such low contrast the identification is not really reliable. Also the broad field probed make the monolayers very small and difficult to identify. Both problems can be solved adopting a 50x magnification objective that enhances the contrast to $\sim$15% and also the flakes looks much larger (Fig.3.3 (b)). The average size of a flake exfoliated on PDMS is 20x20 μm, but flakes of several hundreds μm can be found as well.

- **PMMA/PMGI/Si** TMD flakes on PMMA/PMGI are shown in Fig.3.3 (c-d). Under bright field the contrast of the flake is very low ($\sim$6%) (Fig.3.3 (c)), but it can be dramatically enhanced using a bandpass filter in front of the white light. Adopting the right wavelength range can enhance the contrast of the flake up to 70% for monolayer flakes using a 20x magnification objective (Fig.3.3 (d)). The disadvantage consists of the high sensitivity of the process towards the thickness of the polymeric layer. It is possible that the spin coating process produces unevenly coated silicon substrates, therefore across the substrate the visibility of the flakes will change, forcing the use of an array of filters and choosing every time the most appropriate. Also, not all the polymer thicknesses will be suitable for optical-filter enhanced contrast. The average size of TMD monolayers on PMMA/PMGI is 10x20μm. It is possible to find larger flakes, although their lateral dimension very rarely exceed hundreds of μm.

- **Silicon** TMD flakes on SiO_2/Si are show in Fig.3.3 (e-f), the contrast under bright field illumination is very high ($\sim$20%) at 50x magnification (Fig.3.3 (e)) and the uniformity

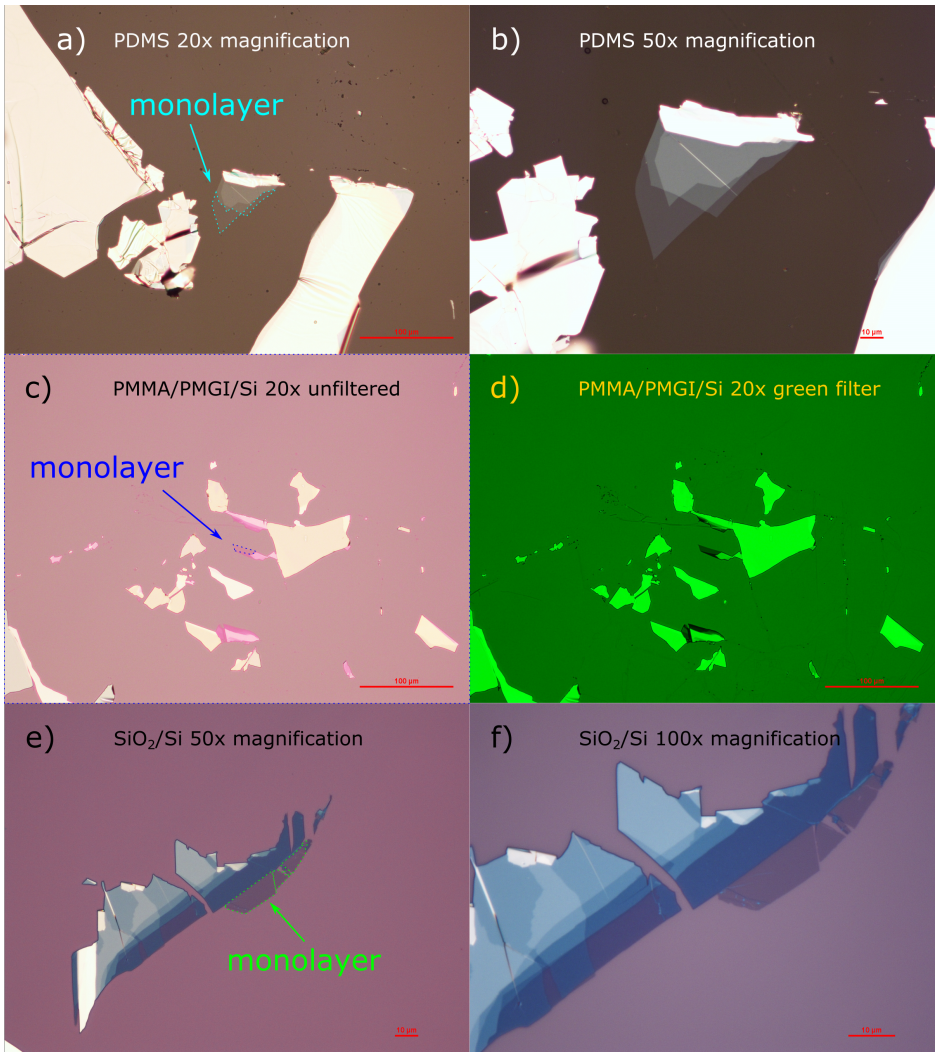

Fig. 3.3 **a)** Bright field image at 20X magnification of a WSe_2 monolayer on PDMS. The monolayer edges are highlighted in cyan. **b)** Same flake at 50X magnification. The contrast is enhanced. **c)** Bright field image at 20X magnification of a WSe_2 monolayer on PMMA/PMGI. The flake monolayer edges are highlighted in blue. **d)** Same image under green filter. The contrast of the monolayer is dramatically enhanced. **e)** Bright field image at 50X magnification of a WSe_2 monolayer on 90 nm SiO_2/Si. The monolayer edges are highlighted in green. **f)** Same flake at 100X magnification. The visibility is increased. In all the images the scalebar is indicated in red.

of the SiO_2 layer make them equally visible across the whole sample surface. The major challenge is in the small size of the flakes, that rarely exceed a lateral size of 20 μm, so it is necessary to use higher magnification (50 and 100X) to have a clear idea about the morphology of the monolayer (Fig.3.3 (f)).

In order to build a heterobilayer, both flakes ideally must be isolated from thick materials, that might prevent the coupling between them and this is a critical parameter to consider [136, 137]. It is possible to overcome this restriction through a rotation of the top and the bottom layers to avoid any matching between thick crystals in proximity of the monolayers. Although for PMMA/PMGI exfoliated material it is possible to have a significant amount of isolated flakes, this chance decreases for SiO_2/Si exfoliated flakes and become negligible for PDMS based exfoliation. Also, as discussed in the introduction, alignment of the crystal axes is vital to observe the PL emission of IX, therefore the fabrication step must take into account this additional constraint. The hexagonal lattice of the TMDs has two main crystal axes, armchair and zigzag, as shown in Fig.3.4 (a). However the atomic lattice structure of the TMD cannot be seen by the mean of an optical microscope.

To generate aligned devices therefore is necessary to identify the crystal axes within the monolayer. The first step is recognizing in the monolayer shape a long straight edge that could probably be a crystal axis of the hexagonal structure [138]. To improve the reliability of the crystal axes attribution, particular combination of straight edges that form an angle of 30°or 60°are searched across the flake, an example is shown in Fig.3.4 (b), in which the straight edges that are aligned at 60°between each other are highlighted by a bold white line. More matches lead to a more reliable flake alignment. This approach is very time saving, however, it is worth pointing out that only some of the monolayers exhibit such long straight edges. Sometimes they are short and therefore the attribution of the crystal axes is unreliable or sometimes they are not straight at all as shown in Fig.3.4 (c). Also, even in samples where the crystal axes of the two flakes are aligned, it is impossible to forecast which edge is aligned with which, and only the even combinations (zigzag/zigzag and armchair/armchair) produces an optically active device. On top of this it is also possible that long edges do not match with any crystal axes, but are instead generated by other causes such as the end of single crystalline domain in the bulk material or other macroscopic effects, which are

impossible to track down from an image of an exfoliated flake. This constraint, joint with a lateral extension of the monolayer that must be large enough to perform optical investigation, is a strong limitation on the amount of devices that can be assembled.

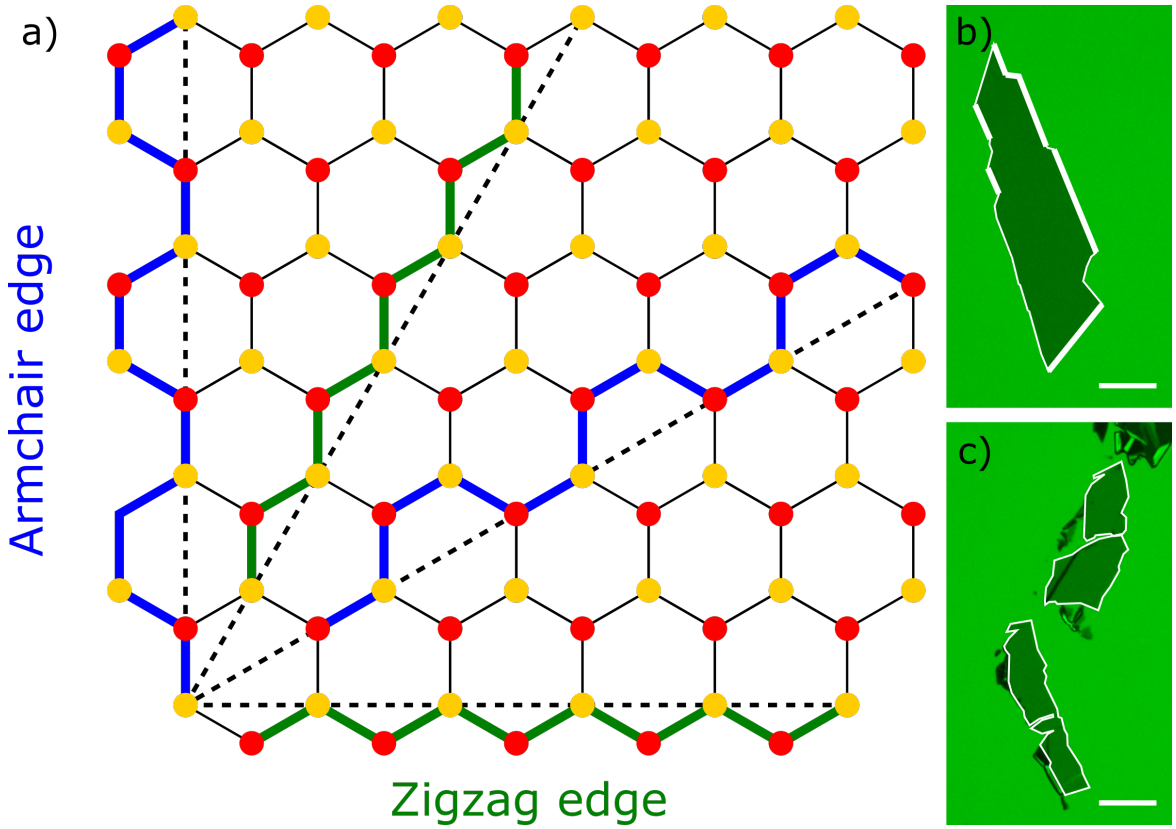

Fig. 3.4 **a)** Schematic structure of a TMD monolayer. Yellow circle indicate the chalcogen atoms, red circles indicate transition metal atoms. The black dashed line indicate an increase of 30°each. The correspondent crystal axes are highlighted in green and blue for zigzag and armchair respectively. **b)** WSe_2 flake exfoliated on PMMA-PMGI. The edges are highlighted in white, the bold edges indicate the identified crystal axes. All of them are rotated by a multiple of 30°. **b)** WSe_2 flake exfoliated on PMMA-PMGI. No crystal axes could be identified. The scalebar is 10 μm.

Before moving into the heterobilayer fabrication, a special mention is for hBN exfoliation. hBN compared to TMDs is almost transparent due to its huge energy gap, also it is synthesized in the form of little crystals that are impossible to handle singularly. For this reason, the tape must be cut in a long and narrow stripe to act as a hook to catch few hBN bulk crystals. Then it is peeled multiple times on a sticky surface of another piece of tape, until the surface is

uniformly covered. Since in this work hBN act as an encapsulation layer for the heterobilayers it is exfoliated only on 90 nm SiO_2/Si. The thickness of the hBN can be deduced by the color of the flake [12]. Dark blue flakes are thinner, generally a few nm. Those flakes are excellent to act as top layers for the encapsulation process, since they are thin enough to protect the TMD from the exposure to chemicals and contaminants, but at the same time are not thick enough to reduce significantly the PL emitted. Due to its transparency in the visible range, it is almost impossible to identify a monolayer hBN with this approach [12], but for the purpose of this work it is not required to use such thin flakes. Light blue flakes are 20-30 nm thick and act perfectly as bottom flakes for the encapsulation. Usually they are much larger than thin flakes, offering a very good base for the heterostructure assembly process. Yellowish, greenish and pinkish hBN flakes are much thicker and they are still viable as bottom encapsulation layer, but the TMD flakes deposited on top would be almost invisible on such thicker substrates. An important requirement of hBN is its flatness. Since every edge of the hBN terraces can scatter light and also induce a nonuniform strain profile on the adjacent TMDs, it is necessary to check that is even and uniform, before using a specific hBN flake [131]. For this reason the flake images are loaded with a picture manipulation software and the contrast is manually enhanced to evidence the hBN terraces. If no inshomogenities can be detected, the hBN is flat, otherwise the uneven area must be excluded from the useful regions.

3.3 Transfer setup and procedures

After the micromechanical cleavage and the flake hunt process, the microscope images of the desired flakes are ready for the alignment step. In an image editor such as Inkscape all the images of the desired flakes are loaded, and each undergo a crystal axes identification step. Once that the crystal axes are reliably identified, the silhouettes of the target flakes will be overlapped and rotated, until the alignment of the identified crystal axes is perfect and also

the underlying hBN is proved to be large enough to support the device. Depending on the alignment it might be necessary to replace one of the flakes with a different one to make the fabrication process possible. Once everything is set, the next step is the physical assembly of the device. To achieve this is necessary to use an optical microscope modified to equip a transfer setup, shown in Fig.3.5 (a-b). Under the microscope is positioned an XY stage, controlled by two micrometric screws. On top of that is placed a 5x5 cm hotplate capable to heat up to 150°C. The hotplate stage can rotate over 360°allowing the alignment of the substrate with a half degree precision. In the center of the hotplate there is a hole connected to a pump. This feature allows the substrate to be held in position for the whole duration of the transfer. On the left there is a mechanical arm placed on a series of micromanipulators. This allows the control of the arm in XYZ directions. The pitch and roll of the arm can be also adjusted, to make it perfectly parallel to the hotplate surface. The Z-axis is equipped with a coarse and a fine micrometer screw to have a better control of the vertical displacement. The arm is held in place on the micromanipulators by the vacuum system. At the end of the mechanical arm there is a small head connected to the pump. In this way is possible to keep the polymer medium suspended, with the desired flake to transfer facing down towards the target substrate. Everything takes place conveniently under the microscope objectives that allow the process to be followed in real time. It is important to mention that the microscope is equipped with long working distance objectives, otherwise the arm cannot be put in the optical path. Although the presence of membranes, glass or other materials in the optical path cause a blurring of the optical images, it is still perfectly possible to clearly resolve the flakes. If the visibility is too low, it is possible to swap from the ocular view to a camera view, which offers the possibility to increase the contrast of the substrate in the desired optical range.

Depending on the substrate adopted in the exfoliation step, the fabrication steps are completely different, hence each of them will be described separately. There will not be any

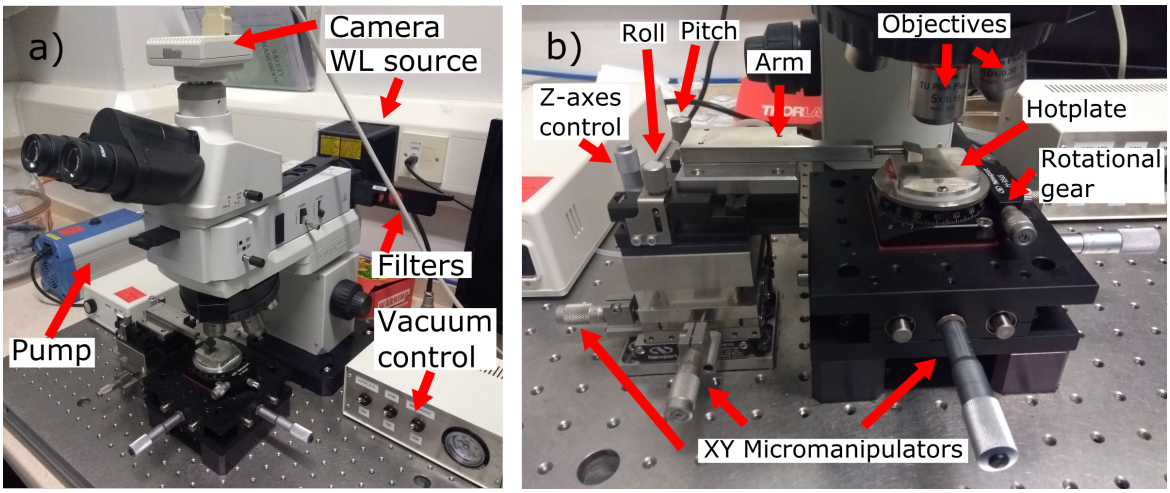

Fig. 3.5 **a)** Large view of the transfer setup. The critical component are indicated by red arrows. **b)** Detail of the mechanical arm and the hotplate. The critical component are highlighted as well.

discussion about wet transfer processes because this approach cause a degradation of the optical properties of the materials, due to their exposition to chemical contaminants [139]. Therefore only dry-peel methods will be discussed and used in this work.

3.3.1 PDMS-based fabrication

Fabricating TMD devices with PDMS is quite easy. The viscoelasticity means that the level of stickiness of a material is directly dependent on the speed of the stress applied; in other words, if the stress is applied quickly the viscosity of the material increases, and consequently its stickiness, and vice versa. Therefore, it is possible to control whether the stamp will release or retain the exfoliated flakes simply reducing or increasing the vertical tension applied. The steps are shown in Fig.3.6. The glass slide with the PDMS on top holding the target flake is flipped down and attached to the mechanical arm. The flake is then aligned with the target location on the substrate and carefully lowered (Fig.3.6 II). In this step, the XY position of both the substrate and the flake is adjusted to keep the structure design. When the PDMS enters into contact with the substrate the color changes drastically. The arm is pushed down until the front of the contact area is conveniently away from the

target flake (Fig.3.6 III). The final step is to slowly raise the mechanical arm. The edge of the contact area will slowly move towards the target flake. In this step it is important to keep the edge moving slowly but constantly, carefully regulating the tension applied on the Z axis of the mechanical arm. When the front is in close proximity of the flake, the speed of the lift is decreased to the minimum as possible (Fig.3.6 IV). It is possible to identify if the flake is deposited checking the optical contrast of the image. Until the target flake is totally released the speed of the lifting must be kept as slow as possible. Once that the contact front is moving away from the transferred flake the arm can be lifted more rapidly. Multiple transfers can be performed in sequence to build from the bottom to the top the desired heterostructure. The most important advantage of this technique is the low sensitivity towards the bottom substrate. With other techniques it is necessary to have a hBN flake as a bottom substrate, however, with PDMS, the transfer can be done directly on almost every substrate (as Au, GaN, InGaP, Distributed Bragg Reflector, etc.) since the parameter that determines the transfer success rate is the surface flatness. Also, it is possible to transfer on top of patterned substrates such as nanopillars [140], photonic structures [141], mechanical resonators [142], etc. The aspect ratio of the substrate make the transfer more challenging, but nevertheless, it is possible. This is a possibility that make this transfer process extremely valuable and particularly efficient for single layer materials and also, unless two flakes are very close with each other (100μm), it is possible to transfer separately all the flakes found on a specific PDMS substrate.

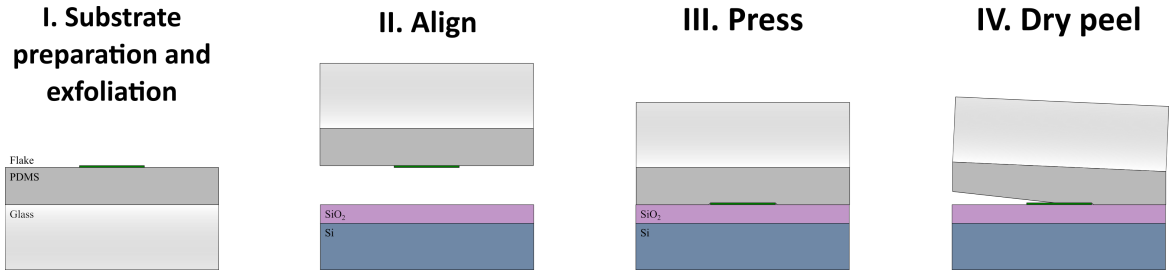

Fig. 3.6 Transfer process for flakes exfoliated on PDMS.

3.3.2 PMMA-based fabrication

This technique is much more complex than the PDMS-based one. It is composed of two separate steps: lifting of the PMMA membranes and the heterostucture fabrication. As described before, the exfoliation is performed on a PMMA/PMGI/Si substrate. To actually be able to use a target flake in a device, the PMMA membrane must be lifted from the silicon substrate. The first step, shown in Fig.3.7 III, is to scratch the PMMA-PMGI membrane with a dental pick. This process is performed under a 5x microscope objective to be sure that the target flake is safely away from the tip of the tool. Very steady hands are necessary since any contact with the dental pick and the polymer layer will result in a piercing or ripping of the PMMA layer, and the consequential failure of the process. The scratch of the membrane must definitely isolate the membrane with the target flake from the rest of the polymeric layer. Once that is done the next step is developing the PMGI layer. MF26A is the chemical adopted in this process, some drops of the solution are transferred with a pair of sharp tweezers in the gap created before, as shown in Fig.3.7 IV. The PMMA membrane is unaffected from the developer, but it must be kept hydrated all the time, constantly checking the process with the microscope, observing the formation of interference fringes slowly finding their way into the sacrificial PMGI layer. Once the PMMA membrane floats free, it can be fished and hung on a metal holder (Fig.3.7 V). It is necessary to wait until the water residues are completely evaporated before the real transfer could take place. The holder is then placed on the mechanical arm and the thin PMMA membrane is aligned with the target hBN flake (Fig.3.7 VI). The arm is slowly lowered down and the XY position is constantly adjusted for both the arm and the substrate. Once that the target flake and the hBN are in proximity, the substrate is heated to 65°C. This promotes the softening of the PMMA. The final step is to check the alignment again and then finalize the approach of the membrane (Fig.3.7 VII). This step can be promoted with a slight touch of the dental pick on the membrane itself. The final step is slowly peeling the PMMA membrane off. Multiple transfers can be performed in

sequence to build the whole device from bottom to top layer. The advantage of this technique is the reliability because the target flake must be deposited on top of a target hBN flake. Due to the strong van der Waals interaction the target flake is deterministically deposited down. Also, the extreme thinness of the PMMA membrane makes the alignment process very easy, due to a good visibility of the flakes. A disadvantage of this process is that the transfer can occur only on top of a hBN flake since the adhesion between the target flake and the PMMA is too strong to be overcome by the interaction forces that take place between the flake and the bare substrate. Another disadvantage is that when the membrane collapse on the substrate, it can be prone to shift a few μm in a random direction. Rotational alignment is not affected, but the lateral shift might cause the reduction or even the total absence of any overlap area between the target and the bottom flake.

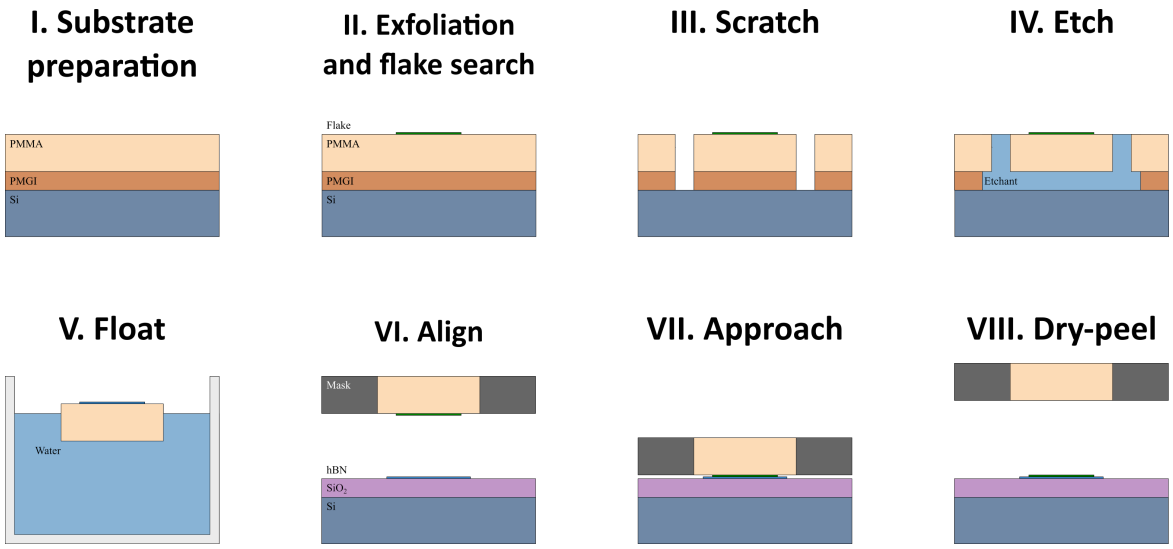

Fig. 3.7 Transfer process for flakes exfoliated on PMMA/PMGI. The first five steps (I-V) are necessary to lift the membrane with the target flake, the last three step is the transfer process.

3.3.3 PC-based fabrication

The PC technique is the most refined state of the art process for vdW heterobilayer fabrication. The overall process is simple to describe but long to set because every single device requires

not less than three steps. As shown in Fig.3.8 I the first step is the preparation of a microscope glass with a small PDMS square (1mm lateral size) that acts as a cushion onto which a PC membrane is stretched. This will be the medium on which will be assembled the whole device. The PC membrane hangs on the mechanical arm facing down, aligned on the target thin hBN flake and carefully lowered down to the target. Once it is in close proximity, the temperature of the hotplate is increased to 85°C and the membrane is lowered down until it is in contact with the substrate. After a few seconds, the membrane is slowly peeled off from the silicon, and the hBN flake is picked up due to the increased stickiness of the PC at high temperatures. This will be the top layer of the whole device. This process can be repeated several times to pick up all the flakes in the desired sequence. The final step is to deposit the whole stack on a target thick hBN flake that will be the bottom layer of the device. Once that the structure is deposited, the temperature can be increased to 150°C close to the glass transition of the PC membrane, which becomes soft. Lifting the mechanical arm up causes the detachment of the glass and PDMS cushion from the PC, which instead will stay on the substrate. The substrate is now displaced laterally until the PC membrane is ripped apart and the bottom stack is isolated from the top glass slide. The PC membrane can be removed in a separate step by washing the sample in chloroform and then in isopropylalcohol. Compared to the other fabrication methods, this is the only one that assembles the device from top to bottom. The advantage of this method is the cleanliness of the interfaces since the flakes never touch any polymer or solvent at any step. Only the top flake is exposed to chemicals, and this is the reason why the first flake it must always be a thin hBN one. Also, the small size of the PDMS cushion makes possible to retrieve almost all the flakes that were previously found on the silicon substrates. Moreover, all the devices assembled with this process are intrinsically encapsulated, enhancing their optical quality as described in the introduction. A tricky part of the transfer is related to the small size of the TMD flakes. Although it is possible to obtain decently sized hBN and graphene flakes from direct exfoliation on silicon

oxide, the size of TMDs rarely exceeds 10 μm so the identification and the alignment of crystal axes is much more challenging. Also, all the structures are suspended on a thin PC layer, which during the fabrication is heated and pressed down multiple times Therefore in very complex structures, formed by many layers, the mechanical stability of the membrane might be compromised.

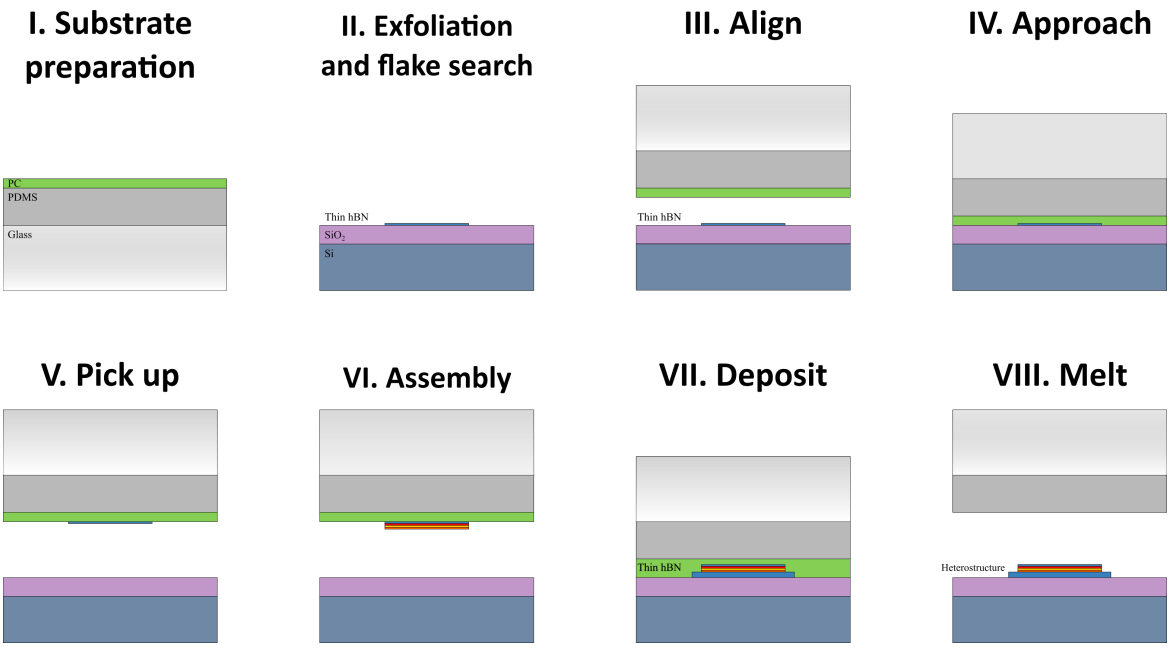

Fig. 3.8 Transfer process for flakes exfoliated on 90 nm SiO_2/Si. The first five steps (I-V) represent the pickup process. These steps might be repeated multiple time to assemble the desired device (step VI). The last two steps show how to release the heterostructure.

3.3.4 Comparison

All the three methods presented offer advantages and disadvantages and there is not a process that totally outshines the others in all the aspects. One important rule of thumb is that the more complex and numerous are the operations performed on a flake, the more the optical properties tend to degrade. On the other hand heterostructures with many layers do necessarily require multiple operations performed on the whole stack. With this in mind, an overview of each process is provided: the PDMS fabrication method is simple, effective and

straightforward. It is the best method to work with single layer devices due to its simplicity and the high yield of the exfoliation process, which is the best of all the three processes. Another figure of merit is related to the possibility to deposit TMDs monolayers on almost every substrate without the aid of bottom hBN flake and also does not require heating at any step. This is particularly efficient for microcavities measurement that requires that the flake is deposited right on top of a DBR substrate, where the interaction between light and matter is maximized. Also, deposition on a patterned substrate is possible.

The PMMA fabrication method makes possible to get larger flakes in a relatively short amount of time, due to the strong interaction between TMD and PMMA. This compensates the additional complexity of the membrane handling. The visibility during the transfer step is the best as possible since only a 1 μm PMMA membrane is put into the microscope optical path. This, linked to the large size of the flakes, ensures the best precision of the alignment, which can be performed with 0.5°precision. The modest temperature involved (65°C) also largely preserves the optical quality of the TMDs.

The PC fabrication method offers the best optical quality since all the samples fabricated with this technique are intrinsically encapsulated and never enter in contact with any chemical in any step. Such quality largely compensates the small lateral dimension of the samples, although the alignment of the crystal axes might be a tricky step. Despite the high temperature required, the absence of contamination on the flake surface makes them as pristine as possible, and the hBN encapsulation protects the flake in the final step when the temperatures are even higher. Moreover, all the materials must be exfoliated on largely commercially available 90 nm SiO_2/Si making the exfoliation and the flake hunt very simple.

3.4 Micro-PL/micro RC optical setup

To analyze the optical properties of direct bandgap semiconductor material, the most widely used and probably also the most powerful tool is a micro-photoluminescence (micro-PL)

setup. It uses photons with an energy higher than the band gap of the target material to excite it. This probing technique is called nonresonant photoexcitation. This process induces the formation of optically generated carriers in the materials, which can then radiatively recombine, emitting a photon at lower energies.

The setup adopted in this work is structured in three different blocks: excitation, optical setup, and detection. Each block is connected to another by optical fibers or free space optical paths.

The excitation block is formed by the components required to generate and guide the laser beam into an optical fiber. For the presented work three CW diode lasers are used: a 532 nm green laser (Roithner Lasertechnik CW532-050 532nm Diode Pumped Laser), a 660 nm red laser (Roithner Lasertechnik ADL-66505TL 660nm Diode Laser), and a 730 nm red laser (Thorlabs HL7302MG 730nm Diode Laser). The most appropriate laser is chosen according to the experiment to perform and the material involved. All of them are filtered by the correspondent narrow bandpass filter and guided into a fiber coupler by a set of mirrors and irises. In their optical path is placed a motorized nutral density (ND) gradient filter to finely control the excitation power. The laser beams are directed into a lens mounted on an XYZ stage that focuses the beam into the end of the fiber.

The laser light is guided by the optical fiber into the main optical setup. Here the laser beam is defocused by the fiber end and made parallel again by another XYZ adjustable lens. Then it encounters a linear polarizer and the appropriate shortpass filter. Another parallel optical path is created for the white light source needed for reflectance contrast (RC) experiments. The white light source is a Thorlab tungsten-halogen lamp which emits from 360 to 2600 nm, connected to a fiber coupler. The fiber adopted has a core of 1μm to reduce the power of the light source and reduce the lateral dimension of the spot size. It channels the light into a fiber outcoupler and the beam is made parallel again by the mean of an XYZ positioned lens. To further reduce the spot size, a homemade telescope is

assembled: the white light beam is focused by a lens and then, in the focal spot is placed a 20μm pinhole. After it, the beam diverges and is made parallel again by another lens. In this way, the size of the white light beam is made equal to the size of the laser beam and both will probe the same area of the sample. The white light beam is directed towards the main optical path by a mirror and made coaxial with the laser beam path. In a similar way, another white light source is made coaxial with both beams to illuminate the sample surface in order to observe its morphology. The optical beams now encounter a cubesplitter that direct them down into a λ-quarter polarizer (that might change the laser excitation from linear to circular), a platesplitter which send the image to a Thorlab camera (to have a wide area image of the sample), and finally is converged to the sample surface by a long working distance 50x objective that collimate it into a spot of 4μm. The PL emission of the sample is collected back from the same objective and then directed up through the same path until the cubesplitter; then a portion of the light continues upwards, where it encounters a mirror that directs it into the collection path. First, it encounters a λ-half polarizer, followed by a linear polarizer, two mirrors and two irises that guide the beam towards the final part of the setup, which is the detection.

An appropriate longpass filter cuts off the laser light, then the beam is collimated again by an XYZ positioned lens that focuses it into an adjustable slit mount in front of a 0.5 m spectrometer, which is equipped with different gratings to get the desired spectral resolution. The detector is a nitrogen-cooled charge coupled device (CCD). Aligning the laser and the white light beam to make the two paths coaxial allows a quick switch between PL and RC configuration without removing the sample from the cryostat. This feature makes possible to collect the two spectra exactly in the same spot.

The samples are mounted inside a cryostat which can be placed under the 50x objective. It is a metallic chamber that can be pumped down to high vacuum ($< 10^{-6}$ Torr) in such way the laser excitation does not induce any chemical reaction on the sample surface with the

molecules present in the air. Also, the sample is placed on a copper holder with a thermally conductive silver paste, inside the copper support there is a coil that can be flushed with a stream of liquid helium. Therefore the sample can be cooled down to cryogenic temperatures (<10K). The helium stream is created by an external pump that sucks the helium from a dewar.

The advantages of this setup configuration are: easy access to the sample, that can be replaced in less than an hour and also the great flexibility of the optical measurements that can be performed. In fact, it is able to perform PL measurement, including polarization resolved, and in the same exact spot, the reflectance contrast of the material can be analyzed. In this way, the emission and absorption of the material can be easy probed at the same time with no change of the sample properties due to thermal cycles or different positions of the device.

Chapter 4

Imaging of Interlayer Coupling in van der Waals Heterostructures Using a Bright Field Optical Microscope

In this chapter the data and the conclusions of a series of experiments are presented performed on several vdW heterostructures to demonstrate how by the means of a modified optical microscope, it is possible to unambiguously identify single layers from multi layer TMDs and monitor the interlayer coupling in vdW heterobilayers.

4.1 Abstract

Vertically stacked atomic layers made of different layered crystals can be held together by van der Waals forces, which can be used for building novel heterostructures, offering a platform for developing a new generation of atomically thin, transparent, and flexible devices. The performance of these devices is primarily defined by the thickness of the individual layers, as well as the coupling between them. The presence of organic residues between the atomic planes can significantly lower interlayer coupling efficiency, leading

to a reduced charge and energy transfer between the layers. The electronic coupling is also affected by the relative orientation of the layers. In this chapteran efficient method is discussed for monitoring interlayer coupling in heterostructures made from transition metal dichalcogenides (TMDs) using photoluminescence imaging (PL imaging) in a bright field optical microscope. The color and brightness in such images are used here to identify mono- and few-layer crystals. We also demonstrate that is possible to selectively image one specific material simply swapping the filter equipped in the bright field microscope. Moreover, the same technique offers an immediate way to track changes in the interlayer coupling of a vertically stacked heterobilayer before and after thermal annealing. We investigate the effect of such steps on the mechanical, electronic and optical properties of the device, and we show that the same approach can reveal the emergence of interlayer excitons after thermal annealing in heterobilayers composed of mechanically exfoliated flakes and as a function of the twist angle in atomic layers grown by chemical vapor deposition. Material and crystal thickness sensitivity of the presented imaging technique makes it a powerful tool for characterization of van der Waals heterostructures assembled by a wide variety of methods, using combinations of materials obtained through mechanical or chemical exfoliation and crystal growth.

4.2 Introduction

Atomically thin materials offer a new paradigm for control of electronic excitations in the extreme two-dimensional limit in condensed matter. Recently, this concept has been developed further with the creation of 2D heterostructures in which individual atomic layers are held together by van der Waals interaction [9, 72, 143, 144]. The weak interlayer bonding loosens the lattice matching requirement, allowing a wide range of materials to be used in one device. Such vdW heterostructures combine unique properties of 2D materials with transparency and extreme flexibility, allowing a range of novel electronic and optoelectronic

devices to be fabricated. Indeed, a wide variety of such devices has been demonstrated, including field-effect transistors [144–149], light-emitting devices [150–153], vertical tunneling transistors[70, 154–156], and photodetectors [154, 157–163]. Stacking of atomically thin semiconductors such as TMDs allows a new approach to band-gap engineering structures with atomically sharp interfaces, in contrast with more traditional III-V semiconductors where the layer boundaries are blurred by the atomic interdiffusion. Type-II band alignment, generally observed in TMD heterobilayers [69, 79, 83, 89, 101, 160, 164, 165], leads to efficient dissociation of optically excited intralayer excitons [84, 166, 167], which is of potential value for photovoltaic and photodetector applications. These devices also open an attractive possibility to access interlayer excitons (IX) formed by electrons and holes localized in adjacent materials [160, 164, 165]. The radiative lifetime can be further increased by the introduction of hexagonal boron nitride spacer layers or rotational misalignment between the TMD layers, making interlayer excitons a promising platform for observation of high-temperature exciton condensation and superfluidity [168]. The long lifetimes in conjunction with valley-dependent optical selection rules in individual TMD monolayers have made interlayer excitons promising for valley index manipulation and valleytronic applications [33]: long-lived (40 ns) valley polarization has recently been demonstrated for interlayer excitons in $MoSe_2/WSe_2$ heterostructures using circularly-polarized optical excitation [169].

Recent advances in growth techniques have allowed lateral [170–176] and vertical [82, 89, 98] vdW heterostructures to be manufactured by epitaxial direct growth. However, the majority of heterostructures employed in the research of electronic and optical properties are still created by stacking exfoliated or chemical vapor deposition (CVD) grown crystals using polymers such as: polymethylmethacrylate (PMMA), polycarbonate (PC), and polydimethylsiloxane (PDMS), as a transfer medium [130–132]. Along with the fast device prototyping, these mechanical dry peel methods offer the ultimate control of the overlap and twist angle between individual layers, enabling control of the degree of the electronic

coupling between them. The electronic and mechanical coupling between the layers is also affected by the fabrication process, leading to organic residues on the crystal surfaces. Thermal annealing in vacuum or inert atmosphere is often used to improve interlayer coupling in vdW heterostructures [81, 82, 105, 108, 164, 167]. Though such thermal treatment can significantly improve the coupling, the efficiency of this method strongly depends on the fabrication procedure used to build a given heterostructure and the annealing conditions themselves.

A fast method for monitoring the coupling between the layers is highly desirable and will enable rapid assessment of the heterostructure properties and quality, which is key for fabrication of novel atomically thin optoelectronic devices. This chapter presents a method for rapid monitoring of the interlayer coupling in vdW heterostructures made from monolayer semiconducting TMDs using a modified bright field optical microscope. We show that photoluminescence (PL) images of a large area of exfoliated or CVD-grown TMD crystals can be obtained using a standard microscope equipped with a white light source and a set of optical edge-pass filters. The presented techniques can be utilized for rapid identification of TMD mono- and even few-layers on various substrates, including PMMA, PDMS and 90 nm SiO_2/Si, commonly used for vdW heterostructure fabrication. Using the color and brightness of the images, the presented techniques can be utilized for rapid identification of TMD monolayers and also to identify their chemical composition at the same time. Also, we show that by using appropriate bandpass filters, selective imaging of individual materials within a van der Waals heterostructure can be achieved. Furthermore, we use this method to assess the changes in the degree of the electronic coupling between the adjacent TMD crystals following thermal annealing. The microscope PL images unambiguously reveal that, while the as-fabricated TMD heterobilayers act as a set of independent monolayers because of the polymer residue between the layers, significant improvement of interlayer coupling

is observed after the thermal treatment. This technique is employed in all the intermediate steps of a heterobilayer fabrication allowing to probe the effect of each step performed.

Using PL imaging, we also investigate the coupling between individual layers in heterostructures composed of exfoliated or CVD-grown TMD monolayers with varying the interlayer twist angles. While all TMD heterobilayers show significant reduction of PL intensity due to intralayer exciton dissociation, the PL quenching is an order of magnitude stronger in samples with small rotational misalignment. The same technique revealed that while heterobilayers with random layer orientation show significant PL quenching due to intralayer exciton dissociation, bright interlayer emission can be seen in rotationally aligned samples. The sensitivity of the TMD PL emission to the individual layer thickness and coupling between different layers makes microscope PL imaging demonstrated here an indispensable tool for vdW heterostructure characterization with wide ranging applications. Previously, a similar technique employing a microscope equipped with a dedicated UV source and a monochrome camera was used to study blinking in two-dimensional semiconductor heterostructures [177]. In our work the imaging relies on the intensity as well as the color of the detected PL, which enables an extended range of experiments on a wide variety of material combinations.

4.3 Experimental procedure and PL imaging of monolayer TMDs

TMD flakes were exfoliated on different substrates (PMMA/PMGI, PDMS and 90 nm SiO_2/Si) as described in section 3.1. Bright field, dark field and PL imaging of 2D TMD crystals was achieved using a commercial bright field microscope (LV150N, Nikon). The schematic of the experimental setup is presented in Fig.4.1 (a). In the PL imaging configuration a 550 nm short-pass filter (FESH0550, Thorlabs) was used to block near-infrared

emission from the white light source. PL signal produced by the sample was isolated using 600 nm long-pass filter (FELH0600, Thorlabs). The short-pass (long-pass) filters were installed into polariser (analyser) slots of the illuminator (LV-UEPI-N, Nikon), allowing quick switching between PL and bright field imaging modes. The PL images of the samples were acquired using a color microscope camera (DS-Vi1, Nikon). While silicon CCD and CMOS sensors have their peak sensitivity at 800 nm, they can detect light with wavelength up to 1.1 μm although their efficiency rapidly decrease for such longer wavelength. Most of the color cameras, however, have a built-in hot mirror that limits their sensitivity to the visible spectrum. In order to enable the detection of near-infrared emission, this mirror was removed. Fig.4.1 (b) shows a bright field image of a WSe_2 flake exfoliated onto a PDMS substrate. The most translucent area in the top right corner of the flake corresponds to the monolayer region. The PL image of the same sample acquired using the experimental set up is shown in Fig.4.1 (e). Even with 1 second acquisition time, the monolayer region is clearly visible in the image due to bright PL emitted by the flake. The PL emission from the bilayer region is two orders of magnitude weaker and requires much longer acquisition times to be detected. Fig.4.1 (e) shows also random variation of PL intensity across the monolayer region that can be caused by non-uniform doping, mechanical strain or presence of structural defects in the flake. The dark lines in the bottom right corner correspond to folds in the sample that can also be seen in the bright field image (Fig.4.1 (b)). The thickness dependence of the PL intensity reflects the changes of the WSe_2 band structure with increasing numbers of layers [178]. While monolayer WSe_2 is a direct bandgap semiconductor, the bandgap becomes indirect for bilayers, leading to a strong quenching of the PL. Fig.4.1 (d) compares PL spectra recorded in different regions of the flake using the micro-PL set up described in section 3.4. The monolayer region shows bright PL with emission peak centered at 1.66 eV (solid blue line). The direct-to-indirect bandgap transition in bilayer WSe_2 leads to a shift of the emission maximum to lower energies, as well as two orders of magnitude reduction

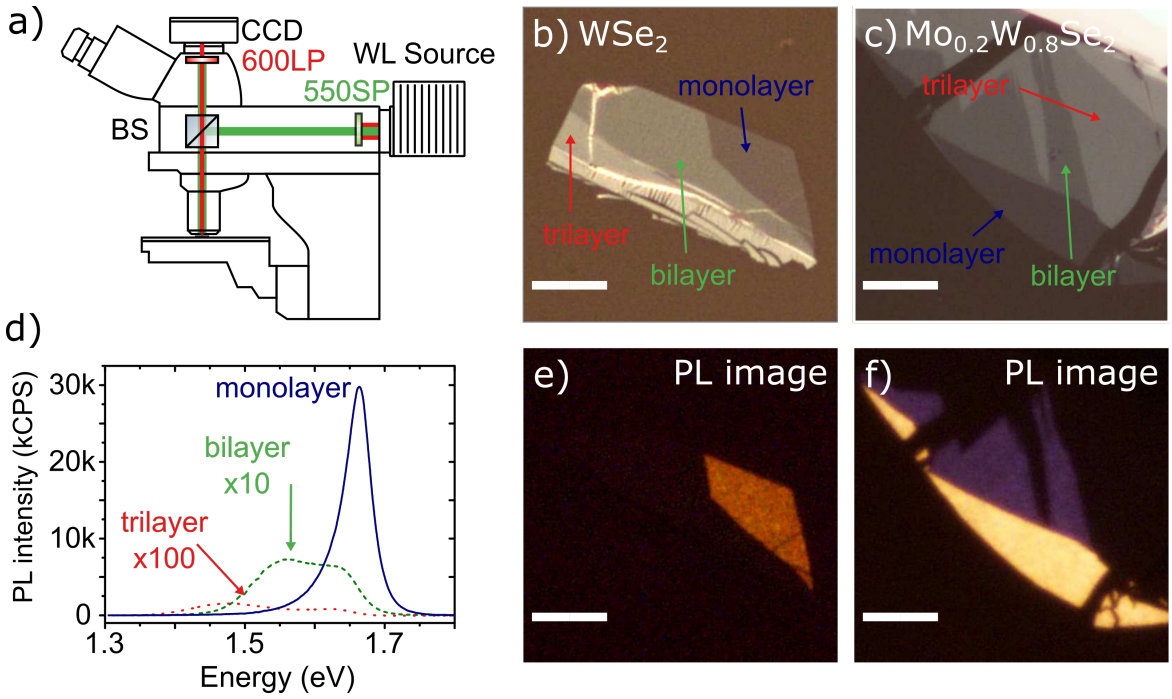

Fig. 4.1 **a)** Schematic representation of the PL imaging setup based on the optical microscope. **b-c)** bright field images of mechanically exfoliated few-atomic-layer crystals on PDMS substrates: WSe_2 in panel b and $Mo_{0.2}W_{0.8}Se_2$ in panel c. **d)** PL spectra recorded in monolayer (blue), bilayer (green), and trilayer (red) regions of the WSe_2 sample shown in panel b. **e)** PL image of the WSe_2 sample acquired with a 1 s acquisition time and 9.6x analog gain on the camera, showing PL from the monolayer region only. **f)** PL image of the $Mo_{0.2}W_{0.8}Se_2$ sample shown in panel c with clearly identifiable regions of a monolayer (yellow) and a bilayer (purple). Image recorded with 1 s acquisition time and 3.4x analog gain.

of the emission intensity (dashed green line). Any further increase of thickness leads to almost complete disappearance of the PL signal (dotted red line). The abrupt change of the PL characteristics with increasing numbers of layers allows PL imaging to be used for sample thickness identification. Fig.4.1 (c) and (f) show a bright field and PL images of a $Mo_{0.2}W_{0.8}Se_2$ sample exfoliated onto a PDMS substrate. Compared to the pure binary compound, the TMD alloy shows much brighter PL emission, making both monolayer and bilayer regions clearly visible in the PL image. The difference in the color reflects the variation of emission spectrum with increasing sample thickness. Similar to WSe_2, the PL spectrum broadens and shifts to longer wavelengths in the bilayer regions. PL at longer wavelengths

appears as a false purple color in Fig.4.1 (f), a feature related to the transmission efficiency in the near-infrared of the color filter arrays in the digital camera used. The thickness sensitivity of PL imaging makes it a convenient tool for rapid identification of TMD mono- and bilayers on various substrates, used in the different fabrication procedures described in chapter three.

Unlike other methods, such as optical contrast measurements [133], or brightness of the flake edges in dark field images, PL imaging relies on the change of the TMD band structure, and therefore, its effectiveness is independent of the type of the substrate used. The exception will be substrates where PL of the TMD monolayers is strongly quenched (for example, when they are placed on gold) or the TMD flakes become strongly strained and their band structure is modified. For such structures, our method provides additional insight into the coupling of the flake and substrate and will highlight any nonuniformity of such interaction through the intensity and color of the PL image. This is shown in Fig.4.2 which contains the bright field images of the WSe_2 flakes shown previously, this time joint with the respective dark field (DF) and PL images. As can be noticed, even if the flakes appears totally different in the bright field images on the three different substrates (PMMA/PMGI, PDMS and 90 nm SiO_2/Si), the PL images, shown in Fig.4.2 (c, f, i), looks extremely similar between each other. The dark filed images shown in Fig.4.2 (b, e, h) clearly shows the monolayer area as the thinnest of the entire image. This can be achieved due to the configuration of the dark field optical microscope. In dark field imaging, the sample is illuminated with light almost parallel to the sample surface, while the collection is always vertical. In this conditions way, all the vertical steps (such flake edges and substrate uneveness) shine with an intensity proportional to their thickness, while flat region appear dark since they do not scatter light. In this way it is possible to identify single layer materials on the substrate. Despite this, the intensity of the scattered light depends on the substrate used, as displayed in Fig.4.2 (b, e, h). On the other hand PL imaging is totally insensitive to the substrate, making the most reliable technique to identify monolayer region of TMDs. It is worth to mention that the dark red

background in Fig.4.2 (f) does not arise from the polymeric substrate, but instead is related to the scattered light of the environment that leaks through the glass slide and the PDMS layer (both transparent) and is detected by the CCD camera. In fact, in presence of thick material, this parasitic light is absorbed and the region looks totally dark. For the other two substrates, this effect is absent due to the complete opacity of the underlying silicon substrate.

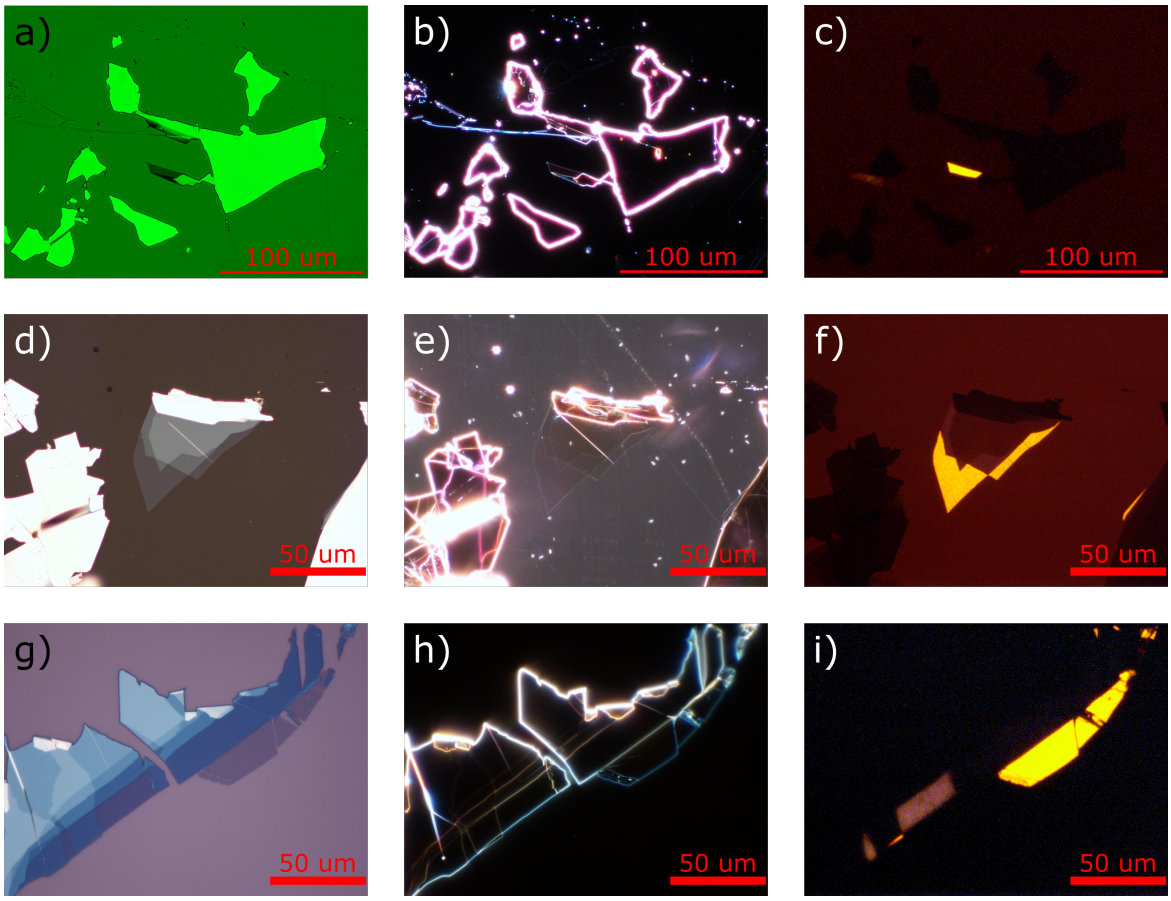

Fig. 4.2 **a)** Bright field image of a WSe_2 flake on PMMA/PMGI substrate. The green color is due to a band edge filter used to enhance the contrast of the monolayer. The scalebar is 100 μm **b)** Dark field image of the same flake. The scalebar is 100 μm. **c)** PL image of the same flake. The image is acquired at 4 sec and 3.4x analog gain. The scalebar is 100 μm. **d)** Bright field image of a WSe_2 flake on PDMS substrate. The scalebar is 10 μm. **e)** Dark field image of the same flake. The transparency and uneven surface of the PDMS causes the prominent background. The scalebar is 10 μm. **f)** PL image of the same flake. The image is acquired at 4 sec and 3.4x analog gain. The scalebar is 10 μm. **g)** Bright field image of a WSe_2 flake on 90 nm SiO_2/Si substrate. The scalebar is 10 μm. **h)** Dark field image of the same flake. The scalebar is 10 μm. **i)** PL image of the same flake. The image is acquired at 4 sec and 3.4x analog gain.

4.4 Selective imaging and monitoring of interlayer coupling in heterobilayers

Fig.4.3 compares bright field images of $MoSe_2$ and WSe_2 flakes exfoliated onto PMMA and PDMS membranes respectively; green illumination was used for imaging of the sample on the PMMA membrane in order to make the monolayer region visible [178]. TMD flakes have very different appearances on these two substrates, with few-layer areas showing negative (positive) optical contrast on PMMA (PDMS). Nevertheless, single layer regions of both samples can be easily identified in PL images (Fig.4.3 (b, e)). Different colors of $MoSe_2$ and WSe_2 in PL images reflect the difference between their emission spectra. Fig.4.3 (c, f) plots room-temperature PL spectra for the monolayer regions of both flakes recorded using the micro-PL set up. For $MoSe_2$, RT PL emission arising from exciton recombination is centered at 1.58 eV and appears pale pink colored in the PL image, while for WSe_2 the RT exciton PL peaks at 1.64 eV has a bright yellow color. Color imaging in digital cameras is achieved through the use of color filter arrays, such as Bayer filter mosaic. The false color in PL images is the result of the difference in the near-infrared transmission efficiency of these filters. With this combination it is therefore possible to unambiguously identify the chemical composition of the flakes looking at their PL images.

The material sensitivity of the PL imaging using a microscope makes it very useful for vdW heterostructure characterization. For the semiconducting group VI TMDs, a heterostructure formed by monolayers of two different materials will have type-II band alignment with the edges of valence and conduction bands located in different materials [51, 179]. The staggered gap in TMD heterobilayers facilitates ultrafast charge separation between the two layers that acts as a dominant decay channel for optically excited intralayer excitons, significantly quenching their PL [84, 167, 180].

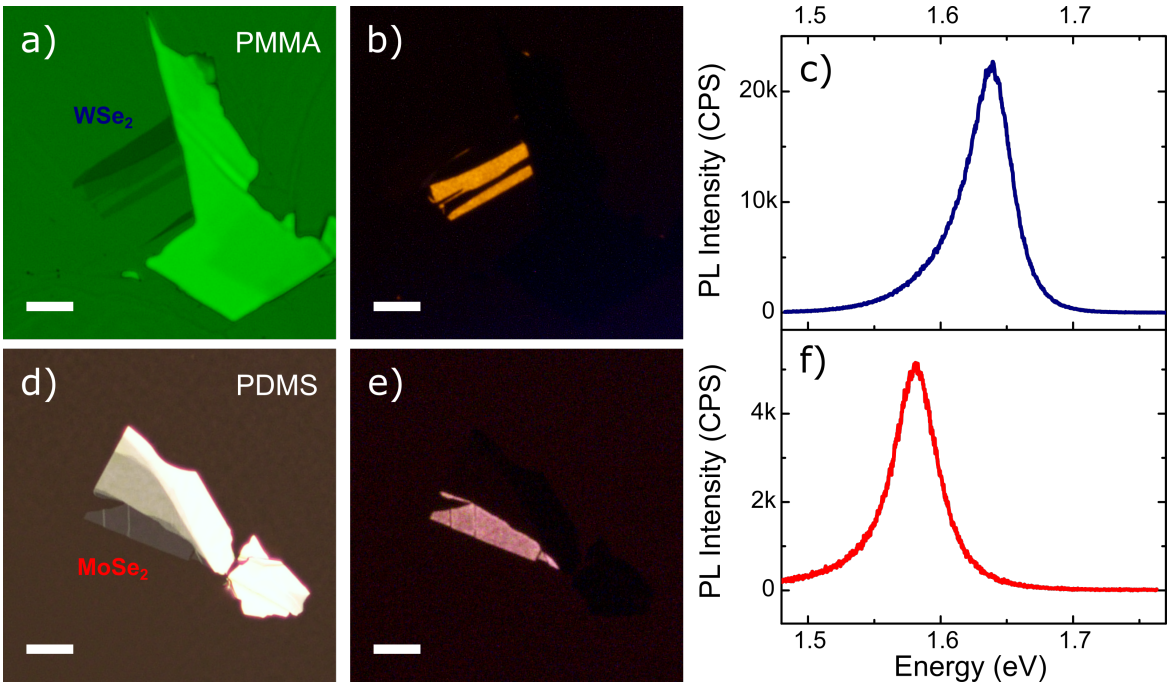

Fig. 4.3 **a)** Bright field image of a WSe_2 flake exfoliated onto PMMA-PMGI substrate under green illumination. **b)** PL image of the sample. The image is acquired at 4 sec and 3.4x analog gain. **c)** PL spectrum recorded in the monolayer region of the sample using a micro-PL setup. **d)** Bright field image of a $MoSe_2$ flake exfoliated onto PDMS. **e)** PL image of the sample. The image is acquired at 4 sec and 3.4x analog gain. **f)** PL spectrum recorded in the monolayer region of the sample using a micro-PL setup. The scalebar in the optical images is 10 μm.

The overall decrease in the PL intensity is related to the nonradiative decay of electron-hole pairs. The intralayer exciton radiative lifetime is of the order of 1 ps [30, 77] while the interlayer excitons radiative decay time exceeds 1 ns [83]. The nonradiative processes are extremely fast in TMDs [82], competing with the intralayer exciton radiative decay, so when the excitons are dissociated due to the charge transfer in the heterostructures, the overall PL intensity is significantly reduced. This process is further enhanced in heterostructures made of misaligned heterobilayers, where the radiative decay of interlayer excitons is suppressed due to the momentum mismatch between the electron and hole localized in different monolayers [87, 181].

The efficient interlayer coupling in TMD heterostructures requires the interface between adjacent layers to be clean of any contamination. As the van der Waals heterostructure fabrication through mechanical stacking relies on the use of a polymer (PMMA, PC, PDMS, etc.) as the transfer medium, it often results in the presence of organic residues between the atomic planes. Fig.4.4 (a) show an optical image of a non aligned $MoSe_2/WSe_2$ heterostructure assembled on Si/SiO_2 substrate using viscoelastic stamping method employing PDMS stamps [130].

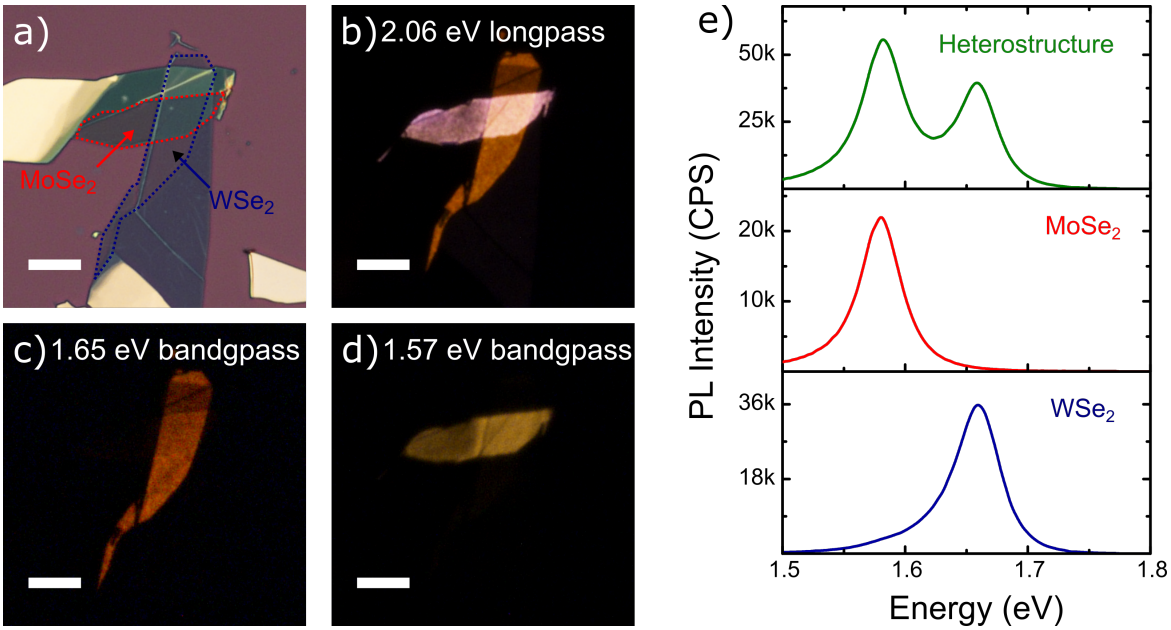

Fig. 4.4 **a)** Bright field image of a $MoSe_2/WSe_2$ heterostructure assembled on a Si/SiO_2 substrate by viscoelastic stamping. **b)** PL image of the sample acquired using a 2.06 (600 nm) longpass filter in front of the microscope camera, showing emission from the monolayer regions of both materials. **c)** Selective PL image of WSe_2 acquired using 1.65 eV (750 nm) bandpass filter for detection **d)** and 1.57 eV (790 nm) bandpass filters for detection. **e)** PL spectra acquired in the heterostructure (top), isolated $MoSe_2$ (middle) and WSe_2 (bottom) regions.

While both TMD crystals have similar appearances in the bright field microscope image, the PL emission of their monolayer regions has noticeably different colors, allowing the two materials to be easily distinguished as discussed before. Furthermore, selective imaging of different materials within the heterostructure can be achieved by replacing the long-pass

filter in the detection path with an appropriate band-pass filter. Fig.4.4 (c-d) shows the PL images recorded using the bandpass filters with the transmission region centered at the emission wavelength of the corresponding material (1.65 eV in panel c and 1.57 eV in panel d, for WSe_2 and $MoSe_2$, respectively). As the signal intensity was lowered by the use of a narrow-band filter, 10 s acquisition time was used for both images. Although emission maxima at room temperature for $MoSe_2$ and WSe_2 are positioned close to each other, the images demonstrate perfect selectivity, showing only the monolayer region of the chosen material. Fig.4.4 (e) plots PL spectra recorded in isolated $MoSe_2$ (solid red spectra) and WSe_2 (solid blue spectra) areas, as well as in the overlap region (top). As it is evident from both PL images and spectra, the emission of the heterostructure consists of the sum of $MoSe_2$ and WSe_2 emission, indicating a weak coupling between the two layers.

The efficient interlayer coupling in TMD heterostructures requires the interface between adjacent layers to be clean of any contamination. As the van der Waals heterostructure fabrication through mechanical stacking relies on the use of a polymer as a transfer medium, it often results in the presence of organic residues between the atomic planes [82, 164] that prevent the electronic coupling of the layer and consequently suppress the charge carriers segregation process. Thermal annealing in a vacuum or inert atmosphere is commonly used to remove organic residues from the surface of 2D crystals [81, 82, 105, 108, 164, 167]. Here we utilize this method to improve interlayer coupling in an existing heterostructure.

Fig.4.5 compares bright field microscope images of the sample before (a-c) and after (d-f) annealing in high vacuum at 120 °C for 2 h. While a part of the isolated $MoSe_2$ monolayer was damaged during the thermal treatment, both isolated WSe_2 and heterostructure regions remain mostly intact. Although the thermal treatment could not completely remove the organic residues trapped between the layers, it has caused their aggregation into small contamination pockets that can be clearly seen in both bright and dark field images.

Comparing the dark-field images acquired before and after annealing, shown in panel (b) and (e), respectively, it is evident that the contamination pockets have formed only in the areas where the two crystals overlap. The effects of the thermal treatment can be clearly seen in the PL image of the sample in Fig.4.5 (c, f). The strongest change of the PL intensity can be seen in the layer overlap region, where both $MoSe_2$ and WSe_2 emission has almost completely disappeared after annealing. The strong quenching of the intralayer PL due to ultrafast charge separation indicates significant improvement of interlayer coupling [83, 169]. While the WSe_2 emission intensity is significantly reduced in all areas covered by $MoSe_2$, bright PL can still be observed in the parts of the heterostructure around the contamination pockets. The positions of these bright spots fully correlate with the pockets seen in panels d and e. However, the absence of the electronic coupling in these regions can only be revealed in the PL image shown in Fig.4.5 (f).

4.5 Investigation of thermal annealing and self-cleaning mechanism process

Fig.4.5 shows the presence of contamination pockets only in the heterostructure area, between the $MoSe_2$ and WSe_2 monolayers and also where the WSe_2 flake overlaps with the thicker $MoSe_2$ flake on top of the image. Freestanding flakes, either monolayers or multilayers, instead do not show any aggregation of such residues. This fact suggests that only in presence of an artificial heterostructure region the thermal annealing causes the aggregation of the polymer contamination. Another effect to take into consideration for the annealing step is how much the thermal treatment will worsen the optical properties of the isolated TMD flakes (in terms of linewidth and intensity) and their heterobilayers. Heating the sample induces the formation of defect bound states, due to the activation of surface reaction between the TMDs atoms and the chemicals that are absorbed on its surface or present in the gaseous phase.

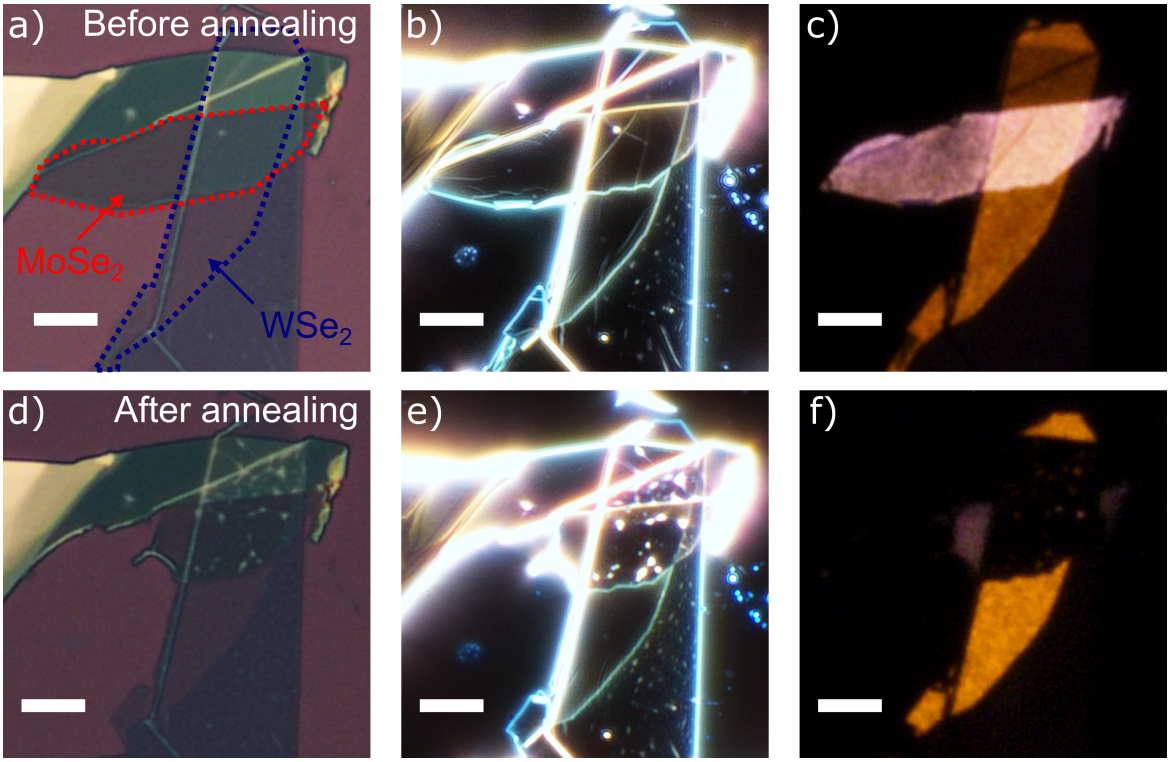

Fig. 4.5 **a-c)** Bright field, dark-field, and PL images of a $MoSe_2$/ WSe_2 heterostructure before the annealing. **d-f)** bright field, dark-field, and PL images of the same structure after annealing in high vacuum at 120°C for 2 hours. All scale bars in the figure correspond to 10 μm. PL images are recorded with a 1 second acquisition time and 9.6x analog gain.

Also, the different thermal expansion coefficient of the TMDs and the substrate (in this case 90 nm SiO_2/Si) causes the accumulation of strain on the chemical structure of the flake itself. Both effects determine the presence of defect bound states, depletion of the PL intensity of the unperturbed excitonic species and broadening of their related linewidth. Investigating this topic is vital for establishing a fabrication method that at the same time ensures the electronic coupling between the two TMD flake, but at the same time preserves their optical properties. Mechanical deterioration of the $MoSe_2$ flakes is also observed in Fig.4.5 (d) indicating that the annealing conditions adopted are too extreme, therefore milder annealing parameters must be searched.

To test this idea, a set of $MoSe_2$ flakes has been fabricated and analyzed by the mean of microscope images and AFM measurements. Each of these samples has been annealed

at a different temperature (50, 70, 80, 90 and 100°) for the same time (2 hours each) and then the same characterization was performed again. The comparison between the AFM profile before and after the thermal process can reveal if the annealing has induced the aggregation of the PDMS contaminant and the eventual presence of morphological damage on the TMD structure. Also, at the end, the set of sample is cooled down and their optical properties analyzed again to establish the relationship between annealing temperature and optical quality.

Fig.4.6 show $MoSe_2$ samples deposited on 90 nm SiO_2/Si. The bright field, PL and dark field images are displayed in column for each sample. The BF and PL images show similar behavior of the flakes, confirming their monolayer nature. The last column shows the AFM image of the monolayer flake. From the profiles across the monolayer/substrate edges, the average height of the two regions is fitted so that the height difference is calculated. The results are summarized in table 4.1. Surprisingly, the thickness of the flakes is of several nanometers, much thicker than the expected value of 0.6 nm relative to a TMD monolayer reported. These results confirm the presence of a polymer contamination layer that acts as a dielectric barrier and causes the absence of coupling in non annealed heterobilayers shown in Fig.4.5. Interestingly AFM images reveal that this contamination layer is rather even across the flake, acting as a continuous envelope, and this explains the total absence of electronic coupling in the heterostructure area observed in Fig.4.5.

Each sample has then been annealed separately in the same vacuum oven at different temperatures, increasing from 50 up to 100°C. Fig.4.7 shows the same sample characterization after the annealing steps. The conditions used for the inset sample are displayed in each of the BF images. By comparing the PL images before and after the thermal treatment, it can be observed that the brightness of the flakes is reduced in all the samples, as expected, but the decrease is non uniform. In fact, the samples annealed at higher temperature show a more pronounced PL quenching than the samples annealed in more mild conditions. This

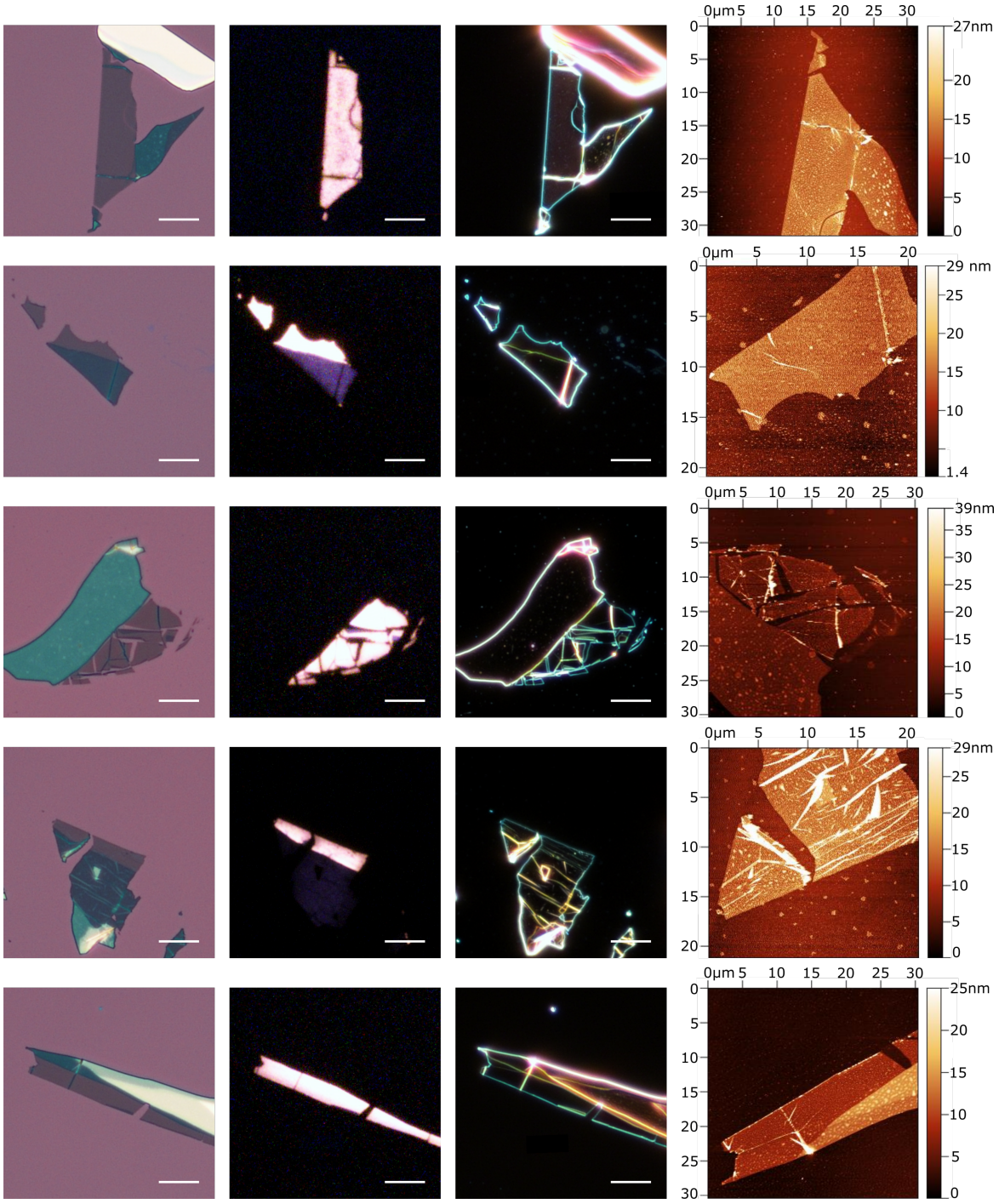

Fig. 4.6 Bright field (first column), PL imaging (second column), and dark field images (third column), of a series of as-fabricated $MoSe_2$ flakes. The last columns show the AFM scan of the flakes.

result shows the effectiveness of the PL imaging to rapidly assess the sample quality in a fast and nondestructive way. The dark field images and the AFM show no significant mechanical damage of the flake structure, indicating that the temperature plays a critical role in the flake mechanical stability. Interestingly, the profiles acquired from the AFM images in the same locus previously analyzed show a similar thickness across the flake edges. The results after annealing, shown in table 4.2, are very close to the one observed in the non annealed samples. This result indicates that the thermal annealing does not act on the contaminant itself, but instead is a catalyst to promote the aggregation of the contaminants trapped between two vertically stacked 2D materials.

Table 4.1 Summary of the values extracted from the AFM profiles before the annealing.

Name	**T**	**Prof. 1** (nm)	**Prof. 2** (nm)	**Prof. 3** (nm)	**Average**	**Error**
S1	50°C	5.8±1.4	5.4±1.6	5.2±2.1	**5.4**	±**1.7**
S2	70°C	10.5±3.2	8.0±3.9	6.7±3.0	**8.4**	±**3.3**
S3	80°C	4.6±2.0	4.2±1.1	4.1±1.3	**4.3**	±**1.4**
S4	90°C	10.1±3.5	8.7±3.5	6.5±1.8	**8.8**	±**2.9**
S5	100°C	6.1±1.1	6.7±1.9	6.3±1.0	**6.3**	±**1.3**

Table 4.2 Summary of the values extracted from the AFM profiles after the annealing.

Name	**T**	**Prof. 1** (nm)	**Prof. 2** (nm)	**Prof. 3** (nm)	**Average**	**Error**
S1	50°C	6.5±2.4	6.3±2.8	6.6±1.5	**6.4**	±**2.2**
S2	70°C	7.2±0.9	6.2±2.0	5.7±1.1	**6.3**	±**1.3**
S3	80°C	3.5±1.0	3.2±0.8	4.4±1.6	**3.7**	±**1.1**
S4	90°C	6.6±2.3	6.1±2.7	4.6±1.6	**5.7**	±**2.2**
S5	100°C	6.7±1.0	5.2±0.9	5.6±1.1	**5.8**	±**1.0**

The samples were then characterized by micro-PL at low temperatures (T<10K) to study their optical quality after different annealing conditions. The PL spectra are shown in Fig.4.8 (a) for all the samples. Panel (b) and (c) of the same image plot the intensity and the linewidth of the PL signal for different annealing temperatures respectively. The emission intensity is significantly reduced even for relatively mild temperatures, dropping by half as the annealing

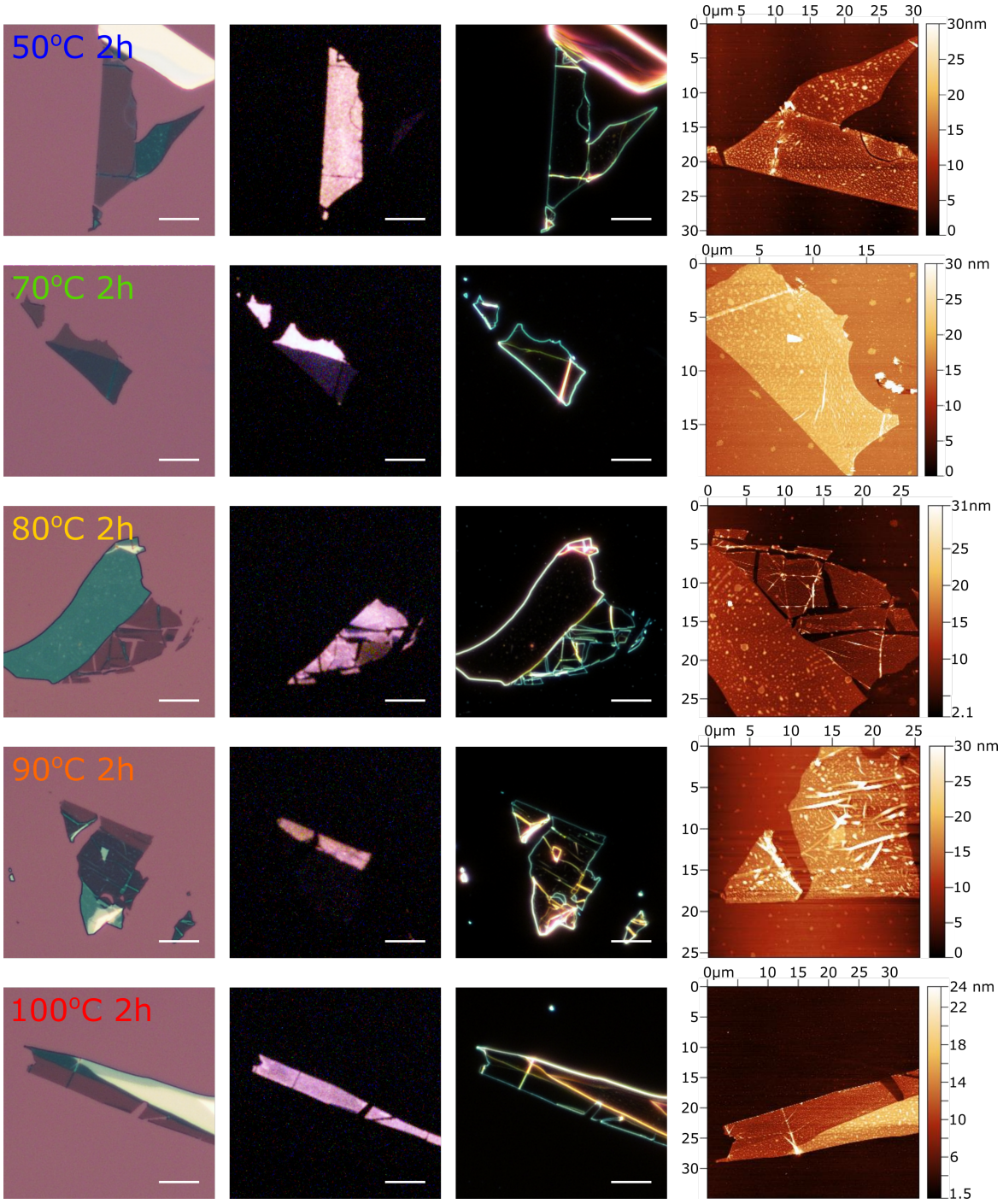

Fig. 4.7 Bright field (first column), PL imaging (second column), and dark field images (third column), of a series of $MoSe_2$ flakes after vacuum annealing. The conditions are displayed in the first column. The last columns show the AFM scan of the flakes after the annealing.

temperature is increased from 50 to 70°C. At the same time the FWHM of the PL peak increases from 8 meV to 12 meV, for the same annealing temperature range. Both trends are observed even for higher temperatures, showing a progressive worsening of the optical quality for both parameters as the annealing condition becomes more extreme. To indubitably

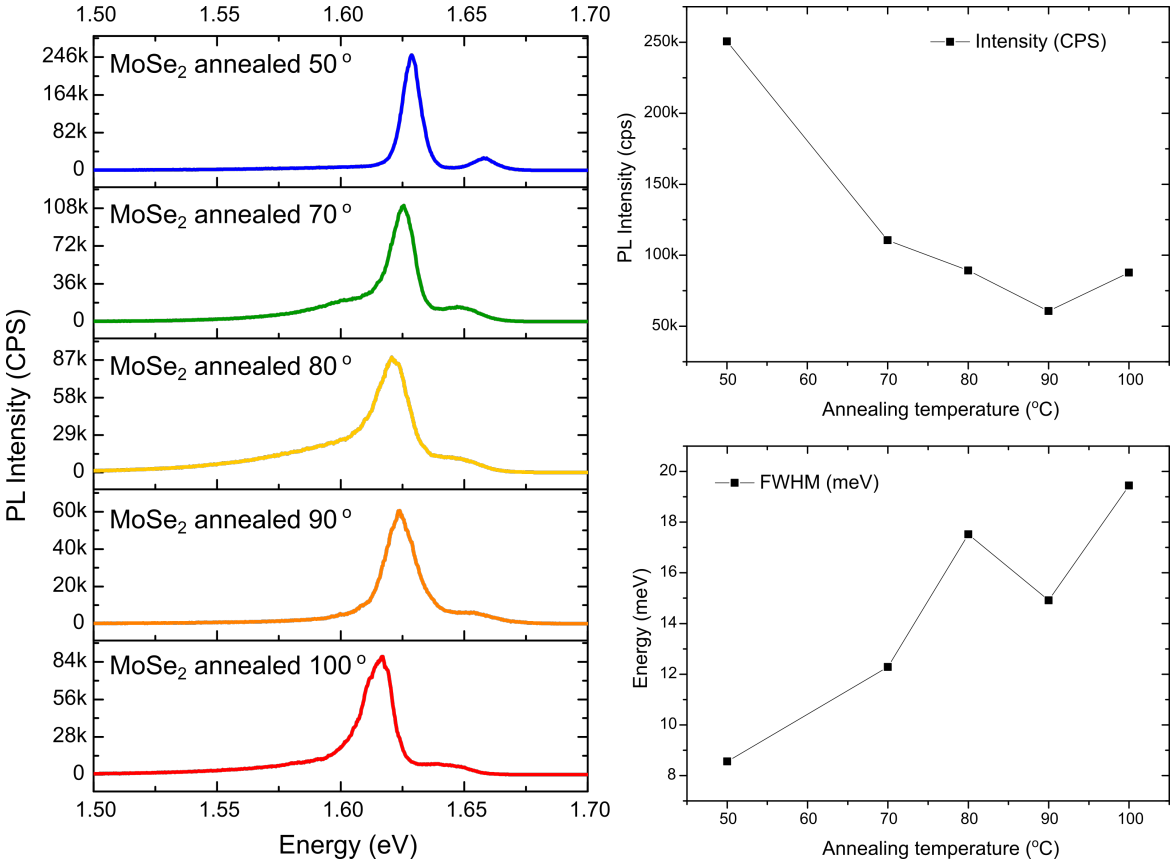

Fig. 4.8 Evolution of the PL optical properties of $MoSe_2$ as a function of the annealing conditions. The details are shown in the inset of the graph on the left. PL intensity and linewidth are shown in the two panel on the right (top and bottom respectively). The spectral analysis was performed at T<10K.

prove that the annealing step doesn't affect the contamination layer, we select sample 1 of the previous batch (annealed at 50°C for 2 hours) to deposit on top of it a WSe_2 monolayer, creating a heterobilayer with a previously annealed flake. Compared to the sample shown in Fig.4.5, in this case the crystal axes of the two flakes were aligned during the fabrication step. The RT PL characterization and optical image of the sample are taken after the top WSe_2 flake

has been deposited. The aim is to demonstrate that without the presence of a heterobilayer the thermal annealing does not remove the polymer contaminant. We deliberately selected the sample annealed in milder conditions to test if this temperature range is adequate to activate the contaminant aggregation. The microscope images of the sample before annealing are shown in Fig.4.9 (a-c). As can be observed the almost perfect triangular shape of the heterojunction confirm the alignment of the crystal axes of the two flakes. Also, in dark field image the heterostructure looks flat with no identifiable defects, but most importantly PL imaging demonstrates that once again in the heterojunction, despite the bottom flake was already annealed, the two materials are not electronically coupled, since the brightness is the sum of the two flake PL emission and there is no evidence of interlayer electronic coupling.

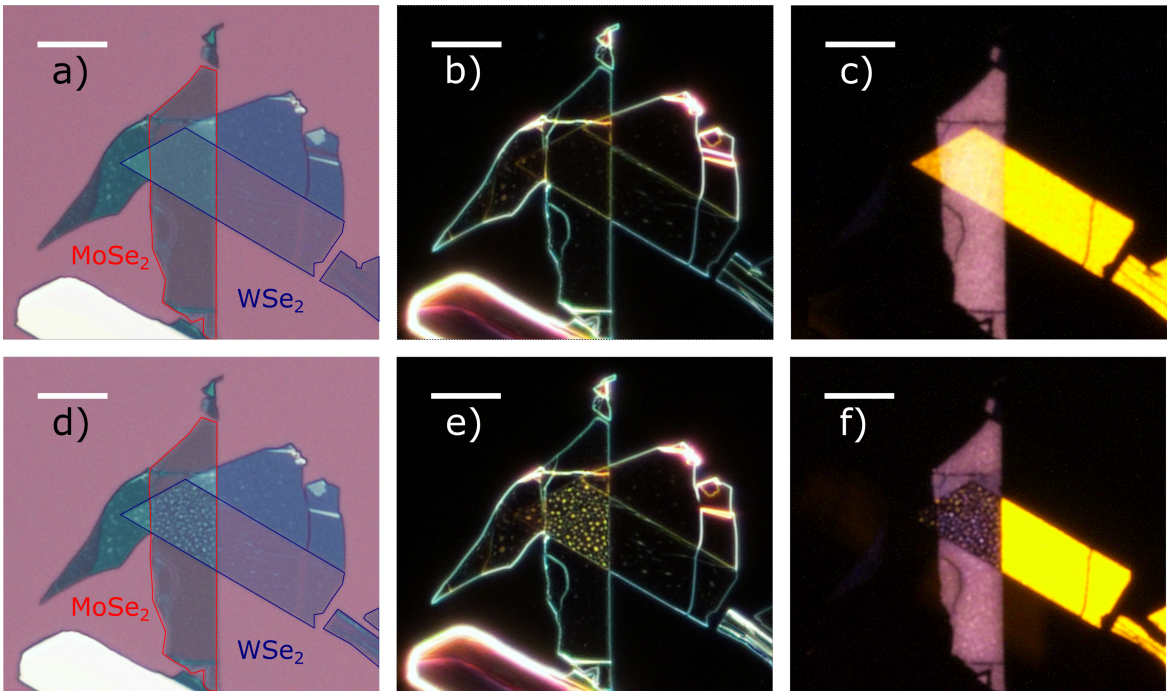

Fig. 4.9 **a-b-c)** Bright field, dark-field, and PL images of a $MoSe_2$/ WSe_2 heterostructure before the annealing. **d, e, f)** Bright field, dark-field, and PL images of the same structure after annealing in high vacuum at 50°C for 2 hours. All scale bars in the figure correspond to 10 μm. PL images are recorded with a 1 second acquisition time and 9.6x analog gain.

Then the sample was annealed again in the same conditions adopted for the isolated $MoSe_2$ flake (50°C for 2 hours). The microscope images of the sample after this step are

shown in the second row of Fig.4.9. It is possible to observe the same effect seen before in Fig.4.5: BF image (Fig.4.9 (d)) show the presence on the heterostructure region of a series of dots that before were absent. Their location matches perfectly with the dark field image and appears only in the overlap region of the two materials. The PL image also shows the strong quenching of PL due to the interlayer electrical coupling and the ultrafast charge separation. In the position of the samples where a of the contamination dot is visible in bright or dark field, a residue of the PL emission can still be observed. This comparison confirms that the annealing conditions adopted are adequate to create an electronically coupled heterobilayer, but such process can only happen when the heterobilayer is fully built.

The optical characterization of the device at RT is shown in Fig.4.10 before and after the second annealing step. The spectra acquired on the heterobilayer region show that, before the annealing, two peaks can be identified, centered at 1.653 eV (750 nm) for the WSe_2 emission and 1.575 eV (790 nm) for the $MoSe_2$ PL emission, respectively (light green line in Fig.4.10 (a)). Their relative PL intensity is expected for optically bright/optically dark materials [79, 166]. After the second annealing step of the heterostructure, the PL spectra, acquired on the same spots, reveals a dramatic quenching of PL intensity, which drops by one order of magnitude and the presence of a peak at 1.56 eV (800 nm) (dark green line in Fig.4.10 (b)). This PL emission originates by the uncoupled regions of the heterostructure kept apart by the polymer contamination pockets.

Low temperature PL data of the device were collected both on isolated flakes and on the heterobilayer region after the annealing and are shown in Fig.4.10 (c-e). The interlayer charge separation in aligned TMD heterobilayers can lead to the formation of interlayer excitons composed of electrons and holes localized in different materials [83, 89, 164, 165]. The lack of any observable emission in the overlap region in Fig.4.9 is a result of the combination of the suppression of the interlayer exciton emission in $MoSe_2/WSe_2$ at room temperature and

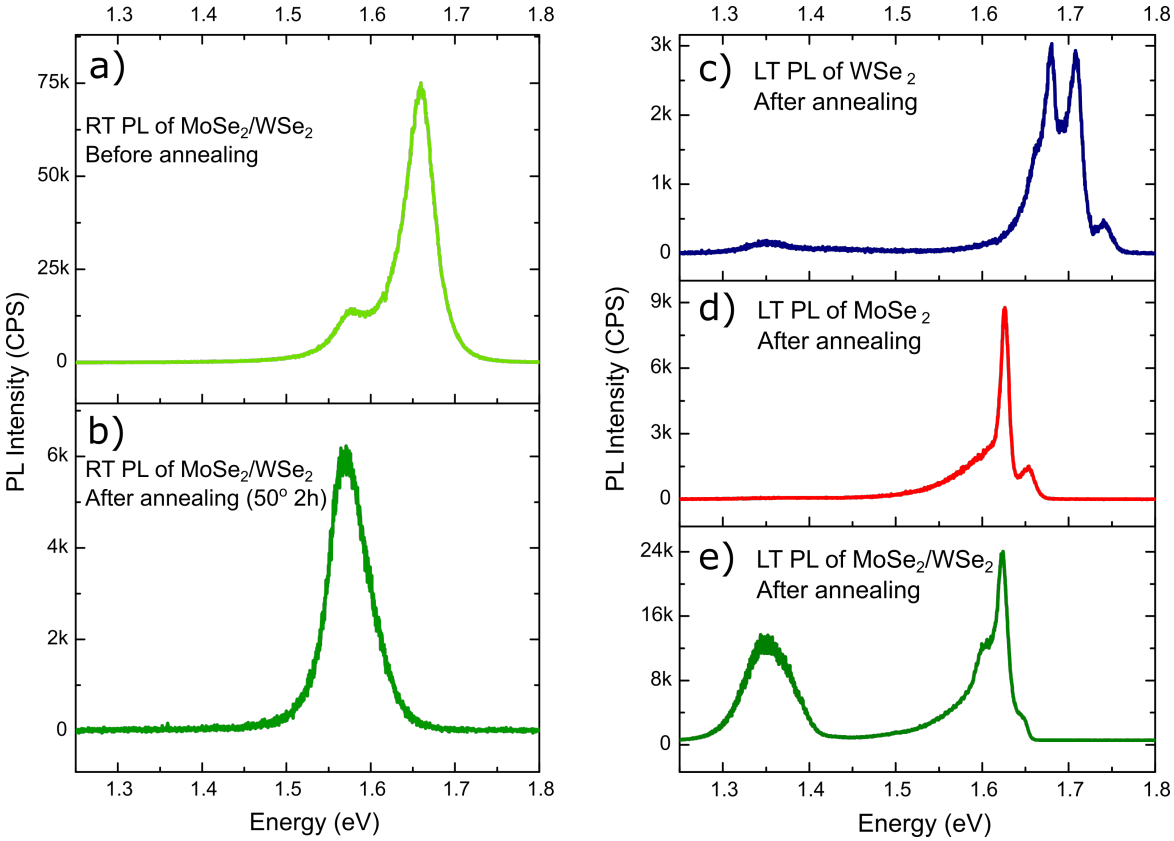

Fig. 4.10 **a-b)** RT PL of the $MoSe_2/WSe_2$ heterostructure before (a) and after (b) the annealing step, the probed location is identical. **c-d-e)** LT PL in three different region of the device after the annealing: isolated WSe_2 (c), isolated $MoSe_2$ (d) and heterobilayer region (e). The peak arising around 1.35 eV is related to the interlayer exciton emission.

the relatively low efficiency of the CCD at the wavelengths above 900 nm where the PL of the interlayer exciton is expected.

A further important consideration is that the momentum-space alignment of K valleys in TMD heterobilayers depends on the relative layer orientation in the real space. In the sample shown in Fig.4.5, the crystal axes in the monolayers are not aligned, which allows real- and momentum-space-indirect optical transitions only, which have a negligible probability. But in the sample shown in Fig.4.9, the observation of IX is possible due to the mutual alignment of the crystal axes. PL spectra of the heterostructure at LT (green line in Fig.4.10 (e)) reveal the rise of a broad PL signal at 1.35 eV ascribable to IX, since the same emission doesn't appear on isolated monolayers (red and blue line in Fig.4.10 (c-d)). This result gives the final

proof of the electronic coupling of the two monolayer and the formation of a heterojunction. This PL emission is localized at such low energy that cannot be detected by the microscope camera, because its sensitivity exponentially decay moving away from the visible region into the infrared.

4.6 Observation of the formation of interlayer excitons in TMD heterobilayers using PL imaging

In this section we demonstrate that PL imaging can also be used to monitor the formation of interlayer excitons in TMD heterobilayers, if their correspondent emission wavelength is withing the region of the high efficiency of the CCD. To investigate this, we have fabricated a set of heterostructures in which crystal axes of mechanically exfoliated flakes were aligned using their terminating edges as a guide. Fig.4.11 shows the bright field (a) and PL (b) images of a $MoSe_2/WS_2$ heterostructure assembled on a SiO_2/Si substrate using PDMS stamping. The edges used for alignment are highlighted by a thicker line. Both images were taken before annealing. The PL emission in the overlap region consists mostly of WS_2 PL, as at room temperature it is several orders of magnitude stronger than that of $MoSe_2$, according to its optically dark nature [79, 166]. The improvement of the interlayer coupling after annealing leads to the aggregation of the polymer residues, clearly visible as spots of different color in bright field image (Fig.4.11 (c)). Also there are significant changes of the heterostructure emission, that can be clearly seen in the PL image in Fig.4.11 (d). The heterostructure region demonstrates a prominent change of PL color, indicating a significant shift of its peak PL energy. In the regions where the the aggregated residues prevent efficient coupling between two materials the PL is also different since it comes from both $MoSe_2$ and WS_2, that act as independent layers.

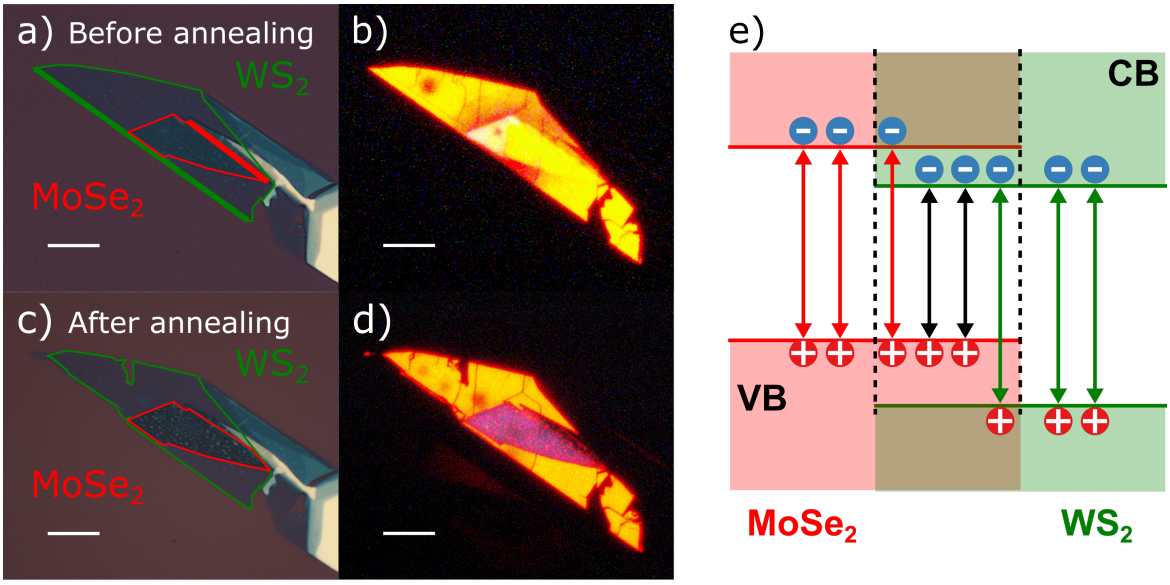

Fig. 4.11 **a-b)** Bright field and PL image of $MoSe_2/WS_2$ heterostructure. The thick lines indicate the crystal axes used for alignment. **c-d)** Bright field and PL image of the device after the thermal annealing. **e)** Band alignment of the presented device. Intralayer exciton (DX) emission is indicated by red and green arrow (for $MoSe_2$ and WS_2, respectively) while interlayer exciton (IX) emission is indicated by black arrows.

Fig.4.12 compares the PL spectra of the heterostructure before (top panels) and after (bottom panels) annealing. Prior to the thermal treatment, the WS_2 RT PL (green line in Fig.4.12 (a)) is nearly two orders of magnitude stronger than that of $MoSe_2$ (red line of the same panel). At low temperature the $MoSe_2$ emission is very similar to an isolated flake (red line in Fig.4.12 (b)) showing two clearly resolved peak for neutral and charged excitons. The WS_2 PL emission (green line in Fig.4.12 (b)) shows also the typical spectra in cryogenic condition with a very dim and structured signal related to the presence of dark states below the bright one. After the annealing step (Fig.4.12 (c-d)), unlike the isolated monolayer regions, WS_2 RT PL in the heterobilayer region is significantly quenched due to the efficient interlayer charge separation (green line in Fig.4.12 (c)). Its intensity drops in fact by an order of magnitude [79, 166]. The slight red-shift of the WS_2 peak is originated by the change in the dielectric environment caused by the reduced vertical distance between the layers [79, 108, 166, 182]. On the other hand, the peak at 1.55 eV (red line in Fig.4.12 (c)) is

enhanced following the annealing, which indicates the formation of interlayer excitons. The emission energy of these excitons is defined by conduction and valence band offsets between the two materials (Fig.4.11 (e)). Unlike $MoSe_2/WSe_2$ heterobilayers, the near-degenerate conduction bands in $MoSe_2/WS_2$ heterostructure result in interlayer exciton states having the optical transition just a few tens of meV below the one for $MoSe_2$ [79]. For this reason at room temperature it is impossible to distinguish the contribution of the $MoSe_2$ PL emission from the IX emission. Nevertheless the increased brightness of the PL at this wavelength and the redshift of the emission suggest the presence of this additional component.

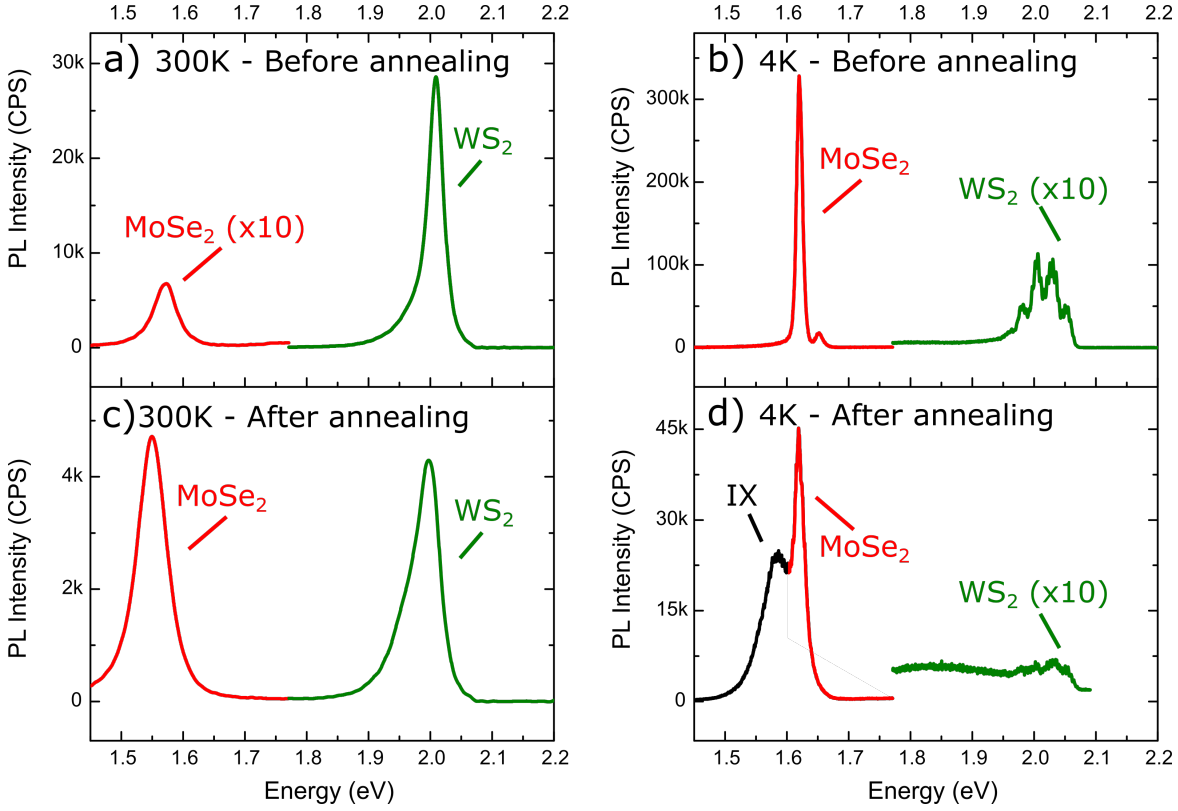

Fig. 4.12 **a)** RT spectra of the $MoSe_2/WS_2$ heterostructure before the annealing. The $MoSe_2$ signal are manually enhanced for visibility, the scaling factor is indicated in the inset. **b)** LT spectra of the device before annealing. **c)** RT spectra of the $MoSe_2/WS_2$ heterostructure after the thermal annealing **d)** LT spectra of the heterostructure after the thermal annealing step. The black part of the spectra indicate the IX contribution.

Low temperature measurements after the annealing revealed a dramatic quench of the WS_2 emission (green line in Fig.4.12 (d)) compared to prior the thermal treatment, and also

the rise of an additional peak few tens of meV below the $MoSe_2$ excitons (black line in Fig.4.12 (d)). These peaks only arise in the heterobilayer region and confirm the formation of interlayer excitons.

4.7 Twist angle dependence of the interlayer charge transfer

PL imaging can be directly applied to study the dependence of the interlayer coupling strength on the relative rotation between the two layers. Fig.4.13 (a) shows a bright field image of the $MoSe_2/WS_2$ sample composed of CVD-grown monolayers; the dashed white line marks the edge of a large triangular WS_2 monolayer. Since terminating edges of triangular TMD monolayers correspond to zigzag directions [98, 183, 184], the rotation angle between two layers can be easily identified by comparing the orientation of the WS_2 flake (indicated by dashed white triangles) with $MoSe_2$ monolayer orientation (colored triangles).

Fig.4.13 (b) shows the PL image of the same region. While isolated monolayer regions of both $MoSe_2$ and WS_2 show bright PL, the intralayer PL intensity in both materials is significantly lowered in the overlap regions. The degree of PL quenching shows clear correlation with the interlayer twist angle with well-aligned heterobilayer regions (P4 and P5) appearing darker than regions with strong rotational misalignment (P1-P3). Spectrally integrated PL intensity can be extracted from the PL images by measuring the average brightness of various regions in the digital image. Here we apply this method for $MoSe_2$ triangles, both overlapping with the WS_2 monolayer and isolated. The average triangle image brightness is calculated as (R + G + B)/3N, where N is the number of pixels in the triangle, and R, G, and B are the intensities in the red, green, and blue channels ranging between 0 and 255.

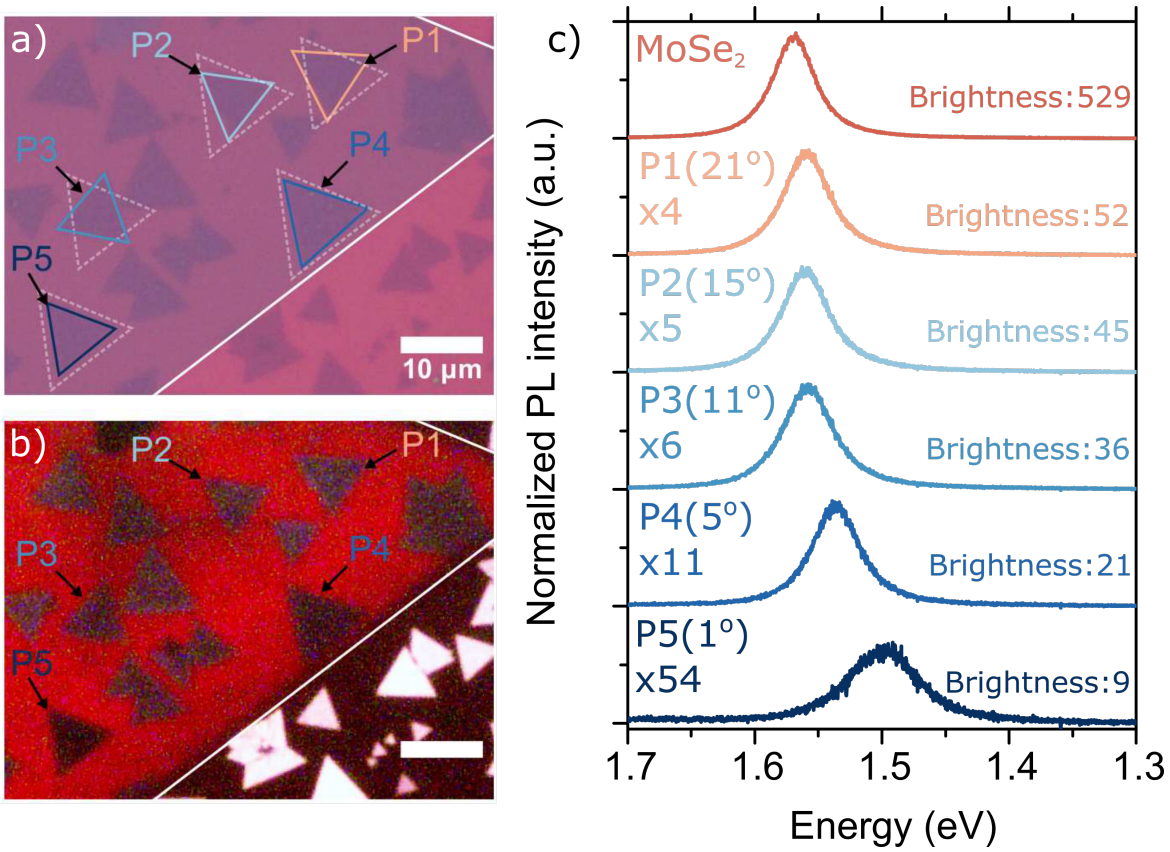

Fig. 4.13 **a)** Bright field image of a $MoSe_2/WS_2$ heterostructure assembled on a SiO_2/Si substrate from individually CVD-grown layers. Dashed white triangles indicate the orientation of the large triangular WS_2 flake, the one visible edge of which is marked by a solid white line. To make the relative rotation angles more obvious, the edges of the selected $MoSe_2$ monolayers were highlighted by solid colored lines. **b)** PL image of the sample showing varying degrees of the intralayer PL quenching in the overlap regions (see dark triangles), recorded with 10 s acquisition time and 9.6x analog gain. **c)** PL spectra measured in the heterobilayer regions with varying twist angles (shown on the right above each spectrum). The spectra are multiplied by the factors shown on the graph (on the right above each spectrum). The brightness indicated above each curve on the left is extracted from the PL image.

The triangle brightness extracted following this procedure shows that the coherently stacked regions (twist angles close to 0°) have more than 5 times lower PL intensity compared to rotationally misaligned areas. To establish firmly the correlation between the PL images and detailed spectral properties of the heterobilayer regions, emission spectra were recorded in the areas with different interlayer twist angles using the micro-PL setup. Fig.4.13 (c) plots normalized PL spectra collected in the regions P1-P5 of the sample, as well as an isolated

$MoSe_2$ monolayer. Scaling factors as well as emission intensity extracted from the PL image are listed above each curve. Compared to the isolated $MoSe_2$ (top curve), the heterobilayer regions demonstrate red-shifted PL with significantly lowered intensity, indicating strong interlayer coupling. It is also evident that the PL quenching becomes stronger with the decreasing interlayer twist angle. While the spectral position of the $MoSe_2$ intralayer exciton peak at 1.56 eV does not show any clear dependence on the relative orientation of the two layers, for the small twist angle, the emission peak red-shifts to 1.49 eV, indicating the change from intralayer to interlayer exciton character. The WS_2 PL shows strong quenching in all heterobilayer regions; however, there is no apparent correlation with the interlayer twist angle. The angular dependence of the PL intensity can be explained by the relative alignment of the $MoSe_2$ and WS_2 bands in the momentum space. The edges of the conduction and valence bands in TMD monolayers are located at the six K points of the Brillouin zone. Originating from the in-plane orbitals of the transition metal atoms, these states hybridize very weakly between the layers [96]. The rotational misalignment of the two layers in the real space leads to a rotation of two Brillouin zones in momentum space. Therefore, the interlayer charge transfer in the vicinity of the K points in the twisted heterobilayer case is a second-order process, which requires phonon or defect scattering to overcome the in-plane momentum mismatch. As the interlayer twist angle decreases, the K valleys come into alignment, significantly improving the efficiency of charge transfer between two layers. This leads to further quenching of the intralayer exciton PL. In coherently stacked heterobilayers, the band gap at the Brillouin zone edge becomes almost direct, leading to the emergence of the interlayer exciton PL [89, 101].

4.8 Conclusions

In summary, we have demonstrated that rapid large-area PL imaging of 2D semiconducting TMD samples can be achieved using a standard bright field optical microscope, rather than a

dedicated optical setup equipped with a spectrometer. The presented technique offers a highly efficient and substrate-material-independent method of flake thickness identification that can be easily combined with flake search in one experimental setup. Furthermore, we have shown that, due to its sensitivity to interlayer charge transfer, this technique can be used to monitor the electronic coupling between individual layers in vdW heterostructures. We have successfully applied this method to investigate interlayer coupling in vdW heterostructures composed of both exfoliated and CVD-grown TMD monolayers. While the presence of organic residues between the atomic planes in TMD heterobilayers fabricated by viscoelastic stamping prevents efficient coupling between the layers, a significant improvement of the coupling efficiency and the formation of the interlayer excitons can be clearly observed in the microscope PL images of the thermally annealed samples. The presented PL imaging techniques has also been applied to assess the interlayer coupling in TMD heterobilayers having various degrees of the rotational misalignment. We have found that the degree of intralayer exciton PL quenching depends on the relative orientation of the two layers, indicating twist-angle-dependent interlayer charge transfer. The high sensitivity of the PL intensity to the charge transfer efficiency makes the presented method a very sensitive tool for investigating the coupling strength in TMD heterostructures with varying interlayer rotation and vertical separation. The short image acquisition times required makes it possible to investigate changes of the interlayer coupling in real time, allowing for example the microscope PL imaging to be used for in situ monitoring of sample annealing or surface functionalization. With increasing industrial and research interest in devices based on semiconductor vdW heterostructures, the PL imaging developed in this work offers a powerful characterization method suitable for both exfoliated and CVD-grown samples at various fabrication stages.

Chapter 5

Band-structure engineering in alloy-based transition metal dichalcogenide van der Waals heterobilayers

5.1 Abstract

Van der Waals heterobilayers represent the ultimate frontier to design and assemble highly tailored electronically-engineered 2-dimensional devices. Heterobilayers are formed by two different single layers of transition metal dichalcogenides (TMDs), directly stacked one on top of the other. This family of physically engineered devices possess widely tuneable optoelectronic properties, leading to brand-new metamaterials with intriguing emerging properties. Their optical response is determined by the type-II band alignment, in which the edges of CB and VB are located in the two different layers due to their band offset.This causes the appearance of interlayer excitons (IX), formed by Coulomb-bounded electrons

and holes confined in the two different single layers. IX possess long radiative lifetimes and a permanent electric dipole, oriented perpendicularly to the plane of the TMDs, which results in enhanced non-linear exciton-exciton interactions.

A fundamental limitation of vdW heterostructures is their inherent dependence on the properties of their constituent TMD monolayer. Although there exist a large choice of properties offered by the family of 2D semiconductors, changes of the device band structure can be achieved only in discrete steps. In contrast using an alloy is a powerful approach to solve this problem, since it allows tuning the properties of TMDs in a continuous way, by replacing a certain percentage of one transition metal atoms in the crystal lattice with another. This approach of chemical engineering allows to tailor finely and continuously their properties, such as energy gap, band offset and spin orbit coupling.

In this work we combine the two tailoring approaches: we fabricate several vertical heterojunctions each composed by a pure TMD (WSe_2) and a different TMD alloy ($Mo_xW_{(1-x)}Se_2$). The assembled devices clearly show the photoluminescence emission originating from IX, which was unreported yet for this type of devices, and also that their peak position, measured at T<10K, can be tuned up to 200 meV, spanning through the whole range of alloy compositions, showing the maximum shift for the alloys that exhibit only minor variations in the intralayer (or direct) exciton (DX) energy of the isolated monolayers. Surprisingly, for W-rich alloy the IX peak does not follow a linear trend as expected but instead pins to the momentum indirect transition which dominate the optical response of the WSe_2 bilayer. This reduction of the band offsets between the two layers changes the nature of IXs from space- to momentum-indirect, causing a modification of the band structure of the device. This is confirmed by the appearance of hybridized optical transitions, a significant decrease of the IX lifetimes and a reduced blue-shift of the IX peak with the increasing excitation power.

This work represents a breakthrough in the design and fabrication of nanoscale devices, demonstrating that it is possible to use TMDs alloys to create vdW heterobilayers to get a

fine and continuous band gap engineering of the electronic properties of a heterostructure based on such materials. But also it sheds light with an experimental approach on the origin and interpretation of the interlayer excitons in vdW heterostructures, intentionally blurring the line between heterobilayer and homobilayer.

5.2 Conceiving the experiment

The aim of this work is to achieve a continuous tuning of the IX by controlling the composition of one of the two materials that form the heterobilayer structure. As discussed in section 2.4.1, the interlayer exciton emission energy depends on their exciton binding energy and on the band offset between the two materials [51, 97, 185]. Taking as a model the simple single valley picture, largely accepted nowadays to describe the IX [81, 88, 186], it was expected that in the *K* point of the BZ of the $Mo_xW_{(1-x)}Se_2$ alloys, as the composition changes, the band gap shrinks and the band offset, in respect to the binary MX_2 material, increases. Therefore if each of these alloys is combined with a specific material, in our case WSe_2, we do expect that the IX emission blue shifts as a consequence of the reduction of the band offset [61, 63].

The schematic structure of the device seen from the side is shown in Fig.5.1 (a) for a generic $Mo_xW_{(1-x)}Se_2$ heterostructure. According to the chemical composition of the alloy its *K* point band structure evolution, compared to WSe_2 *K* point is shown in Fig.5.1 (b). Both the CB and the VB are pushed up in energy, but with different rates, causing the increase of the alloy intralayer excitons (DX) energy (red dashed line) to increase up to the WSe_2 DX energy (blue dashed line) [58]. The key factor is that the energy offset between the two materials increases as they become more chemically different and this should have an effect on the IX energy [63]. This is represented in Fig.5.1 (c) where the band gaps are schematically shown and the alloy composition is displayed with different colors. Considering the IX excitons, their energy is defined by the energy difference between the alloy CB and the WSe_2 VB,

shown as a dashed blue line. Therefore the IX energy is expected to increase, moving into W-rich alloy based heterobilayers [51, 109]. This idea is summarized in Fig.5.1 (c).

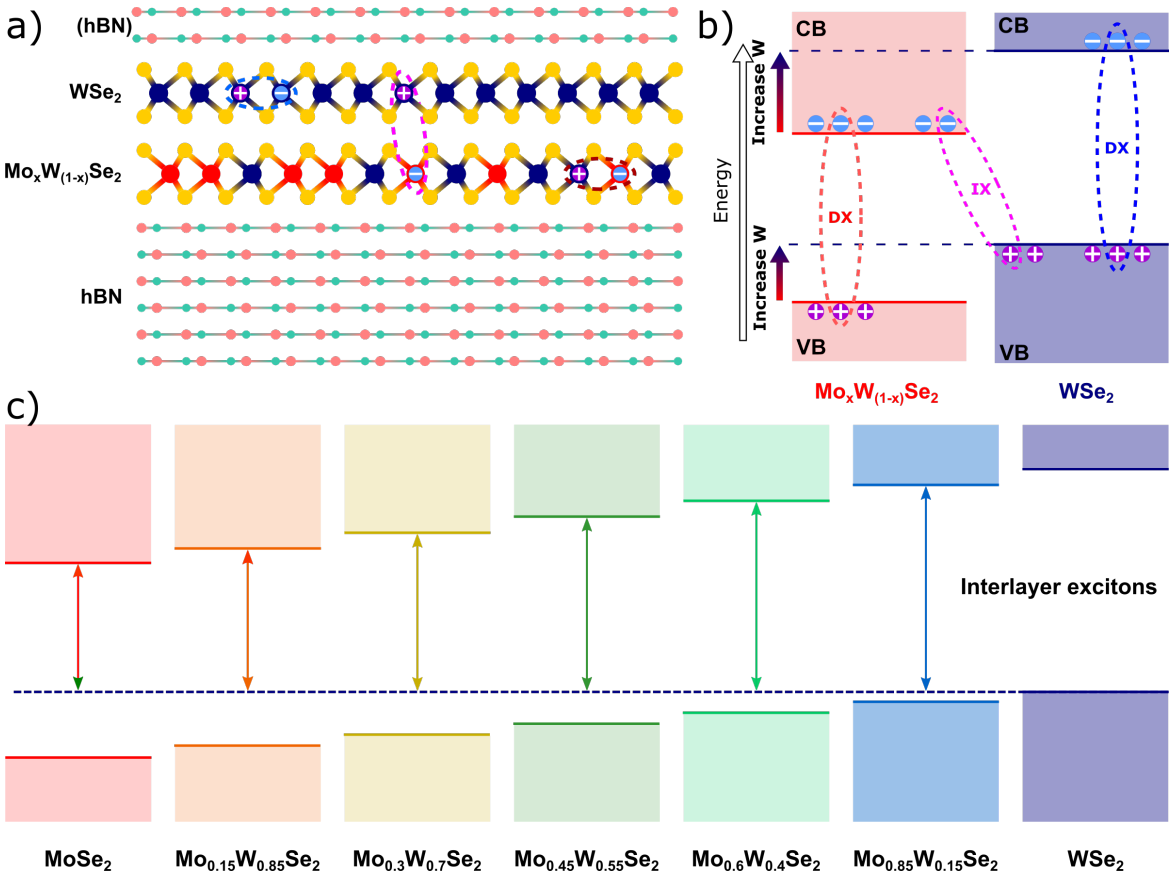

Fig. 5.1 **a)** Lateral view of a random $Mo_xW_{(1-x)}Se_2$ heterostructure. The top layer of hBN may be present or not, depending on the fabrication procedure. The presence of intralayer excitons in $Mo_xW_{(1-x)}Se_2$ (red dashed line) and WSe_2 (blue dashed line) is shown next to the interlayer excitons (purple dashed line). The out of plane orientation of IX is evident. **b)** Corresponding band structure of the device, the gradient arrow indicate the effect of the stochiometry on the alloy band structure. Dashed blue line are the projection of WSe_2 CB and VB excitonic states. **c)** Schematic band structure of the experiment: six different alloys are shown)each one in a differnt color). Each is combined with WSe_2 (dashed blue line). The IX energy increase as the band offset is reduced.

According to this scenario, the IX emission should be tuned very close to the WSe_2 intralayer excitons.

5.3 State of the art

Despite the numerous efforts and progress in fabrication and modeling of TMDs heterobilayers, tuning of interlayer excitons properties by engineering of heterostructure materials is still largely unexplored. In this section the most relevant works concerning this topic are presented.

- **Gate tuning of $MoSe_2$/WSe_2 heterobilayer**

  The common approach for tuning the IX energy is to use a vertical electric field similarly to what has been done in III-V semiconductor double quantum wells [68]. Such experiments have shown that controlling both the PL energy and polarization of IX is possible [128]. The presence of a permanent dipole in IX offers the possibility to control the IX PL emission via Stark effect [83]. Gated heterobilayer devices has shown an energy shift of the IX up to 130 meV due to the induced band offset modification [129]. Also IX population and decay dynamics change under the effect of the applied electric field [169]. All these results are in agreement with the calculation performed on heterobilayers [187]. Electrical gating offers a fine tuning of the IX properties in such devices, but present also some disadvantages: first it is necessary to increase the complexity of the sample, adding a top layer and a bottom layer of graphene that act as 2D electrodes. Then, in between the whole device must be encapsulated in hBN. Its role is to prevent the migration of the optically generated carriers in the TMDs into the highly conductive graphene layers. Consequently this approach have some limitation that cannot be overcome.

- **Gate tuning of bilayer WSe_2**

  A similar approach has been applied in an exfoliated bilayer of WSe_2 [117]. WSe_2 bilayer is a indirect bandgap semiconductor. The band edge states are localized at the Q point of the CB and the K point of the VB, as demonstrated theoretically

end experimentally [96, 188, 189]. The *K* point of the CB exhibits minor changes compared to monolayer samples, as demonstrated by the presence of a main absorption peak at 1.72 eV, similar to the one observed in single layer material, that is attributed to the direct gap transition (*K*-*K*). This result corroborates the fact that the transition from momentum-direct to momentum-indirect band gap from the monolayer to the bilayer discussed in the first chapter is mostly related to the evolution of the *Q* point of BZ instead of the *K* point. Interestingly, in this work the authors still observe a weak direct transition emission in the bilayer WSe_2. In Ref. [117] the sample shows a structured emission at 1.65 eV related to localized excitons (for a detailed description of this phenomena, check section 1.5.2). The momentum indirect transitions (X_I) PL appears at 1.55 eV in a set of peaks whose origin is still not fully identified. A possible explanation presented is the presence of phonon replicas, but is still to be confirmed. When a bias is applied to the device, perpendicularly to the WSe_2 bilayer plane, the X_I emission redshifts by 70 meV, symmetrically for both positive and negative voltages. This indicates that the degenerate band edge states of the two layers of WSe_2 that compose the sample are pushed away in energy, so that the electric field applied lifts the energy degeneracy creating two gate-split states. This structure closely resembles a heterobilayer situation, since a type-II band alignment is created through the applied bias, leading to the carrier confinement in two different layers. Over a certain threshold ($\pm$5V), the X_I PL emission is dominated by a bright signal related to the radiative recombination of spatially confined carriers.

The authors demonstrate a nonlinear power dependence behavior of such emission in both intensity and peak position, related to the rising of a permanent dipole moment. Also, they demonstrate the change of the interlayer exciton dynamics: in unbiased samples (where the carriers are not electrically confined) the lifetime is very short (hundreds of picoseconds), meanwhile in presence of an imposed vertical field the

carriers are spatially confined and the lifetime dramatically increases by two order of magnitude (tens of nanoseconds). Similarly, in biased samples the X_I PL shows a blueshift of 2 meV that abruptly disappears when the gate voltage is reduced or removed.

- **Optical properties of bilayer WSe_2**

  In the previous work the analysis of the momentum indirect transition was not addressed fully. This topic is tackled in another work, focused on the optical properties of bilayer WSe_2 [190]. In this report the authors propose a model for the identification of the momentum indirect optical features that emerge in such material. The authors indicate that the valleys involved are K-Γ, Q-K and Q-Γ for the CB and the VB, respectively. Although a detailed and systematic description of all the optical properties of the bilayer WSe_2 is still lacking, such interpretation is consistent with the other relevant work in this field and sufficient for the aim of this thesis work.

- **Considerations on IX binding energy**

  Most of the work carried out on IX focus on the single particle band structure and very few actually take into account the binding energy of the excitons, which is of fundamental importance in optical experiments. As discussed in chapter one, the TMDs due to the quantum confinement exhibit large binding energies, in the order of 0.5 eV [191, 192]. Although in heterobilayers the carriers are spatially separated and the binding energy is expected to be reduced, it is still important to consider the binding energy of the IX. Moreover, all work on $MoSe_2$/WSe_2 heterobilayers show that the energy splitting between the two IX peaks is in the order of tens of meV [20]. This value is completely overshadowed by the binding energy observed in single layer TMD, which is in the order of several hundreds of meV. Yet a description of the binding energies of the excitonic species in a heterobilayer is still lacking. An experimental approach was carried out by Wilson et al. [96] which performed

μ-ARPES measurements on different $MoSe_2$/WSe_2 heterobilayers demonstrating experimentally the evolution of the VB and theoretically modeling the CB in the device. Combining this investigation with optical measurements, they deduced that the binding energy of the IX is lower than the DX, as predicted, but it is at least 200 meV. They obtained this value considering a momentum direct transition between *K* points of conduction and valence band. This is much higher than the IX binding energies observed in III-V semiconductors [96, 193].

- **Optical investigation of TMD alloys at low temperature**

  As discussed in the introduction the properties of TMDs alloys were studied little at low temperature, due to the difficulties in obtaining samples showing high optical quality. The only paper that reports on the behavior of TMD alloys at both room and low temperature, focuses on the spin orbit engineering [25]. The authors analyzed a set of TMD alloys consisting of three different composition for the $Mo_xW_{(1-x)}Se_2$ alloy, with x= 70, 60, 10%. The flakes were grown by a low-pressure vapor transport (LPVT) technique. Only the monolayers of $Mo_{0.7}W_{0.3}Se_2$ show relatively narrow PL signals while in the other two alloys the PL emissions are much broader and difficult to interpret.

  Additional information about the sign and the values of the SO splitting in the $Mo_xW_{(1-x)}Se_2$ alloys have been extracted from RC measurements. The experimental data for the SO splitting follow the DFT-calculated values only qualitatively. The simulations suggest an almost linear tuning of the SO coupling that should shift from almost 200 meV in $MoSe_2$ to 400 meV in WSe_2. Instead the RC spectra show an abrupt increase of the SO coupling moving from $Mo_{0.7}W_{0.3}Se_2$ to $Mo_{0.6}W_{0.4}Se_2$ and no significant variations for $Mo_{0.1}W_{0.9}Se_2$.

5.4 Optical characterization of TMDs alloys

The first step of our work was to prepare and characterize a set of high quality single layer $Mo_xW_{(1-x)}Se_2$ alloys that are necessary for such investigation. All the materials shown in the rest of the chapter are exfoliated from their respective bulk crystals, provided by HQGraphene. Mechanical exfoliation was performed as described in section 3.1 and cleaved material was exfoliated on PDMS substrates. After the optical identification of the monolayers, they were transferred on 90 nm SiO_2 on Si. Low temperature PL measurements were carried out with the setup described in section 3.4, using a 660-nm CW laser with a power of 20 μW. The results are summarized in Fig.5.2 (a).

Fig.5.2 (a) shows that while tuning the composition of the alloy from $MoSe_2$ (red curve) to WSe_2 (dark blue curve) the spectra significantly change. $MoSe_2$ shows two pronounced and clearly resolved peaks, the first located at 1.663 eV attributed to neutral excitons (X^0), and the second, much more prominent, located at 1.632 eV and attributed to the negatively charged excitons (X^-) in excellent agreement with previous reports [194, 195]. Both peaks show narrow linewidths: X^0 has a linewidth of 12 meV and X^- 11 meV. More importantly, the absence of localized states below the X^- peak shows the high quality of the sample and of the fabrication procedure. Moving into alloys, the PL emission of $Mo_{0.93}W_{0.07}Se_2$ show two clear peaks, similar to $MoSe_2$, identified as X^0 at 1.657 eV and X^- at 1.627 eV. Remarkably, the linewidth is almost identical to $MoSe_2$, moreover there is no emission related to defect-bound states, confirming the exceptional quality of these alloys. The PL peak positions exhibit a strong bowing effect, manifested as a redshift for small concentrations of W in the lattice structure. This is consistent with the data from the literature for these materials. The redshift reaches the maximum value in $Mo_{0.71}W_{0.29}Se_2$ pushing the X^0 down to 1.653 eV. From that point the PL starts to monotonically blueshift as the alloy become more WSe_2-like. An interesting effect can be observed in the lineshape of the emission. Up to $Mo_{0.49}W_{0.51}Se_2$ alloy the PL closely resembles the $MoSe_2$ PL lineshape with a double peak. For x<38% it

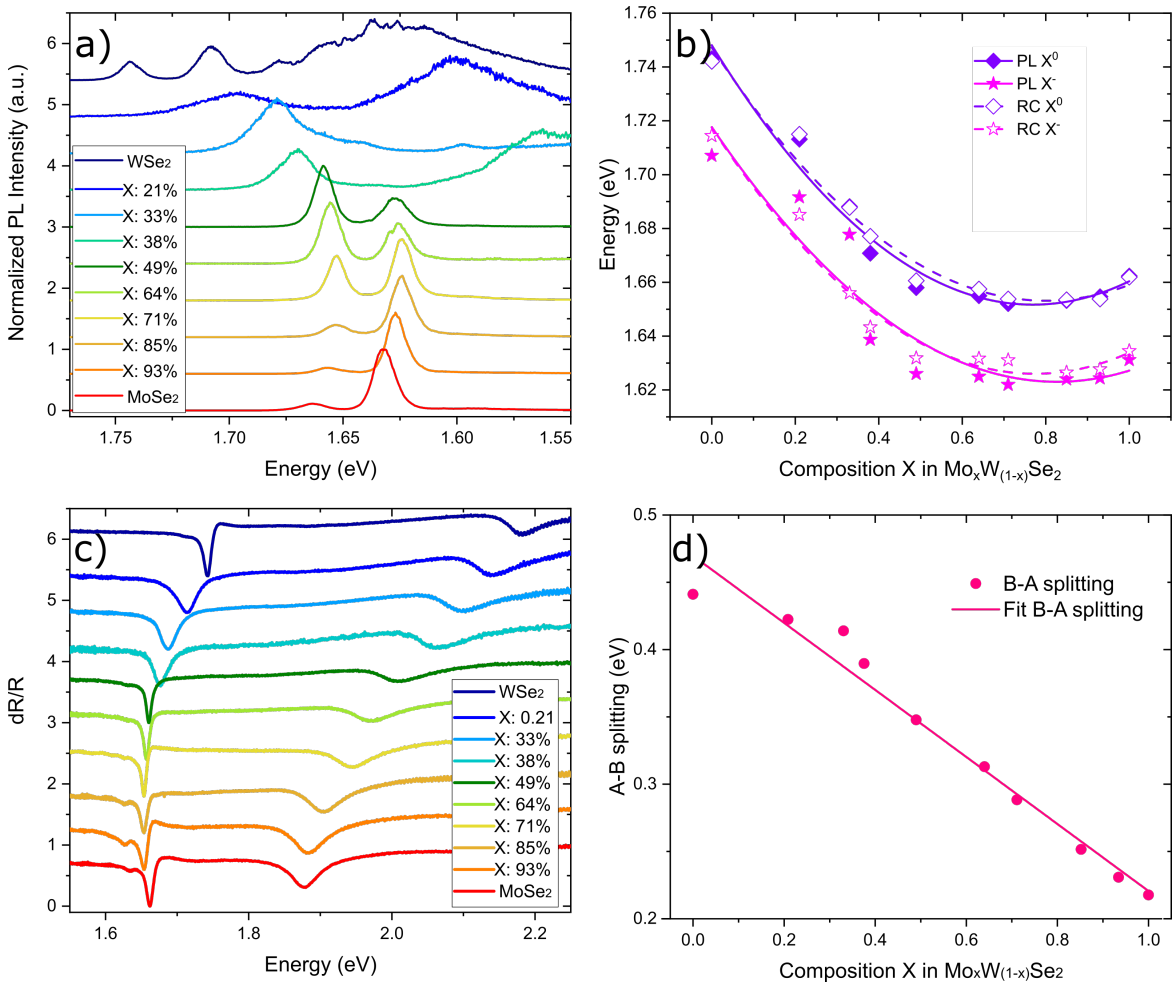

Fig. 5.2 **a)** Normalized PL spectra of isolated $Mo_xW_{(1-x)}Se_2$ alloys. The composition is indicated by the color gradient. **b)** Peak position of neutral (diamond) and charged (stars) excitons from PL (full) and RC (empty) data. **c)** RC spectra acquired on the same spot of the PL data. The parabola fitting is included (solid and dashed line for PL and RC data, respectively). **d)** *A*-*B* exciton energy difference as a function of alloy composition. The solid line is the corresponding linear fit.

drastically changes: the peaks become much broader, the X^- peak almost disappears and other components appear at lower energies. This is likely to correspond to concentration for which the alloy behavior shifts from optically bright (as in $MoSe_2$) to optically dark (as in WSe_2) as predicted by Wang et al. [25].

The peak positions of X^0 and X^- for all materials are extracted by a double Gaussian fit of the PL spectra shown in Fig.5.2 (a) and plotted in Fig.5.2 (b). Here the full violet (purple)

squares (stars) are the experimental data for the neutral (charged) excitons and the solid violet (purple) line represent the parabolic fit of the peaks.

Another interesting insight in the alloy structure is offered by RC spectra. Since RC measurements are insensitive to defects with low density of states, the quality of the spectra is very high even in optically dark alloys. The results are presented in Fig.5.2 (c). Two major features are present: a first sharp absorption, which redshifts from 1.660 eV in $MoSe_2$ to 1.653 eV in $Mo_{0.71}W_{0.29}Se_2$ followed by a blueshift up to 1.742 eV in pure WSe_2. A second broader feature is blueshifting monotonically from 1.877 eV to 2.182 eV as the composition becomes more W rich. Those are related to the *A* and *B* excitons absorption peaks, respectively. There is a third peak at lower energies that can be clearly identified in some of the spectra. This peak is the absorption of the trions, which have a weaker oscillator strength than the neutral *A* excitons because the extra charge bond [26].

After a convolution of the spectra it was possible to extract the spectral position of the neutral and charged exciton absorption, as shown in Fig.5.2 (b). The empty violet (purple) squares (stars) are the experimental data for the neutral (charged) excitons extracted from RC measurements and the dashed violet (purple) line represent the parabolic fit of the peaks.

From the energy difference between the *A* and *B* excitons shown in the RC spectra, it is clear an almost perfect linear dependence of the SO coupling according to the sample composition, as shown in Fig.5.2 (d). This is in contrast to what has been shown before by Wang et al. [25], although their theoretical model predicts a linear dependence. We attribute this to the high quality of our materials and the fact that we study a larger set of materials compositions.

The fitting reveals a bowing parameter *b* of 0.16 and 0.15 eV from PL and RC measurement, respectively, for X^0 (for a more detailed explanation see Section 1.6. The X^- signal exhibits a bowing factor *b* of 0.14 and 0.15 eV for PL and RC, respectively. Such values are

in close agreement with previous theoretical [93] and experimental [59] reports, although previously the data were acquired at room temperature.

5.5 Emergence of IX photoluminescence in alloy-based heterostructures

We now proceed with the discussion of alloy/WSe_2 heterostructures consisting of a vertical stack of $Mo_xW_{(1-x)}Se_2$ and WSe_2 monolayers. The first heterobilayer fabricated was $Mo_{0.85}W_{0.15}Se_2/WSe_2$. The flakes were exfoliated on PMMA-PMGI and then deterministically deposited on each other using a target hBN flake as the substrate. Both TMD flakes showed long and straight edges which we used to identify the directions of the crystal axes [138]. During the fabrication step these edges were carefully aligned with each other with 0.5°precision in order to enhance the IX radiative emission [101]. All the devices presented in this chapter underwent this procedure during the fabrication (for more details see section 3.2).

The microscope image of the sample is shown in Fig.5.3 (a). The $Mo_{0.85}W_{0.15}Se_2$ flake is highlighted by a red silhouette, while the WSe_2 flake is shown in green. This color scheme (red- alloy, green WSe_2) will be used in all images of the devices in this chapter. As can be noticed in Fig.5.3 (a) the enhanced contrast of the overlap area confirms the formation of the heterostructure. It is possible to recognize the alignment of the crystal axes in the two flakes, highlighted by a red and green arrow for alloy and WSe_2, respectively. Fig.5.3 (b) shows a PL image of the sample at room temperature. It is possible to distinguish an intense emission from the uncoupled WSe_2 flake and a dimmer emission from the $Mo_{0.85}W_{0.15}Se_2$ flake according to their optically dark and optically bright nature, respectively.

In the overlap region the complete quenching of the PL emission confirms the formation of the type-II heterostructure [51]. The low PL intensity arises from fast intralayer exciton

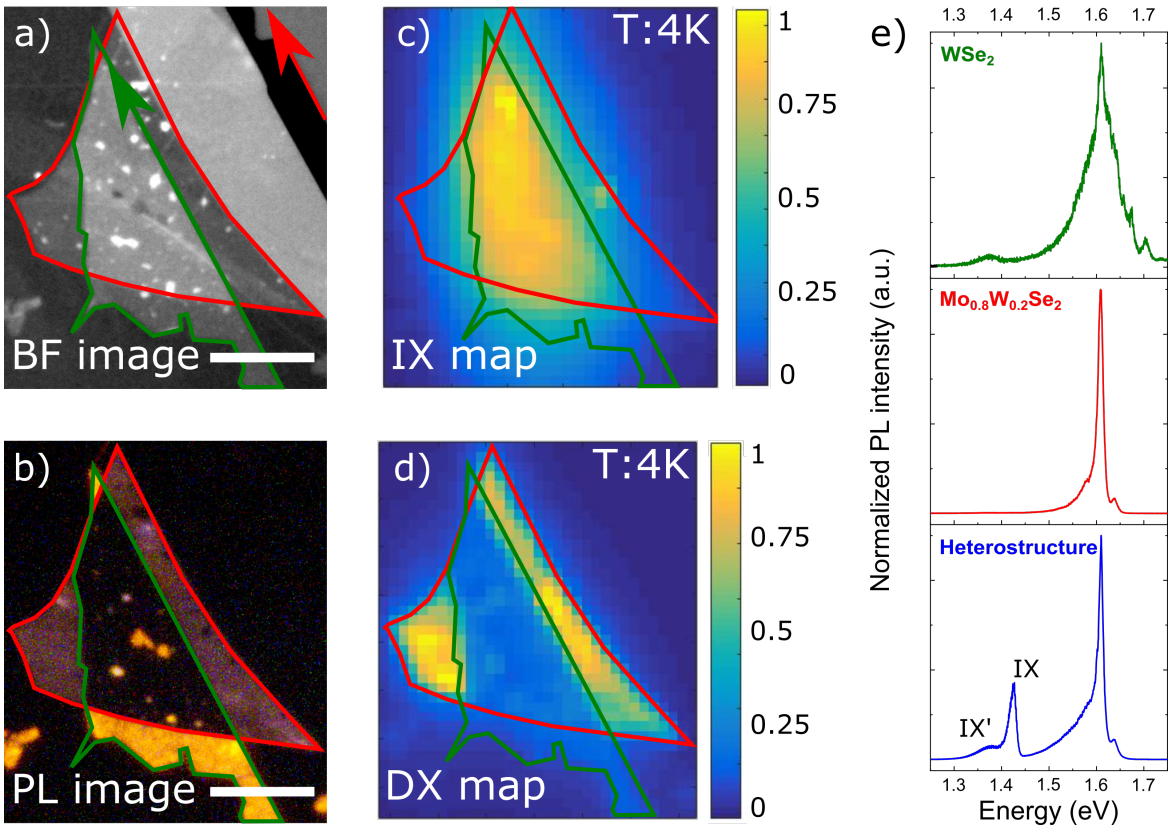

Fig. 5.3 **a)** BF image of the heterobilayer, grayscale color show the enhanced contrast where the two flakes overlaps. The red line is the silhouette of the $Mo_{0.85}W_{0.15}Se_2$ flake while green solid line indicates the WSe_2 flake. **b)** PL imaging of the heterostructure. The quenching of the PL signal in the heterobilayer region indicates the electronic coupling and the charge separation. **c)** LT PL map of the heterostructure in the IX region (1.3-1.45 eV energy range). Bright PL is detected in correspondence of the heterobilayer and absent in the other regions. **d)** LT PL map of the heterostructure in the DX region (1.5-1.7 eV energy range). The image look complementary to the one shown in panel c. **e)** PL spectra acquired in different point of the heterostructure, WSe_2 (green spectra), $Mo_{0.85}W_{0.15}Se_2$ flake (red spectra) and heterobilayer (blue spectra).

dissociation into free carriers which become confined in the two different layers [81–83]. It is possible to distinguish some regions within the heterojunction from which the WSe_2 PL emission is still visible. Comparing these spots with the bright field image in Fig.5.3 (a) it is clear that such spots exhibit a lower or higher contrast than the rest of the heterostructure. This means that the flakes were either pierced in that spot and therefore the heterostructure

was not formed, or some polymer residues were trapped in between the flakes creating a contamination pocket that prevents the electronic coupling between the two flakes [103].

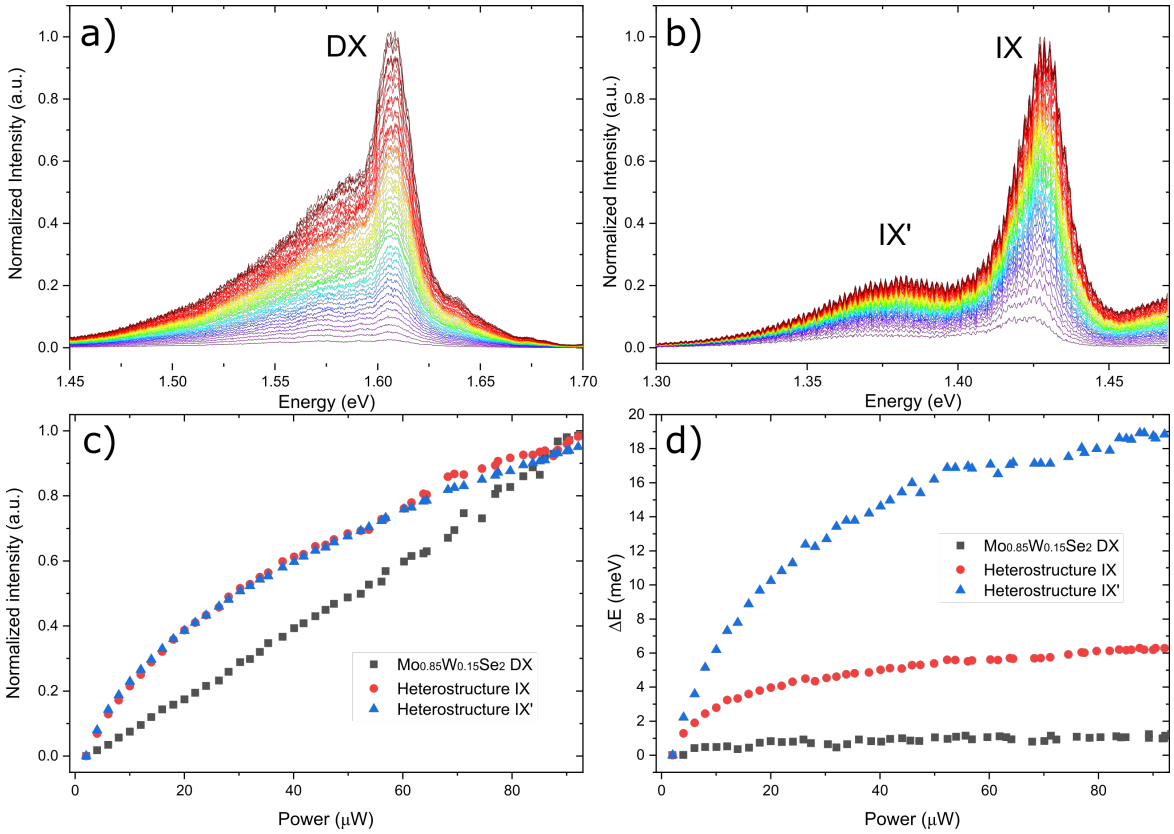

Fig. 5.4 **a)** Power dependence spectra of DX in the heterostructure region. Color gradient indicates the power adopted (violet-low and brown-high) **b)** Powerdependence spectra of IX in the heterostructure region. **c)** Intensity of the DX (gray dots) IX (red dots) and IX' (blue dots) emissions as a function of pumping power. The DX show a linear trend while IX signal show nonlinear trend. **d)** Blueshift of the DX (gray dots) IX (red dots) and IX' (blue dots) under increasing pumping power. The data indicate the shift compared to the original position of the peak.

Fig.5.3 (c-d) shows the PL maps of the sample acquired at cryogenic temperature (T= 4K). Two different spectral ranges are shown: Fig.5.3 (c) show the energy range from 1.45 to 1.3 eV (which is the IX energy range) while fig 5.3d shows the energy range from 1.7 to 1.5 eV (for $Mo_{0.85}W_{0.15}Se_2$ and WSe_2 DX energy range). The flake silhouettes are overlapped with the PL maps to help the identification of the different region of the device. It is seen that the two images are complementary. Fig.5.3 (d) shows the intralayer exciton PL intensity for both

the $Mo_{0.85}W_{0.15}Se_2$ and WSe_2 flakes. Due to their optical bright and dark nature respectively the PL intensity is reversed compared to the image in Fig.5.3 (b) as a consequence of the temperature difference. Most importantly, the low-energy emission, shown in Fig.5.3 (c), emerges only from the heterostructure region and is confined in the overlapping area of the two flakes that constitute the heterostructure.

Fig.5.3 (e) compares the PL spectra for three spots of the sample: isolated WSe_2 flake (green curve), isolated $Mo_{0.85}W_{0.15}Se_2$ (red curve) and the heterostructure (blue curve). In the heterostructure area, the PL at low energy is dominated by two-peaks emission, corresponding to the interlayer excitons. The first peak (*IX*) is at 1.426 eV and has a linewidth of 18 meV while the other peak (*IX'*) is centered at 1.382 eV and has a linewidth of 72 meV. This emission is confined on the heterobilayer area, as displayed in the map shown in in Fig.5.3 (c) and rapidly decays away from the overlap area. Some signals corresponding to this low energy emission can be observed also on the isolated monolayers, as shown in the WSe_2 spectra in Fig.5.3 (e), where PL at low energies can still be observed. This is related to the setup limitations, as where the laser light cannot be totally concentrated on the central spot but is also partially diffused around. Consequently the heterobilayer is excited even when the laser is focused away from the heterostucture, Furthermore the out-of-plane orientation of the IX dipole causes strong PL emission in the direction parallel of the heterostructure plane.

The existence of interlayer excitons in alloy-based heterostructures has never been reported before. We therefore study the basic characteristics of IX in these novel structures. We first probe the behavior of the IX PL under increasing laser power. The IX in $MoSe_2$/WSe_2 heterostructures shows a sublinear trend in PL intensity and also a blueshift of the peak, due to the repulsive interaction between IX (for a more detailed explanation see section2.4.3). The PL spectra of this sample under increasing pumping power are shown in Fig.5.4 (a-b) for the DX and IX, respectively. From this set of measurements the corresponding PL intensities (Fig.5.4 (c)) and peak positions (Fig.5.4 (d)) are shown for the intralayer excitons (black

squares) and the two peaks of the interlayer excitons, labeled as IX (red circles) and IX' (blue triangles). As can be observed from Fig.5.4 (a, c), the power dependence of the DX intensity is linear while both peaks of the interlayer transition show a sublinear trend, as already observed in other heterostructures made from binary TMDs. Furthermore, the DX PL peak shows a negligible shift at increasing pumping power (Fig.5.4 (d) black squares) but both interlayer transitions show a blueshift of up to 20 meV (Fig.5.4 (d) red circles and blue triangles).

In order to obtain the definite proof for the nature of the IX states, we perform PL lifetime measurement on the device. Due to their spatial confinement, interlayer excitons usually show lifetimes of tens of nanoseconds, as observed in several independent studies [80, 100]. The time-resolved PL data are shown in Fig.5.5. The orange dots represent the PL decay

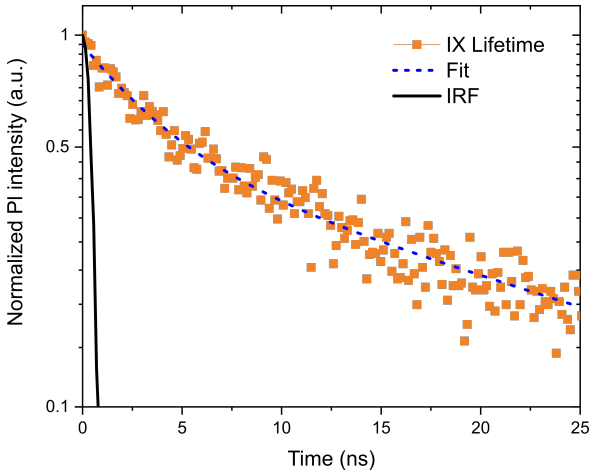

Fig. 5.5 Lifetime of the IX in $Mo_{0.85}W_{0.15}Se_2/WSe_2$ heterostructure. The orange dot indicate the experimental data, blue line is the fitting curve, black line is the IRF.

trace for the IX, and the black line is the instrumental response function. The IX lifetime can be extracted trough a monoexponential fit (blue dashed line of Fig.5.5) giving the value of 19.6 ± 1.0 nanoseconds, in excellent agreement with the literature values for the interlayer excitons, giving the final confirmation of our hypothesis [100, 180, 191].

To summarize, in this alloy based device we observed the rise of a relatively narrow emission lines at low energies, below 1.45 eV, compatible with the formation of the interlayer

excitons. The emission is strongly confined in the heterobilayer region. PL shows sublinear behavior under increasing pumping power in its both intensity and peak position, in stark contrast with the intralayer excitons measured at the same sample position. Also the lifetime is three to four orders of magnitude longer than the reported value for direct excitons, therefore we can conclude that such PL emission is related to the formation of the interlayer excitons in the studied alloy-based TMD heterostructure.

5.6 PL characterization of alloy-based heterobilayers with varied composition of $Mo_xW_{(1-x)}Se_2$

Once that the presence of the interlayer excitons has been unambiguously demonstrated in alloy-based devices, a whole set of heterobilayers has been fabricated with WSe_2 and the available TMD alloys $Mo_xW_{(1-x)}Se_2$ with various x. The materials were exfoliated from the same bulk crystals across the whole project, so the results from different devices can be directly compared between each other. The adopted fabrication procedures were based on the PMMA/PMGI and the PC techniques described in section 3.3.2 and 3.3.3. A total of 30 heterostructure samples were produced for this study to ensure reproducibility and consistency of the data. At cryogenic temperatures all devices show a low-energy emission consistent with the behavior of interlayer excitons.

The results are shown in Fig.5.6 (a). The IX emission show a double peak shape for all devices, and most importantly both peak positions exhibit a clear monotonic blueshift as the W concentration in the alloy increases. The PL spectra were fitted with two Gaussian peaks and the peak positions are extracted and plotted in Fig.5.6 (b). For each x, the data points are the average values of PL measurements on at least 20 spots taken in different position of different samples. The spread of the values obtained in this way is often smaller than the size of the symbol, demonstrating the very good reproducibility between different devices.

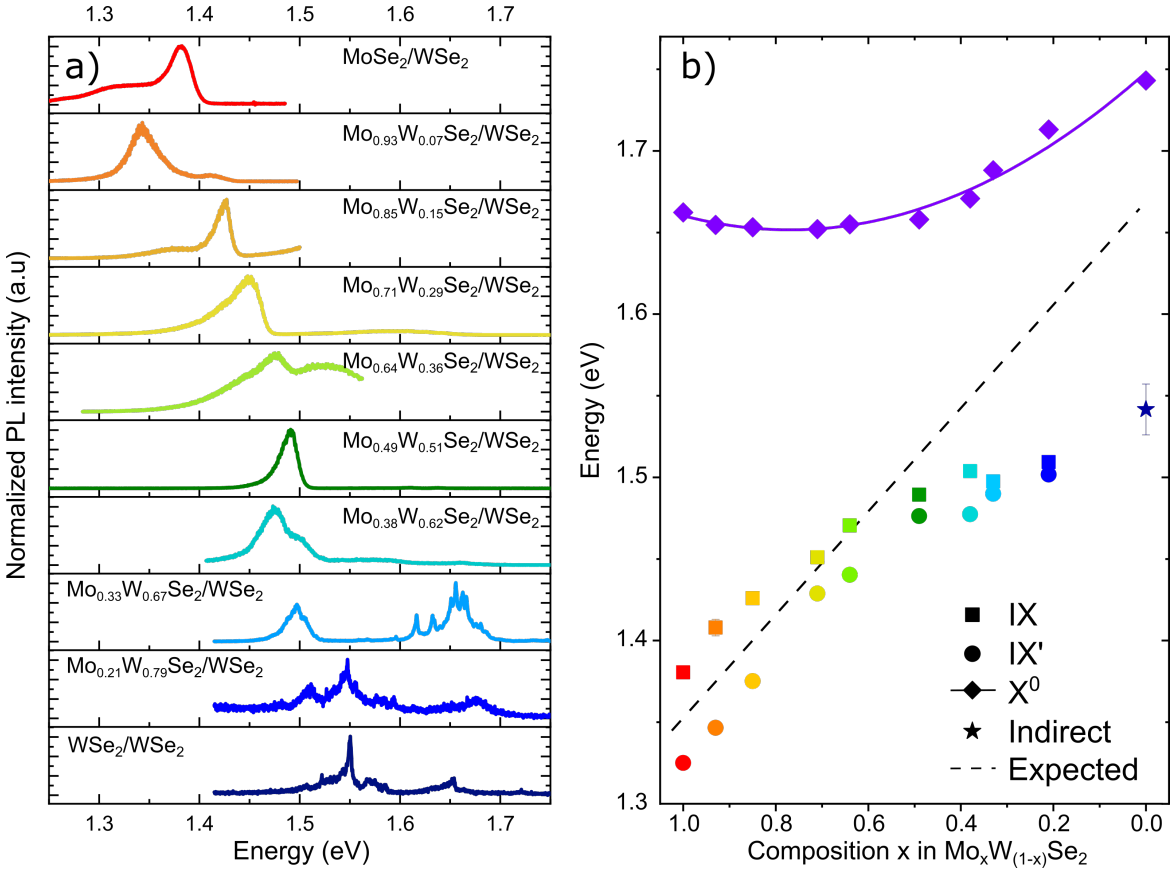

Fig. 5.6 **a)** Normalized PL spectra of the alloy-based heterobilayers. The color gradient indicate the composition of the alloy flakes. **b)** Peak position of the IX (squares) and IX' (circles) as a function of alloy composition, the error bars are contained in the point. Violet solid line and diamonds are the DX of isolated $Mo_xW_{(1-x)}Se_2$ alloys. Dashed black line indicate the expected trend where the IX can be tuned close in energy to DX.

The full squares represent the PL peak labeled *IX*, while the circle indicate the position of *IX'* peaks. The high energy peak blueshifts from 1.38 eV in $MoSe_2/WSe_2$ up to 1.51 eV in $Mo_{0.21}W_{0.79}Se_2/WSe_2$ device, corresponding to a shift of 130 meV. The low energy peak blueshifts as well as the tungsten composition increases, from 1.32 to 1.50 meV, over 180 meV. It is interesting to compare these results with the data gathered from PL in the X^0 exciton from the isolated alloy monolayers, presented previously, and included here again as violet diamonds with the solid violet line as the corresponding fit in Fig.5.6 (b). The IX emission blueshifts more strongly for Mo-rich alloy, moving from 1.38 eV to 1.47 eV (90

meV) moving from $MoSe_2/WSe_2$ to $Mo_{0.49}W_{0.51}Se_2/WSe_2$, while in the same composition range the DX peak position, measured from isolated alloys show very little variation.

The original idea behind this work was to have the possibility to tune the IX energy in close resonance with the DX using the TMD alloys, which offers the possibility to continuously tune the band gap and, most importantly, the band offsets, by varying their chemical composition. This simple idea, representing the expected trend, is illustrated with a linear dashed line in Fig.5.6 (b). We have observed instead a less obvious behavior. Up to x = 0.64 in the $Mo_xW_{(1-x)}Se_2$ composition the behavior indeed resembles a linear trend. Each layer of the heterostructure contributes separately and independently to the transition between the *K* points of the band structure [86]. For $x \leq 0.49$ a gradual transition to a bilayer WSe_2 occurs, which is instead momentum indirect and where the fundamental transition is between the *Q* point of the CB and the *K* point of the VB [96, 190]. This transition is gradual as the alloy composition becomes more W-like. The band structure evolution thus shows a gradual transition from a heterobilayer behavior to that of a homobilayer. Considering the IX peak position shown in Fig.5.6 (a), for the first five structures the trend can be considered almost linear with x, blueshifting constantly as the alloy becomes more W-like. Interestingly in this range, the IX blueshifts over 90 meV, while the $Mo_xW_{(1-x)}Se_2$ DX shows negligible shift due to the bowing effect (violet line in Fig.5.6 (b)). This indicates that, although the energy gap in alloy monolayers alloy is almost constant, the band offsets between the alloy and the WSe_2 gradually change as shown in Fig.5.1 (c).

In the $Mo_{0.21}W_{0.79}Se_2/WSe_2$ PL spectra (blue line in Fig.5.6 (a)) two interesting observation can be made: first the intensity of the IX signal is significantly quenched, compared with the structures with lower x, and also an additional PL signal appears at 1.55 eV. Such emission is extremely similar to the one observed in bilayer WSe_2 (dark blue line of Fig.5.6 (a)), either artificially stacked or naturally exfoliated, and can be related to the momentum indirect emission [117, 189, 190]. To clarify this behavior we fabricated a device which

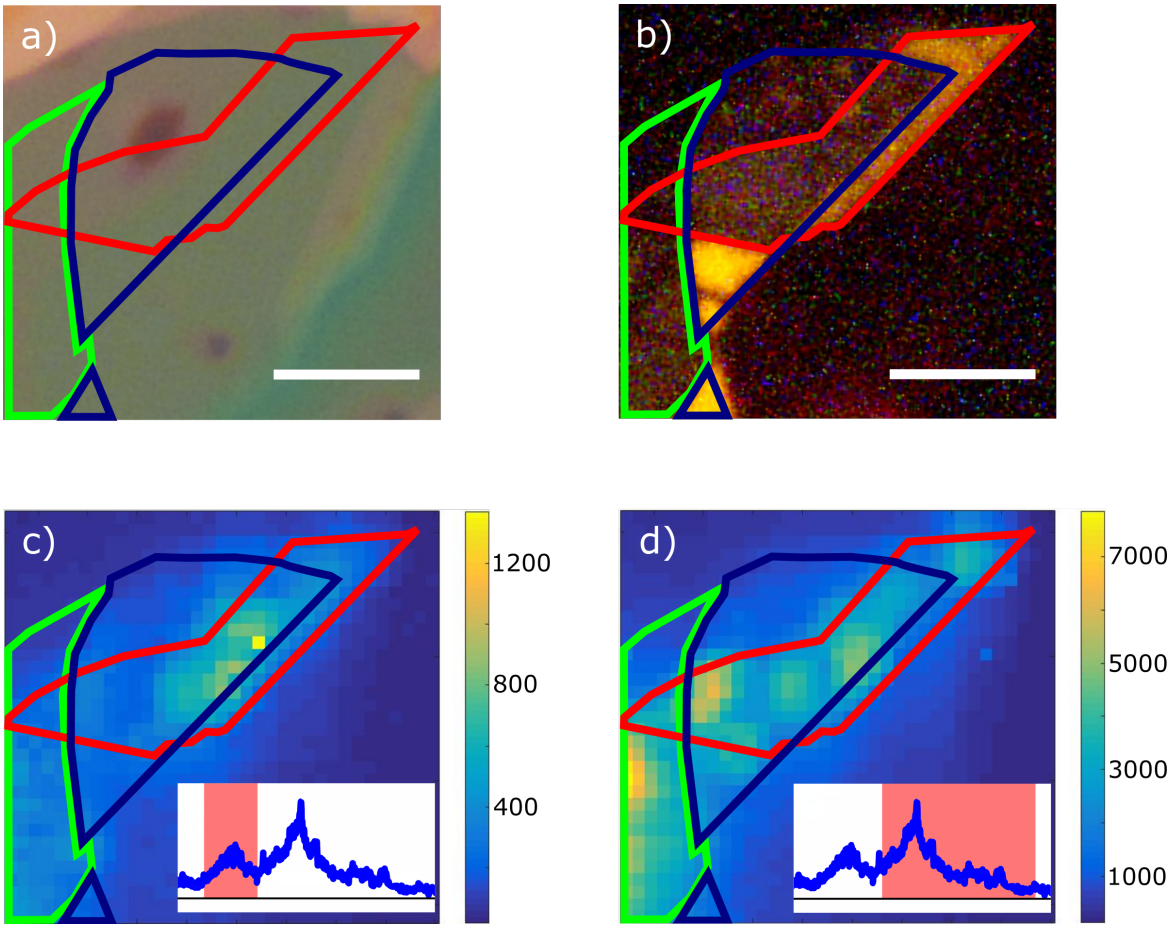

Fig. 5.7 **a)** Bright field microscope image of the $Mo_{0.21}W_{0.79}Se_2/WSe_2$ device. The red silhouette highlight the alloy monolayer, the blue silhouette highlight the monolayer WSe_2 and the light green sihlouette highlight the naturally exfoliated WSe_2. **b)** PL image of the device. It is possible to distinguishing a weak emission arising from both the heterobilayer and the bilayer WSe_2. **c)** Low temperature PL map of the device. The integration range is between 1.512 and 1.503 eV, focusing on the IX emission. The inset spectra show in red the targeted spectral region. **d)** Same LT PL map show in the previous panel but with a different integration range between 1.589 and 1.510 eV, focusing on the momentum-indirect transitions. The spectra in the inset show in red the spectral region.

possesses a naturally exfoliated WSe_2 region and a $Mo_{0.21}W_{0.79}Se_2/WSe_2$ region as well. Fig.5.7 shows the bright field image (Panel (a)) and PL image (Panel (b)) of the device. The different regions are highlighted with different colors: the dark blue line represents the monolayer WSe_2, the red line represents the monolayer $Mo_{0.21}W_{0.79}Se_2$ while the light green indicates the bilayer WSe_2. Panel (c) and (d) of Fig.5.7 show the low temperature PL map of

the sample, with different integration extremes. Panel (c) show the range between 1.512 and 1.503 eV corresponding to the IX residual transition, as shown in the spectra in the inset with the selected energy range (highlighted in red). Panel (d) shows the range between 1.589 and 1.510 eV corresponding to the bilayer WSe_2 momentum-indirect emission, as shown in the spectra in the inset with the selected energy range (highlighted in red). From the comparison of the two images it can be noticed that the IX emission intensity is mostly localized on the heterobilayer region, while the momentum-indirect emission is spread across both the bilayer WSe_2 and the mechanically stacked heterobilayer.

According to this result the logical evidence is that the spatially-confined interlayer excitons are shifting into momentum-confined excitons due to the band structure evolution of the heterobilayer that gradually becomes a WSe_2 homobilayer. This statement is addressed by the pinning of the IX to WSe_2 momentum indirect transition and the coexistence in the $Mo_{0.21}W_{0.79}Se_2/WSe_2$ device of a residual IX emission close to the momentum indirect transition.

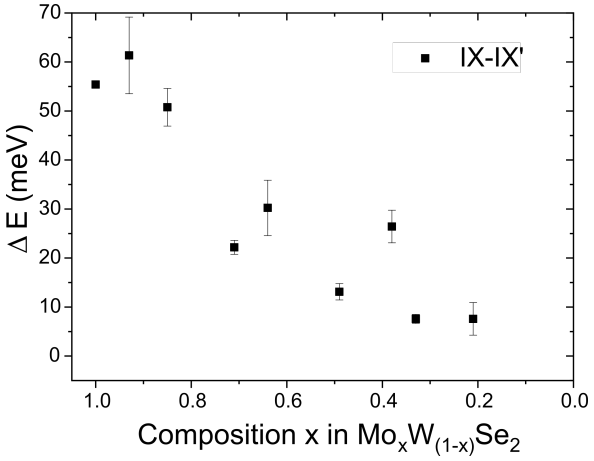

Fig. 5.8 Energy difference between IX and IX' as a function of alloy composition.

Fig.5.8 shows the energy difference ΔE between the high and the low energy IX emission. It can be seen that ΔE reduces as the composition becomes more W-rich, decreasing from 55

meV in $MoSe_2/WSe_2$ down to 8 meV in $Mo_{0.21}W_{0.79}Se_2/WSe_2$. A more detailed explanation of this trend will be provided in the discussion section.

5.7 Reflectance-contrast characterization of alloy-based heterobilayers with varied composition of $Mo_xW_{(1-x)}Se_2$

Devices were investigated also using reflectance contrast in the same positions and conditions as the PL measurements. The results are shown in Fig.5.9 (a). For high x composition in the $Mo_xW_{(1-x)}Se_2$ layer, two clear peaks can be observed in the RC spectra: the higher energy one corresponds to the WSe_2 *A* exciton absorption (for a detailed explanation check section 1.5), while the lower energy one is due to the alloy *A* excitons. Due to the spatial confinement, the interlayer excitons have a much weaker oscillator strength than their intralayer counterpart, therefore no RC signal can be detected at their corresponding energy [86]. Also, as mentioned earlier, their alignment (perpendicular to the heterobilayer plane) may further reduce their absorption. The peak position for both *A* exciton signals is extracted by the fitting of RC spectra acquired in different points of different devices with the average values plotted in Fig.5.9 (b).

For Mo-rich alloy heterobilayers the two absorption peaks are well resolved, with the WSe_2 *A* peak localized around 1.72 eV and the alloy *A* exciton peak observed around at 1.63 eV in $Mo_xW_{(1-x)}Se_2/WSe_2$ for $1 > x > 0.5$, and then abruptly blueshifts for $x < 0.5$ up to 1.72 eV. The RC spectra of the heterobilayers show that the WSe_2 absorption occurs at nearly constant energy in all the devices while the alloy's absorption peaks follows a quadratic dependence on the alloy composition, as expected [93] and observed before in PL emission experiments. The most interesting feature can be observed in the devices with $x \leq 0.4$ of Mo in the alloy. The RC spectrum of $Mo_{0.33}W_{0.67}Se_2/WSe_2$ device reveals the presence of additional peaks: the first one is at 1.71 eV, the second one is at 1.69 eV and the last one is

centered at 1.655 eV. Moving into the next step in composition, the $Mo_{0.21}W_{0.79}Se_2/WSe_2$ device show also three absorption peaks centered at 1.712, 1.695 and 1.66 eV. On the other hand the WSe_2/WSe_2 homobilayer shows only one peak centered at 1.72 eV, as previously reported [117].

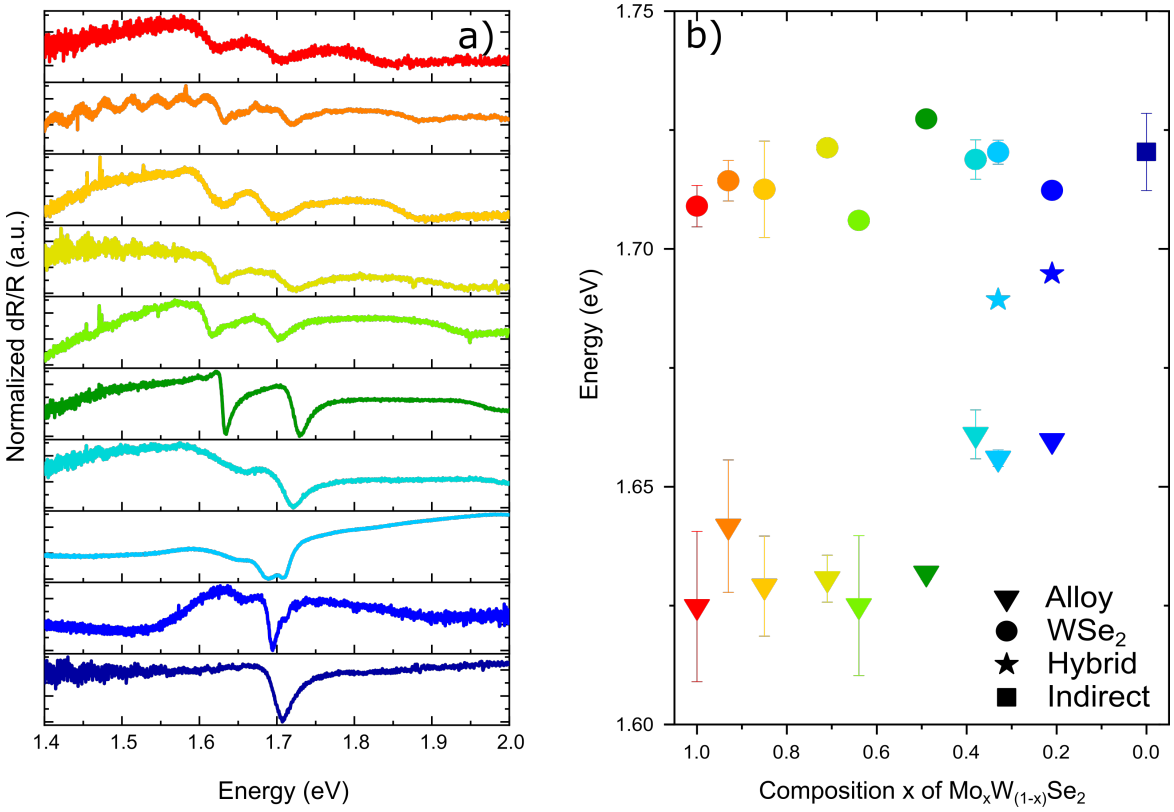

Fig. 5.9 **a)** Normalized RC spectra of the alloy-based heterobilayers. The colors gradient indicate the composition of the alloy flakes. **b)** Peak position of the alloy (triangle) and WSe_2 (circles) absorption peak as a function of the alloy composition in the device. When not displayed the error bars are contained in the point. Square dot indicate the *K*-*K* transition in momentum-indirect WSe_2 bilayer sample. Stars indicate the absorption energy of the hybridized transitions.

This complex evolution of the RC spectra indicates that in the samples with the two energy states of the two TMD layers almost in resonance, the formation of hybrid states occur. Due to the close proximity of the excitonic states of the alloy and the WSe_2 in the CB when the x composition in $Mo_xW_{(1-x)}Se_2$ layer is below 0.4, this two states start to hybridize creating additional states detectable in reflectance contrast measurements. Interestingly,

the PL spectra of the $Mo_{0.33}W_{0.67}Se_2/WSe_2$ device does show a bright IX emission, but in $Mo_{0.21}W_{0.79}Se_2/WSe_2$ heterobilayer the IX transition is quenched. This indicates that the hybridization observed in RC took place before that the Q valley is pushed below the K valley, so the heterobilayer still possesses a momentum direct transition. Also, the PL spectrum of the $Mo_{0.21}W_{0.79}Se_2/WSe_2$ device shows the rise of the momentum indirect transition. Therefore this mean that, considering as end point the band structure of WSe_2 bilayer, the Q valley overcomes the K valley making the fundamental transition momentum indirect. Although this emerging PL emission is a mixed contribution of several momentum indirect transitions [190], we targeted the Q valley because it has been reported to be the band edge state in the bilayer WSe_2 [96, 189, 190]. The presence of a residual IX emission at 1.51 eV indicates that the K point of the heterobilayer CB is still slightly populated by charge carriers. This is consistent due to the close energy proximity of the K point to the Q point and therefore the thermal distribution of carriers, even at cryogenic temperatures, promoted by the optical excitation pumping, is broad enough to sustain the carriers in these high energy valleys.

5.8 Probing the IX behavior

The intralayer excitons, due to the type-II band alignment in the device, possess permanent dipole moments aligned along the direction normal to the plane of the device. This dipoles are parallel between each other creating a repulsive dipolar exciton-exciton interaction [80], as discussed in section2.4.3. This gives rise to nonlinear effects when high density of interlayer excitons are generated in the heterobilayer pumped with sufficiently high optical powers. The most prominent effects are the sublinear increase of the PL intensity and the blueshift of the IX peak at high laser powers, due to the repulsive interaction between IX. The interaction between the IX are larger than between the DX because the size of the former is larger, due

to the enhanced dipole-dipole interaction caused by the separation of the carriers in different layers.

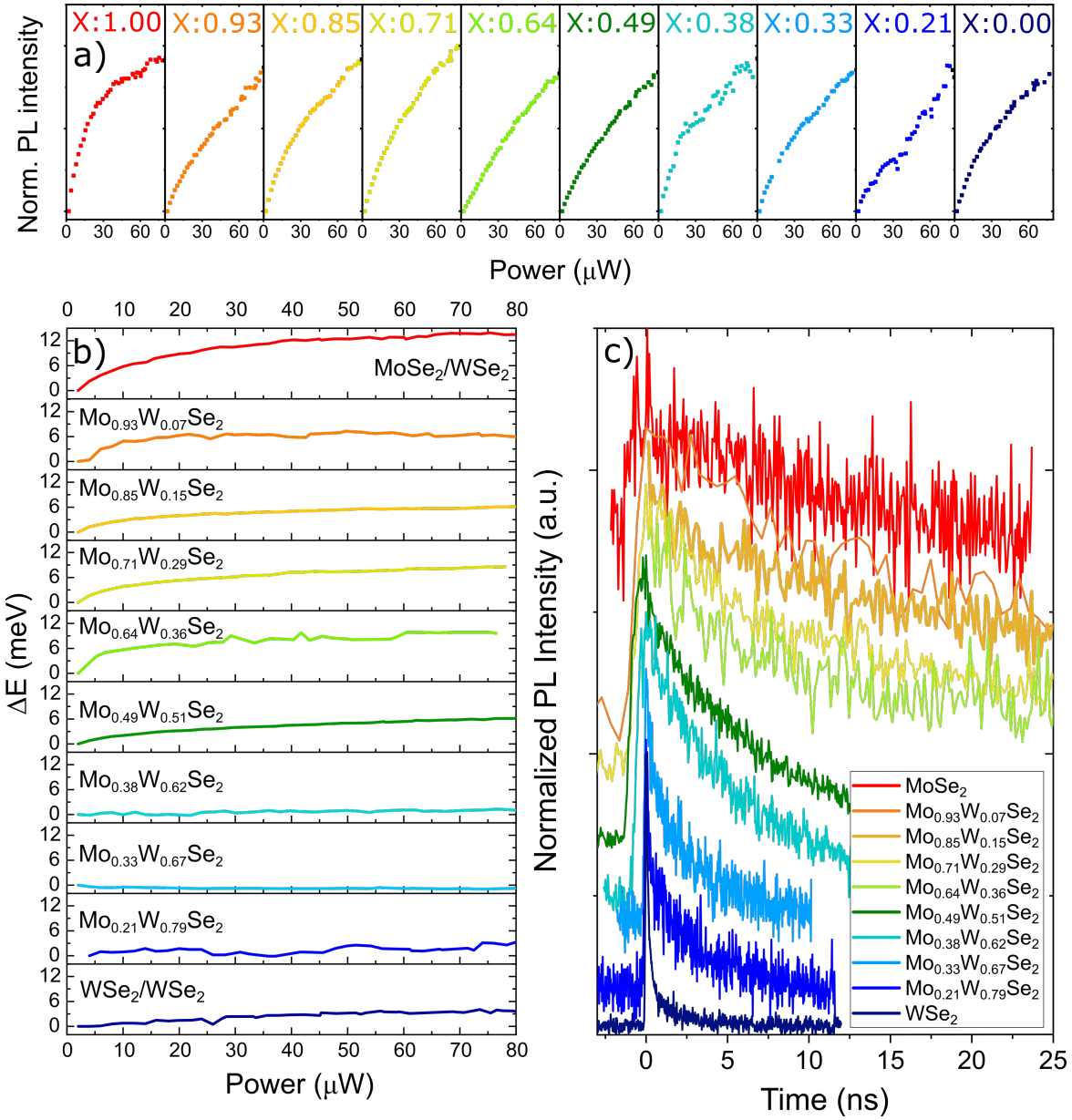

Fig. 5.10 **a)** Intensity of the IX emission as a function of pumping power. The colored label indicate the amount of Mo in the alloy lattice structure. **b)** Blueshift of the IX peak in all the heterobilayers as a function of pumping power. **c)** Normalized PL of IX in different devices as a function of the time. The alloy composition is indicated in the legend.

The power dependences performed on the alloy-based heterostructures reveal also additional details about the dynamics of the IX as a function of the alloy composition. Fig.5.10

(a) shows the evolution of the normalized PL intensity in the different heterostructures for increasing optical excitation powers. For low pumping powers the IX PL intensity tends to have a linear behavior, then it deviates toward a more sublinear dependence for higher powers due to the density-dependent IX-IX annihilation and their long lifetimes. The IX power-dependent intensities show qualitatively similar behavior for all the alloy compositions: it is always possible to observe a sublinear trend of the IX PL intensity. A possible explanation is that in both cases of spatially indirect and momentum indirect excitons their recombination dynamics are dominated by exciton-exciton annihilation which is more pronounced for interlayer exciton than intralayer excitons, due to the stronger interaction and the slower recombination dynamics.

In contrast to the PL intensity, the power dependence of the peak position of the IX in the different devices shows an abrupt change of behavior. A decrease of the blueshift is found, as the heterobilayer becomes progressively more similar to a homobilayer for small x in the $Mo_xW_{(1-x)}Se_2$ composition. The results are illustrated in Fig.5.10 (b). It can be observed that heterobilayers with high Mo- composition ($x > 0.4$) in the alloy layers exhibit a clear blueshift of up to 12 meV when the excitation power is ramped up to 80 μW. On the other hand, in W-rich devices ($x < 0.4$), the IX PL peak shows a weak blueshift, lower than 3 meV.

Table 5.1 IX lifetimes

Sample Composition	τ_1 (ns)	$\Delta\ \tau_1$ (ns)
$MoSe_2/WSe_2$	21.35	$\pm$1.21
$Mo_{0.93}W_{0.07}Se_2/WSe_2$	22.53	$\pm$1.42
$Mo_{0.85}W_{0.15}Se_2/WSe_2$	19.63	$\pm$1.03
$Mo_{0.71}W_{0.29}Se_2/WSe_2$	24.02	$\pm$1.99
$Mo_{0.64}W_{0.36}Se_2/WSe_2$	16.60	$\pm$1.72
$Mo_{0.49}W_{0.51}Se_2/WSe_2$	6.72	$\pm$0.15
$Mo_{0.38}W_{0.62}Se_2/WSe_2$	6.27	$\pm$0.20
$Mo_{0.33}W_{0.67}Se_2/WSe_2$	2.04	$\pm$0.08
$Mo_{0.21}W_{0.79}Se_2/WSe_2$	0.185	$\pm$0.034
WSe_2/WSe_2	0.144	$\pm$0.004

PL lifetimes offer further insight into the exciton dynamics. To acquire the PL decay of the IX in the entire set of samples, we collected the emitted photons with an avalanche diode photodetector (APD) (ID100-MMF50), with a timing resolution of ∼40 ps, and a photon counting card (SPC-130). A 638 nm pulsed diode laser (PicoQuant LDH) is used as excitation source, with 80 MHz repetition rate, which results in a instrument response function (IRF) with ∼150 ps FWHM. Due to the spatial separation of electrons and holes in different TMD layers, the lifetime of interlayer excitons is extremely long compared to intralayer excitons. The results gathered from all studied heterobilayers are shown in Fig.5.10 (c). The lifetimes shown corresponds to the IX peaks in all the alloy based devices and the momentum indirect transition in bilayer WSe_2 (represented by coloured dots in Fig.5.6 (b)). It can be observed that the lifetime of the IX shortens progressively decreasing from tens of nanoseconds in Mo-rich structure (x > 0.6) to few nanoseconds for intermediate composition (0.5 < x < 0.3) down to hundreds of picoseconds in $Mo_{0.21}W_{0.79}Se_2/WSe_2$ and bilayer WSe_2 devices. Although the decay time of momentum indirect transitions of WSe_2 bilayer has been reported to be on a timescale of 25 ps [196], the values presented are significantly longer due to the instrumental resolution of the adopted experimental setup. The numerical values extracted are shown in table 5.1 and also summarized in Fig.5.11 as a function of alloy composition.

Overall, the lifetime decreases by more than two orders of magnitude, and the most abrupt change happens moving from x=0.33 to x=0.21 in the $Mo_xW_{(1-x)}Se_2$ alloy composition, where the transition from spatially confined carrier to momentum indirect band gap was identified. Although the exact values cannot be extracted, this dramatic reduction of the lifetime strongly corroborate the presented hypothesis of a momentum direct to momentum indirect transition in composition-dependent heterobilayers.

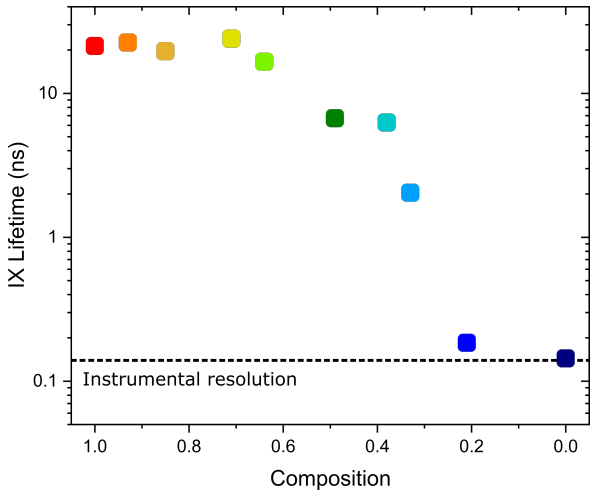

Fig. 5.11 IX lifetime as a function of the sample composition, the *y* axes is in log scale for better visibility. The dashed line indicate the experimental setup temporal resolution limit.

5.9 Discussion

The data presented indicate that, for small x in the concentration of $Mo_xW_{(1-x)}Se_2$ alloy layer embedded in a heterobilayer with a WSe_2 flake, a transition occurs where a more complicated band structure develops, deviating from the simple description of two independent band structure for the two TMDs in the *K* point of the BZ [86]. The results presented in this work require a more complex picture of the heterobilayer band structure, extending to other points of the BZ. We identify the *Q* valley of the CB as the most relevant. In fact, in bilayer WSe_2 the *K* point of the band structure is almost unaffected compared to the monolayer material, but the bilayer is momentum-indirect because the *Q* valley shifts below the *K* valley of the CB. Therefore we have elaborated a more complex picture that takes into the account this additional valley. It is important to remember that in the *Q* point of the BZ both layers of the device contribute as shown from the wavefunction distribution, even when they are definitely different (like $MoSe_2$ and WSe_2) [86] (for a more detailed explanation check section 1.3). All these considerations are done taking into account not the single particle band structure, but rather the excitonic states that are responsible for the optical response of these artificial structures.

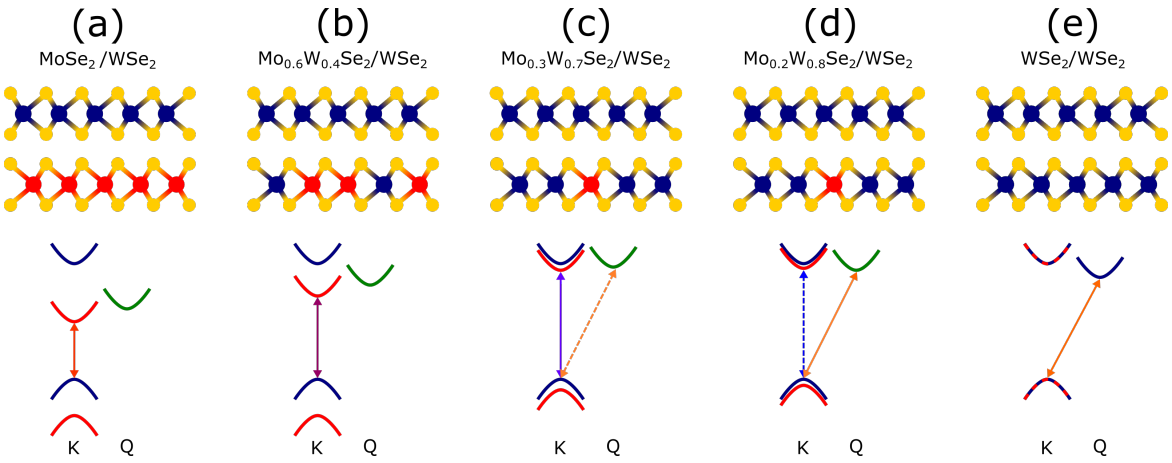

Fig. 5.12 Proposed model of the evolution of the excitonic states in a heterobilayer. The composition is displayed in the top panel. The mid line represent the chemical structure of the heterobilayer. The last line show the evolution of the K and Q valleys. The solid arrow indicate the most energy favorable transition, while dashed lines indicate the competitive transition.

Five different situations illustrating the transition to a hybridized band structure are shown in Fig.5.12. In this figure the red and blue curves represent the excitonic states of $MoSe_2$ and WSe_2, respectively. The green curve instead represent the hybrid dispersion in the Q point [86]. The solid arrow represents the lower energy transition between band edge states, meanwhile the dashed arrow shows the competitive transition, when energetically similar to the ground transition. Panel (a) shows the $MoSe_2/WSe_2$ structure, which was widely investigated and described extensively in Chapter 2. In these structures the carriers are totally spatially separated in the two layers, according to the type-II band alignment. The energy of the IX is ruled by the band offset between these states in the K points of the CB and VB of strongly localized in the $MoSe_2$ layer (red dispersion) and WSe_2 (blue dispersion), respectively. The Q hybrid state (green) is energetically distant and does not contribute to the IX emission. This situation is represented by the model presented by Rivera et al. [86] which describes the conventional picture for the IX.

Panel (b) represents the situation for Mo-rich alloys, as the composition becomes more W-like the band offset is increased, leading to a blue shift of the IX (solid purple arrow).

Despite the presence of W in the lattice structure, the red states of the alloy and the blue states of the WSe_2 are still energetically separated due to the presence of Mo-atoms in the lattice structure. Therefore the optical transition of the heterostructure can still be interpreted considering only the *K* valleys of the BZ.

Panel (c) is the upper limit of the conventional picture of spatially confined IX, that is experimentally confirmed in the $Mo_{0.33}W_{0.67}Se_2/WSe_2$ heterobilayer. In this situation the fundamental transition is still between the two states in the *K* points of the the BZ (violet solid arrow), therefore it is momentum direct. But since the band offset is very small, the WSe_2 and the $Mo_{0.33}W_{0.67}Se_2$ CB states at *K* point hybridize, which causes the appearance of a third hybrid peak from RC measurements.

Panel (d) represents the subsequent device in order of composition: $Mo_{0.21}W_{0.79}Se_2/WSe_2$ in which the conventional picture of IX fails. As can be seen the red state of the alloy and the blue state of the WSe_2 in the *K* point of BZ are almost resonant, leading to a much stronger hybridization. At the same time the evolution of the *K* and *Q* valley reach the point where the *Q* valley moves lower in energy than the *K* point. Hence a momentum indirect transition, very similar to the WSe_2 bilayer, can be observed in PL emission (orange solid arrow). The IX transition (dashed blue arrow) can still be detected. However it is not anymore the energetically favorable state, which causes the strong suppression of IX PL at low temperature. Also the reduced band offset between the two monolayers energy states lift the constraint of spatial confinement for electrons and holes observed for larger x in TMD alloys. Such band structure hybridization represents a transition from spatially-confined excitons with dispersion minimum at the *K* point of the BZ to spatially delocalized excitons with dispersion minimum at the *Q* point of the BZ.

Panel (e) represent the WSe_2 bilayer. The band structure contains a momentum indirect bandgap. The *K*-*K* transition is energetically unfavorable and the PL emission corresponding to this transition is almost negligible.

We now discuss the splitting between IX and IX' peaks observed in the devices where the use of alloys can provide some new insights in the origin of the IX double peak. The data shown in Fig.5.8 clearly reveal a reduction of the splitting as the composition of the alloy in the heterobilayer becomes progressively more W-rich. Considering that in the $Mo_xW_{(1-x)}Se_2$ alloy the CB spin split states progressively approach each other as a consequence of the SO splitting modification and it reaches zero for $0.49 < x < 0.38$ (because the alloy moves from optically bright to optically dark in such interval) we propose the origin of the IX double peak as the spin split states of $Mo_xW_{(1-x)}Se_2$ at the *K* point of BZ. There are some controversial facts to be considered. The splitting observed in $MoSe_2/WSe_2$ heterobilayer is 55 meV, much higher than the 25 meV reported previously [83, 128]. Also, the IX double peak does not shift apart again for alloy compositions x lower than 0.38, as expected [25]. The first fact is the most controversial, since many works show a different splitting of IX PL emission and a different intensity of the two peaks. The second point might be present but masked by the confinement of carriers in the momentum space that progressively causes a loosening of the IX conventional picture. To clarify this double peak origin, further analysis is required, but the use of TMD alloys represent a good approach to shed light on this phenomenon.

5.10 Conclusions

To summarize, in this chapter we present the results of optical investigations on a set of vertical heterobilayers each composed by monolayer WSe_2 and a monolayer of TMD alloy $Mo_xW_{(1-x)}Se_2$ whose composition ranges from pure $MoSe_2$ to pure WSe_2. The optical properties of these devices were fully characterized at low temperature (T<10K) by PL and RC, and in particular by PL maps, power dependences and time resolved PL. The data demonstrate unambiguously the rise of photoluminescence emission from interlayer excitons. These show a blue shift of 200 meV as the alloy composition becomes progressively more W-rich, proving that the chemical control of one of the layers stochiometry is a feasible approach

to achieve a band structure engineering in vdW heterobilayers. Moreover, it revealed that the spectral position of IX does not follow a linear trend with the composition but instead pins to the momentum indirect transition which dominates the optical response of the WSe_2 bilayer. This fact clearly shows that the conventional picture of the IX description in TMD-based heterostructure is incomplete. We show the importance of taking into account the other points of the BZ beyond the *K* valleys. The approach we adopted show how the use of alloys that become progressively resonant with the WSe_2 cause a total rearrangement of the band structure of the device, revealed by the different optical response and properties of the IX. To explain this set of data, we proposed a model for the evolution of the states involved in the formation of excitons. We demonstrate the transition from spatially-confined excitons with dispersion at K=0 to spatially delocalized excitons whith dispersion minimum at $K \neq 0$. This is confirmed by the appearance of hybridized transitions, a significant decrease of the IX lifetimes and a reduced blueshift of the IX peak increasing the excitation power.

This work represents a novel approach in the design and fabrication of nanoscale devices, demonstrating that TMDs alloys can be used to create vdW heterobilayers in which a fine and continuous band gap engineering of the heterostructures can be achieved to tune their electronic properties. It sheds light with a purely experimental approach on the genesis and interpretation of the interlayer excitons in vdW heterostructures, intentionally blurring the line between heterobilayer and homobilayer, revealing the limit of the conventional models. We propose a more extended framework to describe the optical properties of vdW heterobilayers.

Chapter 6

Optical investigation of $Mo_xW_{(1-x)}S_2$ transition metal dichalcogenide alloys

6.1 Abstract

By using TMD alloys it is possible to continuously tune optical properties of atomically thin semiconductors and their band structure. Despite the large amount of theoretical and experimental work focused on the optical properties of the single layer TMD alloys, summarized in section 1.6, there is a lack of knowledge about their behavior in the few layer form. So far the main focus has been mostly on their monolayer form. Particularly, it is unclear how the direct-to-indirect bandgap transition occurs in TMD alloys.

In this work we present a systematical analysis of the optical properties at room temperature of nine different $Mo_xW_{(1-x)}S_2$ materials whose composition spans from x=0% up to x=100%. The optical characterization is performed on mono-, bi- and trilayer samples, adopting a micro-photoluminescence (μ-PL) and micro reflectance contrast (μ-RC) setup. We investigate the evolution of the *A* and *B* excitons and the momentum indirect transition (*I*), that arises in the multilayer materials, for the whole set of chemical compositions. The

tuneability of the PL across the sample stochiometry is shown for *A*, *B* and *I* transitions for the three sample thicknesses.

The data show a parabolic dependence on the composition for the energies of all optical transitions for each sample thickness. We extract a full set of bowing parameters for each optical transition and sample thickness. The constant trend of the indirect gap emission sheds light on the still controversial description of the bandgap of the bilayer MoS_2, suggesting that the band edge states are located in the *Q* point of the CB and the Γ point of the VB. We demonstrate the linear tuning of the spin-orbit splitting and its insensitivity to the sample thickness as a consequence of the orbital localization. We also show the different behavior of *I*-*A* splitting in multilayer samples. This work aims to highlight the effect of alloying in bilayer and trilayer samples, which can be used for create finely tailored bandgap engineered TMD devices.

6.2 Introduction

Creating an alloy is a powerful approach to continuously tune the properties of the material. For TMDs this can be achieved simply by replacing a transition metal atom in the crystal lattice with a different one. Due to the similar transition metal atom Bohr radius and lattice symmetry [47, 61, 63], TMD alloys formed by mixing two transition metal atoms results in a even distribution of molybdenum and tungsten atoms in the crystal structure [47, 52, 58]. TMD alloys are thermodynamically stable and possible to mechanically exfoliate [61]. In such a way many of their properties can be controlled through the crystal stoichiometric ratio in a deterministic way [58, 62, 64]. Alloying does not make the material lose the main features of the chemically pure compounds. In monolayer alloys $Mo_xW_{(1-x)}S_2$, the valence band maximum (VBM) and conduction band minimum (CBM) are still located at the K point of Brillouin zones, allowing them to retain their direct bandgap, as theoretically [197] and experimentally demonstrated [198]. Depending on the alloy compositions the bandgap can

be tuned in different, but broad portions, of the visible and near IR spectrum. Their direct bandgap feature and the broad tuning range make these materials extremely promising for optoelectronic and light harvesting applications [199, 200]. The SO coupling, which is a feature of TMD materials [201–204], is sensitive to the sample chemical composition. The overall modification of the VB spin split states, shift from 148 meV splitting in MoS_2 up to 426 meV splitting in WS_2 [201], moving from parallel (for W rich alloys) to crossed (in Mo rich alloys) respectively [25, 58]. Also relatively to the vacuum level, the band structures of the monolayer MoS_2 and WS_2 are positioned at different energy levels, which create band offsets [51]. This feature make them attractive for developing new devices that rely on valleytronic effects to process information [33, 202].

Similarly to many bulk semiconductors, the band edge PL of $Mo_xW_{(1-x)}S_2$ alloys follows a parabolic dependence as a function of the composition, described by:

$$E^{PL}_{Mo_xW_{(1-x)}S_2} = xE^{PL}_{MoS_2} + (1-x)E^{PL}_{WS_2} - bx(1-x), \tag{6.1}$$

where $E^{PL}_{Mo_xW_{(1-x)}S_2}$ is the PL energy of the specific alloy, x is the molybdenum concentration in the alloy lattice, $E^{PL}_{MoS_2}$ is the PL energy of chemically pure MoS_2, $E^{PL}_{WS_2}$ is the energy of chemically pure WS_2 and b is the so-called bowing parameter that introduce a deviation form the linear behavior.

The bowing effect arises from orbital hybridization [60] and exhibits a different trend for different parts of the BZ, as a consequence of the different involvement of atomic orbitals across the band structure. It has been shown for monolayer MoS_2 that the contribution in the K point of BZ is different for conduction and valence band edge states: CB is mainly composed by transition metal d_{z^2} orbitals, while CB major contribution arises from transition metal $d_{x^2-y^2}$ and d_{xy} orbitals. In both cases the chalcogen orbital contribution is negligible [17]. In addition, another effect takes place when for TMDs alloys, arising from the fact that the orbital contributions for the CB states are different for MoS_2 and WS_2. The projected

density of states in MoS_2 identify the orbitals d_{z^2} as the only one which provide a contribution of the CB state. But in WS_2 such orbitals are accompanied by the $d_{x^2-y^2}$ and d_{xy} in defining the CB states [62]. This causes a pronounced nonlinearity in the evolution of the CB states as the x composition changes in the $Mo_xW_{(1-x)}S_2$ sample.

For the VB the situation is simpler since both Mo and W atoms contributes with their $d_{x^2-y^2}$ and d_{xy} orbitals. The associated wavefunction of such orbitals is spread mostly in the plane of the 2D sheet. Hence they are more coupled to each other and distributed over all cations, independently from their chemical nature. As a consequence of these effects, the VB evolution in $Mo_xW_{(1-x)}S_2$ alloys is expected to be linear as a function of the sample composition. These conclusions are consistent with other relevant work in this field, which showed that the biggest bowing effect is from the lowest unoccupied molecular orbital (LUMO) positions and the highest occupied molecular orbital (HOMO) positions demonstrate no bowing at all [58].

In conclusion, the bandgap evolution is determined by the sum of these two effects: a strong non-linear change of CBM and a linear modification of VBM across all the alloy stochiometric ratio, which results in the the parabolic dependence shown in Eq.6.1.

Despite this well established knowledge for monolayer TMDs alloys, the effect of sample composition for multilayer materials is still totally unexplored. Multilayer TMD alloys were mainly studied through Raman spectroscopy, with both high [58, 205] and low frequency modes [206, 207], with the main aim to calculate the precise stochiometry after the synthesis in a fast and nondestructive way.

Interestingly, in multilayer materials the band edge states are localized away from the K valley. In bilayer WS_2 the CB edge is predicted to be localized at the Q point of the BZ (halfway between the K and the Γ point) and the VB edge is positioned at the Γ point [148]. For MoS_2 the VBM is also located at the Γ point, but the interpretation of the CB is less

trivial, since several works support the idea that it is still confined at the *K* point while others identify the *Q* point as the conduction band minimum [148].

Using TMD alloys is an effective way to monitor the band structure evolution from two materials which are expected to have CB edges located in different valleys. Also the evolution of the Γ and *Q* points of the BZ can be probed. In such states there is a non negligible orbital contribution of the chalcogen *p*-orbitals which might induce a deviation from the expected quadratic model described above.

6.3 Identification of $Mo_xW_{(1-x)}S_2$ flake thicknesses trough optical contrast

A series of $Mo_xW_{(1-x)}S_2$ samples were produced through the micromechanical cleavage procedure described in section 3.1 and exfoliated on PDMS substrates. The flake search process follows similar, but also slightly different criteria compared to what has been presented before. Up to this point, the thesis was focused on monolayers and bilayers. The modifications of the optical microscope, described in section 4.3, allow a straightforward identification of monolayers by using the photoluminescence imaging. For the bilayers, PL can be observed only in optically dark materials (WS_2 and W-rich alloys) since the intensity is high enough to be detected. For bilayer MoS_2 and Mo-rich alloys the intensity is below the detection threshold of the CCD and does not allow a reliable identification of the material thickness. For the purpose of this work it is also necessary to identify trilayer materials and, due to their indirect bandgap, the PL imaging technique is not sensitive enough to identify them, because the PL signal is too low, independently from the sample composition.

This is summarized in Fig.6.1 which shows the bright field (a), dark field (b) and PL imaging (c) pictures of a WS_2 flake, deposited on 90 nm SiO_2 on Si. The flake presents mono- bi- and trilayer regions highlighted by differently colored silhouettes. In PL imaging

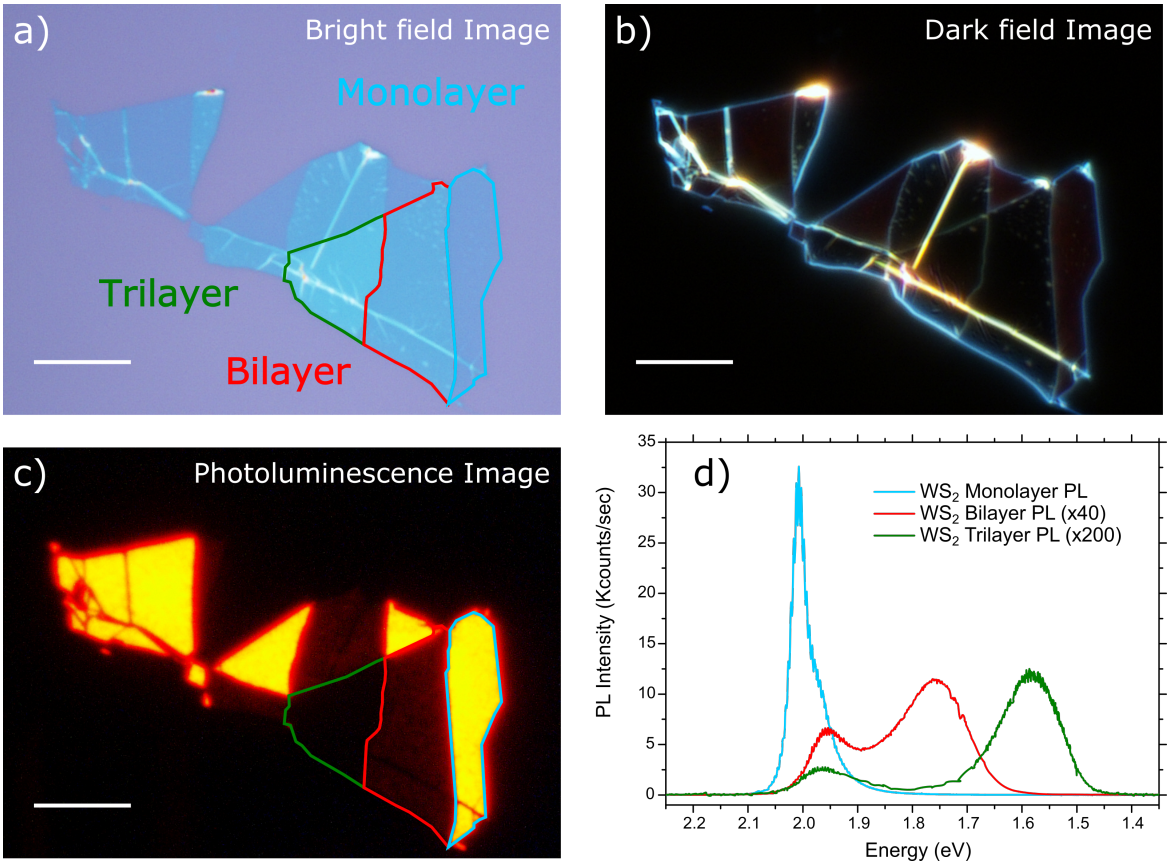

Fig. 6.1 Microscope images of a WS_2 flake on 90 nm SiO_2/Si. Blue, red and green silhouettes highlights monolayer, bilayer and trilayer regions respectively. **a).** Optical bright field image of the sample. **b).** Dark field image. **c).** PL imaging, monolayers shine bright due to their direct gap. **d).** PL spectra of monolayer (blue) bilayer (red) and trilayer (green) compared to each other.

configuration, monolayers are observed as bright areas, due to their direct bandgap (blue spectrum in Fig.6.1 (d) corresponding to blue silhouette in Fig.6.1 (c)). Some emission can still be detected in the bilayer region, despite their indirect gap, that makes the PL one order of magnitude less intense (red spectrum in Fig.6.1 (d) corresponding to red silhouette in Fig.6.1 (c)). Trilayer region does not show any detectable luminescence in PL imaging because the emission is suppressed by two order of magnitude compared to monolayers (green spectrum in Fig.6.1 (d) corresponding to green silhouette in Fig.6.1 (c)).

A possible approach to identify bi- and trilayers might be using the intensity of the edges shown in the dark field images, but when the flakes are standing on a transparent and non

perfectly even substrates, like PDMS, this approach is not reliable enough. Other techniques such Raman or AFM are too time-consuming and not suitable for flake search step on large substrates.

The approach we developed is based on the optical contrast of the flakes and also to the fact that all the materials, independently from their specific chemical composition (in terms of Mo:W ratio), look absolutely identical when exfoliated on PDMS. Since the PDMS is a viscoelastic polymer, it promotes the exfoliation process therefore it is possible to observe large terraced areas where the thickness of the material changes in a single atomic layer steps.

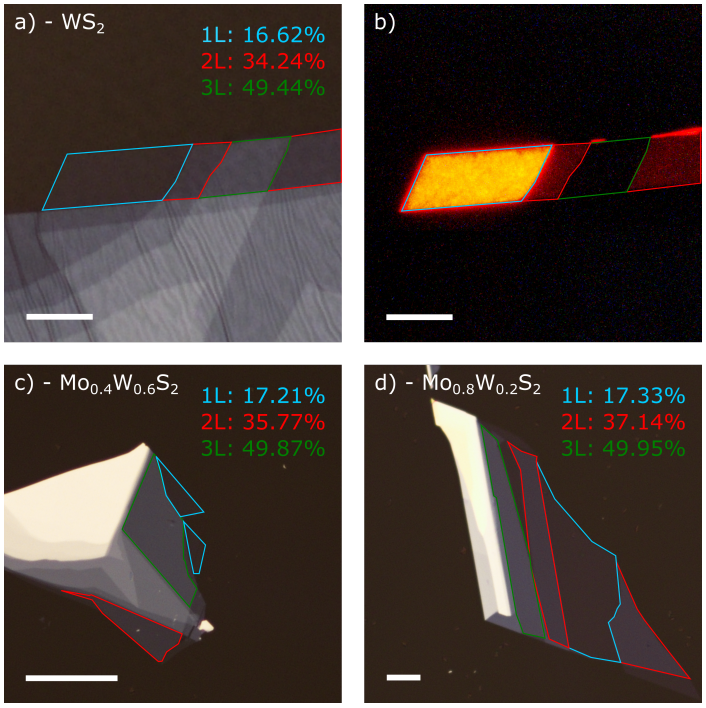

Fig. 6.2 **a)** Bright field image of a WS_2 flake on PDMS. The monolayer, bilayer and trilayer regions are highlighted in blue, red and green respectively. The optical contrast of each thickness is indicated in the inset. **b)** Correspondent PL image of the WS_2 flake. Emission can be detected in monolayer and bilayer areas. **c-d)** Bright field image of $Mo_{0.4}W_{0.6}S_2$ and $Mo_{0.8}W_{0.2}S_2$ flakes both on PDMS. The optical contrast is indicated in the inset for monolayer, bilayer and trilayer areas as well. The scale bar is 10 μm.

Fig.6.2 show three flakes of three different alloy compositions labeled in each image. Starting from the WS_2, which is the brightest, the monolayer and bilayer regions are identified using PL imaging, as shown in Fig.6.2 (b). The expected trilayer area is highlighted in green

and no PL can be observed. Using a software such as ImageJ it is possible to calculate the contrast of the flake area compared to the bare substrate. The contrast value, is expected to be linear with the sample thickness since each layer absorbs almost 15% of the incident light [31]. This linearity is lost for very thick samples (5+ layers), but for 1 to 3 layer range the results were found to be reliable. The contrast value extracted from Fig.6.2 (a) are shown in the inset for mono, bi and trilayer region. It can be noticed that the linearity is almost perfect. With this reference values obtained in a material where PL imaging works also for the bilayer, the technique is extended to the rest of the compositions. The values calculated from other alloys (shown in the insets of Fig.6.2 (c) and (d)) are in excellent agreement with the reference set, confirming its validity.

Once the flakes were identified they were transferred, using dry-peel method, on 90 nm thermal grown SiO_2 on Si substrates, following the method explained in section 3.3.1. Since the optical contrast procedure described above is insensitive to the sample composition, the material composition can still be reliably identified by PL imaging. As the alloy composition is changed from WS_2 to MoS_2, the PL emission redshifts from 2.05 to 1.88 eV. In this energy range the CCD detector employed in the microscope is expected to significantly change its response as a function of emission wavelength. This effect was not very pronounced in the selenide TMD alloys discussed in the previous chapter, since most of their emission is in the near IR portion of the light spectrum. In contrast for $Mo_xW_{(1-x)}S_2$ alloys, the PL tuning range as a function of composition is in the visible range, and thus the CCD show very different colours in PL images, as shown in Fig.6.3.

The results for monolayer flakes are summarized in Fig.6.3. The flakes looks similar in the bright and dark field images (shown in the first and second columns of Fig.6.3), but in PL images the color gradually changes according to the sample composition (as shown in the third column of Fig.6.3). All PL images in Fig.6.3 were acquired in the same condition of exposure and light intensity. PL color shifts from bright yellow for WS_2 and W-rich alloys,

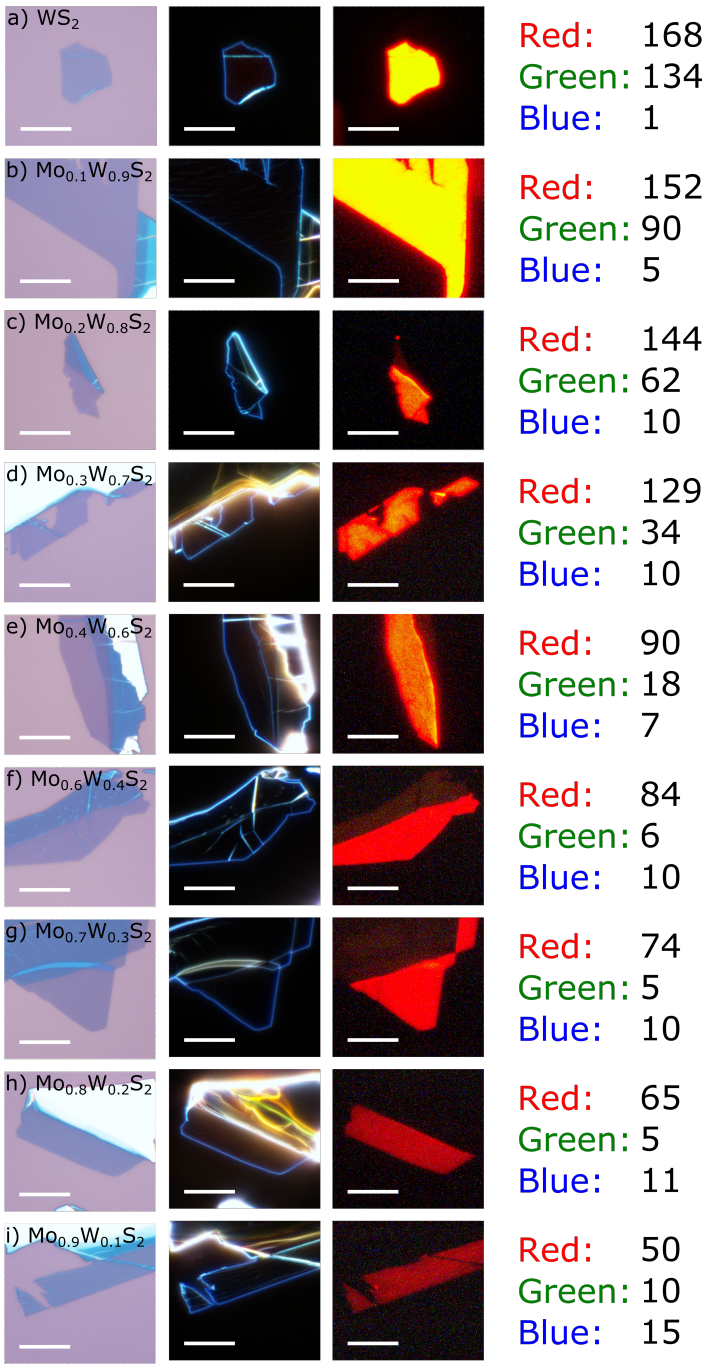

Fig. 6.3 Bright field (first column), dark field (second column) and PL images (third column) of a series of TMD alloy with a composition ranging from WS_2 (**a**) to MoS_2 (**i**). The colors vary from yellow to dark red. In the last column are indicated the values of the red, green and blue channel of the CCD. The scalebar of the sample pictures is 10 μm.

to orange up to x=0.5, intense red for Mo-rich alloys and finally dark red for MoS_2. The signals in the three color channel of the detector are extracted and shown in the last column of Fig.6.3. It can be noticed that the red channel progressively drops with this effect is mostly due to the dimming of the PL as the composition becomes more Mo-rich. The green channel almost immediately drops since the PL wavelength shifts into the red portion of the spectrum. The signal in the blue channel is negligible for all the alloy compositions.

6.4 Optical analysis of monolayer $Mo_xW_{(1-x)}S_2$ samples.

The samples were measured in PL at room temperature using a 532 nm CW diode laser for excitation. All reported experiments in this chapter were carried out in the same experimental conditions. Fig.6.4 (a) show normalized PL spectra from single-layer alloy samples with different stoichiometric ratios. In each spectrum two major component can be identified, labeled as *A* and *A**, corresponding respectively to the neutral and charged excitons emission [76]. Another feature can be detected in samples with Mo $\approx$ 100%, labeled as B. This is related to the *B* exciton radiative recombination, originating from the higher energy transition between the spin-split valence and conduction bands (for more detail see section 1.5.3). This feature appears only in alloys with high Mo concentration, due to the smaller SO splitting in the valence band. The spectra in Fig.6.4 (a) are fitted with Gaussian and Lorentian functions for neutral and charged exciton, respectively. The peak positions are extracted and shown in Fig.6.4 (c) with filled blue dots indicating the extracted PL peak position. Applying the parabolic equation model to the peak position (solid blue line in Fig.6.4 (c) for PL data fitting) maks it possible to calculate the bowing parameter *b* of 0.21 $\pm$ 0.02 eV. The *A* exciton emission redshift from 2.006 eV to 1.884 eV for an overall 122 meV continuously-accessible range.

The reflectance-contrast (RC) data are collected on the same spot of the samples (for more detail see section 3.4). The spectra are shown in Fig.6.4 (b). The two main features

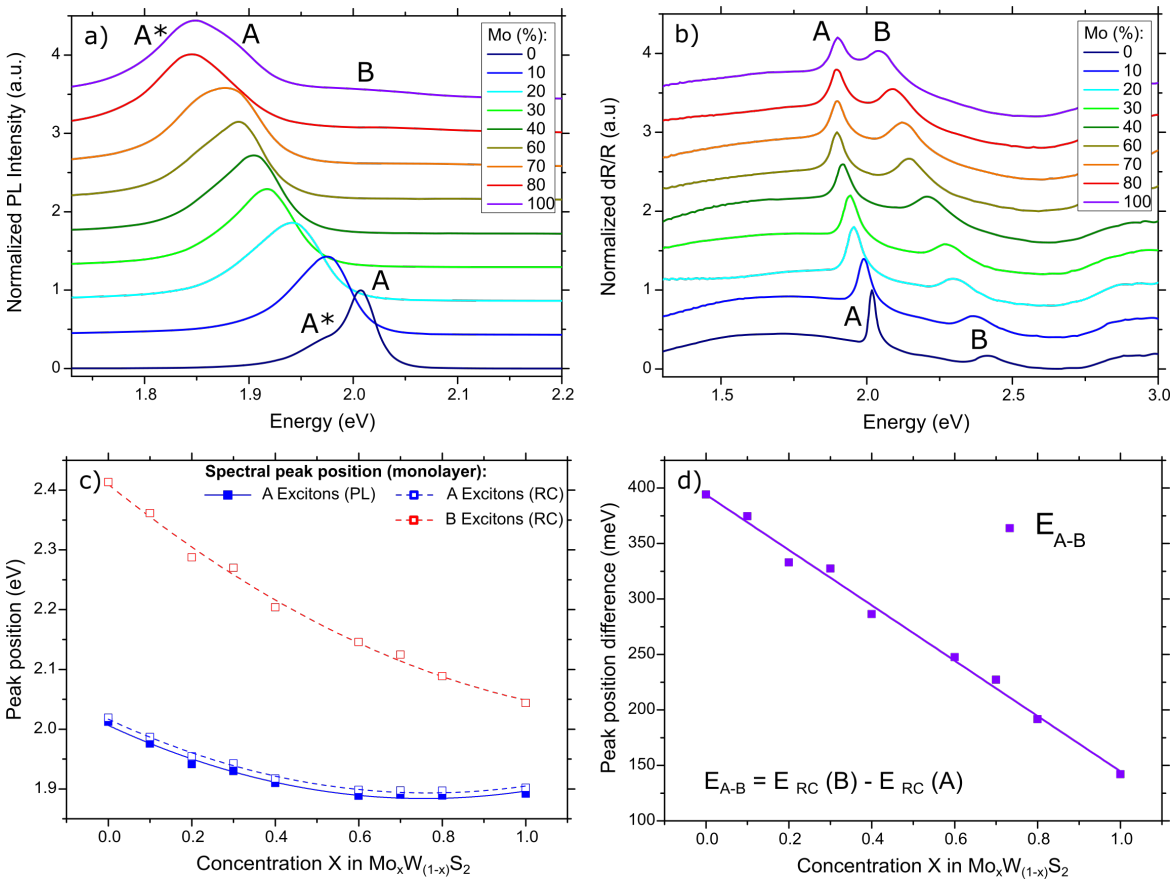

Fig. 6.4 Optical characterization of monolayer $Mo_xW_{(1-x)}S_2$ samples. **a).** Photoluminescence spectra. *A* exciton (A) and charged excitons (A*) emission is detectable in all samples. *B* exciton signal (B) can be detected only for high molybdenum concentrations. **b).** Reflectance contrast spectra. *A* and *B* excitonic transitions are clearly detectable. **c).** Peak position versus x concentration in the sample stochiometry extracted from PL (solid squares and continuous lines) and RC (empty squares and dashed lines) fitting. Blue colour is related to *A* excitons, red colour for *B* excitons. **d).** *A*-*B* exciton splitting in monolayer versus x concentration in $Mo_xW_{(1-x)}S_2$ alloys.

are related to the *A* and *B* exciton absorption. The observed energy separation is a result of the SO splitting, mainly in the valence band. Charged excitons cannot be detected due to their relatively low oscillator strength. The RC spectra were fitted with two Gaussian peaks. The extracted peak positions are plotted in Fig.6.4 (c). Empty blue and red squares represent the *A* and *B* excitons transitions, respectively, along with their respective parabolic fitting (described by eq.6.1).

As the alloy composition becomes more Mo-rich, the *A* excitons absorption redshifts from 2.02 eV to 1.89 eV (over a total range of 130 meV) while *B* excitons absorption redshifts from 2.41 to 2.04 eV (370 meV). The bowing parameter *b* extracted for *A* excitons is 0.210±0.016 eV, while for *B* exciton it is 0.20±0.04 eV. Fig.6.4 (d) shows the energy difference of the *A* and *B* excitons as a function of the alloy composition, linearly decreasing from 394 meV observed in WS_2 to 142 meV for MoS_2.

Our results are in good agreement with previous published work either in terms of linewidth and peak position [208]. The PL linewidth in the presented samples does not exceed 54 meV, for any given alloy composition. This indicates the good quality of the samples and the fabrication process.

The redshift of *A* excitons is related to the reduction of the bandgap in the *K* point of the Brillouin zone. The almost three time larger *B* exciton redshift, compared to the A excitons, is caused in part by the same effect, but is mostly due to changes in the SO splitting in the hole states.

Interestingly the *A*-*B* exciton splitting shows an almost perfect linear dependence as a function of the sample composition, decreasing from 394 to 142 meV, over the 250 meV range, as the material becomes more Mo-rich. This is in contrast with previous reports [47] that shows a nonlinear dependence of the *A*-*B* splitting. As in the case of the selenide alloys, discussed in Chapter 5, we attribute this discrepancy to the broader range of compositions analyzed in our work.

6.5 Optical analysis of bilayer $Mo_xW_{(1-x)}S_2$ samples.

In this section PL and RC data for bilayer $Mo_xW_{(1-x)}S_2$ samples are discussed. Normalized PL spectra measured for alloyed bilayers are presented in Fig.6.5 (a). Each spectrum exhibits the signal of the *A* exciton, and for the alloys with a Mo≥30% the *B* exciton emission can also be identified, as a consequence of the SO splitting reduction. Both transitions are direct

gap in the momentum space, located in the *K* point of the Brillouin zone, similarly to the monolayer samples. Together with these signals, another broad peak appears at much lower energies, labeled in Fig.6.5 (a) as *I*. Due to the indirect gap of the bilayer materials , the *I* spectral feature in WS_2 arises from the radiative recombination taking place between the VB edge located at the Γ point and the CB edge located at the *Q* point along the Γ-*K* direction of the Brillouin zone. For MoS_2 bilayer the situation is less clear, since there are contradictory predictions, the CBM is either located in the *Q* valley at lower energy than the *K* valley, or the CBM is still located in the *K* valley that is still the band edge state [148]. For both scenarios the VBM in the bilayer is still located on the Γ point of the BZ, making the bilayer MoS_2 a momentum indirect semiconductor.

The energy position of *A*, *B* and *I* transitions are summarized in Fig.6.5 (c) (blue, red and green full squares represent each transition, respectively). The quadratic equation fit is then applied according Eq.6.1 (solid blue, red and green line for *A*, *B* and *I* transitions). The *A* exciton redshifts from 1.993 to 1.852 (by 86 meV) as the alloys progressively becomes more Mo-rich, at the same time the *I* transition redshifts from 1.766 to 1.538 eV (by 228 meV). The *b* values are 0.15 ± 0.02 eV, 0.11± 0.12 eV and 0.20± 0.07 eV for *A*, *B* and *I* dependences on x composition in $Mo_xW_{(1-x)}S_2$ samples, respectively. Reflectance contrast data are presented in Fig.6.5 (b). The two signals are related to the *A* and *B* exciton resonances. The indirect gap transition does not appear in the RC spectra due to the negligible oscillator strength caused by the shift of the two valleys involved in the momentum space. Fig.6.5 (c) includes also the RC data for both *A* excitons (empty blue squares) and *B* excitons (empty red squares) and their parabola fittings (dashed blue line and dashed red line, respectively). The bowing parameter obtained is *b* of 0.23± 0.02 eV for *A* exciton and 0.30± 0.04 eV for *B* excitons. Fig.6.5 (d). summarizes the energy difference between *A*-*B* excitons (calculated from RC data, which allow to identify both transitions for all compositions) and *A*-*I* transitions (obtained from PL data) as a function of alloy composition. *A*-*B* exciton separation decreases from 408 meV in

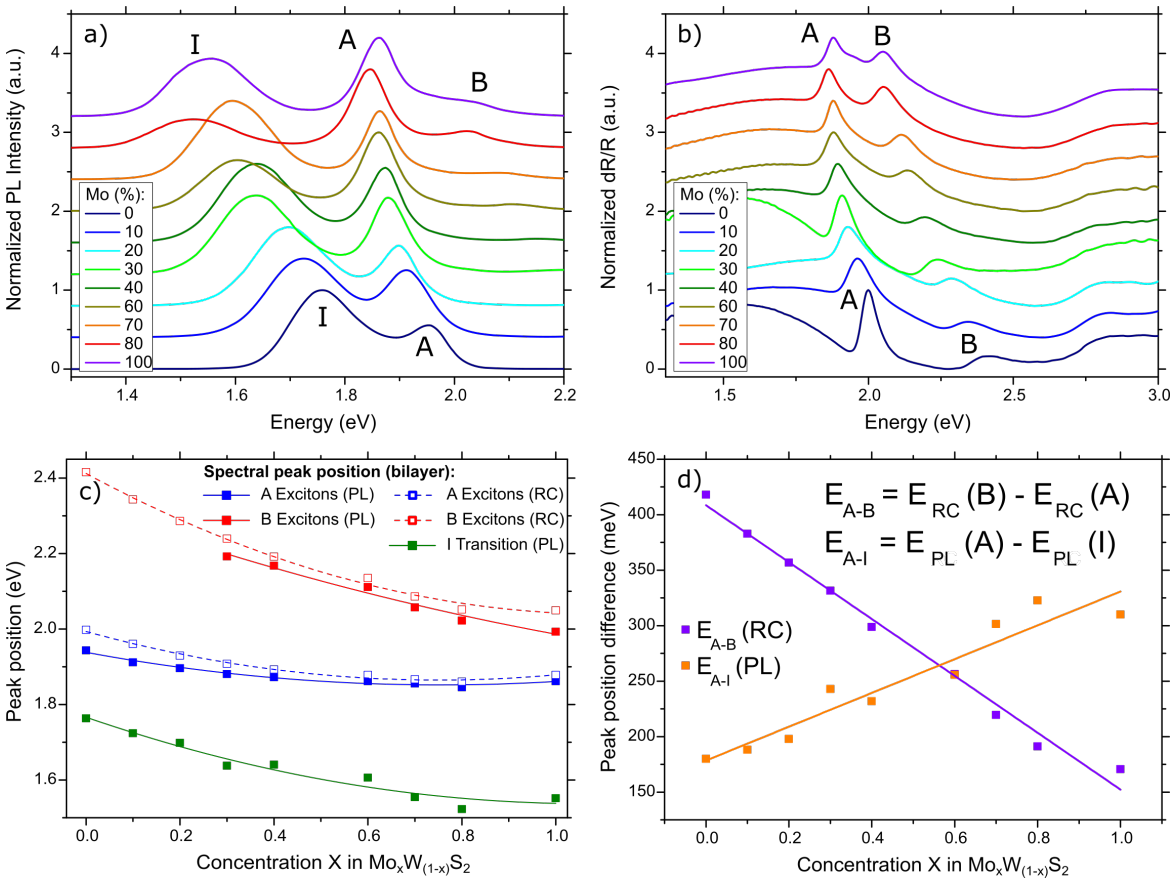

Fig. 6.5 Optical characterization of bilayer $Mo_xW_{(1-x)}S_2$ samples. **a)** Photoluminescence emission spectra. A-exciton (A) and indirect gap emission (I) are detectable for all compositions. B exciton (B) are visible only for high Molybdenum concentrations. **b)** Reflectance contrast spectra. A and B excitonic transition are labeled. **c)** Peak position extracted from PL (solid dots and continuous lines) and RC (empty dots and dashed lines) fitting. Blue colour is related to A excitons, red colour for B excitons, green for indirect emission (I). **d)** A-B excitons splitting (violet, calculated from RC data) and I-A energy difference (orange, calculated from PL data) in bilayer $Mo_xW_{(1-x)}S_2$ alloys.

WS_2 down to 152 meV in MoS_2, similarly to monolayer samples. At the same time, the *I-A* difference increases from 178 meV in WS_2 up to 331 meV in MoS_2.

The most evident effect of the indirect gap nature of the bilayer materials is the strong quench of the PL intensities (Fig.6.1 (d)), because the energetically preferred indirect gap transition mostly occurs in a non-radiative way. Despite this, a residue of the direct gap transition can still be observed. We cannot reliably identify peaks related to charged excitons, previously observed in the monolayer samples.

In the PL spectra in Fig.6.5 (a), it can be noticed that the *A* exciton emission peak redshifts from 1.938 down to 1.852 eV, corresponding to a shift of 86 meV. On the other hand the indirect-gap feature *I* shows a remarkable redshift as the sample composition becomes more Mo-rich. It can be tuned from 1.766 down to 1.538 eV, over a 228 meV range. Interestingly, the peak position of the *I* signal does not show remarkable discrepancies or abrupt change of intensity. This might suggest that the valleys involved are the same for all the sample composition, corroborating the idea that the MoS_2, like WS_2, exhibit the band edges states in the *Q* and Γ point of the band structure. The strong redshift of *I* clearly indicates how the band structure is dramatically affected by the sample composition away from the *K* point of the BZ.

Comparing the RC trend for *A* exciton in mono- and bilayer samples it can be observed that in bilayers the signal is redshifted compared to monolayers. *A* excitons peak position in monolayer samples range from 2.006 to 1.884 eV, while *A* excitons in bilayer sample range from 1.938 to 1.852 eV. *B* exciton signal on the other hand does not show any relevant change moving from mono- to bilayers.

A-*B* exciton difference in bilayer samples (Fig.6.5 (d), violet solid line) drops from 408 to 152 meV as the Mo ratio increases due to the SO-splitting reduction. This trend is very similar to the monolayer's both in terms of energy range and energy difference. These similarities can be explained again considering the orbital contribution at the *K* point of the Brillouin zone. This valley is mainly ruled by strongly localized transition metal *d*-orbitals. Their localization on the transition metal atom centers make them less sensitive to the different quantum confinement and screening effects.

Interestingly the *I*-*A* energy difference show an opposite trend, in fact it increases with x from 178 to 331 meV as the alloy becomes progressively more Mo-rich. This result further highlights the different behavior as a function of the alloy composition of the *K*, *Q* and Γ point of the Brillouin zone. This trend indicates that in the bilayer samples the indirect

gap, which involves a transition between the *K* or *Q* point of the CB and Γ point of the VB, collapses much more rapidly than the momentum direct energy gap in the *K* points of the BZ, as indicated by the green solid line in Fig.6.5 (c). Note that the momentum indirect bandgap evolution follows a parabolic behavior. In contrast the *I*-*A* energy difference is still a linear function of x, as shown by the orange solid line in Fig.6.5 (d).

6.6 Optical analysis of trilayer $Mo_xW_{(1-x)}S_2$ samples.

In this subsection we present the data for the trilayer $Mo_xW_{(1-x)}S_2$ samples. Fig.6.6 (a) shows the normalized PL spectra for alloys with different x in $Mo_xW_{(1-x)}S_2$. Similarly to bilayer samples, three PL peaks can be identified: the indirect gap transition *I*, the *A* and *B* exciton transition. The *B* excitons are detectable for the trilayer samples with $x \geq 0.3$. The PL peak positions are extracted and shown in Fig.6.6 (c). Solid squares represent the peaks for the *A* excitons (blue), *B* excitons (red) and the *I* transition (green). Quadratic fitting according to Eq.6.1 is provided for all the transitions (solid blue, red and green lines for *A*, *B* and *I* transitions respectively). The *A* excitons redshift from 1.943 eV to 1.845 eV as the concentration of Mo in the alloy increases. The *I* peak redshifts as well, moving from 1.576 eV in WS_2 to 1.445 eV in MoS_2. The *b* values extracted from the fitting with the Eq.6.1 are: 0.19± 0.02 eV for the *A* exciton, *b* of 0.13± 0.11 eV for *B* exciton and 0.14± 0.09 eV for the I feature. RC data are shown in Fig.6.6 (b), the two main absorption peaks are related to the *A* and *B* exciton resonances. The RC peak position dependence on x is summarized in Fig.6.6 (c) (empty blue and red squares for *A* and *B* excitons, respectively). The quadratic equation is applied once more (dashed blue and red lines for the *A* and *B* exciton, respectively) and the fitted *b* values are: 0.26± 0.02 eV and 0.33± 0.03 eV for the *A* and *B* excitons, respectively.

Fig.6.6 (d) summarizes the energy difference between *A* and *B* peaks (extracted from the RC data) and the difference between *A* and *I* peaks (from the PL data). The *A*-*B* energy difference decreases linearly as Mo concentration increase, from 412 to 164 meV. This energy

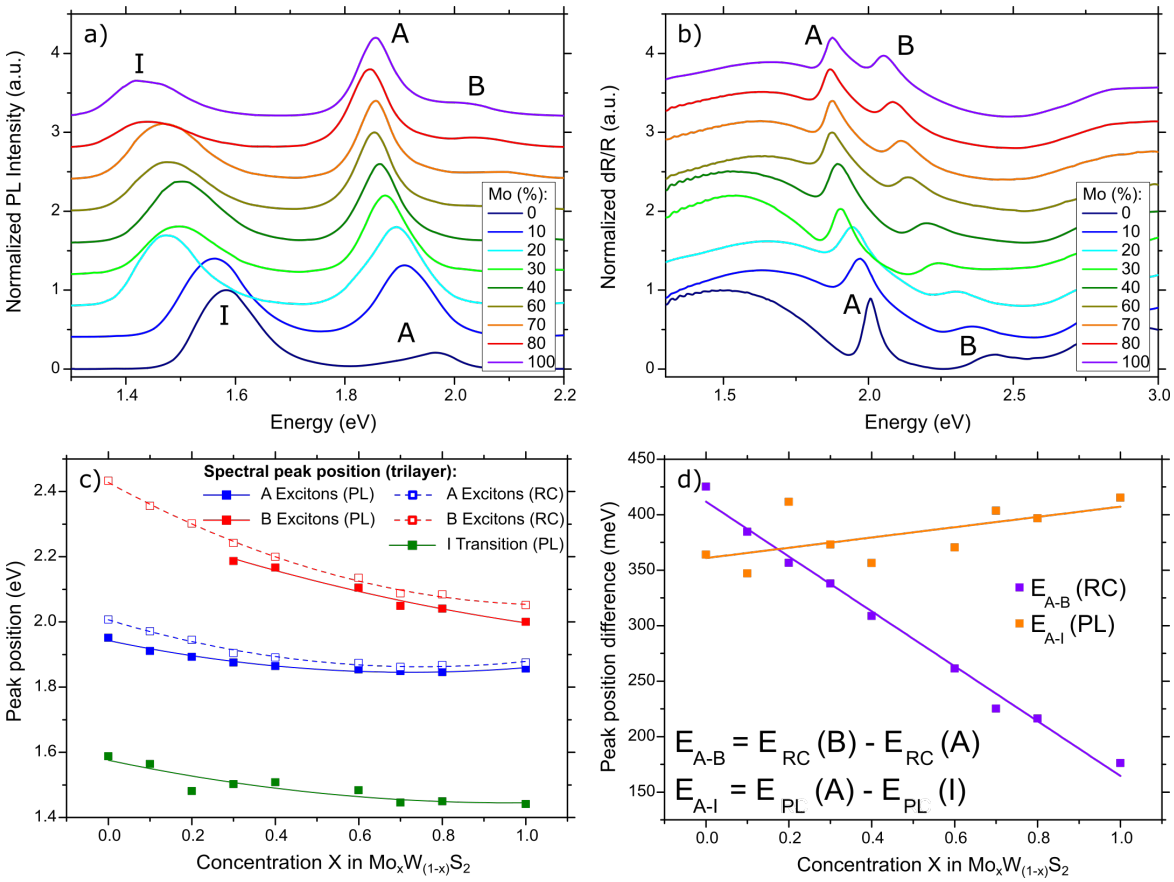

Fig. 6.6 Optical characterization of trilayer $Mo_xW_{(1-x)}S_2$ samples. **a)** Photoluminescence emission spectra. *A* excitons (A) and indirect gap emission (I) are detectable for all compositions. *B* excitons (B) are visible only for high molybdenum concentrations. **b)** Reflectance contrast spectra of the trilayer samples. *A* and *B* excitonic transitions are labeled. **c)** Peak position extracted from PL (solid dots and continuous lines) and RC (empty dots and dashed lines) fitting. Blue colour is related to *A* excitons, red colour for *B* excitons, green for indirect emission (I). **d).** *A*-*B* energy splitting (violet, calculated from RC data) and *I*-*A* energy difference (orange, calculated from PL data) in trilayer $Mo_xW_{(1-x)}S_2$ alloys.

difference is very similar to the one observed in mono- and bilayer samples. In contrast, the *A*-*I* splitting increase linearly from 361 to 407 meV as the alloy composition approach Mo concentration of 100%. It is worth noting that, despite the indirect bandgap of the trilayer alloys, the direct gap transitions of *A* and *B* excitons can be still observed, although the PL signal is suppressed by more than two orders of magnitude, compared to the monolayers (Fig.6.1 (d)).

Moreover the energy range of the *A* excitons in trilayer samples is almost identical to the one observed in bilayers with a similar tuning range. This indicates that the reduction of the at *K* point of BZ happen mostly in the mono-to-bilayer transition, supporting the theory of its small sensitivity to the external environment related to its main contribution by strongly localized transition metal *d*-orbitals.

The *I* signal in the trilayers shows a redshift as the material becomes more Mo-rich, as also observed in the bilayer alloys. Also, the *I* transition occurs at lower energies compared to the bilayer samples. This is caused by reduced quantum confinement effects and leads to a lowering of energy of the CBM in the *Q* point and increase of energy for the VBM in Γ point of the Brillouin zone, resulting in a lowering of the energy transition. For the trilayer materials the ambiguity about the band edge states is totally lifted, since the band edge states are located in the *Q* point of the BZ for the CBM and the Γ point of the BZ for VBM for both MoS_2 [15] and WS_2 [203]. Therefore, the band structure can be approximated to the bulk materials. It is interesting to notice that the *I* feature in the trilayer samples shows a completely different composition-dependent energy shift. It redshift from 1.576 eV down to 1.445 eV as the concentration of Mo increases. The total shift is 131 meV, much smaller compared to the 228 meV observed in the bilayer samples. This observation reveals a different bandgap evolution as a function of sample composition moving from bi- to trilayer.

The *B* exciton signal on the other hand does not show a different trend compared to the bilayer samples, both in terms of the energy and tuning ranges. This result can be explained with the localization of the *d*-orbitals that compose the *K* point of the BZ, making the SO coupling largely insensitive to sample thickness. Hence, the energy difference between *A*-*B* excitons in trilayer samples summarized in Fig.6.6 (d) (solid violet line), show a similar trend to the mono- and bilayer samples. The *A*-*I* energy differences instead shows a significant discrepancy compared to the bilayer samples. In fact their splitting is localized to a different energy range (361 to 407 meV splitting in trilayers versus 178 to 331 meV in bilayers) and

also this trend is less composition dependent, although in both cases it increases with the Mo concentration in the alloy. These differences might be related by the Γ-*Q* indirect gap closure, which reduces the effect of the transition metal composition on the *I* transition and consequently on the *A*-*I* splitting in trilayer samples, although further investigations are required.

6.7 Discussion

In this section all the results gathered from PL and RC are summarized and compared. Table 6.1 show the results for the *A* excitons across the different thicknesses and probing methods. In the table we report the PL energies of MoS_2 and WS_2 both experimental and extracted from the parabola fitting. We include also the bowing parameter extracted. In the last two column we summarize the maximum and minimum values of *A* excitons energies and the overall range (ΔA).

A exciton energies redshift by 68 meV moving from mono- to bilayer but increasing the thickness from bi- to trilayer no redshift is observed. This effect is related to the reduced quantum confinement in the bilayer samples that causes a slight reduction of the energy gap at the *K* point of the BZ. Although it may seems contradictory that the K point has a dependence on the number of layers, it is worth to point out that the *Q* and the Γ valleys for the same increase of thickness show a more pronounced shift, transforming the material in a indirect bandgap semiconductor, hence making the few meV rearrangement in *K* point negligible. Furthermore there is no difference between the bilayer and trilayer samples, corroborating the idea that the *K* point of the band structure is largely insensitive to the sample thickness. The bowing parameters extracted from the quadratic fit of *A* excitons are remarkably high. The minimum value of the fit is found between $0.7 < x < 0.8$, consistent with other values reported in the literature [58, 59].

Table 6.2 summarizes the fitting parameters for the *B* excitons in all the samples. In the table we report the PL energies of the *B* excitons for MoS_2 and WS_2, taken by experimental data and also extracted from the parabola fitting. The bowing parameter extracted is included as well. In the last two columns we summarize the maximum and minimum values of *B* exciton energies and energy splitting between *A* and *B* exciton energies (*A*-*B*).

There is the same discrepancy between PL and RC data described before, but also there is a lack of any observable trend as a consequence of layering. *B* excitons in bilayer and trilayer are energetically positioned in the same range as in monolayers. This evidence indicates that the SO coupling effect, mainly responsible of the *B* exciton trend, is largely insensitive to the number of layers. We identify the origin of these phenomena in the strong contribution of the *d* orbital of the transition metal in the *K* point of BZ, which causes the SO effect and consequently rules the *B* exciton evolution. Note that the bowing parameter can be reliably calculated only for RC data, where the *A* and *B* absorption can be unambiguously identified for all the sample compositions. Interestingly, the *b* values for the *B* excitons are smaller than the energy difference of the two chemically pure materials, in an opposite trend compared to the *A* excitons. This effect might be related to the high tuneability of the *B* exciton through alloying, although further investigations are required.

Table 6.1 Summary of the values extracted from the *A* exciton fitting across the different thicknesses and probing methods (first and second column, respectively). $E^{PL}_{MoS_2}$ indicate the extracted PL energies for the MoS_2 *A* excitons. $E^{PL}_{WS_2}$ indicate the extracted PL energies for the WS_2 *A* excitons. *b* represents the bowing parameter extracted from *A* exciton fitting. $\mathbf{A_{Ex}}$ $\mathbf{\Delta E}$ are the highest and lowest experimental values of the *A* exciton energies. ΔA represents the energy range of the *A* excitons peak as a function of the composition.

N°L	**Met.**	$E^{PL}_{MoS_2}$ (eV)	$E^{PL}_{WS_2}$ (eV)	***b*** (eV)	$\mathbf{A_{Ex}}$ $\mathbf{\Delta E}$ (eV)	$\mathbf{\Delta A}$ (meV)
1L	PL	1.896±0.030	2.006±0.004	0.21±0.02	2.006-1.884	122
1L	RC	1.905±0.022	2.017±0.003	0.21±0.02	2.017-1.893	124
2L	PL	1.861±0.030	1.938±0.004	0.15±0.02	1.938-1.852	86
2L	RC	1.879±0.027	1.993±0.004	0.23±0.02	1.993-1.865	128
3L	PL	1.860±0.032	1.943±0.005	0.19±0.02	1.943-1.845	98
3L	RC	1.879±0.032	2.006±0.005	0.26±0.02	2.006-1.863	143

Table 6.2 Summary of the values extracted from the *B* exciton fitting across the different thicknesses and probing methods (first and second column, respectively). $E^{PL}{}_{MoS_2}$ indicate the extracted PL energies for the MoS_2 *B* excitons. $E^{PL}{}_{WS_2}$ indicate the extracted PL energies for the WS_2 *B* excitons. *b* represents the bowing parameter extracted from *B* exciton fitting. $\mathbf{B_{Ex}}$ Δ**E** are the highest and lowest experimental values of the *B* exciton energies. $A-B$ represents the energy difference between *A* and *B* excitons. The larger and smaller energy difference values are provided. The $*$ indicate a partial set of data.

N°L	**Met.**	$E^{PL}{}_{MoS_2}$ (eV)	$E^{PL}{}_{WS_2}$ (eV)	***b*** (eV)	$\mathbf{B_{Ex}}$ Δ**E** (eV)	$A-B$ (meV)
1L	RC	2.048±0.061	2.410±0.009	0.20±0.04	2.410-2.048	394-144
2L	PL	1.986±0.196	2.322±0.045	0.11±0.12	2.199-1.986*	318-129*
2L	RC	2.043±0.057	2.412±0.008	0.30±0.04	2.412-2043	409-152
3L	PL	1.997±0.180	2.319±0.041	0.13±0.11	2.194-1.997*	318-141*
3L	RC	2.054±0.042	2.428±0.006	0.33±0.03	2.428-2.054	412-164

Table 6.3 Summary of the values extracted from the *I* transition fitting across the different thicknesses and probing methods (first and second column, respectively). $E^{PL}{}_{MoS_2}$ indicate the extracted PL energies for the MoS_2 *I* transition. $E^{PL}{}_{WS_2}$ indicate the extracted PL energies for the WS_2 *I* transition. *b* represents the bowing parameter extracted from *I* transition fitting. $\mathbf{I_{Tr}}$ Δ**E** are the highest and lowest experimental values of the *I* PL peak. $A-I$ represents the energy difference between *A* exciton peak and *I* peak. The larger and smaller energy difference values are provided.

N°L	**Met.**	$E^{PL}{}_{MoS_2}$ (eV)	$E^{PL}{}_{WS_2}$ (eV)	***b*** (eV)	$\mathbf{I_{Tr}}$ Δ**E** (eV)	$A-I$ (meV)
2L	PL	1.54±0.11	1.766±0.015	0.20±0.07	1.766-1.538	178-331
3L	PL	1.44±0.13	1.58±0.02	0.14±0.09	1.576-1.445	361-407

The *A*-*B* exciton difference (illustrated in the last column of table 6.2 for the largest and smallest value across sample compositions) show minor changes as the sample thickness change. This effect is insensitive to the probing technique adopted. Interestingly, compared to previous reports that show a nonlinear dependence [47], our findings identify an almost perfect linearity of the *A*-*B* splitting for all the sample compositions, shifting from 400 meV in WS_2 to 150 for MoS_2. This linear dependence and the insensitivity to layer thickness arises from the minor changes of the *A* and *B* excitons described above, revealing a very strong intralayer localization of the orbitals in the *K* valleys, even when the rest of the band structure undergoes significant changes when the quantum confinement is reduced.

Table 6.3 show the values extracted from the indirect gap (*I*) transition observed in the multilayer samples. In the table we report the PL energies of the indirect transition for MoS_2 and WS_2, taken by experimental data and also extracted from the parabola fitting. Only the PL data are provided since the momentum indirect transitions cannot be detected in RC. The bowing parameter extracted from the parabola fitting is included as well. In the last two columns we summarize the maximum and minimum values of *I* peak position and energy splitting between *A* and *I* exciton energies (*A*-*I*). The *I* peak, for both bilayer and trilayer, follows the parabolic dependence similar to that observed for *A* and *B* excitons. This observed quadratic trend has not been reported previously. It is not trivial, since in the multilayer TMDs the band edge states are located at the *Q* and Γ valleys for CB and VB, respectively, where the orbital composition exhibits a non negligible presence of the chalcogen *p* orbitals.

In bilayer samples the observed trend of *I* peak might indicate that in bilayer $Mo_xW_{(1-x)}S_2$ the band edge state of the CB is always localized in the *Q* point of the BZ, independently from the specific sample composition. This approach can shed some light on the controversial identification of the MoS_2 CB edge state.

Moving from bi- to trilayer, the *I* transition redshifts by hundreds of meV, revealing the extreme sensitivity of the *Q* and Γ point of the BZ towards the sample thickness, even when the quantum confinement effect is reduced as a consequence of layering.

Moreover in bilayer samples the momentum indirect transition is very composition dependent, since it spans over 250 meV range moving from WS_2 to MoS_2. Remarkably this trend is attenuated in the trilayer TMDs alloys, where the *I* peak can be tuned only by 145 meV. Similarly to the *A*-*B* splitting, which gives information on the SO coupling, the *A*-*I* splitting can provide useful information on the valley evolution following alloying, since the *K* valley is insensitive to layer thickness, while the momentum indirect transitions are, since they involve valleys away from the *K* point of the BZ. In the bilayer sample the *A*-*I*

splitting indicates that the suggested Q-Γ indirect gap is reduced as the composition becomes more Mo-rich. This effect is very pronounced since the A-I splitting shifts from 170 meV in WS_2 to 330 in MoS_2. In the trilayer samples this effect is still present, but the evolution of the Q-Γ indirect gap is more modest, spanning from 350 meV in WS_2 to 410 in MoS_2. The energy range is different in the two cases probably as a consequence of the smaller Q-Γ energy difference in the trilayer compared to the bilayers.

6.8 Conclusions

In conclusion, we systematically investigated with PL and RC spectroscopy, the optical properties of a set of nine $Mo_xW_{(1-x)}S_2$ samples in their mono, bi and trilayer form as a function of their composition x. All samples revealed the presence of A and B excitons in PL and RC, but also the PL spectra in the bilayer and trilayer exhibit a low energy peak (I) related to the indirect gap transition. Such features follows the parabolic dependence on x of $Mo_xW_{(1-x)}S_2$. Also, the I peak evolution versus x can be described with the same equation. This result is non trivial, since the orbital contribution away from K=0 in the sample band structure involve a non-neglible contribution from the chalcogen p-orbital. Surprisingly, the tuning range of I feature, as a function of x is 228 meV in the bilayer sample, and 131 meV in the trilayer samples as a consequence of the indirect gap closure of the material. The homogeneous dependence of I peak across the sample composition in bilayer samples suggest that the CB edge state in MoS_2 can be localized in the Q valley independently from the sample compositions. Many independent works address this evidence for bilayer WS_2 while the description of bilayer MoS_2 is less clear due to the close energy proximity of the K and the Q valleys in the CB. On the other hand the band structure at the K point of the Brillouin zone revealed a minimal discrepancy as a function of the material thicknesses, both in PL and RC data. The A-B exciton splitting reveals a linear dependence across the chemical composition of the materials, in contrast to previous reports. This trend was identical for

mono- bi- and trilayer samples. This insensitivity to layer thickness is explained considering the orbital composition in the *K* valley, which exhibits mainly a contribution of transition metal *d* orbitals. Since such states are localized on the transition metal atoms they are less sensitive to the sample thickness.

Finally, the *A*-*I* splitting increases with Mo concentration underlining the different evolution of the *Q*-Γ momentum indirect recombination for the different sample compositions compared to the *K*-*K* transitions. This effect is similar but quantitatively different in the trilayer samples. This work represents a systematic analysis of data that could be applied for simulating the band structure of atomically thin $Mo_xW_{(1-x)}S_2$ alloys.

The results presented indicate that bandgap engineering through alloys have very different effects on different portion of the band structure and it could provide new ideas to design and fabricate chemically engineered atomically thin devices that exploit the valley physics beyond the conventionally adopted *K* valley, enabling their use as novel platform for highly engineered optoelectronical devices with tuneable optical properties.

Chapter 7

Conclusions

In conclusion, in this work an investigation of novel vdW heterobilayers and TMD alloys by the mean of their optical properties is presented.

It described in detail a rapid and large-area PL imaging technique of 2D semiconducting TMD samples, achieved using a standard bright-field optical microscope. The presented technique offers a highly efficient and substrate-independent method of flake thickness identification that can be easily combined with a flake search equipment in one experimental setup. Furthermore, this technique can be used to monitor the electronic coupling between individual layers in vdW heterostructures. This method was applied successfully to investigate interlayer coupling in vdW heterostructures composed of both exfoliated and CVD-grown TMD monolayers. Also the same method has been applied to monitor the effect of thermal annealing on mechanically assembled vdW heterobilayers, along with a spectrally resolved characterization of the optical properties of TMD flakes before and after the thermal annealing step. The PL imaging presented techniques have also been applied to assess the interlayer coupling in TMD heterobilayers having various degrees of the rotational misalignment. The degree of intralayer exciton PL quenching depends on the relative orientation of the two layers, indicating twist-angle-dependent interlayer charge transfer. The high sensitivity of the PL intensity to the charge transfer efficiency makes the presented method a very sensitive

tool for investigating the coupling efficacy in TMD heterostructures with varying interlayer rotation and vertical separation. The short image acquisition times required makes it possible to investigate changes of the interlayer coupling in real time and in a non-destructive way.

Furthermore, the results of a set of vertical heterobilayers each composed by WSe_2 TMD alloy $Mo_xW_{(1-x)}Se_2$ whose composition range from pure $MoSe_2$ to pure WSe_2 are presented. The optical properties of these devices were fully characterized at low temperature (T<10K) by PL, RC, PL maps, power dependences and lifetimes. The rise of a photoluminescence emission originated by IX was unambiguosly demonstrated. This shows a blue shift as the alloy composition becomes progressively more W-rich, henceforth proving that the chemical control of one of the layers stochiometry is a feasible approach to achieve a band structure engineering in vdW heterobilayers. Also, IX does not follow a linear trend with the composition, but instead pins to the momentum indirect transition, which dominates the WSe_2 bilayer optical response. This fact clearly shows the insufficiency of the conventional picture used for the IX description in TMD-based devices and highlights the capital importance of taking into account also the other points of the BZ, beyond the *K* valley. This experiment showed that the use of alloys progressively resonant with the WSe_2 caused a total rearrangement of the band structure of the device, revealed by the different optical response and properties of the IX. A more general model of the excitonic states evolution in these devices is proposed on the basis of the experimental results, which imply the shift from from spatially indirect excitons with K=0 to delocalized excitons with K$\neq$0.

In the last part of this thesis the systematical investigation of the optical properties in emission and absorption of a set of $Mo_xW_{(1-x)}S_2$ samples in their mono-, bi- and trilayer form is reported. All the optical features identified in this set of samples follow the parabolic equation that describe the evolution of the *K* valley in monolayer TMD despite the valley considered were different. The tuning range of the indirect bandgap was analyzed according to sample composition and sample thickness and several observations about the band structure

evolution of these compound were presented. The indirect transition homogeneous evolution across the sample composition led us to the conclusion that the CB edge state in bilayer MoS_2 can be located in the Q valley. The A-B exciton splitting reveal an unreported linear dependence across the chemical composition of the materials, identical for mono-, bi-, and trilayer samples. This insensitivity to layer thickness is referred to the contribution of transition metal d orbitals in the K point of the Brillouin zone. The A-I splitting increase with the Mo concentration underlining the different evolution of the Q-Γ momentum indirect recombination for the different sample compositions compared to the K-K transitions. This effect is similar but quantitatively different in trilayer samples.

7.1 Suggestions for future work

The future field of research that this work opens up involves the use of TMD alloys as chemically tailored platforms, that can be used in more complex optoelectronic devices to enhance their performance and add an extra degree of freedom in the design and fabrication. Also, another exploitation might involve the fabrication and analysis of a vertically-gated alloy-based heterobilayer in which the control of the optical properties and the band gap engineering is achieved through chemical, physical and electrical manipulation. The tunable valley properties of the TMD alloys can be adopted to achieve a valley engineering in alloy based TMD heterobilayer. From the scientific point of view, this thesis shed light on the genesis and interpretation of the interlayer excitons in vdW heterostructures, intentionally blurring the line between heterobilayer and homobilayer, revealing the limit of the conventional models adopted nowadays, and proposing a more extended frame, which is able to describe the optical properties of vdW heterobilayers.

With increasing industrial and research interest in devices based on semiconductor vdW heterostructures, the PL imaging developed in this work offers a powerful characterization method suitable for both exfoliated and CVD-grown samples at various fabrication stages.

This work also represents a novel approach to the design and fabrication of nanoscale devices, demonstrating that it is possible to use TMDs alloys to create vdW heterobilayers to get a fine and continuous band gap engineering of the heterostructures electronic properties based on such materials, enabling their use as novel platform for highly engineered optoelectronical devices with tuneable optical properties.

References

[1] W. Andreoni. The physics of Fullerene-Based and Fullerene-related materials. *Springer*, 2000.

[2] J. C. Charlier et al. Electronic and transport properties of nanotubes. *Reviews of modern physics*, 79:677–732, 2007.

[3] K. S. Novoselov et al. Two-dimensional atomic crystals. *Proc. Natl. Acad. Sci.*, 102:10451, 2005.

[4] K. S. Novoselov et al. Electric Field Effect in Atomically Thin Carbon Films. *Science*, 306:666, 2004.

[5] A. K. Geim et al. The rise of graphene. *Nature Materials*, 6:183, 2007.

[6] Y. M. Lin et al. 100 GHz Transistors from Wafer-Scale Epitaxial Graphene. *Science*, 327:662, 2010.

[7] X. Du et al. Fractional quantum Hall effect and insulating phase of Dirac electrons in graphene. *Nature*, 462:192, 2009.

[8] R. R. Nair et al. Fine Structure Constant Defines Visual Transparency of Graphene. *Science*, 320:1308, 2008.

[9] A. K. Geim et al. Van der Waals heterostructures. *Nature*, 499:419, 2013.

[10] A. Castellanos et al. Why all the fuss about 2D semiconductors? *Nature Photonics*, 10:202, 2016.

[11] J. Li et al. Dielectric strength, optical absorption, and deep ultraviolet detectors of hexagonal boron nitride epilayers. *Applied Physics Letters*, 101:171112, 2010.

[12] R. V. Gorbachev et al. Hunting for Monolayer Boron Nitride: Optical and Raman Signatures. *Small*, 7:465–468, 2011.

[13] M. Chhowalla et al. The chemistry of two-dimensional layered transition metal dichalcogenide nanosheets. *Nature chemistry*, 5:263, 2013.

[14] K.F.Mak et al. Photonics and optoelectronics of 2D semiconductor transition metal dichalcogenides. *Nature Photonics*, 10:216, 2016.

[15] A. Splendiani et al. Emerging Photoluminescence in Monolayer MoS_2. *Nano Letters*, 10:1271, 2010.

[16] E. Mishina et al. Observation of two polytypes of MoS_2 ultrathin layers studied by second harmonic generation microscopy and photoluminescence. *Applied Physics Letters*, 106:131901, 2015.

[17] J. A. Silva-Guillen et al. Electronic Band Structure of Transition Metal Dichalcogenides from Ab Initio and Slater–Koster Tight-Binding Model. *Appl. Sci.*, 6:284, 2016.

[18] G. B. Liu et al. Three-band tight-binding model for monolayers of group-VIB transition metal dichalcogenides. *Physical Review B - Condensed Matter and Materials Physics*, 88:1, 2013.

[19] E. Ridolfi et al. A tight-binding model for MoS_2 monolayers. *Journal of Physics Condensed Matter*, 27:1, 2015.

[20] G. Liu et al. Electronic structures and theoretical modelling of two-dimensional group-VIB transition metal dichalcogenides. *Chem. Soc. Rev.*, 44:2643–2663, 2015.

[21] W. Zhao et al. Origin of Indirect Optical Transitions in Few-Layer MoS_2, WS_2, and WSe_2. *Nano Letters*, 13:5627–5634, 2013.

[22] M. Fox et al. Optical Properties of Solids. 2002.

[23] A. Chernikov et al. Exciton Binding Energy and Nonhydrogenic Rydberg Series in Monolayer WS_2. *Physical Review Letters*, 113:1, 2014.

[24] B. Zhu et al. Exciton Binding Energy of Monolayer WS_2. *Scientific Reports*, 5:9218, 2015.

[25] G. Wang et al. Spin-orbit engineering in transition metal dichalcogenide alloy monolayers. *Nature Communications*, 6:1–7, 2015.

[26] K. F. Mak et al. Tightly bound trions in monolayer MoS_2. *Nature Materials*, 12:207, 2013.

[27] K. Hao et al. Neutral and charged inter-valley biexcitons in monolayer $MoSe_2$. *Nature Communications*, 8:1, 2017.

[28] M. Barbone et al. Charge-tuneable biexciton complexes in monolayer WSe_2. *Nature Communications*, 9:1–6, 2018.

[29] Z. Li et al. Revealing the biexciton and trion-exciton complexes in BN encapsulated WSe_2. *Nature Communications*, 9:1–7, 2018.

[30] K. F. Mak et al. Atomically Thin MoS_2: A New Direct-Gap Semiconductor. *Physical Review Letters*, 105:2–5, 2010.

[31] M. Bernardi et al. Extraordinary Sunlight Absorption and One Nanometer Thick Photovoltaics Using Two-Dimensional Monolayer Materials. *2013*, 13:3664–3670, 2013.

[32] D. Xiao et al. Coupled Spin and Valley Physics in Monolayers of MoS_2 and Other Group-VI Dichalcogenides. *Physical Review Letters*, 108:1–5, 2012.

[33] J. Schaibley et al. Valleytronics in 2D materials. *Nature Reviews Materials*, 1:1–15, 2016.

[34] M. Palummo et al. Exciton Radiative Lifetimes in Two-Dimensional Transition Metal Dichalcogenides. *Nano Letters*, 15:2794–2800, 2015.

[35] X. X. Zhang et al. Experimental Evidence for Dark Excitons in Monolayer WSe_2. *Physical Review Letters*, 115:1–6, 2015.

[36] M. Koperski et al. Optical properties of atomically thin transition metal dichalcogenides: Observations and puzzles. *Nanophotonics*, 6:1289–1308, 2016.

[37] K. P. O'Donnell et al. Temperature dependence of semiconductor band gaps. *Applied Physics Letters*, 58:2924–2926, 1991.

[38] M. Selig et al. Excitonic linewidth and coherence lifetime in monolayer transition metal dichalcogenides. *Nature Communications*, 7:1–6, 2016.

[39] A. Kormanyos et al. k·p theory for two-dimensional transition metal dichalcogenide semiconductors. *2D Materials*, 2:1–31, 2015.

[40] D. Y. Qiu et al. Nonanalyticity, Valley Quantum Phases, and Lightlike Exciton Dispersion in Monolayer Transition Metal Dichalcogenides: Theory and First-Principles Calculations. *Physical Review Letters*, 115:1–5, 2015.

[41] P. San-Jose et al. Inverse Funnel Effect of Excitons in Strained Black Phosphorus. *Physical Review X*, 6:1–12, 2016.

[42] F. Cadiz et al. Ultra-low power threshold for laser induced changes in optical properties of 2D molybdenum dichalcogenides. *2D Materials*, 3:1–8, 2016.

[43] O. A. Ajayi et al. Approaching the Intrinsic Photoluminescence Linewidth in Transition Metal Dichalcogenide Monolayers. *2D Materials*, 4:1–6, 2017.

[44] W. S. Yun et al. Thickness and strain effects on electronic structures of transition metal dichalcogenides: 2H-MX_2 semiconductors (M = Mo, W; X = S, Se, Te). *Physical Review B*, 85:1–5, 2012.

[45] X. Li et al. Graphene and related two-dimensional materials: Structure-property relationships for electronics and optoelectronics. *Appl Phys Rev.*, 4:1–25, 2017.

[46] C. Klingshirn. Semiconductor Optics. 2007.

[47] A. F. Rigosi et al. Electronic band gaps and exciton binding energies in monolayer $Mo_xW_{1-x}S_2$ transition metal dichalcogenide alloys probed by scanning tunneling and optical spectroscopy. *Physical Review B*, 94:1–6, 2016.

[48] Z. Yin et al. A review of energy bandgap engineering in III–V semiconductor alloys for mid-infrared laser applications. *ScienceDirect*, 51:6–15, 2007.

[49] Q. Fu et al. Synthesis and Enhanced Electrochemical Catalytic Performance of Monolayer $WS_{2(1-x)}Se_{2x}$ with a Tunable Band Gap. *Advanced Materials*, 2:4732–4738, 2015.

[50] J. Mann et al. 2-Dimensional Transition Metal Dichalcogenides with Tunable Direct Band Gaps: $MoS_{2(1-x)}Se_{2x}$ Monolayers. *Advanced Materials*, 2:1399–1404, 2014.

[51] J. Kang et al. Band offsets and heterostructures of two-dimensional semiconductors. *Applied Physics Letters*, 102:22–25, 2013.

[52] Q. Feng et al. Growth of Large Area 2D $MoS_{2(1-x)}Se_{2x}$ Semiconductor Alloys. *Advanced Materials*, 26:2648–2653, 2014.

[53] L. Yang et al. Large-area synthesis of monolayered $MoS_{2(1-x)}Se_{2x}$ with a tunable band gap and its enhanced electrochemical catalytic activity. *Nanoscale*, pages 10490–10497, 2015.

[54] X. Wang et al. Controlled Synthesis of Highly Crystalline MoS_2 Flakes by Chemical Vapor Deposition. *Journal of the American Chemical Society*, 135:5–8, 2013.

[55] S. M. Eichfeld et al. Highly scalable, atomically thin WSe_2 grown via metal-organic chemical vapor deposition. *ACS Nano*, 9:2080–2087, 2015.

[56] Y. Kobayashi et al. Bandgap-tunable lateral and vertical heterostructures based on monolayer $Mo_{(1-x}W_xS_2$ alloys. *Nano Research*, 8:3261–3271, 2015.

[57] X. Duan et al. Synthesis of $WS_{2x}Se_{2-2x}$ Alloy Nanosheets with Composition-Tunable Electronic Properties. *Nano Letters*, 16:264–269, 2016.

[58] Y. Chen et al. Tunable Band Gap Photoluminescence from Atomically Thin Transition-Metal Dichalcogenide Alloys. *ACS Nano*, 7:4610–4616, 2013.

[59] M. Zhang et al. Two-Dimensional Molybdenum Tungsten Diselenide Alloys: Photoluminescence, Raman Scattering, and Electrical Transport. *ACS Nano*, 8:7130–7137, 2014.

[60] N. Tit et al. Origins of bandgap bowing in compound- semiconductor common-cation ternary alloys. *Journal of Physics: Condensed Matter*, 21:1–6, 2009.

[61] L. M. Xie et al. Two-dimensional transition metal dichalcogenide alloys: preparation, characterization and applications. *Nanoscale*, 7:18392–18401, 2015.

[62] J. Xi et al. Tunable Electronic Properties of Two-Dimensional Transition Metal Dichalcogenide Alloys: A First-Principles Prediction. *Journal of Physical Chemistry Letters*, 5:285–291, 2014.

[63] L. Y. Gan et al. Order-disorder phase transitions in the two-dimensional semiconducting transition metal dichalcogenide alloys $Mo_{1-x}W_xX_2$ (X = S, Se, and Te). *Scientific Reports*, 4:1–5, 2014.

[64] A. Kutana et al. Engineering electronic properties of layered transition-metal dichalcogenide compounds through alloying. *Nanoscale*, 6:5820–5825, 2014.

[65] K. Kosmider et al. Large spin splitting in the conduction band of transition metal dichalcogenide monolayers. *Physical Review B - Condensed Matter and Materials Physics*, 88:1–7, 2013.

[66] M. Konig et al. Quantum Spin Hall Insulator State in HgTe Quantum Wells. *Science*, 318:766–771, 2007.

[67] J. Kasprzak et al. Bose–Einstein condensation of exciton polaritons. *Nature*, 443:409–414, 2006.

[68] P. Cristofolini et al. Coupling Quantum Tunneling with Cavity Photons. *Science*, 336:704–707, 2012.

[69] H. Fang et al. Strong interlayer coupling in van der Waals heterostructures built from single-layer chalcogenides. *Proc. Natl. Acad. Sci.*, 111:6198–6202, 2014.

[70] T. Roy et al. Dual-Gated MoS_2 /WSe_2 van der Waals Tunnel Diodes and Transistors. *ACS Nano*, 9:2071–2079, 2015.

[71] J. He et al. Electron transfer and coupling in graphene-tungsten disulfide van der Waals heterostructures. *Nature communications*, 5:1–5, 2014.

[72] K. S. Novoselov et al. 2D materials and van der Waals heterostructures. *Science*, 353:1–11, 2016.

[73] J. Xue et al. Scanning tunnelling microscopy and spectroscopy of ultra-flat graphene on hexagonal boron nitride. *Nature Materials*, 10:282–285, 2011.

[74] R. Decker et al. Local Electronic Properties of Graphene on a BN Substrate via Scanning Tunneling Microscopy. *Nano Letters*, 11:2291–2295, 2011.

[75] J. H. Chen et al. Intrinsic and extrinsic performance limits of graphene devices on SiO_2. *Nature Nanotechnology*, 3:8–11, 2008.

[76] F. Cadiz et al. Excitonic Linewidth Approaching the Homogeneous Limit in MoS_2-Based van der Waals Heterostructures. *Physical Review X*, 7:1–12, 2017.

[77] S. Dufferwiel et al. Exciton–polaritons in van der Waals heterostructures embedded in tunable microcavities. *Nature communications*, 6:1–7, 2015.

[78] A. F. Rigosi et al. Probing Interlayer Interactions in Transition Metal Dichalcogenide Heterostructures by Optical Spectroscopy: MoS_2/WS_2 and $MoSe_2$/ WSe_2. *Nano Letters*, 15:5033–5038, 2015.

[79] F. Ceballos et al. Probing charge transfer excitons in a $MoSe_2$-WS_2 van der Waals heterostructure. *Nanoscale*, 7:17523–17528, 2015.

[80] P. Nagler et al. Interlayer exciton dynamics in a dichalcogenide monolayer heterostructure. *2D Materials*, 1:1–12, 2017.

[81] X. Hong et al. Ultrafast charge transfer in atomically thin MoS_2/WS_2 heterostructures. *Nature Nanotechnology*, 9:1–5, 2014.

[82] Y. Yu et al. Equally efficient interlayer exciton relaxation and improved absorption in epitaxial and non epitaxial MoS_2/WS_2 heterostructures. *Nano Letters*, 15:486–491, 2015.

[83] P. Rivera et al. Observation of long-lived interlayer excitons in monolayer $MoSe_2$-WSe_2 heterostructures. *Nature communications*, 6:6242, 2015.

[84] F. Ceballos et al. Ultrafast Charge Separation and Indirect Exciton Formation in a MoS_2-$MoSe_2$ van der Waals Heterostructure. *ACS Nano*, 8:12717–12724, 2014.

[85] Y. Yu et al. Anomalous Light Cones and Valley Optical Selection Rules of Interlayer Excitons in Twisted Heterobilayers. *Physical Review Letters*, 115:1–5, 2015.

[86] P. Rivera et al. Interlayer valley excitons in heterobilayers of transition metal dichalcogenides. *Nature Nanotechnology*, 13:1004–1015, 2018.

[87] Y. Wang et al. Interlayer coupling in commensurate and incommensurate bilayer structures of transition-metal dichalcogenides. *Physical Review B*, 95:41–45, 2017.

[88] H. P. Komsa et al. Electronic structures and optical properties of realistic transition metal dichalcogenide heterostructures from first principles. *Physical Review B - Condensed Matter and Materials Physics*, 88:1–7, 2013.

[89] H. Heo et al. Interlayer orientation-dependent light absorption and emission in monolayer semiconductor stacks. *Nature Communications*, 6:1–7, 2015.

[90] K. Kosmider et al. Electronic properties of the MoS_2-WS_2 heterojunction . *Physical Review B*, 87:1–4, 2013.

[91] H. Terrones et al. Novel hetero-layered materials with tunable direct band gaps by sandwiching different metal disulfides and diselenides. *Scientific Reports*, 3:1–7, 2013.

[92] B. Amin et al. Heterostructures of transition metal dichalcogenides B. *Physical Review B - Condensed Matter and Materials Physics*, 92:1–6, 2015.

[93] S. Tongay et al. Two-dimensional semiconductor alloys: Monolayer $Mo_{1-x}W_xSe_2$. *Applied Physics Letters*, 104:1–5, 2014.

[94] A. M. v. d. Zande et al. Tailoring the Electronic Structure in Bilayer Molybdenum Disulfide via Interlayer Twist. *Nano Letters*, 14:3869–3875, 2014.

[95] C.S. Liu et al. Theory of indirect exciton photoluminescence in elevated quantum trap. *Physica E: Low-Dimensional Systems and Nanostructures*, 63:193–198, 2014.

[96] N. R. Wilson et al. Band parameters and hybridization in 2D semiconductor heterostructures from photoemission spectroscopy. *ArXiv*, page 1601.05865, 2016.

[97] N. R. Wilson et al. Determination of band offsets, hybridization, and exciton binding in 2D semiconductor heterostructures. *Science Advances*, 3:1–7, 2017.

[98] Y. Gong et al. Vertical and in-plane heterostructures from WS_2/MoS_2 monolayers. *Nature Materials*, 13:1135–1142, 2014.

[99] J. R. Schaibley et al. Directional interlayer spin-valley transfer in two-dimensional heterostructures. *Nature Communications*, 7:13747, 2016.

[100] B. Miller et al. Long-lived direct and indirect interlayer excitons in van der Waals heterostructures. *Nano Letters*, 17:5229–5237, 2017.

[101] P. K. Nayak et al. Probing evolution of twist-angle-dependent interlayer excitons in $MoSe_2$/WSe_2 van der Waals heterostructures. *ACS Nano*, 11:4041–4050, 2017.

[102] J. S. Ross et al. Interlayer exciton optoelectronics in a 2D heterostructure p–n junction. *Nano Letters*, 17:638–643, 2017.

[103] E. M. Alexeev et al. Imaging of interlayer coupling in van der Waals heterostructures using a bright-field optical microscope. *Nano Letters*, 17:5342–5349, 2017.

[104] M. Z. Bellus et al. Tightly bound trions in transition metal dichalcogenide heterostructures. *ACS Nano*, 9:6459–6464, 2015.

[105] M. H. Chiu et al. Spectroscopic signatures for interlayer coupling in MoS_2-WSe_2 van der Waals stacking. *ACS Nano*, 8:9649–9656, 2014.

[106] D. H. Luong et al. Tunneling photocurrent assisted by interlayer excitons in staggered van der Waals hetero-bilayers. *Advanced Materials*, 29:1701512, 2017.

[107] S. Mouri et al. Thermal dissociation of inter-layer excitons in MoS_2/$MoSe_2$ hetero-bilayers. *Nanoscale*, 9:6674–6679, 2017.

[108] K. Wang et al. Interlayer coupling in twisted WSe_2/WS_2 bilayer heterostructures revealed by optical spectroscopy. *ACS Nano*, 10:6612–6622, 2016.

[109] F. A. Rasmussen et al. Computational 2D Materials Database: Electronic Structure of Transition-Metal Dichalcogenides and Oxides. *J. Phys. Chem. C.*, 119:13169–13183, 2015.

[110] M. M. Ugeda et al. Giant bandgap renormalization and excitonic effects in a monolayer transition metal dichalcogenide semiconductor. *Nature Materials*, 13:1091–1095, 2014.

[111] K. He et al. Tightly Bound Excitons in Monolayer WSe_2. *Physical Review Letters*, 113:1–5, 2014.

[112] S. Latini et al. Interlayer Excitons and Band Alignment in MoS_2/hBN/WSe_2 van der Waals Heterostructures. *2017*, 17:938–945, 2017.

[113] M. Danovich et al. Localized interlayer complexes in heterobilayer transition metal dichalcogenides. *Physical Review B*, 97:1–18, 2018.

[114] J. Kunstmann et al. Momentum-space indirect interlayer excitons in transition-metal dichalcogenide van der Waals heterostructures. *Nature Physics*, 14:801–805, 2018.

[115] B. Radisavljevic et al. Single-layer MoS_2 transistors. *Nature Nanotechnology*, 6:147–150, 2011.

[116] H. Fang et al. High-performance single layered WSe_2 p-FETs with chemically doped contacts. *Nano Letters*, 12:3788–3792, 2012.

[117] Z. Wang et al. Electrical Tuning of Interlayer Exciton Gases in WSe_2 Bilayers. *Nano Letters*, 18:137–143, 2018.

[118] B. Laikhtman et al. Exciton correlations in coupled quantum wells and their luminescence blue shift. *Physical Review B*, 80:1–12, 2009.

[119] L. V. Butov et al. Magneto-optics of the spatially separated electron and hole layers in $GaAs/Al_xGa_{1-x}As$ coupled quantum wells. *Physical Review B*, 60:8753 – 8758, 1999.

[120] N. Kumar et al. Exciton-exciton annihilation in $MoSe_2$ monolayers. *Physical Review B*, 89:1–12, 2014.

[121] D. Sun et al. Observation of rapid exciton-exciton annihilation in monolayer molybdenum disulfide. *Nano Letters*, 14:5625–5635, 2014.

[122] S. Mouri et al. Nonlinear photoluminescence in atomically thin layered WSe_2 arising from diffusion-assisted exciton-exciton annihilation. *Physical Review B*, 90:1–5, 2014.

[123] M. J. Shin et al. Photoluminescence saturation and exciton decay dynamics in transition metal dichalcogenide monolayers. *J. Korean Phys. Soc*, 65:1–6, 2014.

[124] Edbert Jarvis Sie. Coherent Light-Matter Interactions in Monolayer Transition-Metal Dichalcogenides. *Springer*, 2018.

[125] E. Torun et al. Inter- and intra-layer excitons in MoS_2/WS_2 and $MoSe_2/WSe_2$ heterobilayers. *ArXiv*, page 1803.05483, 2018.

[126] Kolobov et al. Two-Dimensional Transition-Metal Dichalcogenides. *Springer*, 2016.

[127] M. Combescot et al. Bose–Einstein condensation and indirect excitons: a review. *Reports on Progress in Physics*, 80:1–44, 2017.

[128] A. T. Hanbicki et al. Double Indirect Interlayer Exciton in a $MoSe_2/WSe_2$ van der Waals Heterostructure. *ACS Nano*, 12:4719–4726, 2018.

[129] A. Ciarrocchi et al. Control of interlayer excitons in two-dimensional van der Waals heterostructures. *ArXiv*, page 1803.06405, 2018.

[130] A. Castellanos-Gomez et al. Deterministic transfer of two-dimensional materials by all-dry viscoelastic stamping. *2D Materials*, 1:1–8, 2014.

[131] C. R. Dean et al. Boron nitride substrates for high-quality graphene electronics. *Nature Nanotechnology*, 5:722–726, 2010.

[132] T. Uwanno et al. Fully dry PMMA transfer of graphene on h -BN using a heating/cooling system. *2D Materials*, 2:1–10, 2015.

[133] C. Casiraghi et al. Rayleigh imaging of graphene and graphene layers. *Nano Letters*, 7:2711–2717, 2007.

[134] A. c. Ferrari et al. Raman Spectrum of Graphene and Graphene Layers. *Physical Review Letters*, 97:1–4, 2006.

[135] P. Blake et al. Making graphene visible. *Applied Physical Letters*, 91:1–3, 2007.

[136] S. J. Haigh et al. Cross-sectional imaging of individual layers and buried interfaces of graphene-based heterostructures and superlattices. *Nature Materials*, 11:764–767, 2012.

[137] A. V. Kretinin et al. Electronic Properties of Graphene Encapsulated with Different Two-Dimensional Atomic Crystals. *Nano Letters*, 14:3270–3276, 2014.

[138] S. Neubeck et al. Direct determination of the crystallographic orientation of graphene edges by atomic resolution imaging. *Appl Phys Lett*, 97:2010–2012, 2010.

[139] E. H. Lock et al. High-Quality Uniform Dry Transfer of Graphene to Polymers. *Nano Letters*, 12:102–107, 2012.

[140] C. Palacios-Berraquero et al. Large-scale quantum-emitter arrays in atomically thin semiconductors. *Nature Communications*, 8:1–6, 2017.

[141] T. Galfsky et al. Broadband Enhancement of Spontaneous Emission in Two- Dimensional Semiconductors Using Photonic Hypercrystals. *Nano Letters*, 16:4940–4945, 2016.

[142] N. Morell et al. High Quality Factor Mechanical Resonators Based on WSe_2 Monolayers. *Nano Letters*, 16:5102–5108, 2016.

[143] M. Y. Li et al. Heterostructures based on two-dimensional layered materials and their potential applications. *Materials Today*, 19:322–335, 2016.

[144] Y. Liu et al. Van der Waals heterostructures and devices. *Nature Reviews Materials*, 1:1–17, 2016.

[145] T. Roy et al. Field-effect transistors built from all two-dimensional material components. *ACS Nano*, 8:6259–6264, 2014.

[146] S. Das et al. All two-dimensional, flexible, transparent, and thinnest thin film transistor. *Nano Letters*, 17:2861–2866, 2014.

[147] G. H. Lee et al. Highly Stable, Dual-Gated MoS_2 Transistors Encapsulated by Hexagonal Boron Nitride with Gate-Controllable Contact, Resistance, and Threshold Voltage. *ACS Nano*, 9:7019–7026, 2015.

[148] Y. Liu et al. Toward Barrier Free Contact to Molybdenum Disulfide Using Graphene Electrodes. *Nano Letters*, 15:3030–3034, 2015.

[149] X. Cui et al. Multi-terminal transport measurements of MoS_2 using a van der Waals heterostructure device platform. *Nature Nanotechnology*, 10:534–540, 2015.

[150] j. S. Ross et al. Electrically tunable excitonic light-emitting diodes based on monolayer WSe_2 p–n junctions. *Nature Nanotechnology*, 9:268–272, 2014.

[151] R. Cheng et al. Electroluminescence and Photocurrent Generation from Atomically Sharp WSe_2 /MoS_2 Heterojunction p–n Diodes. *Nano Letters*, 14:5590–5597, 2014.

[152] F. Withers et al. WSe_2 Light-Emitting Tunneling Transistors with Enhanced Brightness at Room Temperature. *Nano Letters*, 15:8223–8228, 2015.

[153] F. Withers et al. Light-emitting diodes by band-structure engineering in van der Waals heterostructures. *Nature Materials*, 14:301–306, 2015.

[154] L. Britnell et al. Field-Effect Tunneling Transistor Based on Vertical Graphene Heterostructures. *Science*, 343:947–950, 2012.

[155] L. Britnell et al. Resonant tunnelling and negative differential conductance in graphene transistors. *Nature Communications*, 4:1794–1795, 2013.

[156] Y. Lin et al. Atomically thin resonant tunnel diodes built from synthetic van der Waals heterostructures. *Nature Communications*, 6:1–6, 2015.

[157] M. Buscema et al. Photocurrent generation with two-dimensional van der Waals semiconductors. *Chemical Society Reviews*, 44:3691–3718, 2015.

[158] M. Buscema et al. Photovoltaic effect in few-layer black phosphorus PN junctions defined by local electrostatic gating. *Nature Communications*, 5:1–6, 2014.

[159] M. M. Furchi et al. Photovoltaic Effect in an Electrically Tunable van der Waals Heterojunction. *Nano Letters*, 14:4785–4791, 2014.

[160] C. Lee et al. Atomically thin p–n junctions with van der Waals heterointerfaces. *Nature Nanotechnology*, 9:676–681, 2014.

[161] Y. Deng et al. Black phosphorus-monolayer MoS_2 van der Waals heterojunction p-n diode. *ACS Nano*, pages 8292–8299.

[162] M. Massicotte et al. Picosecond photoresponse in van der Waals heterostructures. *Nature nanotechnology*, 11:1–6, 2015.

[163] W. J. Yu et al. Unusually efficient photocurrent extraction in monolayer van der Waals heterostructure by tunnelling through discretized barriers. *Nature Communications*, 7:1–9, 2016.

[164] S. Tongay et al. Tuning Interlayer Coupling in Large-Area Heterostructures with CVD- Grown MoS_2 and WS_2 Monolayers. *Nano Letters*, 14:3185–3190, 2014.

[165] C. Lui et al. Observation of interlayer phonon modes in van der Waals heterostructures. *Physical Review B - Condensed Matter and Materials Physics*, 91:1–7, 2015.

[166] D. Kozawa et al. Evidence for Fast Interlayer Energy Transfer in $MoSe_2$/WS_2 Heterostructures. *Nano Letters*, 16:4087–4093, 2016.

[167] Zhang et al. Interlayer Transition and Infrared Photodetection in Atomically Thin Type-II $MoTe_2$/MoS_2 van der Waals Heterostructures. *ACS Nano*, 10:3852–3858, 2016.

[168] M. M. Fogler et al. High-temperature superfluidity with indirect excitons in van der Waals heterostructures. *Nature communications*, 5:1–5, 2014.

[169] P. Rivera et al. Valley-Polarized Exciton Dynamics in a 2D Semicondcutor Heterostructure. *Science*, 351:688–691, 2016.

[170] C. Huang et al. Lateral heterojunctions within monolayer $MoSe_2$-WSe_2 semiconductors. *Nature Materials*, 13:1096–1101, 2014.

[171] X. Duan et al. Lateral epitaxial growth of two-dimensional layered semiconductor heterojunctions. *Nature Nanotechnology*, 2014:1024–1030, 9.

[172] Y. Gong et al. Two-Step Growth of Two-Dimensional WSe_2/$MoSe_2$ Heterostructures. *Nano Letters*, 15:6135–6141, 2015.

[173] S. Yoshida et al. Microscopic basis for the band engineering of $Mo_{1-x}W_xS_2$-based heterojunction. *Scientific Reports*, 5:1–6, 2015.

[174] H. Li et al. Lateral Growth of Composition Graded Atomic Layer $MoS_{2(1-x)}Se_{2x}$ Nanosheets. *Journal of the American Chemical Society*, 137:5284–5287, 2015.

[175] M. Li et al. Epitaxial growth of a monolayer WSe_2-MoS_2 lateral p-n junction with an atomically sharp interface. *Science*, 349:524–528, 2015.

[176] A. Pant et al. Fundamentals of lateral and vertical heterojunctions of atomically thin materials. *Nanoscale*, 8:3870–3887, 2016.

[177] W. Xu et al. Correlated fluorescence blinking in two- dimensional semiconductor heterostructures. *Nature*, 541:62–67, 2017.

[178] P. Tonndorf et al. Photoluminescence emission and Raman response of monolayer MoS_2, $MoSe_2$, and WSe_2. *Optics Express*, 3:4908–4916, 2013.

[179] V. O. Ozcelik et al. Band alignment of two-dimensional semiconductors for designing heterostructures with momentum space matching. *Physical Review B*, 94:1–9, 2016.

[180] C. Robert et al. Exciton radiative lifetime in transition metal dichalcogenide monolayers. *Physical Review B*, 93:1–10, 2016.

[181] K. S. Vasu et al. Van der Waals pressure and its effect on trapped interlayer molecules. *Nature Communications*, 7:1–6, 2016.

[182] M. S. Kim et al. Simultaneous Hosting of Positive and Negative Trions and the Enhanced Direct Band Emission in $MoSe_2$/MoS_2 Heterostacked Multilayers. *ACS Nano*, 10:6211–6219, 2016.

[183] Q. Ji et al. Chemical vapour deposition of group-VIB metal dichalcogenide monolayers: engineered substrates from amorphous to single crystalline. *Chemical Society Reviews*, 2015:2587–2602, 2015.

[184] D. Zhu et al. Capture the growth kinetics of CVD growth of two-dimensional MoS_2. *npj 2D Materials and Applications*, 8:1–7, 2016.

[185] C. Gong et al. Band alignment of two-dimensional transition metal dichalcogenides: Application in tunnel field effect transistors. *Applied Physical Letters*, 103:1–4, 2013.

[186] H. Zhu et al. Interfacial Charge Transfer Circumventing Momentum Mismatch at Two-Dimensional van der Waals Heterojunctions. *Nano Letters*, 17:3591–3598, 2017.

[187] S. Gao et al. Interlayer Coupling and Gate-Tunable Excitons in Transition Metal Dichalcogenide Heterostructures. *Nano letters*, 17:7809–7813, 2017.

[188] Z. Gong et al. Magnetoelectric effects and valley-controlled spin quantum gates in transition metal dichalcogenide bilayers. *Nature Communications*, 4:1–6, 2013.

[189] D. Voß et al. Atomic and electronic structure of WSe_2 from ab initio theory: Bulk crystal and thin film systems. *Physical Review B*, 60:14311–14317, 1999.

[190] J. Lindlau et al. The role of momentum-dark excitons in the elementary optical response of bilayer WSe_2. *Nature Communications*, 9:1–7, 2018.

[191] C. Poellmann et al. Resonant internal quantum transitions and femtosecond radiative decay of excitons in monolayer WSe_2. *Nature Materials*, 14:889–894, 2015.

[192] I. Kylänpää et al. Binding energies of exciton complexes in transition metal dichalcogenide monolayers and effect of dielectric environment. *Physical Review B - Condensed Matter and Materials Physics*, 92:1–6, 2015.

[193] R. Gillen et al. Interlayer excitons in $MoSe_2$/WSe_2 heterostructures from first principles. *Physical Review B*, 97:1–7, 2018.

[194] J. S. Ross et al. Electrical control of neutral and charged excitons in a monolayer semiconductor. *Nature Communications*, 4:1–6, 2013.

[195] H. Liu et al. Molecular-beam epitaxy of monolayer and bilayer WSe_2: A scanning tunneling microscopy/spectroscopy study and deduction of exciton binding energy. *2D Materials*, 2:1–8, 2015.

[196] G. Wang et al. Exciton dynamics in WSe_2 bilayers. *Applied Physics Letters*, 105:1–5, 2014.

[197] X. Wei et al. Modulating the atomic and electronic structures through alloying and heterostructure of single-layer MoS_2. *J. Mater. Chem. A*, 2:2101–2109, 2014.

[198] Y. Gong et al. Band Gap Engineering and Layer-by-Layer Mapping of Selenium-Doped Molybdenum Disulfide. *Nano Letters*, 14:442–449, 2014.

[199] Q. H. Wang et al. Electronics and optoelectronics of two-dimensional transition metal dichalcogenides. *Nature Nanotechnology*, 7:699–712, 2012.

[200] V. Podzorov et al. High-mobility field-effect transistors based on transition metal dichalcogenides. *Applied Physics Letters*, 84:3301–3303, 2004.

[201] Z. Y. Zhu et al. Giant spin-orbit-induced spin splitting in two-dimensional transition-metal dichalcogenide semiconductors. *Physical Review B - Condensed Matter and Materials Physics*, 84:1–5, 2011.

[202] X. Xu et al. Spin and pseudospins in layered transition metal dichalcogenides. *Nature Physics*, 10:343–350, 2014.

[203] H. Zeng et al. Optical signature of symmetry variations and spin-valley coupling in atomically thin tungsten dichalcogenides. *Scientific Reports*, 3:1–5, 2013.

[204] R. Suzuki et al. Valley-dependent spin polarization in bulk MoS_2 with broken inversion symmetry. *Nature Nanotechnology*, 9:611–617, 2014.

[205] Y. Chen et al. Composition-dependent Raman modes of $Mo_{1-x}W_xS_2$ monolayer alloys. *Nanoscale*, 6:2833–2839, 2014.

[206] X. Qiao et al. O. *Applied Physics Letters*, 106:1–5, 2015.

[207] T. Livneh et al. Determining alloy composition in $Mo_xW_{(1-x)}S_2$ from low wavenumber Raman spectroscopy. *Journal of Raman Spectroscopy*, 48:773–776, 2017.

[208] W. Zhao et al. Evolution of Electronic Structure in Atomically Thin Sheets of WS_2 and WSe_2. *Journal of Physics and Chemistry of Solids*, 72:474–478, 2011.